Università degli Studi di Cagliari
Facoltà di Scienza della Terra
Settore scientifico Geochimica e Vulcanologia

CORSO DI DOTTORATO DI RICERCA-XX CICLO

PhD Thesis

"DYNAMICS OF ASH ERUPTIONS AT VESUVIUS"

Candidata

Claudia D'Oriano

Tutore:
Raffaello Cioni

a.a. 2006/2007

Unum scio me nihil scire

(Socrates, 470-339 BC)

CONTENTS

ABSTRACT

In the recent years, continuous ash emission activity, related to mid-low intensity, long lasting eruptions, has been increasingly described to occur at different volcanoes worldwide. At the same time, a retrospective analysis of the stratigraphic successions at Vesuvius revealed that such type of eruptions have occurred repeatedly in the last 4000 years of activity. This type of activity has been overlooked in the past and the mechanism of ash production in these eruptions is not yet clear. The detailed study of the deposits suggests that these eruptions are dominated by discrete phases of repeated emission of a highly fragmented mixture, alternated with violent strombolian episodes. In this study we presents morphological, textural and compositional data on the products of two ash eruptions representative of the whole variability of this activity at Vesuvius (Italy), occurred in the periods between the "Avellino" and "Pompeii" Pumice eruptions (AP3, 2,710±60 years B.P.) and after the 512 A.D. eruption, (AS1a). Juvenile fragments from different ash layers throughout the studied stratigraphic sections were randomly hand-picked, and fully characterized in terms of external morphology, particle outline parameterization, groundmass texture (in terms of Crystal and Vesicle Size Distributions) and glass composition. Ashes generated during these eruptions show large variability of all the investigated features: results have been interpreted in terms of fragmentation processes, transport and dispositional mechanisms, dynamics of magma ascent ant timing of the eruption, allowing to define a scenario for this type of eruptions useful both for hazard assessment and emergency planning. .

Tab.1 *Symbols used*

	Symbols
D	Partitioning coefficient between crystals and melt (glass)for trace elements
d	Particle diameter
G	Crystal growth rate (length/time)
J	Crystal nucleation rate (length/time)
L	Crystal size
n	Number of compositional analyses
n°	Nuclei number density (number/unit volume/size)
N_A	Number of microlites per unit area (number/reference area)
s_n	Average crystal linear size
σ	Standard deviation
τ	Resident time for kinetic of nucleation and crystallization (time)
φ	Fraction microlites (volume per cent)
Φ	$-\log_2(d)$
R^2	Mean square deviation

1. INTRODUCTION

Explosive eruptions commonly produce and disperse large amounts of volcanic ash, fragments with a diameter smaller than 2 mm produced by mechanical fragmentation of magma and/or country rock. Ash-producing eruptions cover a wide range of styles, and are controlled by magma properties as composition, crystal content, temperature, and dissolved gases, and by the eventual interaction with external fluids like groundwater or surface water. Correspondingly, volcanic ash holds information about magma dynamics within the volcanic conduit, where fragmentation occurs and eruption style is decided. Indeed, ash fragments can be seen as small tesserae of an instantaneous picture of the magma features at the moment of fragmentation, with only minor or no modifications after the entrance in the atmosphere for the very rapid quenching related to their small size (Heiken, 1972).

Those eruptions generally considered responsible of important ash production are the Plinian eruptions, the most energetic from the point of view of primary, magmatic fragmentation (Fig. 1.1a), and the whole range of phreatomagmatic (hydromagmatic) eruptions, which typically produce fine ash deposits by a fragmentation mechanism involving explosive vaporization of external water by magmatic heat (Fig. 1.1b; Self and Sparks, 1978). On the other side, eruptions characterized by a low magmatic explosivity, like hawaiian or strombolian eruptions, are generally not able to generate and disperse large amounts of ash (Fig. 1.1c).

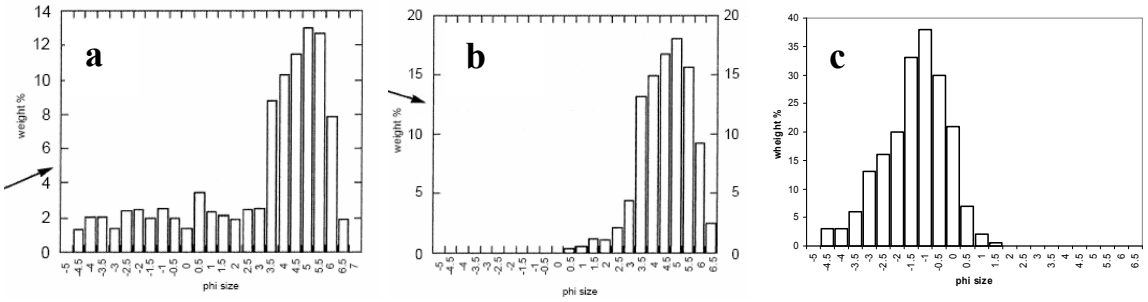

Fig.1.1 a) Grain size distribution of the fine ash layer of magmatic origin associated to a Plinian pumice deposit of Arenal Volcano (Costa Rica); b) Grain size distribution of the fine ash layer (phi=-log2 (diameter in mm)) of phreatomagmatic origin from the Agnano Monte Spina deposits at the Phlegraean Fields (Italy); c) Grain size distribution of a typical strombolian deposit.

Ash formation is believed to depend on the kinetic of gas evolution, the crucial factor being the number of bubbles per unit volume which may be present at a certain time in the magma, and by the efficiency of the conversion of magmatic heat into mechanical energy (Cashman et al., 2000; Zimanowski et al., 2003).

In the last years, the volcanological community has increasingly focussed his attention on the occurrence ash-dominated eruptions, mainly after the direct observations of many of these eruptions worldwide. Such eruptions have been described as long-lasting episodes of mid-low intensity activity associated with continuous or pulsating ash emission, and generating weak plumes, less than 10 Km in height (Bonadonna et al., 2005).

These ash-dominated events have been directly or indirectly documented at many volcanoes:

1) Mt Etna (Italy): during the final stage of the July-August 2001 eruption, a sustained to pulsating phase of ash explosions occurred, dispersing large amounts of ash and inducing severe problems to the economics and managerial policy of the neighbouring communities (Taddeucci, et al. 2002, Taddeucci, et al 2004, Taddeucci, et al 2004).

2) Tungurahua volcano (Ecuador), after 80 years of rest, in August 1994 entered into a new eruptive phase, lasting up to date. The new magmatic, andesitic activity was characterized mainly by high frequency of phreatic and strombolian explosions, gas, ash and tephra emissions, which produced ash showers and occasionally minor lahars due to the accumulation of ash on the flanks of the volcano. Since the beginning of the new eruptive activity in late 1999, the volcano exhibited different eruptive cycles, usually every 12 to 18 months, up to the spring-summer of 2006. In the eruptions of the 16th to the 17th of August of 2006, which had a very high social and economic impact, ash and gas clouds reached a length of at least 800 km and a width of some 200 km, mainly towards the western side of the volcano (Toulkeridis, 2007).

3) Popocatepetl, (Mexico): activity from 1994 to 1997, was characterized by several ash intermittent eruptions (Martin-Del Pozzo et al., 2007).

4) Ono et al. (2005), from geological investigations around the Naka-dake cone, in the Aso caldera (Japan), found that the past-6000 years of activity of this volcano were characterized by the emission of black ash as principal product, alternated with strombolian activity and small lava flows.

Stratigraphic studies at Vesuvius have highlighted the presence of thick ash fall-out sequences related to mid-low intensity eruptions, starting from the Avellino Pumice eruption, about 3900 years B.P. (Cioni et al., 2007). The definition of an eruptive scenario for this type of events, generally overlooked during the preceding research activity at Vesuvius, is fundamental for civil defence purposes, especially due to the peculiar problems raised by their long duration and large dispersal of their products. Problems with the interpretation of this type of activity essentially arise from the difficulty to separate unequivocally the deposits derived from different events, being generally absent in these sequences prominent erosional or alteration discontinuities and due to the low rate of sedimentation involving contemporaneous deposition and reworking by external agents of the ash. Again, the mechanism of ash production is not clear: some of these eruptions show in fact evidences of magma-water interaction, while other deposits have no clear textural evidences of the presence of condensed steam at deposition. All these problems have to be addressed to reach a more complete understanding of dynamics of these events.

These low-mid intensity ash eruptions can have a strong impact on the environment and on the humans and animals health. Even though their hazard implications are clearly lower than that associated with pumice and ash deposition related to the large Plinian or subplinian events (Santacroce, 1987), they assume however an important role in the definition of the scenario for a short-term, mid-magnitude, expected event at Vesuvius. Indeed, ash plumes produced by explosive volcanic eruptions are transported by wind and can be found up to thousands of kilometres from their source. The presence of an impermeable ash cover on loose sediments favours rapid erosion by rain fall rather than infiltration, which favours mud-flow formation. The fallout of a few millimeters of volcanic ash in standing water may cause serious temporary pollution, increasing water acidity through the leaching of the volatile components (essentially chlorine and sulfur), inducing serious problems to water supply systems (Blong, 1984). Moreover, the potential for the inhalation of volcanic ash as a hazard to human respiratory health has become increasingly apparent (Rojas-Ramos et al., 2001; Horwell et al., 2003). Also the socio-economical impact of such small-size, ash producing eruptions can be impressive. The 1995–1996 Vulcanian eruptions of Mt. Ruapehu, New Zealand (Johnston et al. 2000) may provide an up-to-date picture of the problem. During these eruptions, only a few

millimetres of ash were dispersed during some main outbursts; this caused very high economic costs, with damage to hydroelectric power facilities, the interruption of air and road traffic, and water and grass contamination lethal to livestock.

The aim of this work is to understand the driving processes of continuous ash emission activity occurred at Vesuvius in the last four millennia. With this in mind, we selected two different eruptions which can be considered as the end-members of a large spectra of activity. AP3 eruption, related to the period of activity between the "Avellino" and "Pompeii" Plinian eruptions (Andronico and Cioni, 2002), is representative of events dominated, both in the fragmentation and depositional processes, by explosive interaction of magma with external water. Conversely, AS1a eruption, related to di Middle Age activity (Cioni et al., 2007), appears to completely related to primary, magmatic gas-driven explosivity. The products of the two eruptions have been studied by describing sedimentological and stratigraphical features of the deposits and by analysing the morphological, textural and compositional features of the ash particles. Although a great number of study exists about the physical and textural features of the products of large eruptions, ash particles related to low intensity eruptions still lack an in-depth study relating dynamics of their formation with the associated eruptive processes.

2. ANALYTICAL METHODS

The methods commonly used in volcanology to describe pyroclastic fragments have been widely discussed in many papers since the pioneering studies of Walker and Croasdale (1971) and Heiken (1974). The description and characterisation of the fragments of the studied eruptions were obtained using a selection and in some cases an improvement of the currently universally used methods, trying to put together classical methods derived from tephrochronology with some of the recently developed techniques of textural characterization of the fragments. Volume and grain size of the deposits were studied to derive the power of dispersion and fragmentation efficiency of these mid-low intensity eruptions. The study of the external morphology of the juvenile material may help in understanding the fragmentation processes, marking if they were related to purely magmatic or hydromagmatic, or ductile or fragile mechanisms. Textural analysis was used for understanding the kinetic of vesiculation and crystallization that occur during the rise of the magma along the conduit, and crystal size distribution was used to extract information on the time scale of crystallization, and the timing of the eruptions. Ash fragments were studied trying to associate the external features with the internal texture and geochemistry of single fragments.

2.1 Volume of the deposit

The volume of a tephra deposit characterises the magnitude of an eruption, because it is strictly correlated with the volume of the erupted magma. Various methods have been developed for estimating ejected volumes from isopach maps (Rose et al., 1973; Walker, 1981a,b; Pyle, 1989 and 1995; Fierstein and Nathenson, 1992) and this topic has caused some controversy (Rose, 1993). A major difficulty in estimating volumes is extrapolation beyond the preserved area of the deposit. Such limitations in field data require extrapolation and interpolation and, hence, some assumptions about thickness area relationships. Several field-based (Fierstein and Hildreth 1992; Scasso et al., 1994) and numerical studies (Bursik et al., 1992; Sparks et al., 1992; Bonadonna et al., 1998) have shown that methods based on the exponential decay of deposit thickness away from the

vent can significantly underestimate the total volume, particularly for eruptions that produce a significant amount of fine ash.

In this thesis, the reconstruction of isopach maps for the deposits of the main beds of each member of the studied eruptions allowed the calculation of their volume and dispersal features by using the methods of Pyle (1989).

In 1989, David Pyle showed that the thickness of many deposits decreases exponentially with distance from the vent and that in a graph of ln (T) vs $A^{1/2}$, where A is the area enclosed in an isopach of thickness T, data for individual deposits plot on a straight line. He proposed that the volume of a deposit could be determined from three parameters: the thickness half-distance (*bt),* the eccentricity of the elliptical isopach (α) and the thickness at the origin (T_0):

$$V=13.08 T_0 \, b_t^2 / \, \alpha$$

The thickness half-distance was defined as the distance along the dispersal axis of the deposit over which the thickness decreased to half of its value. By integrating the volume with respect to area rather than thickness, Fierstein and Nathenson (1992) showed that the actual shape of the isopach was not important and they characterised the dispersal of the deposit by the slope (–k) of the straight line on a ln (T) vs $A^{1/2}$ plot. In their notation, where k=ln2 √α/b,√π, the volume is:

$$V=2 \, T_0 / k^2$$

where T_0 is extrapolated from the thickness T of an isopach with area A by:

$$T_{0=} T \exp (k \, A^{1/2})$$

Pyle (1989) and Fierstein and Nathenson (1992) also showed that many well documented fallout deposits plotted as two straight-line segments with the proximal slope steeper than the distal one. The presence of several segments in a graph of ln (T) vs $A^{1/2}$ was later theoretically explained by Bonadonna et al., (1998) as the result of the difference between settling behaviours of coarse and fine particles, an idea already proposed by Rose (1993).

2.2 Grain size analysis

Total grain size distribution of fall-out deposits is considered a crucial eruptive parameter. Firstly, it can be used to infer fragmentation and erupting style by linking particle size to the initial gas content and water-magma interaction (Houghton and Wilson, 1989; Kaminsky and Jaupart, 1998). Second, it is an important constraint for sedimentation models that help understanding plume dynamics (Bursik et al., 1992; Sparks et al., 1992). Third, it is necessary for hazard mitigation plans as it is used in tephra-dispersal modelling to asses the risk and vulnerability of populations (Barberi et al., 1990; Connor et al., 2001; Bonadonna et al., 2002a) and because it give important indication of the level of particulate pollution dangerous for human health (Moore et al., 2002; Horwell, 2003).

Samples were collected at multiple sites, from primary fall deposits at measured stratigraphic sections, with sampling intervals dictated by changes in grain size and colour. Samples from each stratigraphic horizon were dry-sieved at whole-phi intervals from –2 to 3 phi (4–0.125 mm) by mechanical agitation, and for intervals from 3 to 12 phi (0.125–0.00024 mm) by Laser-diffraction analysis. The used techniques are summarised below.

- For the grain size intervals from –2 to 3 phi (4–0.125 mm), total samples were sieved at the INGV of Pisa. Ash samples were dried in an oven first at 60 ^{o}C, then sieved and at 1 phi interval and weighed, and the weight percent of each fraction was calculated. Key variables that influence sieving results include particle shape, presence of very fine particles, initial sieve loading, time and method of agitation, and aggregation of the powder. Reproducibility is often poor due to these variables, especially for very fine-grained samples. Percentiles and other grain size parameters (after Inmann 1952; Walker 1973) were calculated on a log-normal basis using a Microsoft Office Excel calculation template.

- For the grain size interval from 3 to 12 phi (0.125–0.00024 mm), the fraction ≤ 0.125 mm, left from the mechanic sieving, was analysed by Laser-diffraction at the Earth Science Dept., Univ. of Cosenza (Calabria, Italy). Particles suspended in a weak electrolyte solution are drawn through a small aperture, separating two electrodes between which an electric current flows. The voltage applied across the aperture creates a "sensing zone". As particles pass through the aperture (or "sensing zone"), they displace their own volume of electrolyte, momentarily increasing the impedance of the aperture. This change in

impedance produces a pulse that is digitally processed in real time. The Coulter Principle states that the pulse is directly proportional to the tri-dimensional volume of the particle that produced it. Analyzing these pulses enables a size distribution to be acquired and displayed in volume and diameter (μm). In addition, a metering device is used to draw a known volume of the particle suspension through the aperture; a count of the number of pulses can then yield the concentration of particles in the sample. One sample takes approximately five minutes to run. Samples should be dried and sieved to exclude particles > 2000 μm (2 mm) diameter. Assuming that the density of the particles ≤ 0.125 mm is not influenced by lithological heterogeneities, the density of the particles was set at 2500 kg/m^3 and the volume percent of particles of the same size is directly converted in weight %.

2.3 Sample preparation for morphological and textural studies

The studied samples were prepared in order to collect a complete set of morphological, textural, and compositional data on each single ash fragment (Cioni et al., 2007). Ash samples, in the size range 1- 0.125 mm, were observed at the stereomicroscope for the component analyses. About 30 juvenile fragments (from the 0.5-1 mm size interval) were randomly hand-picked from each sample, and than mounted on double-adhesive tape on a glass slide (Fig. 2.1a).

The choice of this grain-size represents a compromise between sample representativeness and suitability of performing reliable analytical work on the single grains.

Single clasts were photographed both using a digital camera at a stereomicroscope and at the Scanning Electron Microscope (SEM) for external morphology description. The glass slide was then embedded in epoxy resin and polished until a surface approximately containing the maximum diameter of the fragments was exposed (Fig. 2.1b). These mounts were used for SEM inspection, back-scattered electrons (BSE) imaging of the textural features and for analytical purposes of the individual clasts.

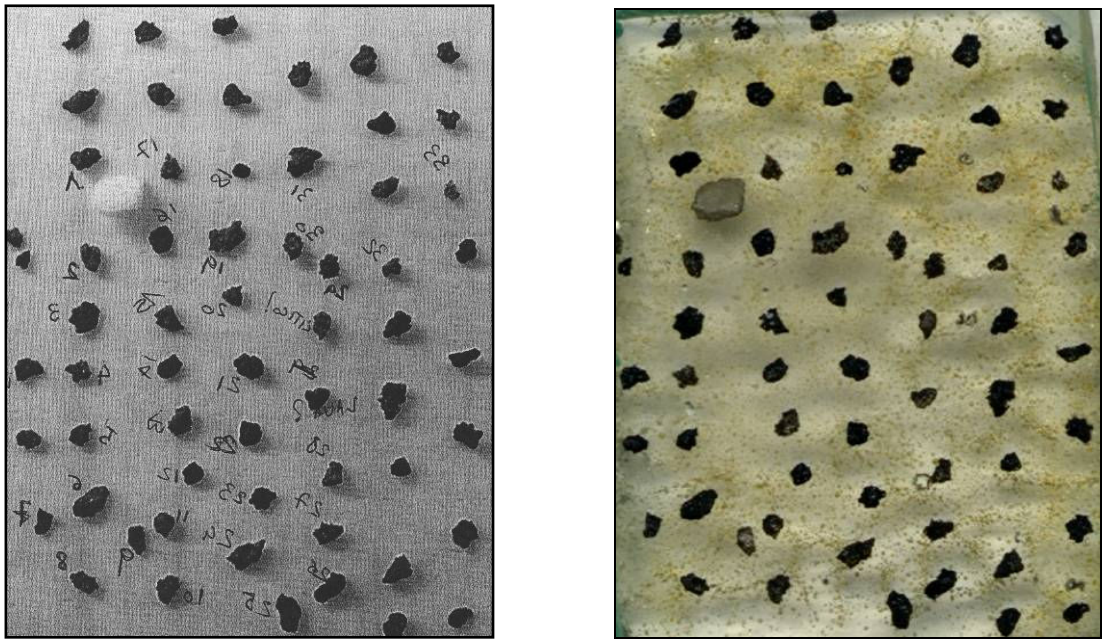

Fig.2.1 Preparation of sample for the study of the: a) external morphology; b) compositional and textural features

2.4 Morphology of the single ash fragments

The shape of volcanic particles is controlled by the rheology of the erupted magma and by processes of magma fragmentation and subsequent modification during transport and deposition. As a result, classification of volcanic particle shape can offer insights into the style of an eruption particle transport, and sedimentation.

Discrimination between ash fragments generated by different processes has been discussed by several authors on the base of the external morphology (Sheridan and Marshall, 1983; Heiken and Wohletz, 1985 ; Heiken, 1972; Andronico and Cioni, 2002; Sulpizio et al., 2005). To date, quantitative techniques for describing volcanic particle shape have been developed, typically relying on measurements of multiple shape elements such as planarity, convexity, concavity, number of corners, compactness, circularity, and elongation (Honnorez and Kirst, 1975; Eirìksson et al., 1994; Dellino and La Volpe, 1996). External morphology of ash fragments was examined for discriminating between magmatic and phreatomagmatic fragmentation (Büttner et al. 1999), and to got information about the post-fragmentation history of juvenile fragments (Dellino and La Volpe 1995). Low magnification (80x to 100x) images of selected single fragments were captured at an

acceleration voltage of 20 kV and working distance of 10 mm with a Philips SEM at the Dept. of Earth Sciences of the University of Pisa.

2.4.1 External morphology characterization

The relationship between volcanic particle shape and processes of formation is complicated by numerous, frequently interrelated, parameters that can influence particle morphology. The roles of magmatic variables such as magma viscosity, temperature, volatile content, cooling rate, and the effects of interaction with water are not well understood. Nevertheless, studies of natural deposits and results of experimental work have suggested some correlations between particle shapes and magma fragmentation processes (Walker and Croasdale, 1971; Heiken, 1972; Wohletz, 1983; Fisher and Schmincke, 1984; Heiken and Wohletz, 1985, 1991; Dellino and La Volpe, 1995; Zimanowski et al., 1997; Büttner et al., 1999). In particular, distinct particle shapes have been attributed to fragmentation driven by exsolution of volatiles (magmatic) versus interaction with external water (hydrovolcanic or hydromagmatic).

As a general rule, those vesicular particles with cuspate features were considered clearly produced by magmatic fragmentation, constrained primarily by factors that control vesicle growth, such as viscosity, temperature, and volatile content of the magma. The morphology of ash from eruptions of high viscosity magmas (ryolithic, dacitic, and some andesitic magmas) is entirely dependent on shape of vesicles in the rising magma before disintegration. The concavities, troughs, and tubes on grain surfaces are consequence of broken vesicle walls. In some cases droplets of silicic melt with viscosities low enough assume a fluidal shape.

In contrast, poorly vesicular clasts, often fine grained, with a predominance of blocky morphologies were generally assigned to hydromagmatic fragmentation. The shapes of this particles are constrained not only by the properties of the magma and the manner of its ascent but also by other factors, such as the ratio of water to magma, water turbulence, and hydrostatic pressure, that dictate the style and energy of its interaction with water (Wohletz, 1983; Sheridan and Wohletz, 1983; Kokelaar, 1986; Wohletz, 1986).

The shape of lithic fragments in ash should be controlled by the mechanical properties of the wall rock broken up by spalling or explosive expansion of gases in the magma as it

approaches the surface. Generally, most lithic fragments of ash size are equant and slightly rounded, indicating some possible rounding by particles grinding against each other during the eruption (Heiken, 1972; Houghton and Smith, 1993).

We classified the external morphology applying the classical descriptive observations suggested by Heiken and Wohletz, (1985 and 1991) on secondary electron images, acquired at different magnifications. These authors provide a full characterization of the volcanic ash based on particle shape, vesicularity, external surface texture, and eventual occurrence of surface alteration or secondary minerals, and on the base of the occurrence of these features, they distinguish the different processes of emplacement (Tab.2.1).

Textural characteristics	**Emplacement mode**		
	Flow (rhyolithic)	**Fall (rhyolitic)**	**Surge (basaltic)**
1. Edge modification by abrasion	*Present* Generally high with some resultant rounding	*Generally absent*	*Present* Generally high with some resultant rounding
2. Degree of vesicularity of glass	*Moderate to high* Tubular (high-aspect ratio) vesicles and coalescing bubbles	*Moderate to high* Variety of vesicles shapes	*Low to Moderate*
3. Adhering particles	*Abundant* Especially in vesicles	*General absent*	*Moderately abundant* Only in vesicles or hollows
4. Glass characteristics		Smooth surface, vesicular glass coating on crystals	Some in grains with drop-like fusiform surface
5. Breakage character of clasts		Broken crystals with curved fractures surfaces. Fracture faces undamaged by small-scale pitting	Equant, blocky grains common, particularly with large, smooth fracture surfaces
Minor features (breakage character)	Crystals broken along single cleavage planes. Vesicles tend to control grain shape of glass.	Shards often plate-like in fine fraction. Vesicles tend to control grain shape of glass.	Fractures surfaces influenced little by presence of vesicles.

Tab.2.1 Diagnostic surface features of flow, fall and surge (modified from Sheridan and Marshall, 1983).

2.4.2 Definition of quantitative shape parameters

The potential of morphological analysis as a geologic tool cannot be fully realized without an effective quantitative method for characterizing particle shapes, due to problems related to subjective interpretation in the description of the external morphology.

In more recent studies (Eirìksson et al., 1994; Dellino and La Volpe, 1996; Büttner et al., 2002; Riley et al., 2003; Cioni et al., 2007) products of magmatic and hydromagmatic fragmentation are distinguished by multiple shape parameters such as rectangularity, compactness, circularity and elongation. All of these techniques provide the means to uniquivocally describe volcanic clasts, potentially allowing correlation between their shapes and eruptive conditions.

In the present study, quantitative parameters of ash grain morphology were obtained by processing SEM secondary electron images of each grain. The shape parameters were measured on the external outline of the particles, defined as the projection of the particle outline on the horizontal plane (Maria and Carey, 2002). This outline was then filled and converted into a binary image using Adobe Photoshop® software, and the morphological parameters of interest were measured using the ImageJ software (http://rsb.info.nih.gov/ij) (Fig. 2.2).

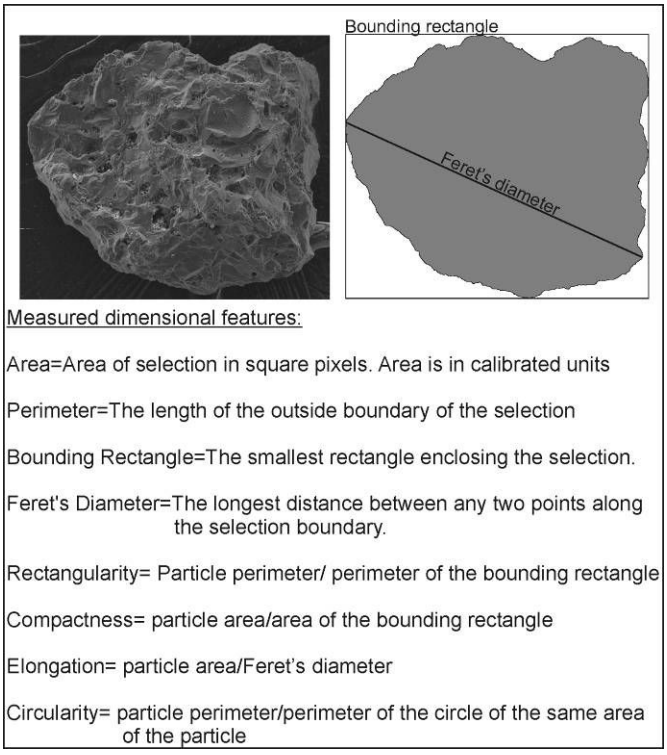

Fig.2.2 Secondary electrons SEM image processed and made binary for measuring the external shape parameters (rectangularity, compactness, elongation and circularity). Dimensional features and shape parameters are defined.

Four non-dimensional shape parameters were measured on each clast: rectangularity, compactness, elongation and circularity. They are defined as non dimensional parameters in the sense that they are not dependent from the size of the particles. Rectangularity is the ratio between the particle perimeter and the perimeter of the smallest rectangle that circumscribes the particle. Perfect rectangles show value of 1. Compactness corresponds to the ratio between the particle area and the area of the smallest rectangle that circumscribes the particle. The compactness value varies between 0-1, where 1 corresponds to a rectangular shape. Elongation is the ratio between the particle area and the length of the longest segment measurable in the particle. Circularity is defined as the ratio of the particle perimeter and the perimeter of the circle with the same area of the particle. The value 1 corresponds to a perfect circle (Fig. 2.3).

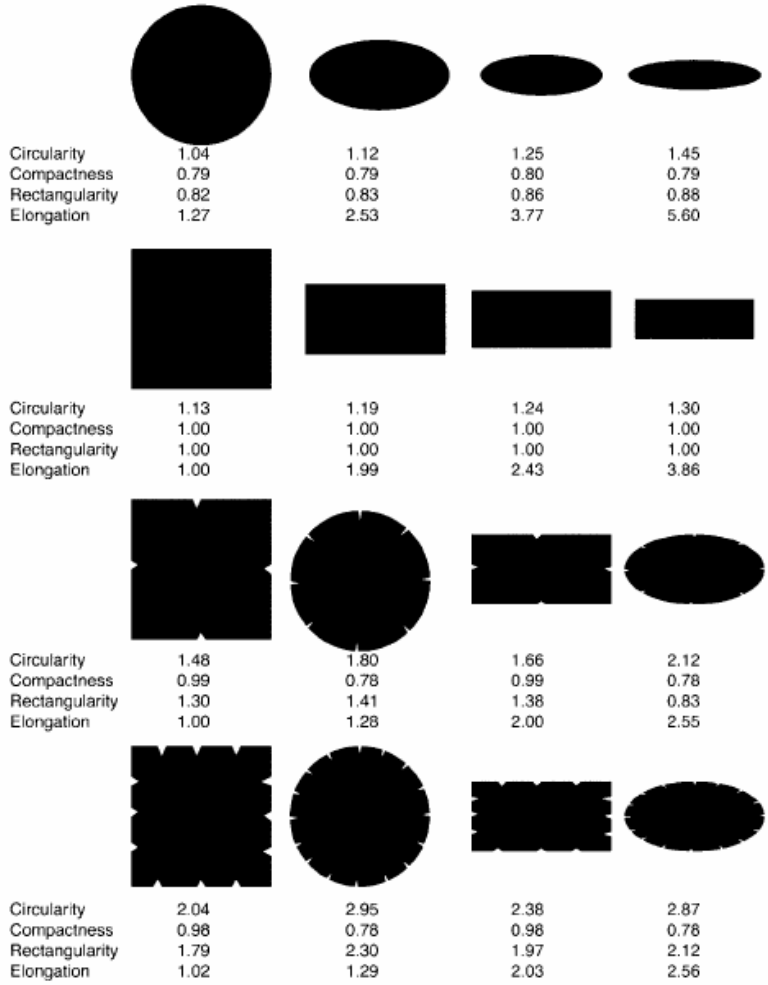

Fig.2.3 Chart of synthetic objects with the respective shape parameters (Büttner et al., 2002).

2.4.3 Statistical analysis

One method for testing the effectiveness of a parameterisation technique is to determine if ash particles of different shape can be distinguished by multivariate analysis. Using shape parameters as input variables, we performed cluster and principal component analysis with MATLAB® software. Shape parameters were standardized prior to running the program. The standardization process subtracts the mean for a given variable from each value and then divides the difference by the standard deviation within the variable.

The goal of the principal components analysis is the reduction of information in a system characterised by more than three variables, starting from the suggestion that into data sets with many variables, groups of variables often move together. This method takes the advantage of simplifying the system by replacing a group of variables with a single new variable. The software generates a new set of variables, called principal components. Each principal component is a linear combination of the original variables. All the principal components are orthogonal to each other so there is no redundant information The first principal component is a single axis in space. When each observation is projected on that axis, the resulting values form a new variable, and the variance of this variable is the maximum among all possible choices of the first axis. The second principal component is another axis in space, perpendicular to the first. Projecting the observations on this axis generates another new variable. The variance of this variable is the maximum among all possible choices of this second axis. The full set of principal components is as large as the original set of variables. But it is commonplace for the sum of the variances of the first few principal components to exceed 80% of the total variance of the original data (Davis, 2003; Jackson, J. E., 1991).

Cluster analysis was then applied to the extracted Principal Components, accounting for the maximum variability of the system. The used clustering model produces a hierarchical tree with normalized Euclidean distance (root mean-square distance) as a measure of dissimilarity between particles. Between-cluster distances were calculated according to the Complete Linkage (farthest neighbour) method, which takes the distance between two clusters as the distance between the two farthest members of those clusters. For the cluster tree models, each sample is represented by an horizontal line and is joined to its nearest neighbour by a vertical line. The Euclidean distance scale at the top of the diagram shows

the degree of similarity or correlation between particles within a cluster or between clusters. Particles within a cluster that extends to a low value of Euclidean distance are more highly correlated with one another than particles within a cluster that extends to a higher value. Assembling the particle images in accordance with the cluster tree is useful for visually assessing the grouping of shapes dictated by the model (Maria and Carey, 2002)

2.5 Petrography

After polishing, thin sections containing ash fragments were observed at the optical microscope for petrographyc studies. The mineralogical assemblage and crystal shape and content, the vesicle shape and content and the spatial arrangement of crystals represent a fundamental step for the characterisation of the ash products. This is decisive for the distinction between juvenile material and lithic fragments, as well as it gives an idea of the textural features and intrinsic variability of the erupted magma.

2.6 Geochemistry

Bulk rock

Centimeter-sized scoria were selected for XRF analyses from the coarsest beds of investigated eruptions. They were washed in demineralized water and dried for several hours at 60 °C, before powdering in agate mills. XRF analyses were performed on powder pellets with a Philips PW1480 spectrometer at the Earth Science Dept., Univ. of Pisa (Italy).

Glass and minerals composition

Major elements in glass and minerals were determined by energy dispersive X-ray analysis using EDAX DX4 on a Philips XL30 SEM at the Earth Science Dept., Univ. of Pisa, at an accelerating voltage of 20 kV, beam current of 0.1 nA and working distance of 10 mm. In order to reduce Na losses, matrix glass was analysed in raster mode, using windows in the range from 5x5 μm, in highly crystalline samples, to 10x10 μm. The analytical error measured on mineral and glass standards is always lower than 5-10 wt%,

increasing at low concentrations. In order to check for microscopic inhomogeneities of the matrix glass, 2 to 3 raster windows were analyzed in 5 to 10 clasts for each sample, and the results on each clast averaged. Care was used in avoiding areas close less than a few microns to groundmass crystals.

2.7 Trace elements analysis of matrix glass: Laser-ablation ICP-MS

During the PhD thesis, the LA ICP-MS instrumentation at the P. Zuddas lab., Earth Science Dept., Univ. of Cagliari, was first used. Setting up of the instrument was a side work of this project, and in the following we present a detailed report of activity done and established experimental conditions.

2.7.1 Instrumentation and peculiarity of LA-ICP-MS

Experiments were carried out using a Perkin Elmer Elan DRC-e ICP-MS, coupled with a New Wave Research UP 213 series laser ablation (D'Oriano et al, in prep.).

The ICP-MS standard instrument configuration consists of a plasma (luminous volume of partially ionised gas) as ion source (ICP), generated from radio frequency magnetic fields induced by a copper coil, wounded around the top of a partly demountable glass torch, with removable alumina injector. Quadrupole is used as mass analyser, which progressively select ions with specific mass to charge ratio. Ions are detected by a Channel Electron Multiplier (CEM), at the end of which there is a computer for data collection and processing.

The laser ablation system consists of a rod of Yttrium Aluminium Garnet ($Y_3Al_5O_{15}$) doped with approximately 3 wt% Nd_2O_3, working at wavelength of 213 nm. The type of laser is Q-switched, that leads to the formation of a single large output pulse by releasing the energy stored in the cavity as shorter pulse with both higher average and peak power. He gas was used as carrier inside the ablation cell and mixed with Argon, the makeup gas, before entering the ICP.

Ablation spot diameter ranges between 20 and 100 μm. The selection of the spot size utilised for the ablation is a critical parameter that must be adjusted according to

application. Analysis of small samples, for example, requires a reduction in the size of ablation crater, without changing sensitivity. Modern instruments allow lowering of the laser energy and/or a reduction in the laser spot size (and thus volume of material ablated) while giving the same low limit of detection (LLDs) as older systems, and thus offer the potential to generate data from smaller glass shards.

The pulse energy ranges from 0.02 and 2 mJ. It is controlled by an optical attenuator, that take the advantage of the linear polarization of the laser beam.

The laser ablation device is equipped of a video-camera for high resolution sample viewing, ensuring the visual focus of the sample, the identification of the area to be analysed and the observation of the laser ablation process ok-vive. The system is connected with a computer, on which a specific software is installed, for the selection of the specific instrumental parameters during the analysis.

2.7.2 Operating conditions

To achieve the maximum intensity across the full mass range, the ICP-MS parameters, such as the RF power, ion lens voltage and mass calibration, were optimised by continuously aspirating a solution of 10µg/l of Mg, In, Ce, Ba and U in 0.5% HNO_3. The nebuliser gas flow was adjusted so that CeO/Ce results < 3% and doubly charged ion production as measured by Ba^{2+}/Ba^{+} was < 3%.

To determine trace element concentrations in the ablated material, data were collected by peak hopping. Mass resolution was set to 0.7 atomic mass unit (AMU), and the peak intensity for each element was obtained measuring the signal intensity at the center point in the mass range defined for each element. The dwell times (measurement times on each isotope during one quadrupole sweep) was 10 ms per AMU, one sweep of the mass range per replicate and 300 replicates per analysis, including 80 replicates on the dry gas to establish the background prior to ablation. Total analysis time was 2 min per spot, including backgrounds (Fig. 2.4).

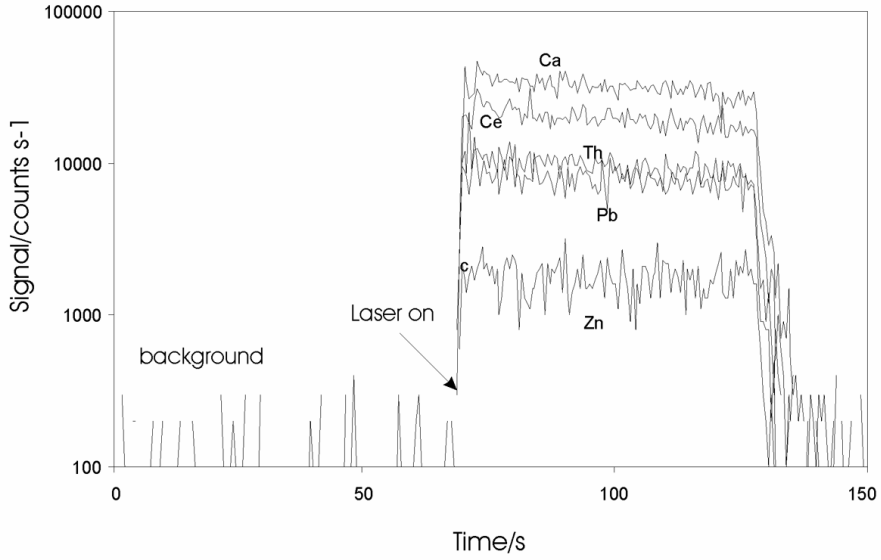

Fig.2.4 Real time window of the signal intensity during time for each element. The first 60 s of the analysis the laser is switch off for the background acquisition.

The signal detection was performed in dual modes, ion counting and analog, operating simultaneously. Data were collected in time-resolved graphics mode to monitor possible compositional heterogeneities that might be present in the sample at the scale of the laser sampling, and to monitor the inter-element fractionation that can occur during a laser ablation analysis. The instrument operated with the autolens on. Operating conditions utilised in this work are summarised in Table 2.2 both for the ICP-MS and LA devices.

Instrumental parameters

ELAN DRC-e ICP-MS	
Nebulizer gas flow	0.86 l min^{-1}
Auxiliary gas flow	1.40 l min^{-1}
Plasma gas flow	15.5 l min-1
Lens voltage	7.50 V
ICP RF power	1200 W
Auto lens	on
New Wave research UP series 213 Laser Ablation	
He carrier gas Flow	0.67 l min^{-1}
Energy (10Hz)	0.028-0.28 mJ
Spot size	20-50 μm
Laser frequency	10 Hz

Tab.2.1 Instrumental parameters both for ICP and LA instruments.

2.7.3 Reference materials

NIST 610 and NIST 612, partially certified reference material by the National Institute of Standards and Technology (NIST), were utilised for the calibration and optimisation of the instrument. These are silicate glasses spiked with a range of trace elements at a nominal concentration of 50 and 500 μg g^{-1} respectively. Pearce et al., (1997) recently compiled a database of published data for these reference material in order to provide an interim working value for a wide range of elements (Tab. 2.3).

	Pearce et al.1997		Gao et .al 2002
ELEMENTS	**NIST610**	**NIST612**	**BCR-2**
Li	484.6	41.54	9
Ba	356.4	34.73	-
Na	-	-	23400
Mg	465.3	77.44	21650
Si	-	-	-
Ca	-	-	-
Sc	441.1	41.05	33
Ti	434	48.11	13500
V	441.7	39.22	416
Cr	405.2	39.88	18
Co	405	35.26	37
Ni	443.9	38.44	-
Zn	456.3	37.92	19
Rb	431.1	31.63	48
Sr	497.4	76.15	346
Y	449.9	38.25	37
Zr	439.9	35.99	188
Nb	419.4	38.06	-
Cs	360.9	41.64	1.1
Ba	424.1	37.74	683
La	457.4	35.77	25
Ce	447.8	38.35	53
Pr	429.8	37.16	6.8
Nd	430.8	35.24	28
Sm	450.5	36.72	6.7
Eu	461.1	34.44	2
Gd	419.9	36.95	6.8
Tb	442.8	35.92	1.07
Dy	426.5	35.97	-
Ho	449.4	37.87	1.33
Er	426	37.43	-
Tm	420.1	37.55	0.54
Yb	461.5	39.95	3.5
Lu	434.7	37.71	0.51
Hf	417.7	34.77	4.8
Ta	376.6	39.77	-
Pb	413.3	38.96	11
Th	450.6	37.23	6.2
U	457.1	37.15	1.69

Tab.2.3 Trace elements concentration of the reference materials: from Pearce at al., (1997) NIST610 and NIST612, and from Gao et al., (2002) BCR-2.

For the calibration of microbeam analyses and as quality control of the analyses, the BCR-2 glass, a standard prepared from Columbia River basalt by the US Geological Survey, was routinely utilised (Tab. 2.3) (Gao et al., 2002).

2.7.4 Calibration strategy

Calibration of analyses in laser ablation ICP-MS requires the knowledge of one element in the sample to act as an internal standard. This can be either a major or trace element in the sample, the concentration of which is determined with alternative techniques (EPMA). The concentration of an unknown element is calculated from the following equation, assuming that the calibration curve is linear and passes through the origin (Perkins and Pearce, 1995):

$$Cel_{unk} = \frac{Cel_{rm}}{\left(ACPSel/ACPSis\right)_{rm}}\left(\frac{ACPSel}{ACPSis}\right)_{unk}\left(\frac{Cis_{unk}}{Cis_{rm}}\right)$$

where C = concentration; el = analyte element; i.s. = element selected as internal standard; rm = in the reference material; unk = in the unknown sample; ACPS = area counts per second (i.e. the integrated counts normalised to the dwell time per peak). This equation can be expressed more simply as:

Concentration = slope of calibration X (analyte counts / internal standard counts) X correction factor for differences in internal standard

The use of an internal standard accounts for any variation in the amount of ablated material reaching the plasma (the 'ablation yield') between samples and calibration standards, and any difference in concentration of the internal standard is corrected during calculation of concentrations. This also means that the reference material used to produce the calibration should not have necessarily the same matrix composition as the unknown, although a difference in matrix composition may introduce further complications (Pearce et al., 2007). Calibration requires that the background corrected signal from all or part of

an ablation of a sample be referenced to that from a standard material. Background signals are usually obtained measuring the 'gas blank', i.e. with no ablation, either performed 60 seconds prior to initiating ablation. (Günther et al., 1999). The same operating conditions between analysis of standard and of unknown have been maintained to overcomes effects of differential element fractionation between standard and sample (Perkins and Pearce, 1995).

Calibration was performed using NIST 610 and NIST 612 as external calibration sample in conjunction with internal standardisation using ^{44}Ca, CaO concentration of samples was measured by energy-dispersive X-ray (EDS-SEM) technique, at the Earth Science Dept., Univ. of Pisa.

2.7.5 Main results

In order to constrain the variation of detection limits as a function of spot size, analyses were carried out at 40 and 15 μm spot size with a laser power of 0.15 and 0.028 mJ, respectively. At a spot size of 40 μm, the detection limit ranges between 0.001 and 1 ppm for all the elements, except for Si, Ca, Ti and Cr, due to the stringent relationship between sensitivity and background. The elements with high-abundance isotopes show Low Limit of Detection between 0.001 and 0.01 ppm, while for the other elements LLDs are higher than 0.01 ppm. By decreasing the spot size from 40 to 15 μm, the detection limits increase about one order of intensity without any significant fractionation among the different elements.

The precision (RSD% = standard deviation / average value * 100) of the LA-ICP-MS instrument depends on the acquisition parameters, on the total number of ions of analyte detected, on the analyte concentration and on spot crater. It was calculated from 16 replicates in one day, using a spot size of 40 μm, a laser output energy of 0.28 mJ and a repetition rate of 10 Hz on NIST612. The accuracy (RD% = (average value - reference value) / reference value * 100) corresponds to the relative deviation of the average concentration obtained in this study from the reference values (Pearce et al., 1997). Average values are reported in Table 3 and shown in Figure 5. The precision ranges between the 3% and 8%, increasing toward the higher mass, and reaching the maximum

value for ^{11}B. Accuracy is always better than 5%, and for all elements it has a negative value related to an overestimation of the concentrations with respect to the certified one.

For the *in situ*-analysis of the trace elements, single ash fragments were selected on the base of the textural features. In particular, only grains that contain a glass volume big enough to be resolved by a 30 μm laser radiation were analysed. Instrumental parameters used for the analyses are summarized in Table 2.4.

Instrumental parameters	
ELAN DRC-e ICP-MS	
Nebulizer gas flow	0.86 l min^{-1}
Auxiliary gas flow	1.40 l min^{-1}
Plasma gas flow	15.5 l min-1
Lens voltage	7.50 V
ICP RF power	1200 W
Auto lens	on
New Wave research UP series 213 Laser Ablation	
He carrier gas Flow	0.67 l min^{-1}
Energy (10Hz)	0.028 mJ
Spot size	25 μm
Laser frequency	10 Hz

Tab.2.4 Operating conditions utilized for the trace elements analysis

2.8 Textural investigations

Textural characterisation of pyroclasts from explosive volcanic eruptions has proven to be an important support to other approaches (i.e. field, theoretical and experimental) in studying the physical processes that control the eruptive styles, magma vesiculation, fragmentation and conduit ascent to the Earth surface of explosive eruptions (Houghton and Wilson, 1989; Klug and Cashman, 1994, 1996; Gardner et al., 1996, 1998; Hammer et al., 1999; Polacci et al., 2001; Klug et al., 2002). To date, a framework has been established to investigate: 1) the importance of bubble deformation and coalescence in developing permeability to allow efficient gas escape in highly viscous magma (Klug and Cashman, 1994, 1996; Polacci et al, 2008); 2) the role of microlites in increasing magma viscosities and constraining bubble growth, thus affecting magma fragmentation (Klug and

Cashman, 1994), and in recording syn-eruptive or inter-eruptive degassing (Gardner et al., 1998; Hammer et al., 1999); 3) how crystal textures and microlites nucleation can record conditions of magma decompression (Geschwind and Rutherford, 1995; Cashman and Blundy, 2000; Polacci et al., 2001; D'Oriano et al., 2005).

Two backscattered (BSE) images were captured for each ash grain at magnification of 250x and resolution of 2048x1600 pixel. In this way the acquisition of a little number of images is needed, due to the high images resolution, so allowing to recognise objects larger than 10 μm in size. Moreover, using the same scale for all the clasts, problems of scale-dependence resolution are avoided. Quantitative measures of the groundmass features include vesicle and crystal shape, size and content.

2.8.1 Vesicles shape, size and content

Vesicles characterisation was obtained by manual reconstruction of bubble contour, and graphic deconvolution of incipient bubble coalescence. Bubbles were isolated from the images using the tools of Adobe Photoshop®. For automated analysis of groundmass vesicularity, binary images were used to estimate the percent area of vesicles. Vesicularity (area fraction of vesicles), vesicle number density (number of vesicles per unit area, N_A), and vesicle size and shape were measured from binary images obtained from the BSE images, using the freeware software ImageJ. The circularity and the elongation of the vesicles (defined as in Fig. 2) were calculated using ImageJ software. All the textural parameters were obtained in two-dimensions to allow for comparison between samples. Vesicularity of ash fragments was classified basing on the scheme proposed by Houghton and Wilson (1989) (Tab. 2.5).

% Vesicularity	Description
0-5	Not vesicular
5-20	Incipiently vesicular
20-40	Poorly vesicular
40-60	Moderately vesicular
60-80	Highly vesicular
>80	Extremely vesicular

Tab.2.5 Classification of the pyroclasts on the base of the ranges of vesicularity (Houghton and Wilson, 1989).

2.8.2 Crystal content

As first approximation, automated analyses of groundmass crystallinity were obtained measuring the percentage area occupied by crystals of leucite, pyroxene, and plagioclase, estimated on the base of the grey tone typical of a specific mineralogical phase in the backscattered images. Data were recalculated on a vesicle free basis. This automated method possibly shifts toward highest values the upper range of groundmass crystal content, due to the occasional presence in some of the analyzed clasts of phenocrysts which contribute to increase the area occupied by the crystals, and also due to the similar grey tone that characterises matrix glass and leucite microlites. We consider as microlites all the crystals smaller than of 150 μm. Phenocrysts are defined as those crystals larger than 250 μm, and the population between phenocrysts and microlites is defined as microphenocrysts.

2.8.3 Crystal size distribution (CSD)

In the following, for the characterization of microlite number density, crystallinity, and average crystal size for all of the clasts, a subset of five clasts was selected for analysis of shape and crystal size distribution. For the initial characterization, 418 images on the 108 clasts selected from the studied eruptions, were processed. A minimum of two images at 250x of magnification was deemed sufficient to characterize a relatively homogeneous clast. For each image, leucite, pyroxene and plagioclase microlites were digitalised using Corel Draw$^{11®}$ software, assigning a colour at each mineral.

All measurements were made using the image processing public domain application ImageJ. Microlites were distinguished from microphenocrysts and broken phenocrysts by their euhedral habit and small size.

Because only groundmass textures were examined, all terms describing crystal textures refer to microlites alone. Therefore, "crystallinity," φ, refers to the volume fraction of *microlites* in the groundmass only.

Measurements of N_A, φ, and crystal shape required different treatments of edge-intersecting crystals. As suggested by Higgins (2006), microlites not touching the image edges were counted for use in number density (N_A) calculations (Fig. 2.5). Because total microlite area is required for φ measurements, all edge-intersecting crystals were included in the point counts. For crystal size and shape determinations, only those crystals completely contained within the image were outlined. The minimum (breadth) and maximum (length) dimensions of each crystal were measured using ImageJ.

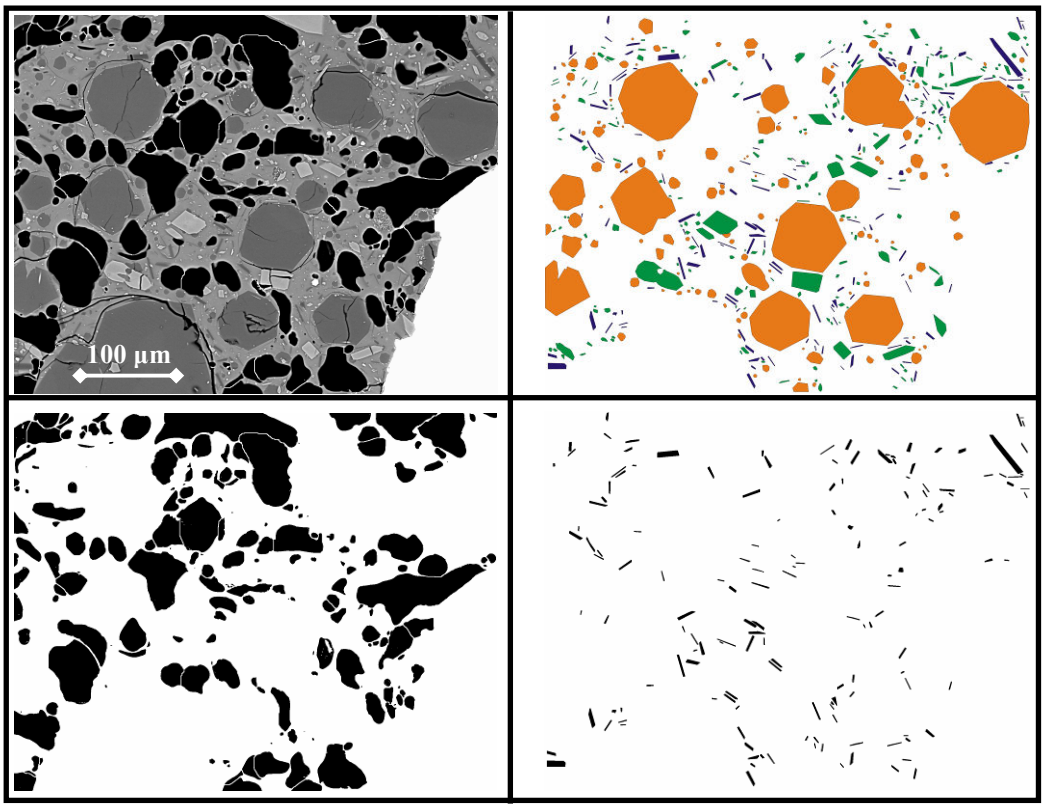

Fig.2.5 Textural quantifications steps: 1) original BSE images at 250x of magnification; 2) Digitalised images for all the mineralogical phases (Leucite in orange; pyroxene in green and plagioclase in blue); 3) reconstructed and in some cases decoalesced vesicles; 4) isolated plagioclase crystals.

Crystallinity, number density, and mean size

Crystal number density (number of crystals per square millimeter) and φ were calculated on a phenocryst- and vesicle-free basis, so that the relevant area in each backscattered electron (BSE) image consists of only glass and microlites. We refer to this as the "reference area," obtained by subtracting phenocryst and vesicle areas from the total image area (Fig. 2.6).

Measurements were weighted by image reference area when combined to determine average values for each clast. Microlite number densities were obtained by manual identification to obtain a per area (per square millimeter) count. Image crystallinities were obtained from the total area of crystals per cent.

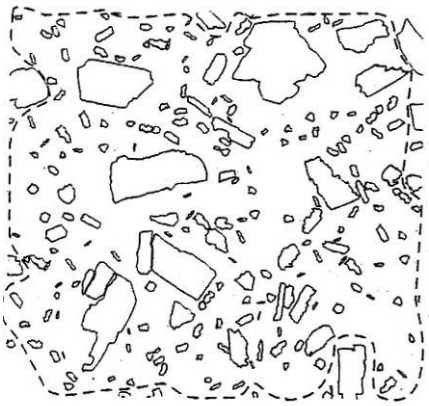

Fig.2.6 A solution proposed by Higgins, (2006) for the problem of the edge effects in textural measurements. Our "reference area" do not consider crystals not completely content in the dotted line.

Microlite shape

Shape of crystals growing in the melt is controlled by the kinetics of crystallization (specifically, the relative growth rates of individual crystal faces) and may provide information about the degree of undercooling experienced by sequential batches of magma en route to the surface (Lofgren, 1980; Hammer et al., 2002). Higgins (1994) showed that a statistical analysis of the two-dimensional intersections of a random plane with a single crystal can be used to obtain its true (three-dimensional) aspect ratio. The aspect ratio has

three parameters, the short, intermediate, and long dimensions (S = short; I = intermediate/short; L = long/short). Measurements necessary for the analysis are the shortest (S) and longest (L) dimensions of the crystal in thin section (two dimensions). Higgins (1994) showed that for randomly oriented slices through the crystal and crystals modelled as parallelepipeds, the modal value of the aspect ratio (*S*/*L*) in a two-dimensional slice is equal to the ratio of the short (S) to intermediate (I) dimension in three dimensions S/I. The ratio I/L is more difficult to determine, but can be estimated from the skewness of the with/length *(w/l)* distribution as follows:

Skewness = (mean *w/l* - mode *w/l*) / standard deviation *w/l*

and

I/L = Skewness + 0.5

These equations are not accurate for near equant shapes. This treatment is also valid for a population of crystals of varying size if all of the crystals have the same shape. Using measurements of microlite breadth and length, and applying the techniques from Higgins (1994), the three-dimensional axis ratios were computed (Fig. 2.7). The average shortest, intermediate, and longest dimensions (a, b, and c, respectively) of microlites may then be calculated by combining the axial ratios (S, I, and L) with the average crystal linear size, s_n, obtained from N_A and f measurements:

$$a = s_n(I^{1/2})$$

$$b = s_n(I^{1/2})$$

$$c = s_n(L / I)$$

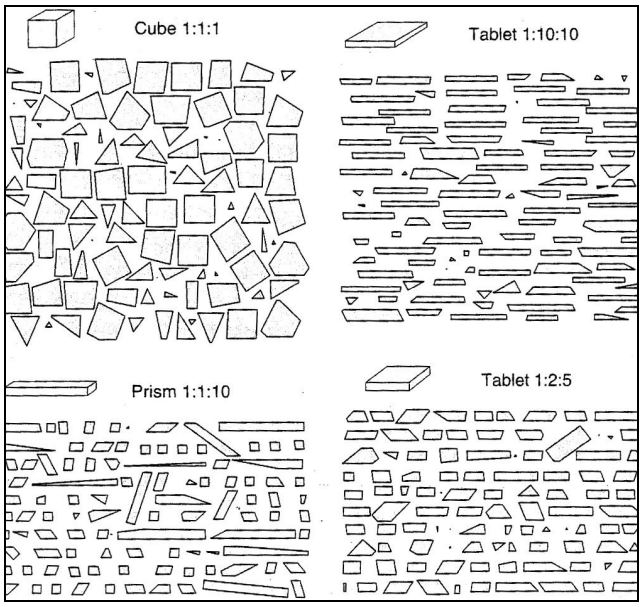

Fig.2.7 Intersection of random planes with regular geometric figures. Tablets tend to give elongated intersections, which are commonly thought to indicate a lath shape, whereas prism commonly have a rectangular cross-section (Higgins, 2004).

Microlite crystal size distributions

Crystal size distributions (CSDs) can provide information about the rates of nucleation and growth of crystal populations if time scales of crystallization are known, and vice versa. Determination of CSDs from thin section measurements requires both a choice of linear characteristic size, ***L***, and conversion of measurements from a per area to per-volume basis. Errors in the conversion include the cut effect (resulting from sectioning through edges and corners), the intersection problem (in which small crystals are intersected less frequently than large crystals) and distortions introduced by the non-spherical habit of most crystals (Ripley, 1981; Russ, 1986; Underwood, 1970).

We have used the CSD Corrections 1.37 (Higgins, 2000) software for converting two dimensional intersection data gathered from thin sections to true three dimensional crystal size distributions (CSD). Corrections are made for the intersection probability effect and partial corrections for the cut section effect. The program constructs a solid of the dimensions indicated by the Short, Intermediate and Long dimensions. The orientation of

the solid is constrained by the nature of the fabric (massive or foliated or lineated), the quality of the foliation (weak to strong) and the orientation of the desired section (parallel or normal to the fabric). This is sectioned by a plane placed a random distance from the centre of the solid. The outline of the intersection of the solid with the plane is determined and the length and width calculated. The distribution of these lengths and widths is used to correct the two dimensional data for the cut section effect. The most likely intersection length (or width) is used to correct for tailing to smaller intersections. There is no tailing correction for intersections larger than the most likely intersection. This is rarely a problem if wide bins are used for the frequency distribution. After these tailing corrections have been made, corrections for the intersection probability effect are applied.

The tailing corrections are applied sequentially. That is, the n_{th} bin has n-1 corrections for all larger crystal size bins. For this reason it is best to restrict the number of bins – 8 to 10 is usually the maximum (Higgins, 2000).

The resulting CSD is a linear regression over most of the range in size measured. The rest of each distribution was fit to a linear function in order to determine the average crystal size and rates of nucleation and growth. As described by Randoph and Larson (1971) and Marsh (1988; 1998), and as applied by Cashman (1992, 1993), Higgins (1996a), Waters and Boudreau (1996), and Wilhelm and Woerner (1996), among others, the slope of the curve relating frequency to linear size, for an open, steady-state, system is equal to the average crystal size:

$$slope = -1(averageL) = -1/G\tau$$

where G is the average linear growth rate and τ is the duration of crystal growth. Therefore, if τ is known, the average linear crystal growth rate can be determined, and on the other hand, if growth rate is known, it is possible to estimate the duration of the crystallisation processes. The nucleation rate, J, is the product of the average growth rate and the number density of crystals having zero size (y-intercept value, n°):

$$J = n°G$$

Moment statistics used in the calculation of nucleation rate and number density are sensitive to the extrapolated population densities, n, at $\boldsymbol{L} = 0$ (n°, the y-intercept). If the

crystals are *not* exponentially distributed over the entire range of sizes, the values of these parameters will be under- or overestimated. For example, if the downturn in population density at the smallest size classes is real, not a sampling artifact, the number density obtained using the extrapolated intercept is an overestimate. Again, this assumption is difficult to assess, since the smallest-sized crystals can be difficult to recognize and measure given the limits of resolution using electron-beam imaging techniques. Similarly, the extrapolation of the curve to infinitely large sizes may boost the volume percent crystals as estimated using CSD theory. Given that the crystals in question are microlites rather than phenocrysts, the supposition that large crystals exist, even in very small numbers, is probably not valid.

3. THE SOMMA-VESUVIUS VOLCANIC COMPLEX

Hazard assessment at Vesuvius represents one of the biggest challenge for the volcanological community, and it is fundamental to study its past behaviour if we want to make previsions about how it will awake in the future. The importance of this volcano, become the most famous of the world after the finding of the ruins of the roman town of Pompeii, buried by the AD 79 eruption narrated by Pliny the Younger in two letters to the historian Tacitus, it is easily understood if we consider its tendency to generate explosive eruptions. Moreover, on its slopes and within 10 km from the summit crater, more than 700,000 people live today (Fig. 3.1), while the outskirts of Naples itself are only 15 km far from the vent.

At the present time Vesuvius is in a quiescent state, lasting since 1944. During its life, Vesuvius experienced many times long rest periods, which, in some cases, lasted centuries or dozens of centuries. The present senseless urbanization of the area around Vesuvius results in a situation of extremely high risk. An unexpected or undervalued eruption would have today heavy consequences, not mitigable under contingent solicitation.

Fig.3.1 Mt. Vesuvius cone inside the Mt. Somma caldera. It should be noted the high population density that live behind the slope of the volcano.

An extensive network of seismic and gravimetric stations, a combination of a GPS-based geodetic array and satellite-based synthetic aperture radar, are currently used to perform an extensive and continuous monitoring of the volcano, in order to measure the ground movement, and together with the local surveys and the chemical analyses of gases emitted from fumaroles, are all intended to track magma rising underneath the volcano. Scientists are now confident that in the case of a near reactivation of the volcano, the monitoring network would be able to detect adequately in advance the ongoing changes.

These direct methods of study must be correlated with field studies and laboratory analyses of deposits and products from past eruptions, trying to understand the modalities of past eruptions of the volcano, and to suggest what we can expect in the future.

This is obviously fundamental to risk mitigation, but another point, equally important for the assessment of the hazard and probably hardest to solve, concerns the forecasting of type and size of the future eruption. Mostly based on the results of past research, an emergency plan was established in 1995, to be periodically updated and verified, dimensioned on a Subplinian Maximum Expected Event (MEE) (Cioni et al., in press). The definition of the spectrum of possible eruption scenarios based on past activity represents an irreplaceable tool for the correct setup and tuning of civil protection contingency plans and hazard mitigation measures.

3.1 Eruptive history of Somma-Vesuvius volcanic Complex (SVC)

The Somma Vesuvius Complex (SVC) is located in the Campanian Plain, a tectonic graben bordered by Mesozoic carbonate platforms, down faulted during the Pliocene and perhaps Pleistocene as a consequence of the stretching and thinning of the continental crust related to the opening of the Tyrrhenian basin (Ippolito et al., 1973; Ortolani and Aprile, 1978; Scandone, 1979; Ortolani and Pagliuca, 1987; Patacca et al., 1990). The Campanian Plain is bordered to the northeast by NW–SE-trending faults and to the south and north by NE–SW-trending faults (Fig. 3.2). SVC has a maximum altitude of 1281 meters and covers an area of about 480 sq. km.

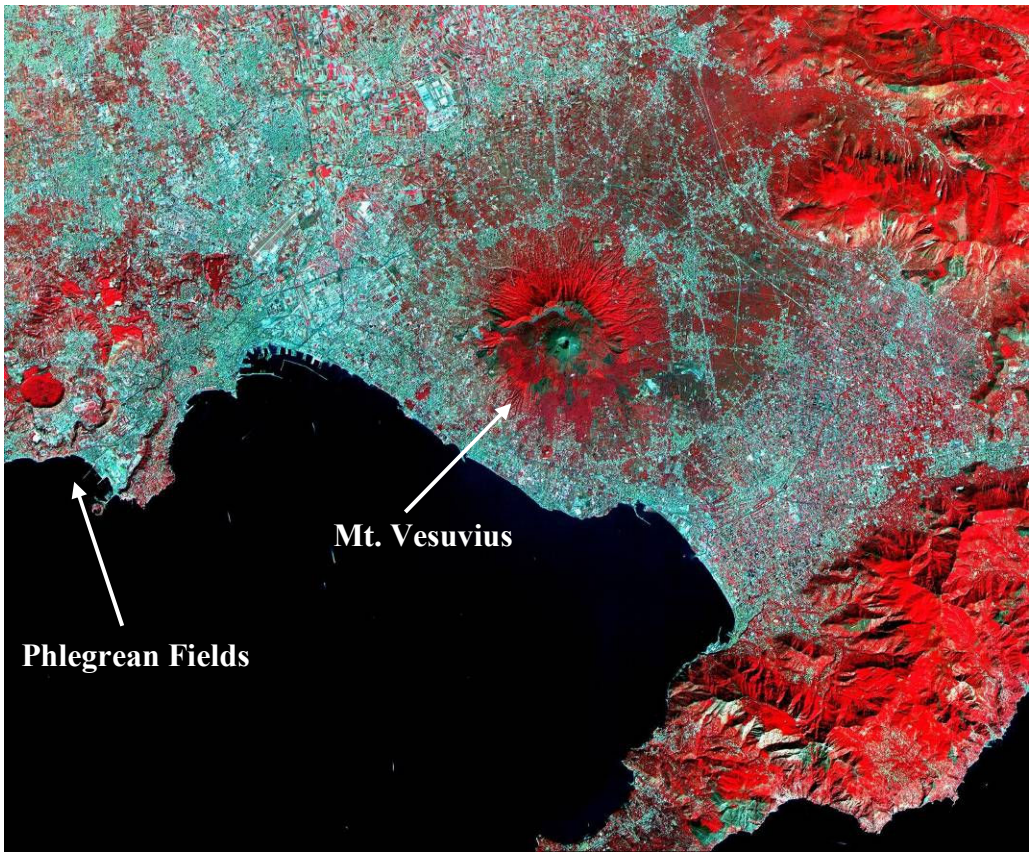

Fig.3.2 ASTER image of Mt. Vesuvius and the surrounding geological structures.

Volcanism in the area of Somma-Vesuvius has been present at least from 400 ka, with an activity mostly effusive, as indicated by lava flows interlayered with tuffs and marine sediments, drilled at 1.350 m of depth (Bernasconi et al. 1981; Santacroce, 1987). These deposits are buried by the Campanian Ignimbrite, the product of the greater eruption of Campi Flegrei, occurred around 39,000 years ago. The activity of the present Mount Somma followed such event (Fig. 3.3).

The present shape of SVC is the result of several vertical collapses of an old stratovolcano, the original apex of which was approximately 500 m north of the present Vesuvius crater, at 1600-1900 m elevation. Caldera collapse accompanied the four Plinian eruptions that occurred in the last ca.18,000 (Cioni et al., 1999).

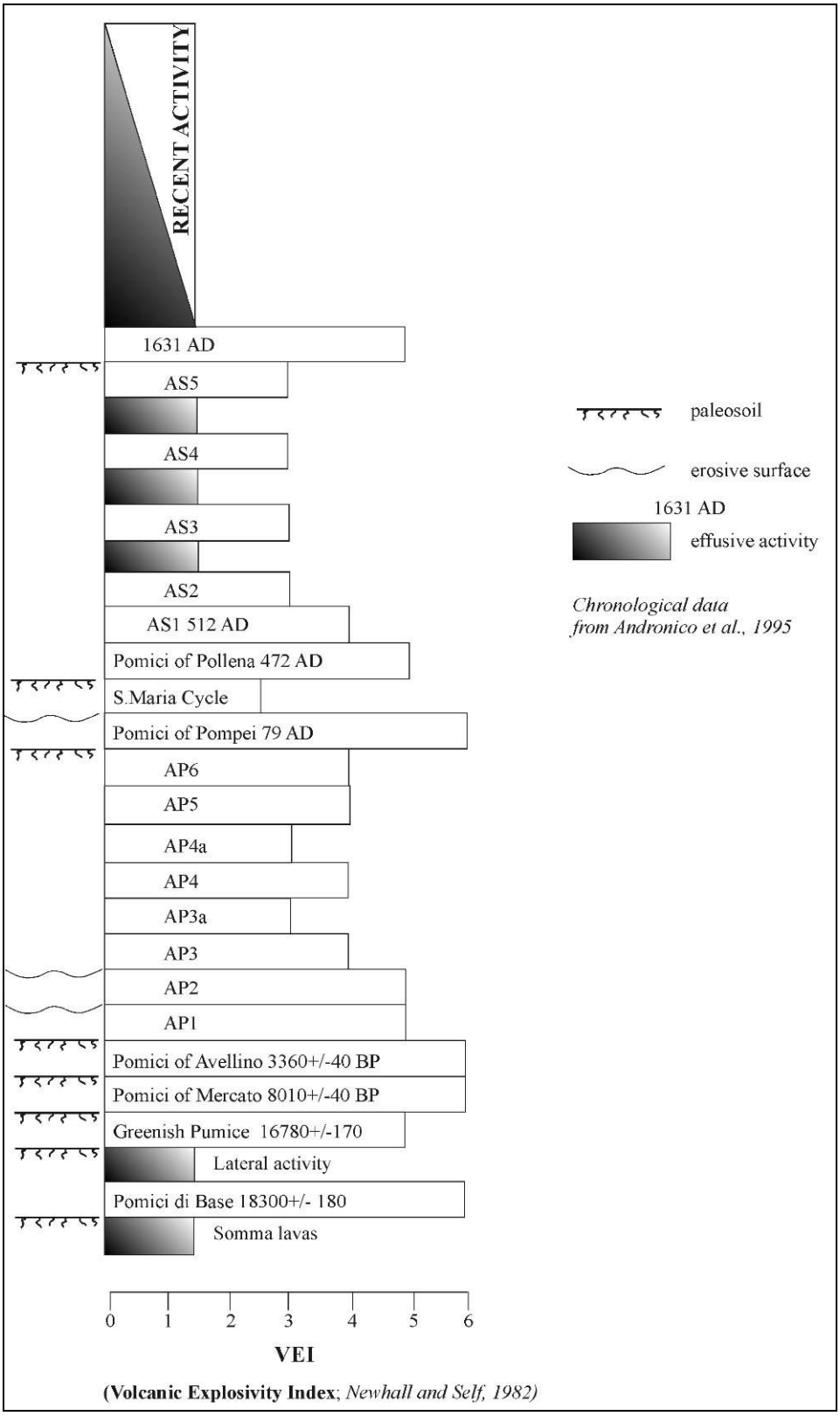

Fig.3.3 Schematic chronological section of the Vesuvius activity (modified by Cioni et al., 1995)

The oldest Plinian eruption is the Pomici di Base (18,3 ka; Arnò et al., 1987; Andronico et al., 1995; Bertagnini et al., 1998; Cioni et al., 1999), which determined the beginning of the collapse of the volcano of Mt. Somma and the formation of the caldera.

This eruption was followed by an effusive activity along the east side of the volcano and by a period of quiescence interrupted by the sub-Plinian eruption of the Greenish Pumices (16.7 ka; Arnò et al., 1987; Andronico et al., 1995). After the Greenish Pumice eruption the activity of the volcano was characterized by a long period of quiescence, during which two minor eruptions possibly occurred, interrupted 8,000 years ago by the Plinian eruption of the Mercato Pumice (Johnston Lavis, 1884; Lirer et al., 1973; Delibrias et al., 1979; Cioni et al., 1999). During the period of quiescence following the eruption of the Mercato Pumice, a thick paleosol containing numerous traces of Bronze Age human takeovers developed, covered by the deposits of the Plinian eruption of the Avellino Pumice (3,3 ka; Rolandi et al., 1993a; Andronico et al., 1995; Cioni et al., 1995, 1999). This eruption was followed by a period of intense explosive activity dominated by 6 main eruptions (Andronico and Cioni, 2002), varying from sub-Plinian to phreato-Plinian (AP1 and AP2 members) and from violent Strombolian to Vulcanian (AP3–AP6 members), with some minor intervening events. The last of this eruption (AP6) was temptatively related with an eruption account at 217-216 B.C (Stothers and Rampino, 1982), and was followed by a period of quiescence interrupted by the Plinian eruption of the AD 79 ("Pompeii") (Lirer et al., 1993; Sigurdsson et al., 1985; Cioni et al., 1992, 1996, 1999). After the "Pompeii Pumice" eruption, the volcano grew discontinuously (with minor summit collapses), and experienced periods of open conduit and persistent activity (both strombolian and effusive), occurred in the first to third centuries, in the fifth to eighth centuries, in the tenth to twelfth centuries, and in 1631–1944, as indicated by a combination of field and historical data (Andronico et al., 1995; Cioni et al., in press).

High intensity, explosive eruptions sporadically occurred between these periods, the two largest being the Subplinian events of AD 472 (also known as "Pollena" eruption, Rosi and Santacroce, 1983; Arnò et al., 1987; Lirer et al., 2001; Mastrolorenzo et al., 2001; Sulpizio et al., 2005) and AD 1631 (Arnò et al., 1987; Rolandi et al., 1993b).

These two eruptions left thick deposits of fallout and pyroclastic flow sequences that cover all the volcano (Rosi and Santacroce, 1983; Rosi et. al., 1993). Although their products have a volume an order of magnitude lower than those of the Plinian eruptions and are dispersed on a smaller area, the two eruptions had a remarkable impact on the territory, with serious damages for environment and population, particularly well documented for the eruption of 1631.

The great eruption of 1631 is the last largest explosive eruption of Vesuvius. It occurred after a long, even though not well known, period of quiescence. After this violent eruption, the inhabitants living at the base of the volcano, became accustomed to its activity and were inclined to record only the most notable events. Since this time, the volcano entered a stage of semi-persistent, mild activity (small lava fountains, gases and vapour emission from the crater) repeatedly interrupted by short-lasting rests (from months to only few years), with numerous effusive-explosive eruptions. During this period the main explosive eruptions were of limited magnitude (VEI 3). The last eruption of Vesuvius occurred in 1944, characterized by the emission of lava flows, lava fountain and, at the end, by a conspicuous emission of ash (Marianelli et al., 1999).

According to the geophysical data (Auger et al., 2001) and petrological study (Marianelli et al., 1999; Fulignati et al., 2000; Santacroce et al., in press), the magmatic system of Somma-Vesuvius during the last activity was characterised by the presence of a shallow magma reservoir, refilled during the eruptions with magma coming from a deeper (8 to 11 km) reservoir. Fluid inclusions in older Mt. Vesuvius explosive and effusive products indicate crystallization depths between 4 and 10 km. Before Plinian eruptions, magma rises from the deeper reservoir and stock in a shallow magmatic chamber localised at about 3-5 km of depth, and before the strombolian activity, less than 2 km of depth. In the shallow magmatic chamber the new magma mixes with the magma residual of the previous eruptions and with the periodically arriving mafic magma batches from the depth.

The volcano has been quiescent since 1944. Over the past few centuries, the periods of quiescence have varied from 18 months to 7½ years, making the current dormancy the longest in the last 400 years. While Vesuvius is not thought likely to erupt in the immediate future, the danger posed by future eruptions is seen as very high in the light of the volcano

tendency towards sudden extremely violent explosions and the very dense human population on and around the mountain. From more than 60 years the volcano is in a complete quiescence state, characterized by low-temperature fumaroles (less than 100°C) and moderate to low seismic activity (about 100 earthquakes per year with magnitudes between 0.5 and 3.6), and it is difficult to predict when it may erupt explosively again.

3.2 Eruption types

As briefly mentioned in the previous paragraph, the Vesuvius eruptive history was punctuated by eruption characterized by different styles of activity. In a recent work, Cioni et alii, (2007) presented a critical review of published and unpublished stratigraphic and compositional data, leading to a compilation of a database of the explosive activity in the past 18,000 years. The wide spectrum of explosive styles and the general behaviour of the volcano were characterized in terms of time frequency of the events, Magnitude vs. Intensity relationships, and Intensity vs length of the repose time. The types of explosive eruptions taken into account are:

Plinian eruptions

Sub-Plinian eruptions (further subdivided in Subplinian I and Subplinian II)

Violent Strombolian eruptions

Ash emission events

Mild strombolian (mixed explosive-effusive) activity

Of each eruption, the general features of their deposits and the physical parameters estimated from the deposits themselves were pointed out in order to give an idea of the impact on the environment and human settlements, and to highlight the different intensity and duration of each past eruptive scenario (Tab. 3.1 and 3.2).

Eruption type	Main Fallout deposits	Pyroclastic Density Currents (PDC) deposits	Ash Fall deposits
Plinian	Compositionally zoned (Mercato Pumice is the only exception), massive to faintly stratified, thick pumice beds. The stratification is given by vertical grain-size variations. Maximum thickness from 10 m (Pomici di Base) to 1 m (Avellino Pumice) in the medial sectors.	Complex interlayerings of PDC deposits in the form of thinly laminated, plane parallel to dune bedded ash beds, or massive, topographically controlled, matrix supported, pumice-bearing lobes. lithic –rich, massive to stratified, matrix supported deposits are present in all the eruptions.	Ash fallout deposits, up to 10-15 km downwind, during the opening phase Regionally dispersed, thick sequences of Accretionary-lapilli bearing ash blankets during the waning phase of the eruption.
Sub-Plinian I	Compositionally zoned (Greenish Pumice is the only exception), stratified (Greenish, AD 472) or massive (AD 1631) pumice and scoria beds. The stratification is marked by the interposition of thin ash layers. Maximum thickness from 3 m (Greenish Pumice) to 0.5 m (AD 1631) in the medial sectors.	Major topographically controlled, massive to internally stratified, Ash- and Lithic-rich PDC deposits related to the caldera collapse and to the final phreatomagmatic phase (AD 472, AD 1631). Minor, cross-laminated, dune bedded PDC deposits.	Ash fallout deposits, mainly dispersed on the slopes of the volcano, during the opening phase (Greenish Pumice, AD 1631). Regionally dispersed, thinly stratified, often accretionary lapilli-bearing, coarse and fine ash beds, during the final phreatomagmatic phase.
Sub-Plinian II	Compositionally zoned, thinly stratified, poorly to moderately sorted, scoria beds. Thin ash interlayers, sometimes accretionary lapilli-bearing. Maximum thickness ranges from 1 m (AD 512) to 0.5 m (AP2) in the medial sectors.	Thin, cross laminated, ash deposits from diluted PDCs, confined to narrow sectors along the slopes of the volcano (AD 512) or radially dispersed in the vent area (AP1 and AP2) .	Thin, accretionary lapilli-bearing ash fall deposits during the opening phase mainly dispersed on the volcano slopes. Bedded sequence of massive, accretionary lapilli-bearing ash deposits and vesiculated tuffs during the final phase. Thickness of few decimeters on the slopes of the volcano.
Violent Strombolian	Massive to crudely stratified, coarse to fine scoria lapilli. The deposits of many post-1631 eruptions have lithic rich, clast supported lapilli beds interlayered or on top of the sequence. The clasts of these lithic-rich beds present a distinctive red-ash coating. The total thickness of the lapilli beds ranges from few centimetres (e.g. AD1707, AD1730) to 1 m (PM2, PM3).	Hot avalanches restricted to the summit cone (AD1944) or to the upper slopes of the volcano (AD1822).	Thin phreatomagmatic (Lithic-rich and Accretionary lapilli-bearing) fine ash beds dispersed up to the medial sectors during the final phreatomagmatic phase.
Continuous ash emission	Sequences of laminated to stratified fine ash fall beds interlayered with Thin, well sorted to faintly stratified, massive beds of scoria Lapilli. Thickness ranges from 0.5 m (AP3) to few centimetres (eruptions of Middle Age activity) in the medial sectors		

Tab.3.1 Definition of the Vesuvius eruptive scenarios (from Cioni et al., 2007)

Eruption type	**Repose** years	**Volume** Km3 *(VEI)*	**Peak MDR** Kg s-1	**Column height** Km	**PDC**	**Duration**
Plinian	10^2 - 10^3	10^0 - 10^1 *(5)*	10^7 - 10^8	> 20	Yes	hours
Sub-Plinian I	10^2	10^{-1} - 10^0 *(4)*	10^7	15 - 20	Yes	hours
Sub-Plinian II	10^2	10^{-2} – 10^{-1} *(3)*	10^6 - 10^7	10 - 15	Minor	Hours - days
Viol.ent Strombolian	10^1 - 10^2	10^{-3} – 10^{-1} *(3-2)*	10^5 - 10^6	5 - 10	Minor Avalanching	Hours - days
Continuous ash emission	10^1 - 10^2	Up to 10^{-2} *(3-2)*	< 10^5	< 5	No	Weeks - Months ?
Mild strombolian	10^0 - 10^1	10^{-3} (2)			No	

Tab.3.2 Physical parameters estimated from the deposits of the different eruption styles (modified from Cioni et al., 2007). MDR = mass discharge rate; PDC = pyroclastic density currents.

In the present thesis, we have focussed our attention on the continuous ash emission eruptions, that have been overlooked in the past at Vesuvius, unlike of the most violent explosive episodes, such as the Plinian, sub-Plinian and violent strombolian eruptions.

3.4 Ash eruptions at Vesuvius

Stratigraphic studies conduced all around the volcano have highlighted the presence of deposits related to mid-intensity explosive events in the periods between: 1) the 3500 BP Avellino and AD 79 Pompeii Pumice eruptions (AP1-AP6); 2) the AD 79 Pompeii Pomice and AD 472 Pollena eruptions (S. Maria Cycle); 3) the AD 512 and AD 1631 eruptions (AS) (Andronico et al., 1995; Rolandi et al., 1998); and 4) the AD 1631 and 1944 eruptions (Arrighi et al., 2001).

Several stratigraphic sections (Tab. 3.3, Fig. 3.4) have been studied, giving a general characterisation of the depositional features and of the products of the continuous ash eruptions.

Eruption	Section	Locality	Distance from the vent (Km)	Coordinates
AP3-AS1a	S1	S. Pietro	3.66	0455244-4519181
AP3	S2	Via Cupa Miano	9.43	0461099-4521620
S. Maria Cycle	S3	Villa Telesi	4.06	404858.05-142847.8
S. Maria Cycle	S4	Palomba	12	0456195-4520869
AS1a	S5	Crossodromo Quarry	3.07	0455035-4518122
AS1a	S6	Vallone Profica	3.43	0455031-4519356
AS1a	S7	Avini	4.83	404819.8-142858.91
AS1a	S8	Pescinale	4.32	0455190-4520746
AS1a	S9	Raggi	8.62	405034.13-143134.60
AS2-AS3	S10	Fabbrocini	4.42	0454656-4518214

Tab.3.3 Stratigraphic sections positions

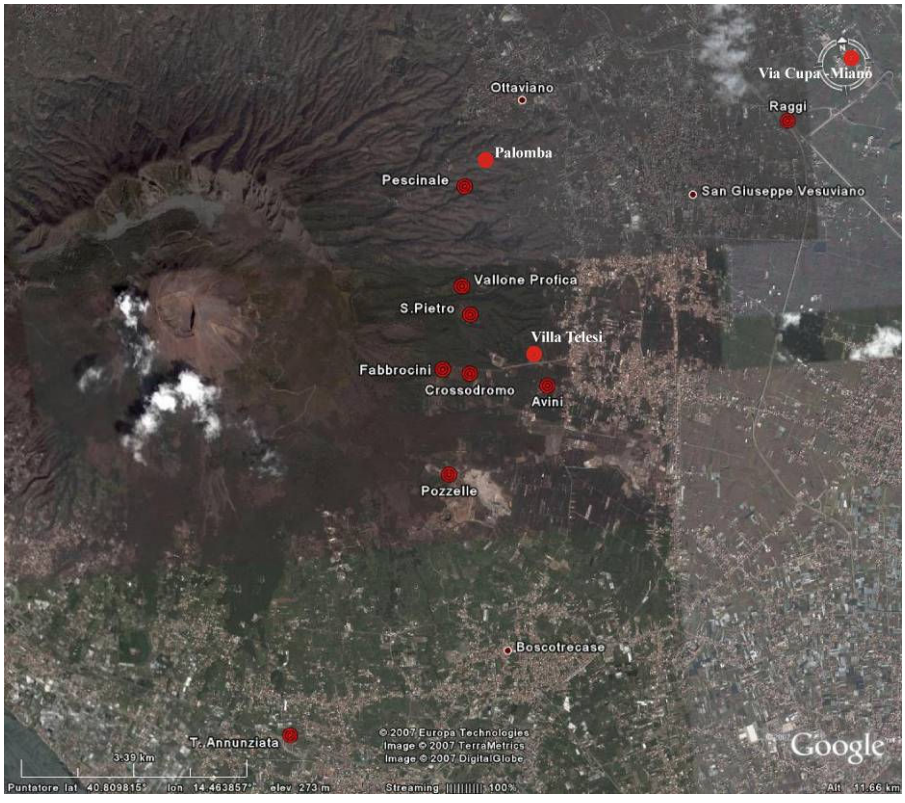

Fig.3.4 Stratigraphic section distribution around the Vesuvius area

Activity between the Avellino and Pompeii Plinian eruptions (AP1-AP6)

The eruptions occurred during this period of activity were well documented by Andronico and Cioni (2002), and here their main results are briefly summarised here.

The stratigraphy of the AP deposits shows that the 1,600 years separating the two Plinian eruptions of Avellino and Pompeii were characterized by a higher frequency of volcanic activity than the preceding interplinian periods. Deposits are characterized by complex sequences of fallout, massive to thinly stratified, scoria-bearing lapilli layers and fine ash beds (Andronico and Cioni, 2002).

From stratigraphic studies in an area of about 300 Km^2 in around the volcano, AP1-AP6 deposits were recognised and mapped. This sequence of eruptions records two main styles of activity, each involving complex relationships between magmatic and phreatomagmatic phases. The Authors distinguished two sub-Plinian to phreato-Plinian events (AP1-AP2), and four mixed, violent Strombolian to Vulcanian, events (AP3–AP6), the deposits of which were separated by thin paleosols, humified layers, and primary erosive unconformities (Tab. 3.4).

Formations	Members	Beds	Age	Eruption style	Volume (km^3)	Composition
Pompeii Pumice Formation (PPF)	Pompeii Pumice		A.D. 79 (Lirer et al. 1973)	Plinian	2.8	Phonolite tephrites to phonolites
	AP6		217–216 B.C. (Stothers and Rampino 1983; Rolandi et al. 1998)	Prevalently violent Strombolian		Tephritic phonolites to phonolites
	AP5	A,B		Violent Strombolian (A) to Vulcanian (B)	0.084	Tephritic phonolites
	AP4a			Phreato-Plinian		Tephrite phonolites to phonolites
	AP4	A,B,C		Violent Strombolian (B) to Vulcanian (A, C)	0.122	Tephritic phonolites
	AP3a			Phreatoplinian		Tephritic phonolites to phonolites
	AP3	A,B,C	2,710±60 years B.P. (Rolandi et al. 1998)	Violent Strombolian (B) to Vulcanian (A, C)	0.15	Tephritic phonolites
	AP2	A, B, C, D	3,000±200 years B.P. (Santacroce 1987) 3,225–1,140 years B.P. (Rolandi et al. 1998)	Sub-Plinian (A) to Phreato-Plinian (B, C, D)	0.143	Phonolite tephrites to phonolites
	AP1	A, B, C, D	3,220±65 years B.P. (Andronico et al. 1995) 3,420±100 years B.P. (Rolandi et al. 1998)	Sub-Plinian (A) to Phreato-Plinian (B, C, D)	0.147	Tephritic phonolites to phonolites

Tab. 3.4 Stratigraphic scheme and main features of the different AP members (from Andronico and Cioni, 2002).

The AP1-AP2 events were erupted by a vent located 3 km west of the present crater of Vesuvius, in correspondence of the Piano delle Ginestre area, as for the earlier Avellino eruption. They were characterized by the deposition of a complex sequence formed by an alternation of accretionary lapilli-bearing fallout, pumice and ash-fall layers, and stratified fall layer, formed by thin lapilli beds alternating with thicker, plane-parallel, indurated, coarse and fine ash.

Juvenile material from these two eruptions shows a wide variety of morphologies. It varies from pumice with thin, commonly tubular, frequently coalescing, vesicles, showing a generally elongated shape, related to high energy magmatic eruptions, to fragments coated by adhering fine ash, with mostly spherical vesicles, and frequently filled by micron-sized ash, to blocky, dense fragments with conchoidal external surfaces cutting a glassy matrix.

Following the first two eruptions, the stratigraphic succession records the deposition of four main eruptions (AP3–AP6 members) and at least two minor events (AP3 α and AP4 α members), totalling more than 4 m in thickness on the south-eastern slopes of the volcano. The succession consists of a monotonous sequence of fallout deposits largely represented by accretionary lapilli, massive to laminated ash, alternated with only minor lapilli beds. As a general rule, the dispersal of all these deposits indicates a shift in the position of the eruptive vent from Piano delle Ginestre to the area of the present crater. Juvenile fragments have a lower vesicularity than those from the AP1 and AP2 members. Clasts, characterised by delicate, thin, protruding tips and sharpen rims, show a generally blocky shape and a glassy groundmass, with an external surface interested by diffuse pitting. Scoria fragments, characterized by large, spherical to ovoid vesicles, with a lower degree of glass pitting and ash infilling of vesicles, are also present.

Pumice and scoria from AP1 and AP2 members show a large variability, from tephritic phonolites to phonolites. A normal sequence of extraction from the more evolved to the less evolved material is generally observed in each member, suggesting the tapping of compositionally stratified reservoirs. Products of AP3, AP4, and AP5 members have a tephri-phonolitic composition, with a slight shift toward less evolved terms with time.

Activity between the Pompeii and Pollena eruptions (Santa Maria cycle)

The Santa Maria eruption is separated from the top of the Pompeii Pumice deposit by an erosive surface with very scarce evidence of humification. The related deposits are well exposed on the eastern sector of the volcano, and are characterised by a complex sequence, constituted mainly by dark, thinly laminated ash (Fig. 3.5).

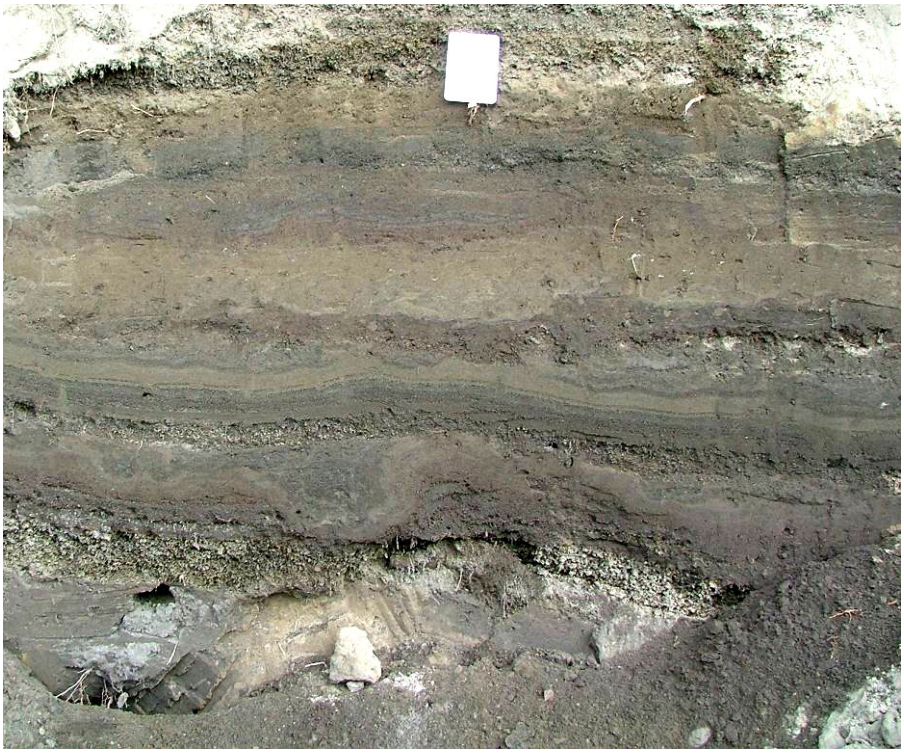

Fig. 3.5 Sedimentological features of S. Maria eruptions at S3

The main sedimentological features of this eruption can be described referring to the stratigraphic section of Villa Telesi (S3), located at about 4 Km from the vent. For the sake of simplicity, the sequence was subdivided in five parts, which include three ash layers and two lapilli beds (Fig. 3.6).

The first ash layer consists of an alternation (20-26 cm thick) of fine and coarse, dark-grey ash, showing sometimes discontinuous lamination (sheet-washing), at the top of which, a well sorted, 1 cm thick, lapilli bed is present. A yellow, 1 cm thick, hardened level is always present in the middle part of this layer (Unit A).

At the top, 7 cm of fine lapilli and coarse ash with reverse grading constitute the first lapilli layer. Juvenile material is highly vesicular, and consists of glassy material, with rare crystals of leucite, pyroxene and dark mica (Unit B).

The second ash layer is a complex sequence made of fine, well sorted, slightly bioturbated and laminated ash (17 cm thick, Unit C). Coarse, massive ash beds are alternated with fine ash, in part weakly stratified and reworked. In the middle part, a poorly sorted, coarse ash and lapilli layer is present (2 cm thick, summit Unit C_L), followed by 10 cm of fine, massive, reworked ash. At the top, 7-8 cm of fine and coarse ash, in discontinuous lamination, partially reworked, and reddish at the top occurs, followed by 5 cm of coarse and fine, massive, reddish, reworked, normally graded ash.

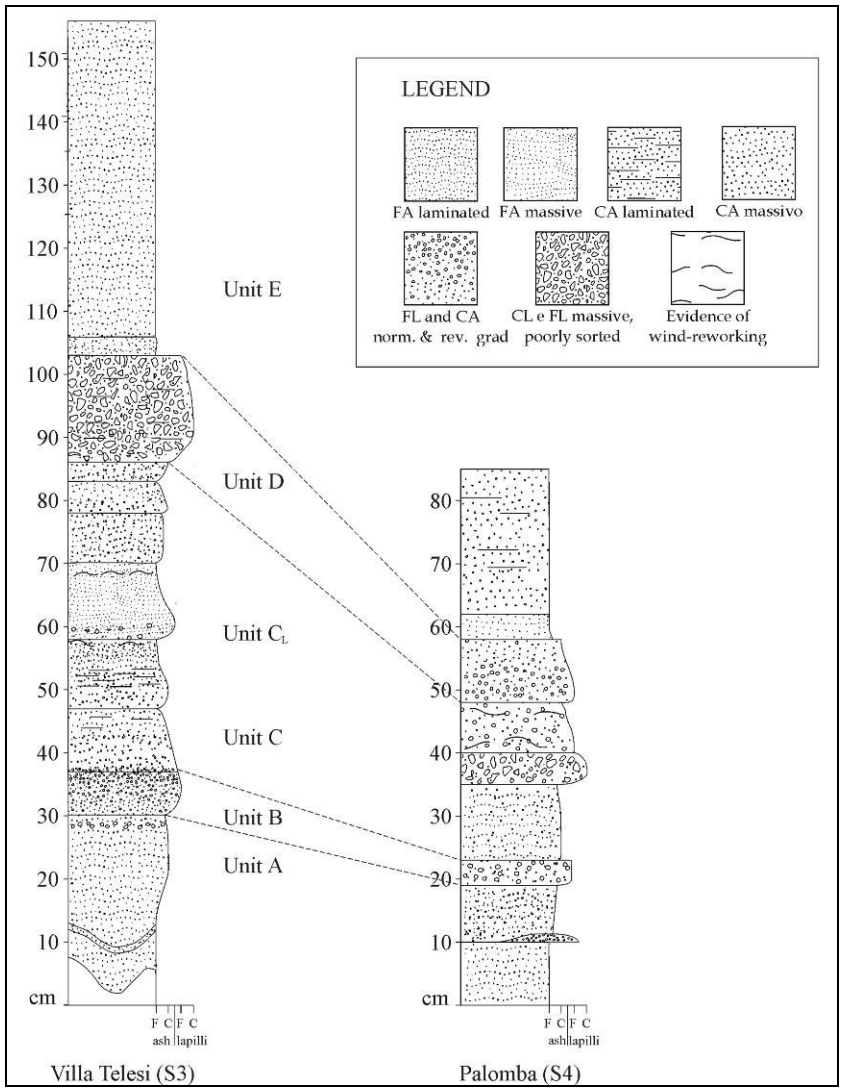

Fig.3.6 Stratigraphic correlation of Santa Maria Cycle deposits

The second lapilli rich layer (Unit D) has a thickness of 23 cm, and consists of a stratification of fine and coarse lapilli with colour banding, changing from yellow, to grey, to reddish. At the top, a coarse, reddish and massive stratified ash rich bed is present. A fine, yellow, massive and reworked ash (3 cm thick) split this layer from the uppermost ash sequence.

The last ash layer is formed by 50 cm of an alternation made of light-grey and yellow fine ash (Unit E), the top of which is in contact with the soil of the 472 AD deposit. In a distal outcrop, (S4, 12 Km from the vent), a reduction of the thickness of the deposits occurs, from about 150 cm to 85 cm; the three lapilli-rich beds are well correlated with the proximal section, while the other ash rich layer are affected by modification of the thickness and inner structures (Fig. 3.6).

The products of this eruption have a phonolitic tephrite bulk rock composition, with phenocrysts of green pyroxene, leucite and rare phlogopite, and an hipocrystalline groundmass with microlites of clinopyroxene and leucite. Juvenile material is mainly made of light glass, with minor dark, highly crystallised scoria.

Activity between the 512 A.D. and 1631 A.D. eruptions

In the Middle Age, shortly after the 512 A.D. eruption, Vesuvius activity was characterised by several explosive episodes dominated by continuous, long-lasting ash emission directly form the vent. Related deposits have been identified as thick, repetitive air fall sequences of fine and coarse ash layers, suggesting an origin related to mid-low intensity eruptions. These caused the formation of low-level, ash charged, weak plumes, with a column height less than 10 Km above the vent area and an eastward dispersion, depositing ash up to about hundred of kilometres.

The mid-low intensity eruptions were generally alternated with episodes of strombolian activity, that produced centimetric to decimetric, well-sorted, lapilli beds.

The stratigraphic studies conduced all around the volcano allowed the reconstruction of at least five different major eruptive events (AS1-AS5), each characterised by the emplacement of complex fall-out sequences, only separated by slight unconformities. The limits between each eruption were fixed in correspondence of erosive surfaces and transition in colour and grain size of the products. At each event we referred using the

informal stratigraphic (Hedberg, 1994) name AS, an acronym for "*Attività Storica*" (Historic Activity) associated to a number, indicating the stratigraphic position (AS1- AS5; Fig. 3.7).

In the present work some minor refinements to an already established stratigraphic framework were done, improving the temporal definition of this complex period of activity.

The AS1 was referred, on the base of historical chronicles and stratigraphic studies, to the A.D. 512 eruption, defined as a Subplinian II event (Cioni et al., 2007). The related deposits were generated by the emplacement of 8 main eruptive units (Cioni et al., in prep.), characterised by a lower intensity and magnitude with respect to the other subplinian eruptions of Vesuvius, and by the very minor occurrence of pyroclastic density currents (PDC) during the eruption. At the beginning a low intensity phreatomagmatic pulses deposited thin, ash fallout up to the medial sectors, and lasted few hours. This phase were followed by a mainly magmatic phase, the only able to produce PDC, interlayered with minor phreatomagmatic episodes, that produced short eruptive pulses (minutes to hours) at intervals of a few hours to days. Unsteadily sustained convective columns occurred during each pulse, recorded by the deposition of strongly stratified, poorly to moderately sorted, scoria-lapilli fallout, dispersed over the volcano slopes and up to the plain at the feet of the volcano. The final phase was mainly phreatomagmatic and consisted of repeated emission of low-level ash plumes possibly lasting for many weeks after the end of the paroxysmal phase, during which stratified sequence of cohesive ash fall beds and vesiculated tuffs were emplaced (Cioni et al., 2007).

Juvenile material is represented by two principal types of material: 1) highly vesicular, brown, flat scoria, characterised by a smooth external surface, sometimes with bread crust structures; and 2) microvesicular, dark grey, scoria.

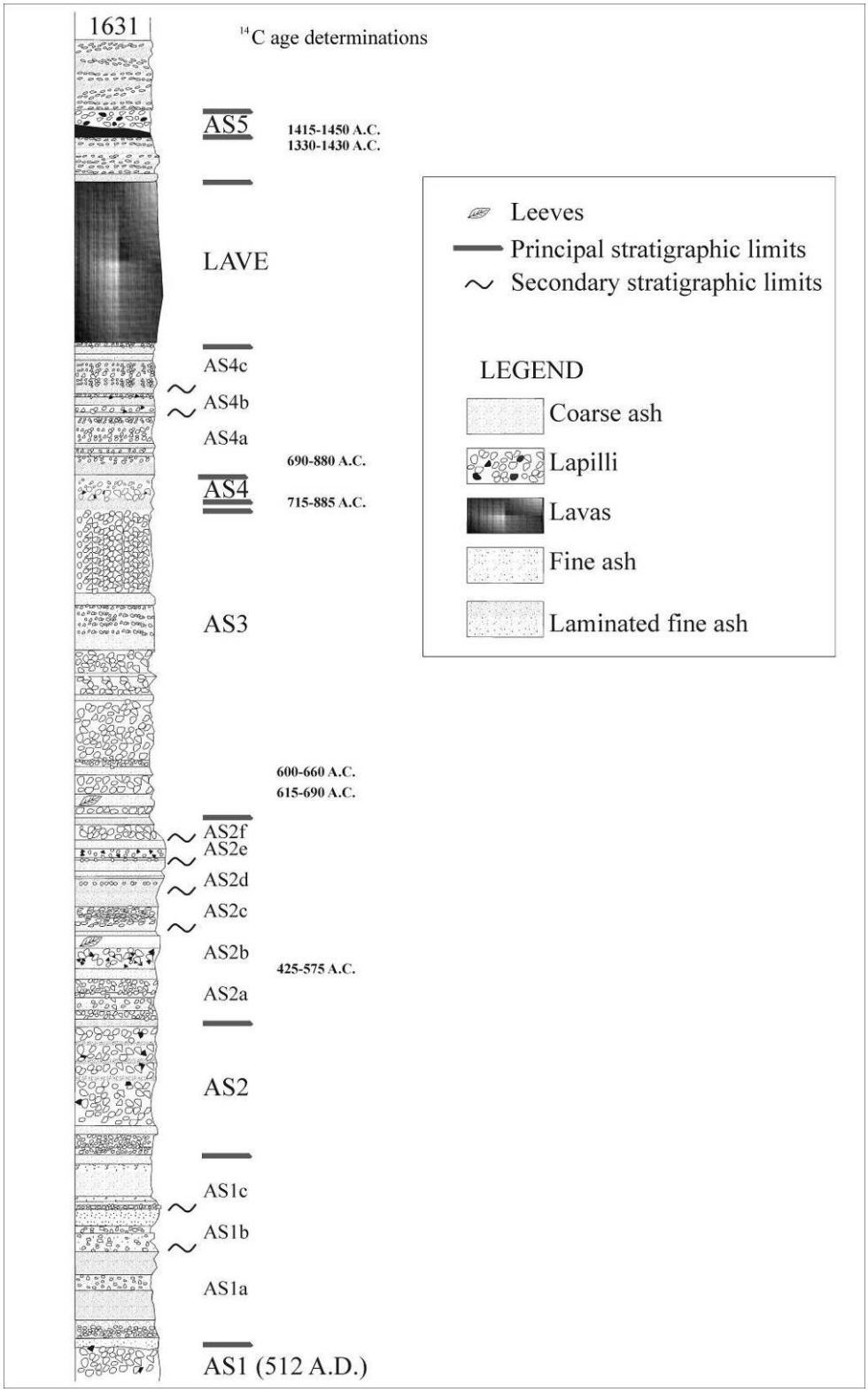

Fig. 3.7 Reconstructed stratigraphic section of the Vesuvius activity between the 512 AD and 1631 eruptions.

At the top of AS1, a 10 cm thick layer, constituted by reworked light brown ash and characterised by an uppermost eroded surface, represents the transition to the following cycle of activity, lasted between the V-VI centuries. Three minor eruptions (AS1a-AS1c) are recorded by ash fall-out layers, alternated with minor lapilli beds. The related deposits are exposed in few sites, located in the eastern sector of the volcano, as far as 10 Km from the vent (Fig. 3.4). Their total thickness range between 30 cm in distal outcrops to 150 cm at 3.5 Km from the vent. As a general rule, this eruptive sequence is characterized by the alternation of beds with different sedimentological features, related to different phases of activity (Fig. 3.8). Fine, massive, poorly sorted ash and stratified, very poorly sorted, coarse and fine ash are interstratified with well sorted, minor lapilli beds, mixed with fine ash. The products of this activities are made of heterogeneous juvenile material, showing high variability of crystal and vesicle content, despite their similar chemical composition.

Fig. 3.8 AS1a-AS1c sequence at Crossodromo Quarry (S5)

Lateral variations of the entire succession are shown in Fig. 3.9. Single Units show the same sedimentological and stratigraphic characteristic, showing thickness variations and

difference of the inner structures of the single depositional layer, possibly influenced by local changes of wind directions and effects of erosion.

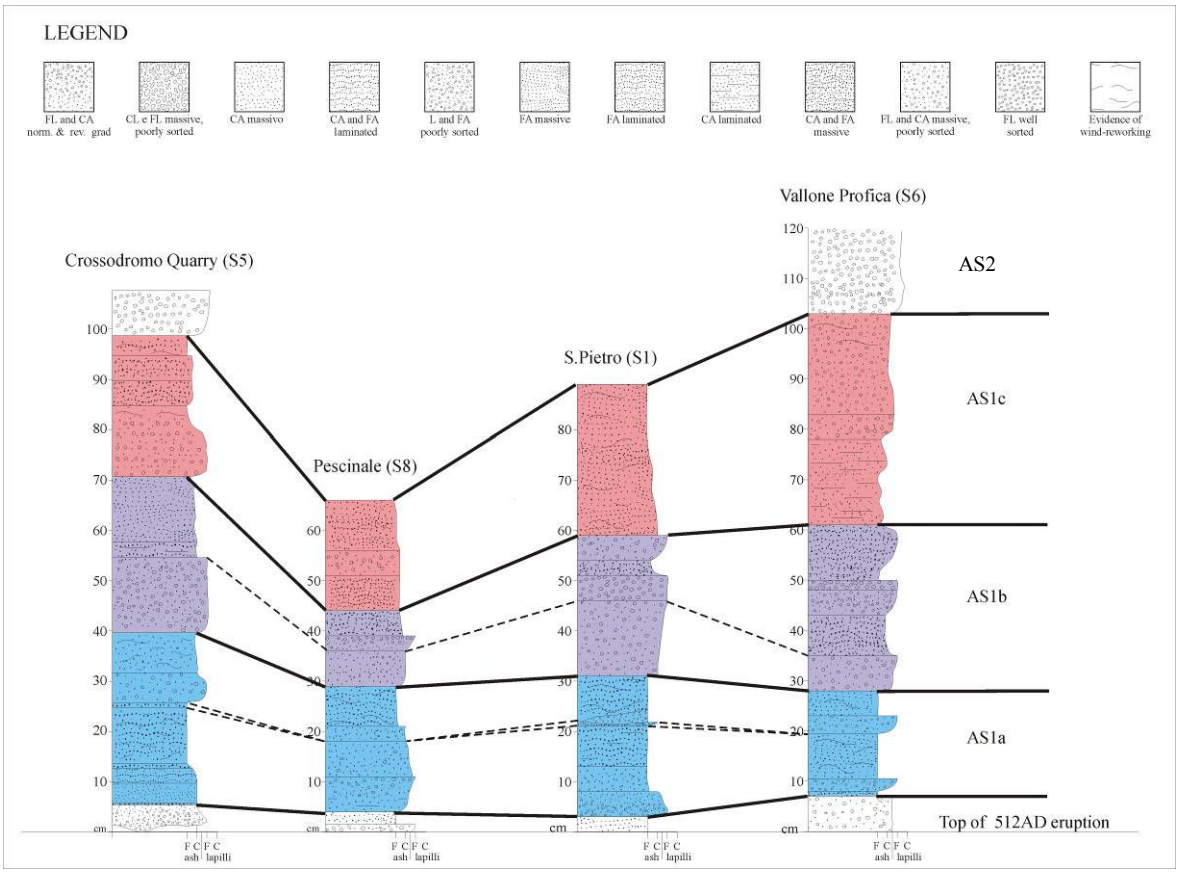

Fig. 3.9 Lateral variations of the AS1-AS2 stratigraphic succession

The reconstruction of the isopach maps for the deposits of the AS1a-AS1c sequence allowed the calculation of its volume and dispersal features. Isopach maps evidence that the dispersion of the products occurred in the eastern direction, showing that vent position was in correspondence of the present cone (Fig. 3.10).

Using the method of Pyle (1989), the minimum volume of the deposit was estimated at about $1.3x10^8$, $8x10^7$, and $9x10^7$ m3, respectively for AS1a, AS1b and AS1c Units.

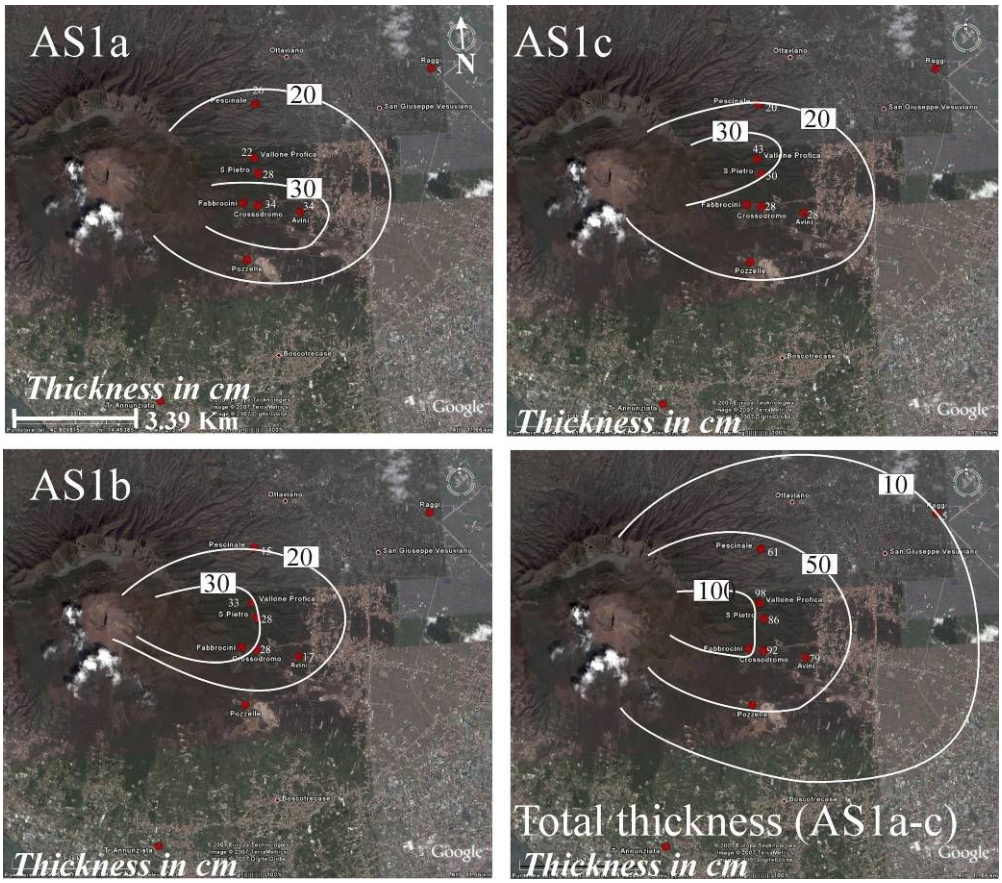

Fig. 3.10 Isopach maps for the single units AS1a, AS1b and AS1c, and total thickness.

The contact with the AS2 event is set in correspondence to a fine, reworked ash layer with a thickness of 3-6 cm. This eruption occurred with relatively highest energy with respect to the preceding activity, generating a thick (about 25 cm), well sorted lapilli bed, dispersed in the NE and SSE direction. Lapilli are constituted by dark, highly vesicular scoria, with a general low crystal content.

The following AS2a-AS2e succession generated a complex sequence, characterized by an alternation of well sorted, fine lapilli beds and fine and coarse, massive ash. Lapilli consist of dark to yellow scoria, which, in the last case, is coated with ash (Fig. 3.11). Fine ash beds with evidence of wind reworking contain traces of organic matter (leaves), suggesting that the activity had a discretized character, with impulse of low energy spaced out by time intervals.

Fig. 3.11 AS2-AS3 sequence at Crossodromo Quarry (S5)

At the top of these events, a coarse lapilli-rich bed indicates the onset of the AS3 eruption, occurred around the VII Century. The related deposits are dispersed toward East and reflect the emplacement of three main scoria lapilli beds, interlayered with minor coarse, sometimes with evidence of wind reworking, ochre ash layers, with a total thickness of about 2 m. Also in this case, traces of leaves are present along the succession, within the ash layers. The juvenile material consists of dark, aphiric, flat lapilli, sometimes coated by ash. At the top of the succession, a reworked ash rich bed marks the transition to the AS4 deposit.

This cycle of activity continued with a period of open conduit activity, characterised by prolonged, high energy, strombolian phases, interlayered with short periods of ash plume fallout (AS4, AS4a-AS4c), and were closed by the lava emission activity occurred at about 1000 A.D.

The two eruptions studied in this work belong to the activity occurred in the Avellino Pompei period (eruption AP3) and the AS1-AS2 (AS1a). Both the eruptions deposited ash fallout ash sequences related to mid-low intensity activity, although showing some differences connected with the occurrence of the interactions of magma with external water, evident in AP3 while totally lacking in AS1a.

In the following, the results of the stratigraphic investigations and the physical parameters (grain size distributions and volume) of the two eruptions, studied in detail, are reported.

4. AP3 ERUPTION (2,710±60 years B.P.)

4.1 General settings

AP3 member consists of a fallout sequence mainly formed by ash beds and minor scoria layers. It has been subdivided into three main beds, basing on colours changes and grain size of the products (Fig. 4.1).

The base is represented by an accretionary lapilli-rich, normally graded, vesiculated ash layer (bed A). It is formed by massive, light-colored, fine ash and minor coarse ash laminations. In a few outcrops, this bed directly rests on a discontinuous, humified layer containing small, charred, vegetal remains.

The transition toward the overlying bed B is marked by a change in colour, correspondent to an abrupt change in the microscopic texture of juvenile shards. Bed B is an ubiquitous, coarse-grained fall deposit. Two main units are recognized. Unit B1 consists of a massive layer formed by light green-coloured, sometimes banded, scoria. Unit B2 is formed by an alternation of thin layers of dark, poorly vesicular, ash-coated lapilli and cohesive fine ash.

At the top, a complex sequence of fine-grained, faintly laminated, accretionary lapilli-bearing, ash layers is present (bed C). It represents the thickest bed (up to 1 m) of the AP3 member, possibly deposited by repeated eruptive pulses. It is very difficult to correlate the different layers forming bed C because of their variable main direction of dispersal.

In distal outcrops, up to about 14 Km from the vent, the deposit is constituted by three layers, correlated with A, B, C beds of the proximal section (Fig. 4.2). At the base, bed A consists of 5 cm thick, massive layer, formed by light ash. Bed B is a 4 cm thick, well sorted, lapilli-bearing layer. At top, bed C consists of a 15 cm thick, accretionary lapilli-bearing layer, at the top of which are deposited 6 cm of lapilli.

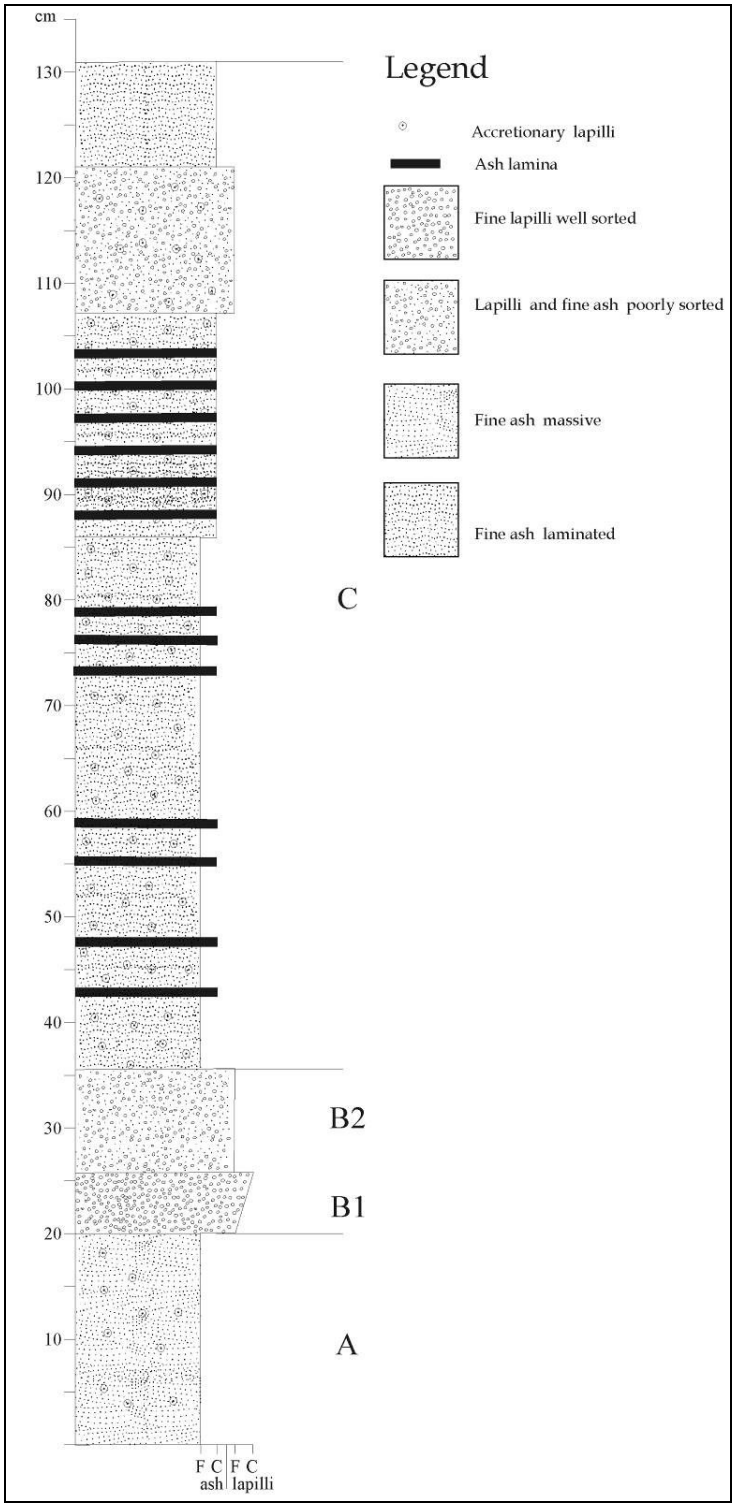

Fig.4.1 Stratigraphic section of the deposit of AP3 eruption at S.Pietro quarry (S1)

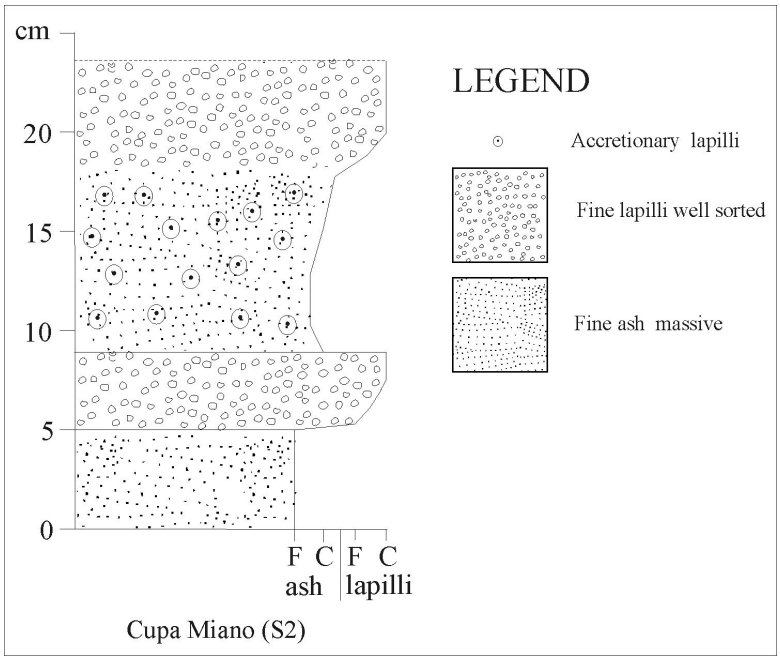

Fig.4.2 AP3 member distal deposit (S2) and collected samples.

Isopach maps indicate that in the three phases of the eruption, the dispersal axes for the products changed from SE to NE, in particular during the deposition of bed B (Fig. 4.3). Indeed, while unit B1 is dispersed in a very narrow SE-trending lobe, unit B2 is dispersed toward the NE. Bed C shows complex stratigraphic features, possibly due to deposition by repeated eruptive pulses. This reflects in a hard correlation of this bed between different outcrops (Andronico and Cioni, 2002).

From the method of Pyle, the estimated total volume of the whole AP3 deposit, resulted 1.5 x 10^8 m^3. Volume of the single beds were also calculated, giving $1.6x10^5$, $6x10^2$, $1.6x10^5$ and $8.2x10^5$ m^3, respectively for bed A, B1, B2 and C.

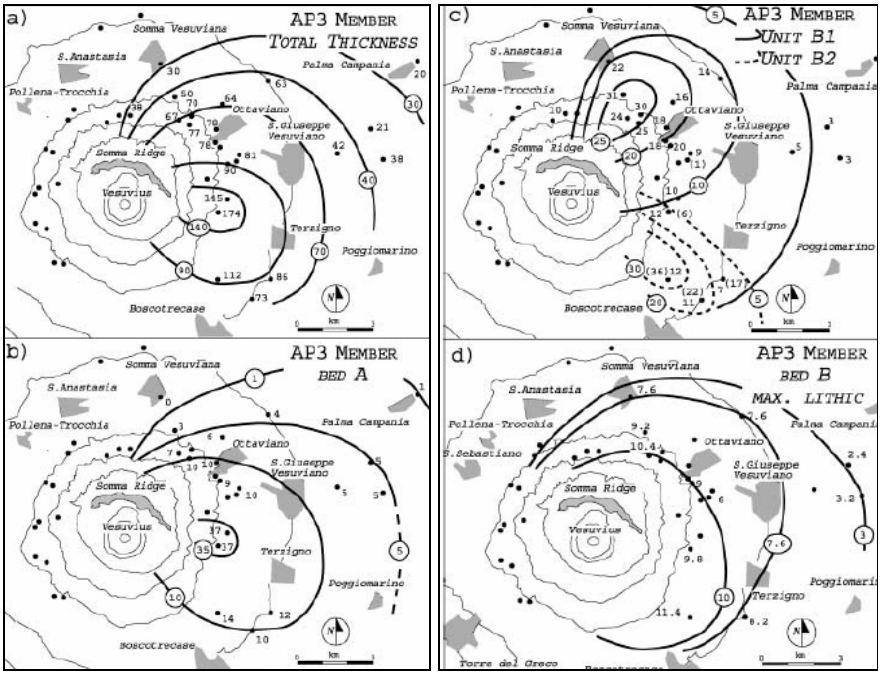

Fig. 4.3 Isopach (thickness in cm) and isopleth maps of the maximum lithic (diameter in mm) for the AP3 member. **a** Total thickness of the AP3 member; **b** AP3 member bed A; **c** AP3 member beds B1 and B2; **d** maximum lithic for the bed B (Andronico and Cioni, 2002)

Andronico and Cioni (2002) estimated the peak magma discharge rates (MDR) from isopleth maps of the maximum lithics in AP3 bed B. They found that the measured clast dimensions were close to the lower range of applicability for the method. The inferred peak MDR was of 3×10^6 kg/s (Wilson and Walker, 1987), corresponding to column heights of about 10 km. MDR values are one order of magnitude lower than those of most known Plinian and sub-Plinian events of Vesuvius (Carey and Sigurdsson, 1987; Rolandi et al., 1993a, 1993b; Rosi et al., 1993). Using the method proposed by Carey and Sparks (1986), Andronico and Cioni (2002) also calculated values of maximum column height of around 12 km, and a tropopause wind speed of ~15 m/s. These values correspond to MDR about two times larger than those calculated with the previous method. No MDR estimation was possible using these classical methods on the ash-rich beds always present in the different members. The MDR values given above must so be considered as a maximum estimation of the flow rate range.

4.2 Collected samples and grain size analysis

The stratigraphic features of this eruption are well exposed at S1, where it shows the maximum thickness of 1.7 meters. This section was extensively sampled for sedimentological, textural and compositional investigations of the eruption products (Fig. 4.4a,b,c,d). Grain size analyses were performed on 10 samples collected in proximal and distal outcrops, at different height along the stratigraphy. The calculated Inman grain-size parameters are shown in Tab. 1.1.

Bed A (samples VSM48 and VSM49 of figure 4) is a very poorly sorted, 20 cm thick layer formed by fine ash mixed with accretionary lapilli. Grain size distribution shows a quasi-symmetric, (low, positive skewness) curve, with a mode at 5Φ (Fig. 4.5).

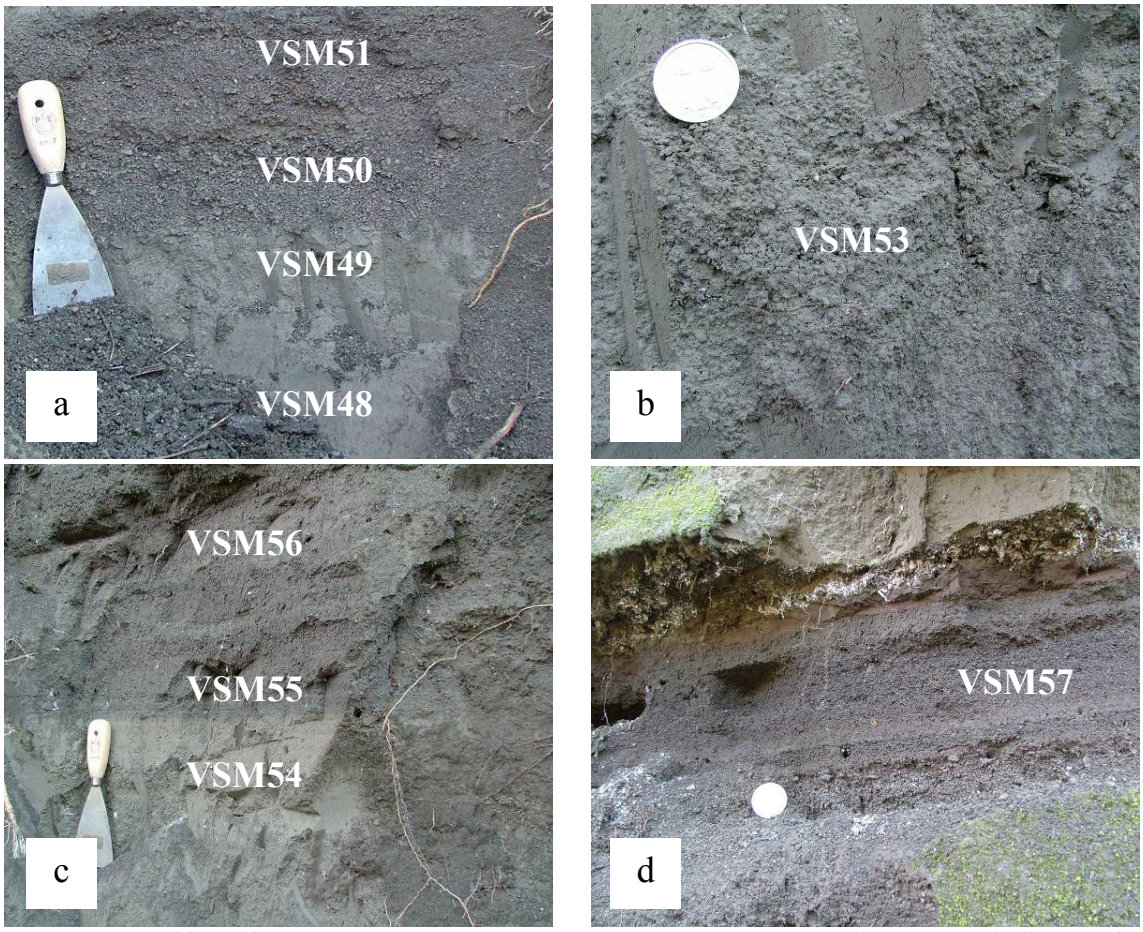

Fig.4.4 AP3 depositional features and collected samples: a) Beds A and B; b) base of bed C; c) middle part of bed C; d) top of bed C).

Beds B1 and B2 (respectively VSM50 and VSM51 of Fig. 4.4) are poorly sorted, lapilli-rich layers with a total thickness of 15 cm, characterized by a fine-tailed grain size distributions, showing two modes respectively at 0Φ and 1Φ (Fig. 4.5).

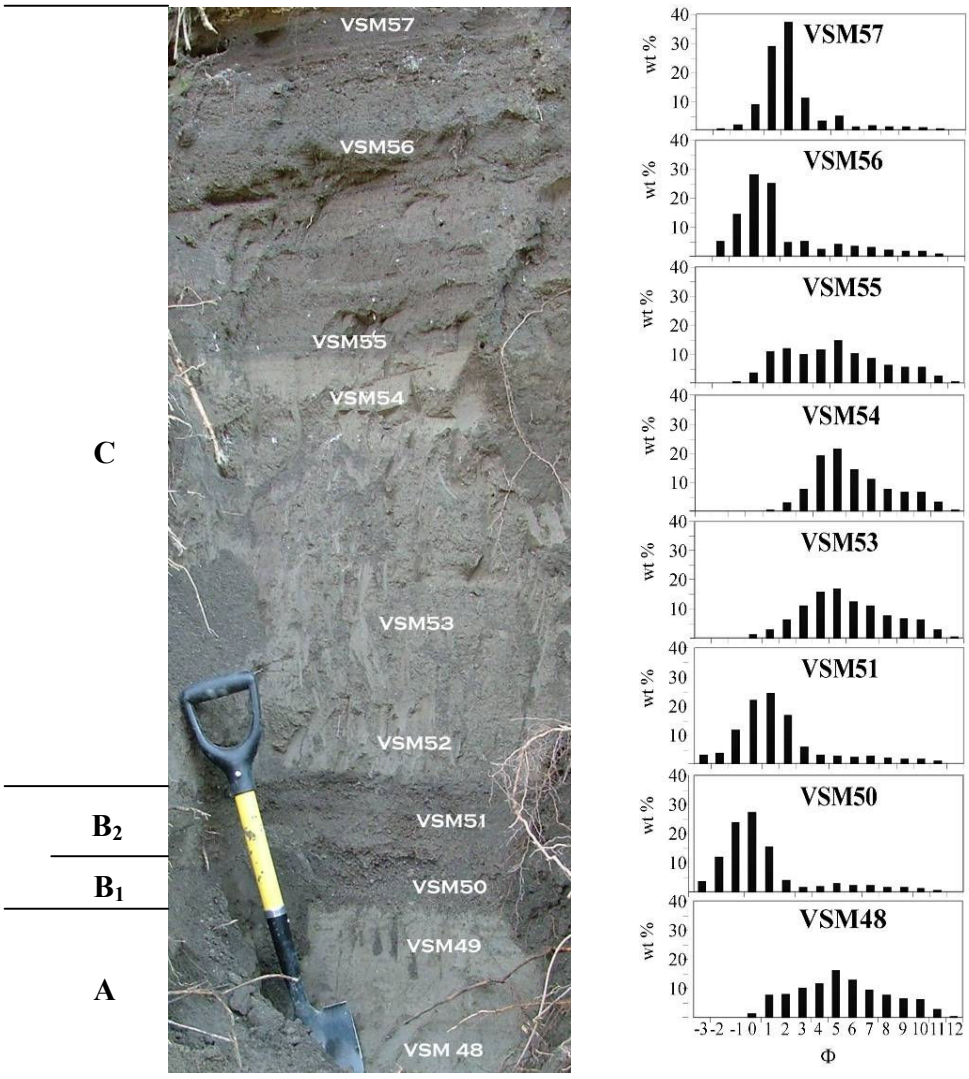

Fig.4.5 AP3 deposit at S. Pietro Qaurry and and grain size analyses of the principal layers. $\Phi = -\log_2 (d)$, where d is the particle diameter in mm

The base of bed C (sample VSM53 of Fig. 4.4) consists of a weakly stratified accretionary lapilli bed, with a thickness of 50 cm, at the top of which about 20 cm of fine ash are present (samples VSM54 and VSM55 of Fig. 4.4). Grain size distributions are characterised by very poorly sorted, fine-tailed curves, with modes at 5Φ (Fig. 5.5). The top of bed C shows a total thickness of 25 cm, and it is formed by 15 cm of a fine lapilli mixed with fine pisolitic ash (VSM56), and, at the top, by 10 cm of fine ash (VSM57). Grain size distributions are characterised by a bimodal, very poorly sorted, fine-tailed curves, with a mode that shift from 0Φ in VSM56 to 2Φ in VSM57. A second, less pronounced peak occurs, for both the samples, at 5Φ (Fig. 5.5).

Distal samples VSM61 and VSM63 were collected respectively at 8 cm and 21 cm from the base of the S2 (Fig. 4.6). They show very poorly sorted, fine-tailed grain size distributions, with mode respectively at 1Φ and 4Φ. VSM61 shows a second peak at 5Φ.

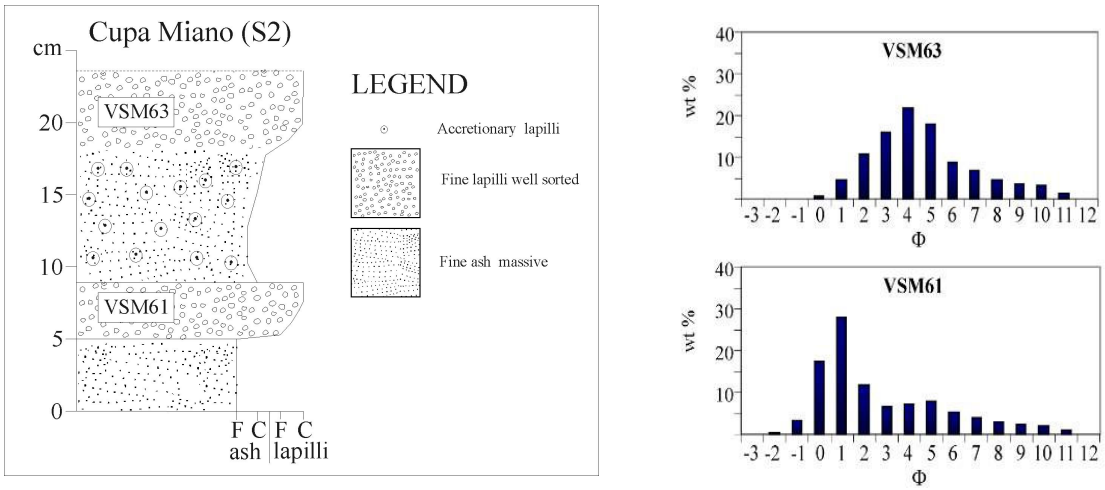

Fig.4.6 Distal Grain size distributions for samples VSM61 and VSM63 at S2.

Sample	Bed	Φ_5	Φ_{16}	Φ_{25}	Φ_{75}	Φ_{84}	Φ_{95}	MdΦ	$\sigma\Phi$	$\alpha\Phi$
VSM48	A (prox)	0.49	1.89	2.82	6.81	7.95	9.67	4.72	3.03	0.07
VSM50	B1 (prox)	-2.88	-1.98	-1.60	0.57	1.60	6.62	-0.60	1.79	0.23
VSM51	B2 (prox)	-2.28	-1.12	-0.65	1.71	2.80	7.15	0.45	1.96	0.20
VSM53	C (prox)	1.18	2.54	3.25	6.85	7.97	9.68	4.79	2.72	0.17
VSM54	C (prox)	2.24	3.29	3.76	6.87	8.05	9.73	4.95	2.38	0.30
VSM55	C (prox)	0.12	1.12	1.88	6.37	7.59	9.55	4.18	3.23	0.06
VSM56	C (prox)	-2.01	-1.23	-0.79	1.62	4.02	7.48	0.11	2.63	0.49
VSM57	C (prox)	-0.62	0.20	0.51	1.97	2.71	5.19	1.29	1.26	0.13
VSM61	B (distal)	-0.92	-0.28	0.15	4.07	5.30	8.17	1.11	2.79	0.50
VSM63	C (distal)	0.93	2.00	2.57	5.39	6.55	8.98	3.83	2.28	0.20

Tab. 1.1 Grain-size parameters of the AP3 beds. Φn = size (in Φ units) corresponding to the *n* cumulative percent. *Md*Φ, $\sigma\Phi$ and $\alpha\Phi$ correspond respectively to the values of the median diameter, sorting (graphic standard deviation) and skewness of the grain size distribution, as defined by Inmann (1952).

4.3 Characterization of the juvenile material of AP3 eruption

The products of the AP3 eruption are mostly made of juvenile materials (pumice, scoria, accretionary lapilli and loose crystals), and in minor part of lithics fragments, which consist of altered leucite and pyroxene-bearing lavas and very rare skarn aremunlitic material.

Juvenile fragments are largely heterogeneous, showing a variability of the physical, textural, and, in some cases, compositional features. As a general rule, ash fragments vary between two end members: a) light, glassy, vesicular pumice and b) dense, highly crystallised, poorly vesicular scoria (Fig. 4.7). Both types are characterized by a porfiritic index of 1-5%, with a mineralogical assemblage represented by rare, mm-sized phenocrysts of leucite, pyroxene and biotite set in a groundmass of leucite, plagioclase and pyroxene, with variable glass.

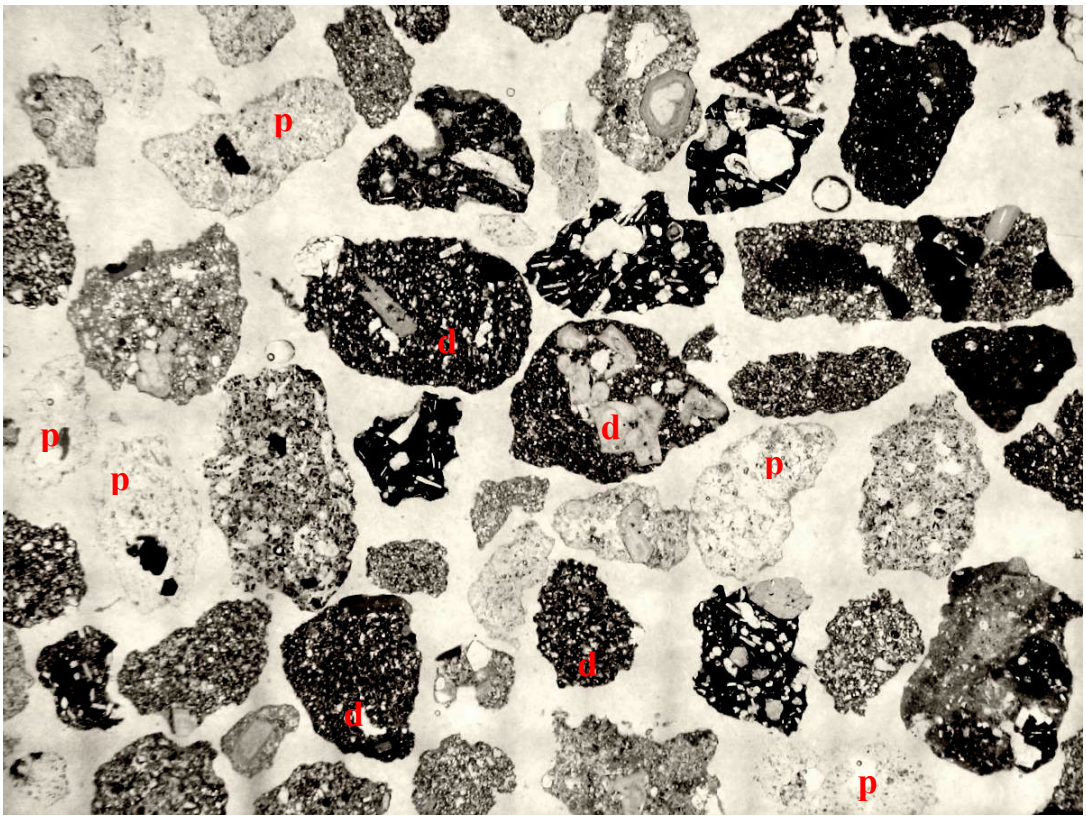

Fig.4.7 Component analyses of fragments in the 1 mm size fraction belonged to bed B. P = pumice-like clasts; d = dense fragments.

All the intermediate terms between these types exist. In particular, poorly vesicular, crystal-poor, glassy fragments are well represented (Fig. 4.8a). Moderately vesicular, crystal-rich fragments are characterised by irregularly shaped vesicles, with diktytaxitic texture; bubble coalescence seems to occur in a preferential direction, resulting in structures of vesicles alignment similar to fractures (Fig. 4.8b). Coalescence is generally nearly complete; only rounded remains of the septa, which originally separated vesicles, are preserved, suggesting an early occurrence of coalescence. The large amount of coalescing vesicles relative to the total vesicularity of fragments suggests an important role of permeability in magma degassing. In some cases the, pumice-like portion of the magma includes or envelops the dense, dark portion (fig. 4.8c).

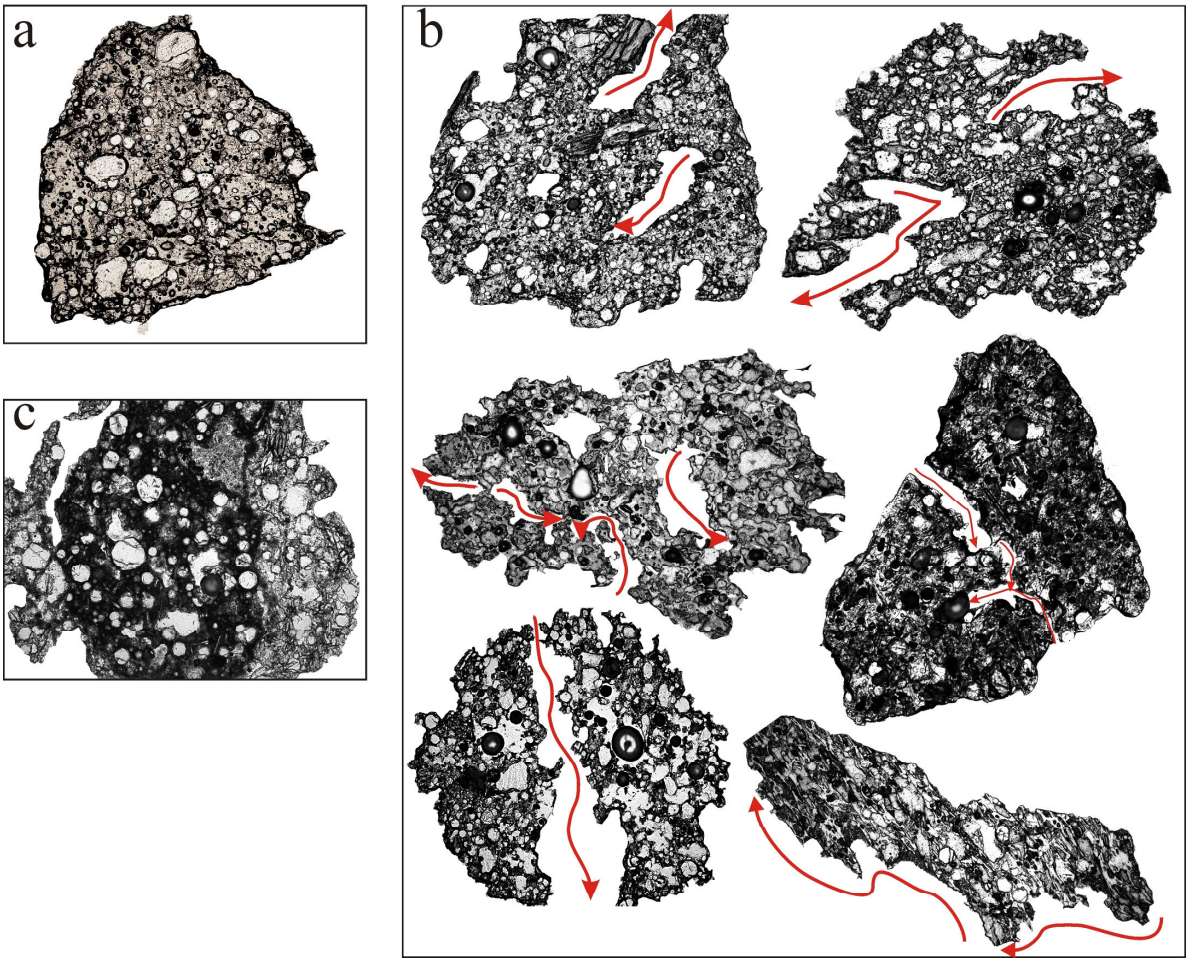

Fig.4.8 AP3 ash fragments selected in the size range of 1-0.5 mm a) glassy, poorly vesiculated; b) coalescent vesicles in a moderately vesicular crystal-rich fragments (red arrows follow the coalescence paths); c)pumice-like portion of magma including the denser part.

4.3.1 External morphology

Andronico and Cioni (2002) described secondary electron images of the ash fragments from this eruption in order to characterise their external morphology. They found that fragments from beds A and C have delicate, thin, protruding tips and sharpened rims, reinforcing the suggestion that these ash-bearing beds represent fallout rather than pyroclastic

density current deposits. Fragments from these two beds generally show a blocky shape (Fig. 4.9a), and have a glassy groundmass. Micron-sized ash clusters are also abundant. Vesicles are spherical to ovoid and commonly filled by ash aggregates. Septa separating vesicles are very thick and the external, curviplanar surfaces of the fragments are more similar to the conchoidal, contraction fractures that often penetrate the grains rather than to vesicle walls. They show a diffuse pitting (Fig. 4.9b), with rounded, sometimes coalescent micron-sized holes developed on an orange peel-like or scaly surface.

Scoria fragments from bed B are characterised by large, spherical to ovoid vesicles separated by thick septa. With respect to the fragments of beds A and C, this scoria shows a less developed glass pitting and ash infilling of vesicles.

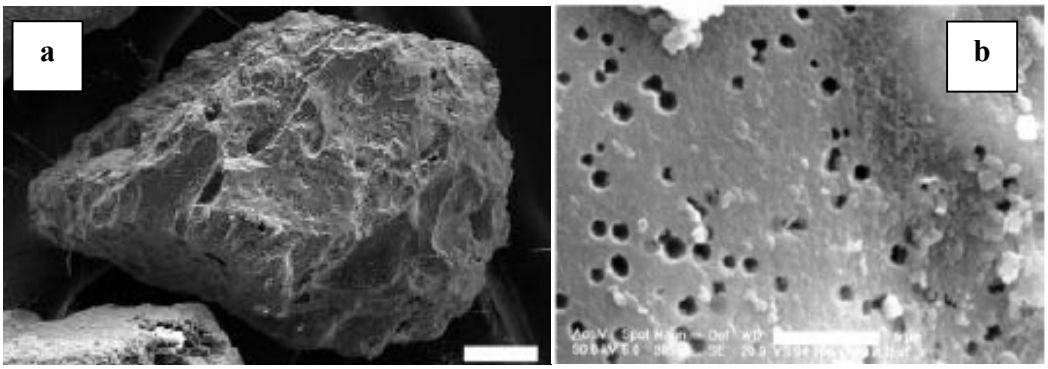

Fig.4.9 SEM images of the external morphology of AP3 fragments: a) blocky shape; b) pitting on the surface of the clast from beds A and C.

4.3.2 Particle outline

The quantitative morphologic study of the AP3 products was carried out on 30 fragments, randomly selected from each investigated sample, in the size range 1-0.5 mm. Starting from optical images of each single ash particle, four shape parameters were measured, specifically rectangularity, compactness, elongation and circularity (for detail see chapter 2).

Average values and standard deviation of the measured shape parameters are summarised in Table 4.2.

	Rectangularity	**Compactness**	**Elongation**	**Circularity**
proximal				
VSM48	0.915 (0.043)	0.697 (0.053)	1.999 (0.354)	1.252 (0.061)
VSM49	0.900 (0.036)	0.690 (0.051)	1.899 (0.202)	1.232 (0.054)
VSM50	0.936 (0.056)	0.682 (0.057)	2.057 (0.356)	1.295 (0.081)
VSM51	0.942 (0.064)	0.678 (0.044)	1.961 (0.342)	1.301 (0.107)
VSM53	0.928 (0.062)	0.692 (0.048)	1.887 (0.263)	1.267 (0.094)
VSM54	0.914 (0.047)	0.711 (0.042)	1.847 (0.248)	1.232 (0.067)
VSM55	1.037 (0.112)	0.686 (0.047)	1.932 (0.299)	1.423 (0.152)
VSM56	0.940 (0.041)	0.689 (0.052)	2.014 (0.302)	1.291 (0.058)
VSM57	0.967 (0.064)	0.677 (0.047)	1.975 (0.352)	1.337 (0.108)
distal				
VSM61	0.937 (0.0339)	0.697 (0.049)	1.939 (0.266)	1.278 (0.062)
VSM63	0.929 (0.048)	0.702 (0.042)	1.924 (0.278)	1.263 (0.068)

Tab.4.2 Mean values and standard deviation (in bracket.) of the measured shape parameters for each investigated layer.

Values of the rectangularity <1 are peculiar of an object with a smooth, corner-free, external surface, in accordance with the low values of the compactness, correlated with rounded shapes. Intermediate elongation values and high circularity, instead, are suggestive of flat objects (Büttner, 2002).

However, the frequency histograms of the shape parameters show bimodal and platikurtik distributions, indicating that different types of fragments coexist in the same stratigraphic layer (Fig. 4.10).

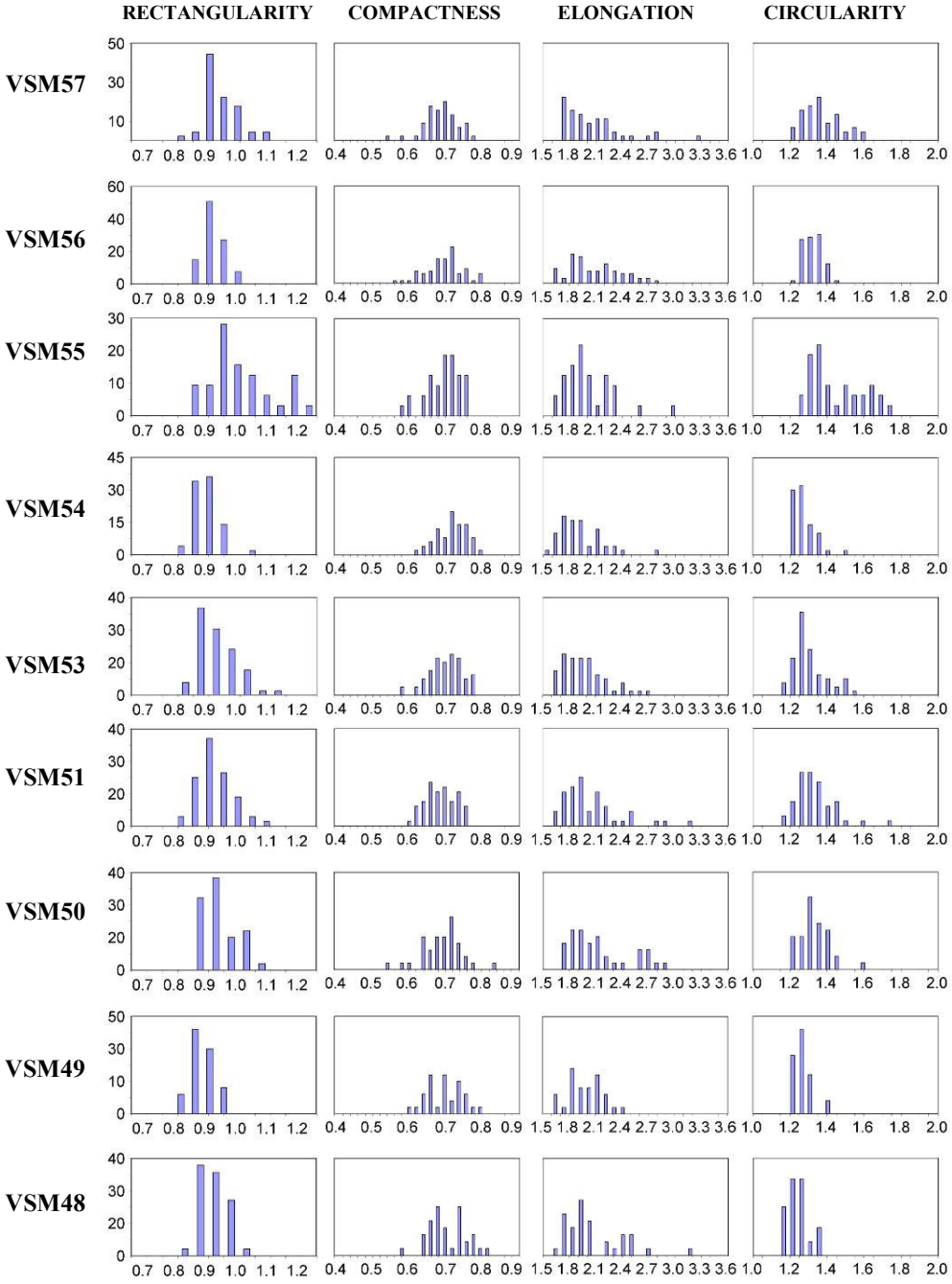

Fig.4.10 Histogram of frequency (%) for the measured shape parameters.

Therefore, we applied the multivariate statistical analyses (Principal Component Analyses) and cluster analyses to our samples for the individuation of the most representative external shapes of ash fragments ejected during the eruption.

Results of Principal Component Analyses show that the first two principal components, F1 and F2, account for the 87.5 % of the total variance (Tab. 4.3), with F1 that explains the 53% of the total variance and F2 the 35%. Because nearly all of the variance is accounted for by these two components, the ash particles can be represented by their factor scores, on a two-dimensional x–y plot, with very little loss of information. (Fig. 4.11).

Variables	Eigenvalue	F1	F2	F3	F4
1	2.0542	-0.4531	0.6313	-0.0660	0.6260
2	1.3770	0.3326	0.6599	0.5663	-0.3650
3	0.4697	-0.4972	-0.3676	0.7804	0.0932
4	0.0196	-0.6610	0.1759	-0.2568	-0.6828
tot. var%		**52.395**	**35.1231**	**11.981**	**0.5009**

Tab.4.3 Results of the Principal Component Analyses

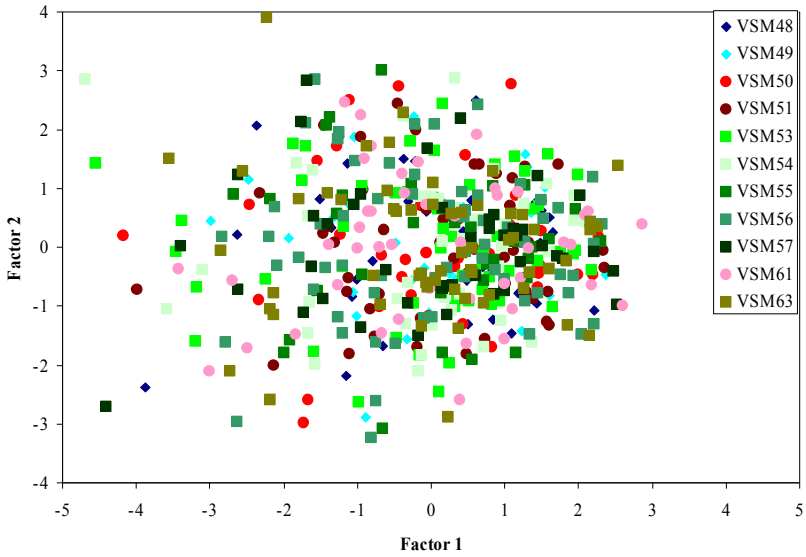

Fig.4.11 Binary plot of scores produced by principal components analysis

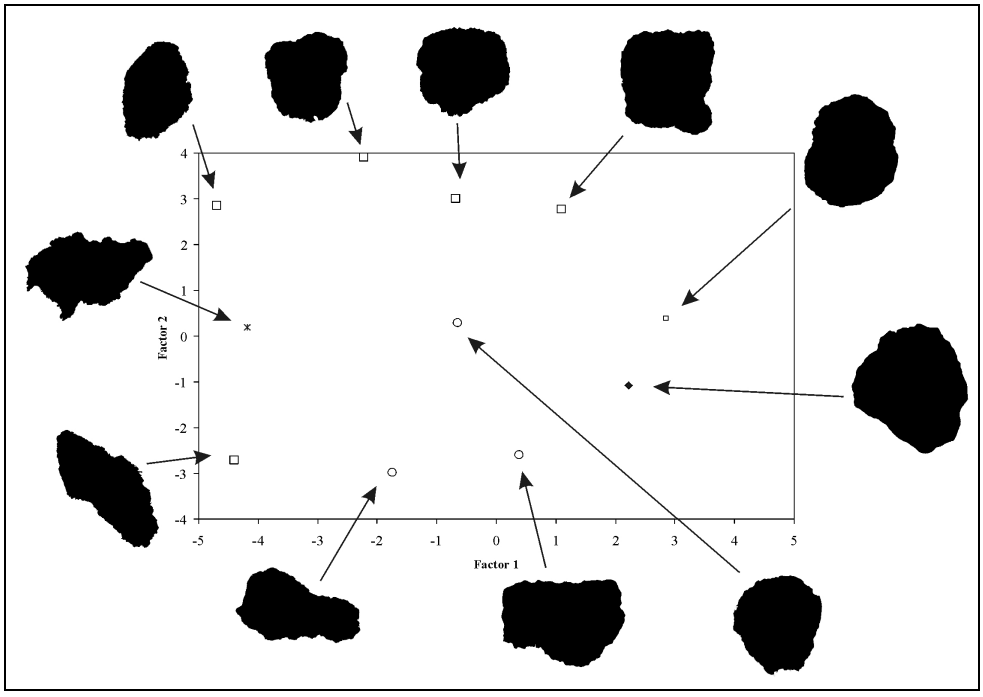

Fig. 4.12 Discriminating diagram obtained from PCA of particles outlines on selected particles. Miniature of particles contours are insert for visualization.

In the plot, the clasts are arranged according to the following scheme: 1) clasts plotting on the left side of the diagram are characterised by high elongation and low compactness; 2) clasts plotting on the upper part are characterised by rectangularity of about 1 and high compactness; 3) clasts plotting on the right side are characterised by circularity near 1 and by low value of the other shape parameters; 4) clasts plotting in the lowest part of the diagram are characterised by high elongation and by low value of the other shape parameters (Fig. 4.12).

Cluster analyses was performed on the principal components F1 and F2 and was used for grouping ash fragments with similar external morphology with respect to the measured shape parameters. At least three groups were created, indicated in Fig. 4.13: high spherical-sub rounded (HR-SR), low sphericity (LS) and very angular fragments (VA).

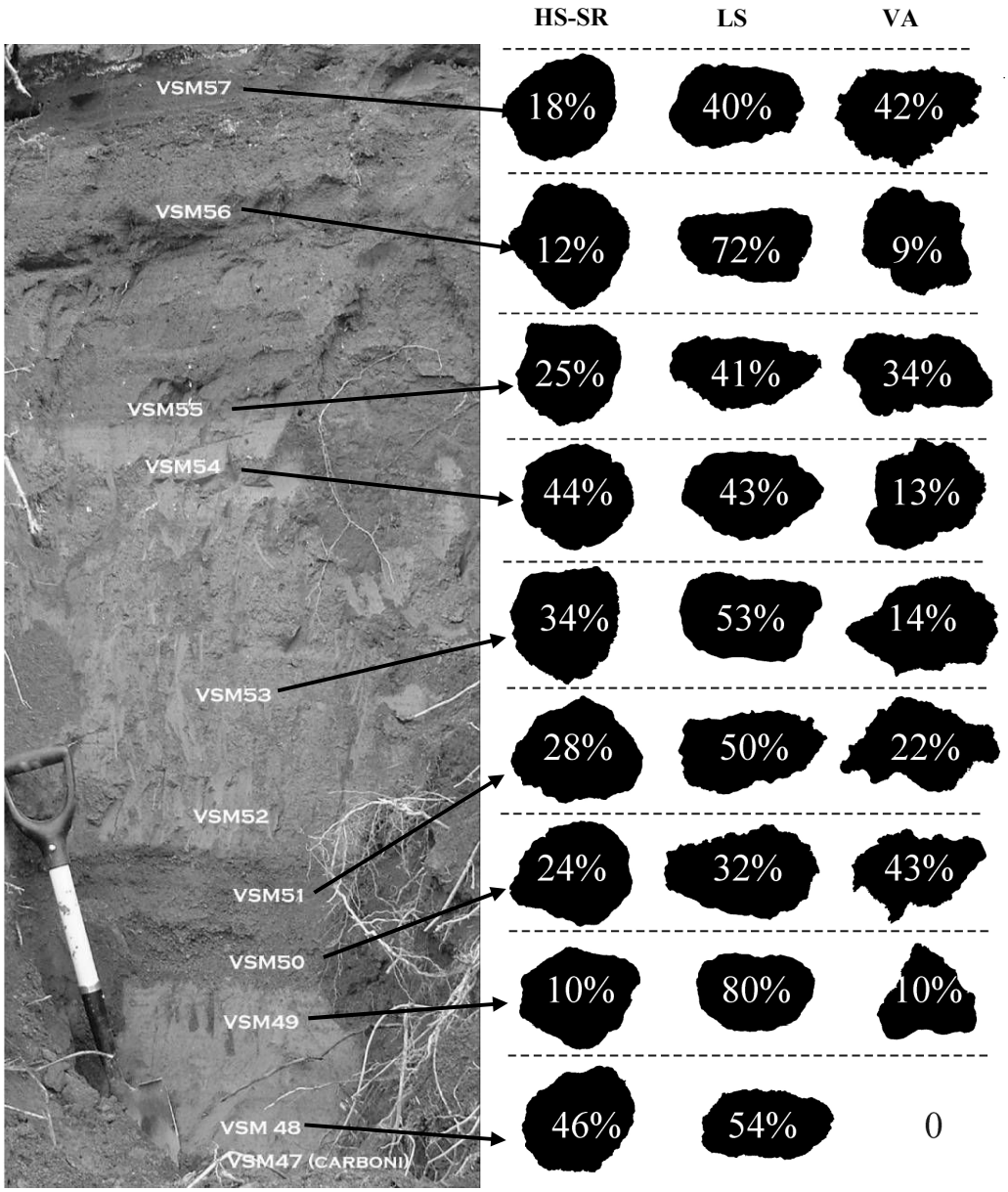

Fig.4.13 Types of outlines discriminated on the base of the cluster tree analyses.; HS = high spherical; SR = sub rounded; LS = low spherical; VA= very angular. Number indicate the % occurrence of each type in the investigated samples.

The 52% of the total analysed fragments shows a low spherical (LS) external shape, with an overall corner-free morphology, but in some cases showing protruding tip, that ranges, from sample to sample, from 32% to 80 %. This shape possibly reflects the presence of the elongated structures related to the coalesce of the bubbles, described above (see Fig. 4.8b).

Very angular (VA) fragments are characterised by uneven outline and represent the 21 % of the whole set of analysed fragments. With the exception of samples VSM50 and VSM57, in which VA fragments are largely represented (respectively 43 % and 42 %), and of sample VSM48, in which they totally lack, VA fragments occur with an abundance of 10-34 % in the other layers.

HS-SR fragments include the 27 % of the total fragments. They are characterised by an almost spherical external shape and smooth surface, maybe due to recycling inside the crater.

Distal samples were also investigated, in order to verify if the relationships between the different type of fragments are preserved in distal outcrops. Samples VSM61 and VSM63 are once again characterised by the occurrence of three type of fragments, indicated as HS-SR, LS and VA (Fig. 4.14). Moreover, looking at the percentage of occurrence of the three types, it is possible to correlate, with only small variations, VSM61 with the bed B, in particular with the sample VSM51, and VSM63 with the top of C, in particular with sample VSM55.

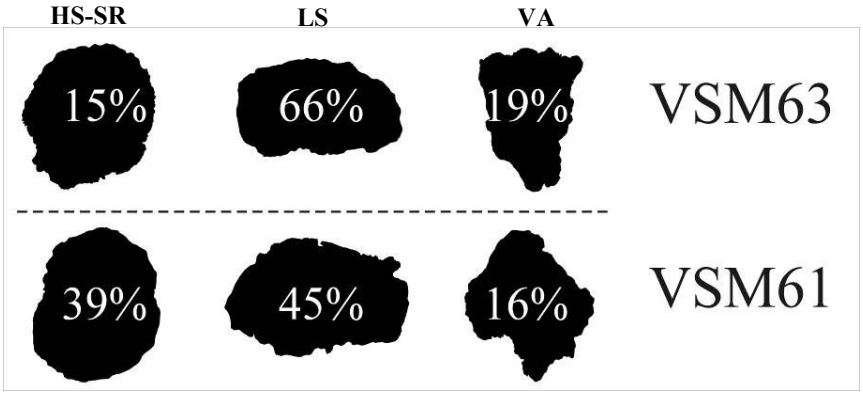

Fig. 4.14 Types of outlines discriminated on the base of the cluster tree analyses for the samples collected in distal outcrops.

4.3.3 Groundmass texture

Analyses of groundmass texture, major and trace elements composition of the matrix glass, and crystal size distributions, were performed on four samples, selected from the base, the middle part, and the top of the stratigraphic succession S1 (respectively VSM48, VSM51, VSM54, VSM56).

The groundmass of the ash fragments is characterized by a general isotropic texture, with crystals set in a light-coloured matrix with variable glass content. The dominant minerals are leucite, pyroxene and plagioclase. Leucite forms euhedral, hexagonal to rounded shaped crystals, occasionally containing laths of pyroxene as inclusions. Generally the glass around the crystals is interested by radial fractures, related to the transformation from a cubic to a pseudo-cubic structure, associated with the decrease of temperature (Deer et al., 1993). Pyroxene are euhedral, lozenge-shaped crystals, with occasionally swallowtail morphology, and are compositionally zoned. Plagioclase are euhedral, tablets-shaped crystals.

Groundmass texture was characterised describing the relationships between crystal content, (i.e. glass content) and vesicularity of ash fragments. Four groups of fragments were defined: 1) Moderately Vesicular, Glassy (MVG); 2) Dense, Crystal-Rich (DCRC); 3) Moderately Vesicular, Crystal-rich (MVC); 4) Poorly Vesicular, Glassy (PVG). Their occurrence along the stratigraphic succession was then quantified.

- Moderately Vesicular, Glassy (MVG) clasts are characterised by a vesicularity index ranging between 40-64 vol %, with an incipient bubble coalescence. Septa separating vesicles are very thick. In some cases vesicles are stretched (tube pumices) in a preferential direction (Fig. 4.15). The groundmass is glassy, with low crystal content (Fig. 4.16).

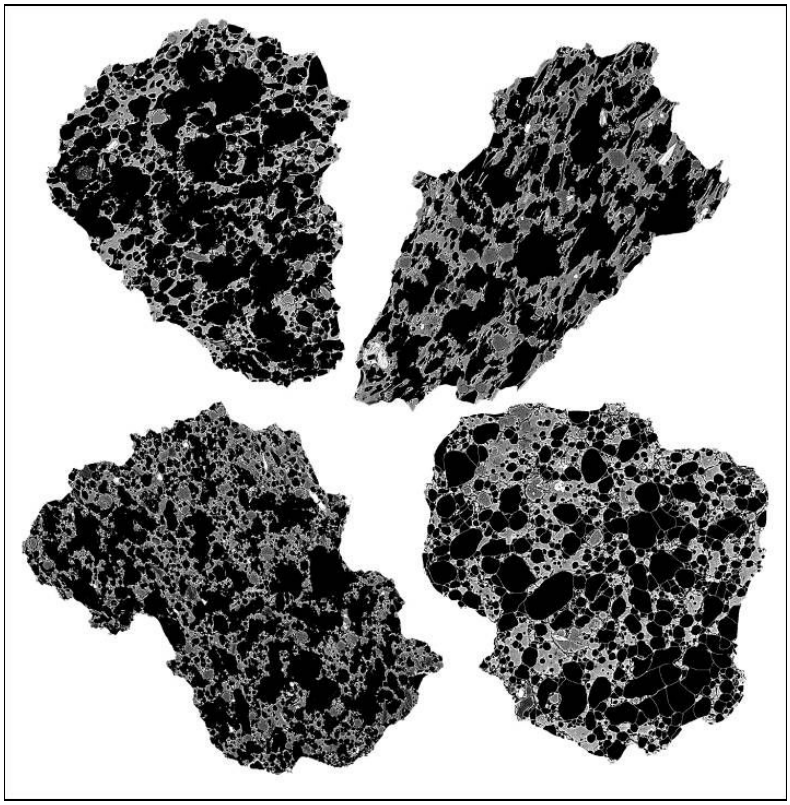

Fig.4.15 Selected MVG fragments in the size range of 1-0.5 mm.

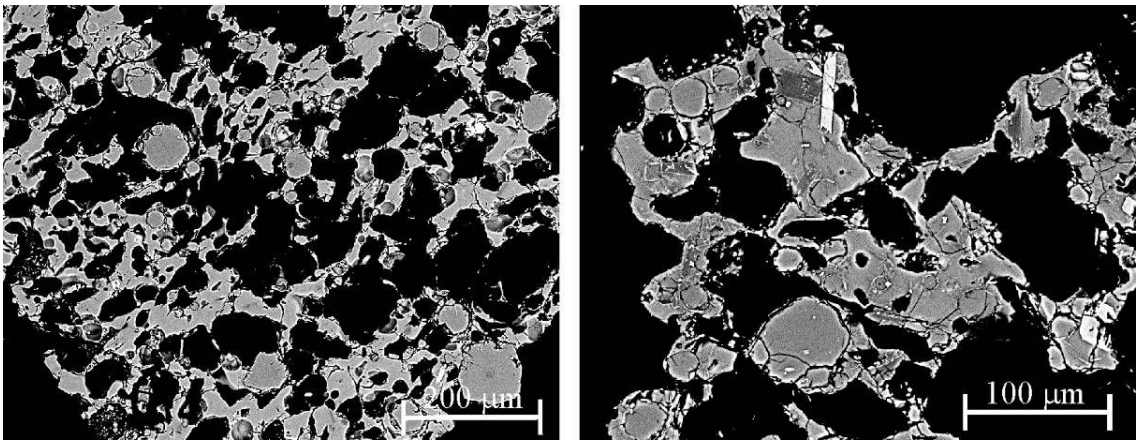

Fig.4.16 Groundmass textures of selected MVG clasts

- Dense, Crystal-Rich (DCR) fragments are poorly vesicular (bubbles in the range range 27-38 vol %) clasts, characterized by irregularly shaped bubbles, showing complex coalescence (Fig. 4.17). Groundmass is holocrystalline (Fig. 4.18).

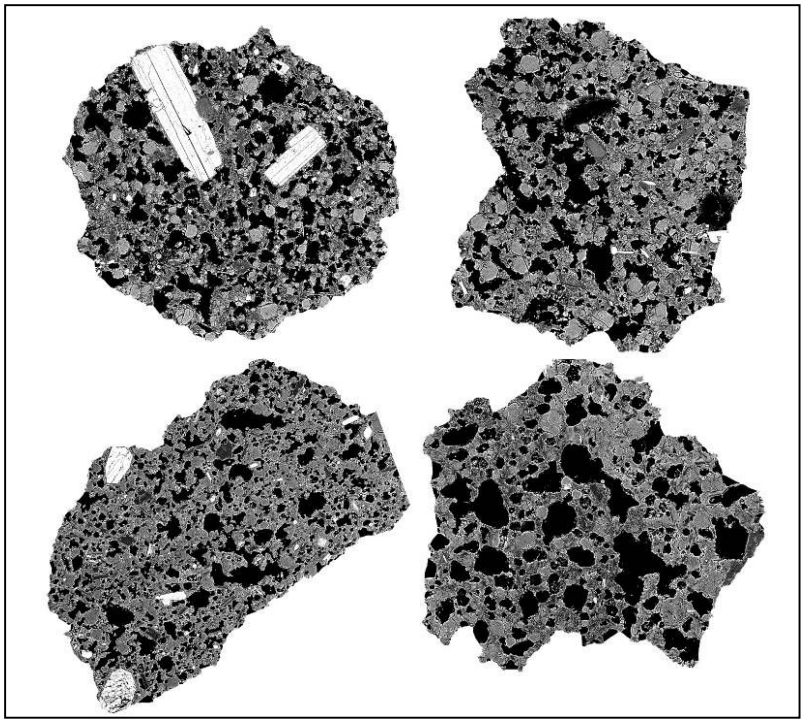

Fig.4.17 Selected DCR fragments in the size range of 1-0.5 mm.

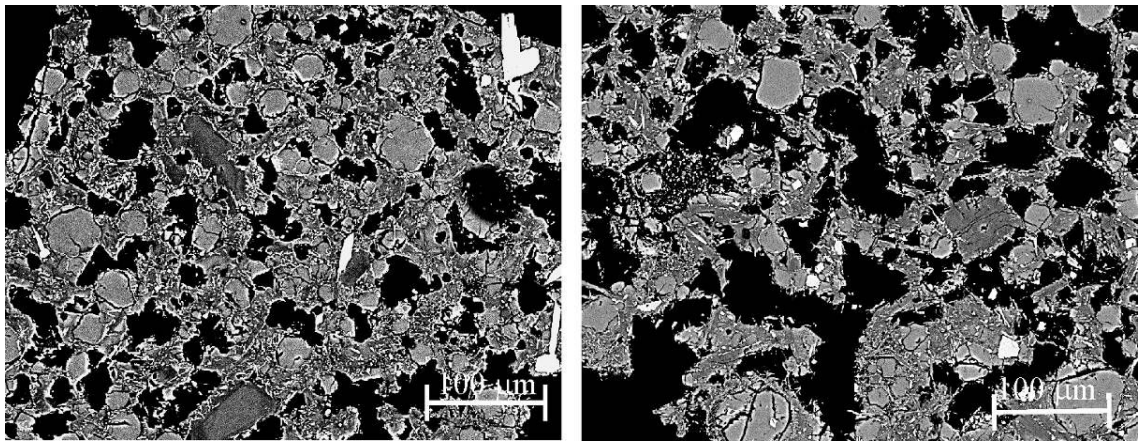

Fig.4.18 Groundmass textures of DCR fragments.

- Moderately Vesicular, Crystal-rich (MVC) fragments are characterised by moderate vesicularity (50-55 vol%), with irregularly shaped, sometimes coalescent bubbles. Vesicles are inhomegeneously distributed within the clast (Fig. 4.19), and sometimes coalescing along a preferential direction. The groundmass is almost holocrystalline (Fig. 4.20).

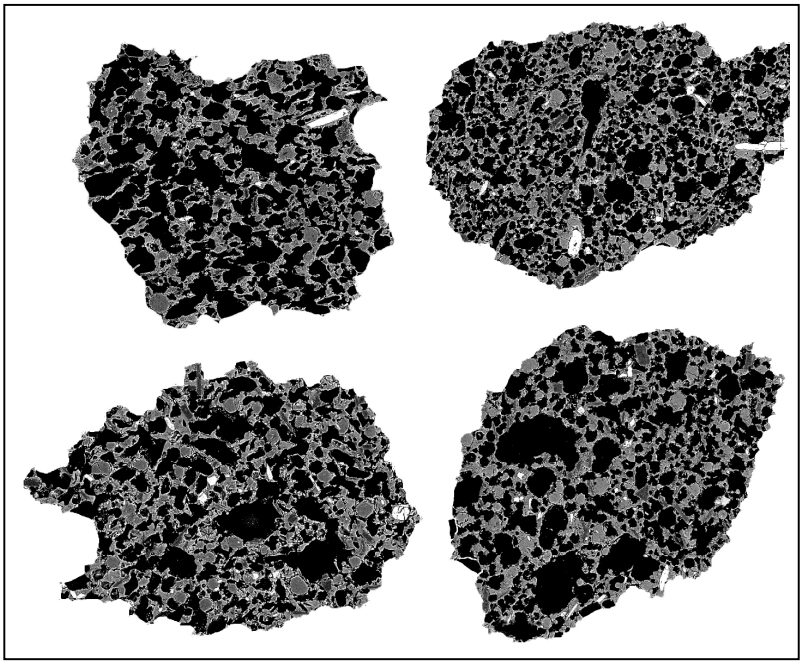

Fig.4.19 Selected MVC fragments in the size range of 1-0.5 mm.

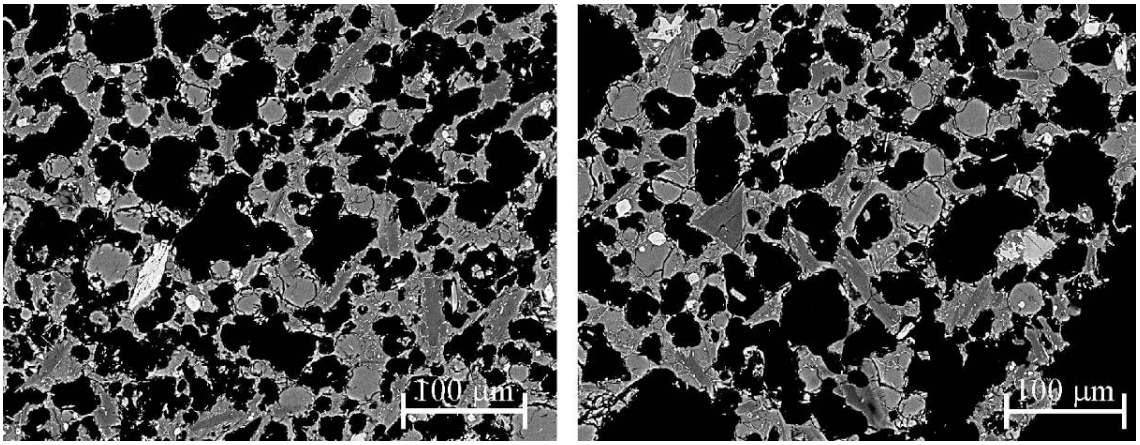

Fig.4.20 Selected groundmass textures form MVC clasts.

- Poorly Vesicular, Glassy (PVG) fragments are characterized by a vesicularity index ranging between 15-25 vol % (from incipiently to poorly vesicular), with rounded and rarely coalescent bubbles (Fig. 4.21). Groundmass is glassy, with a low crystal content (Fig. 4.22).

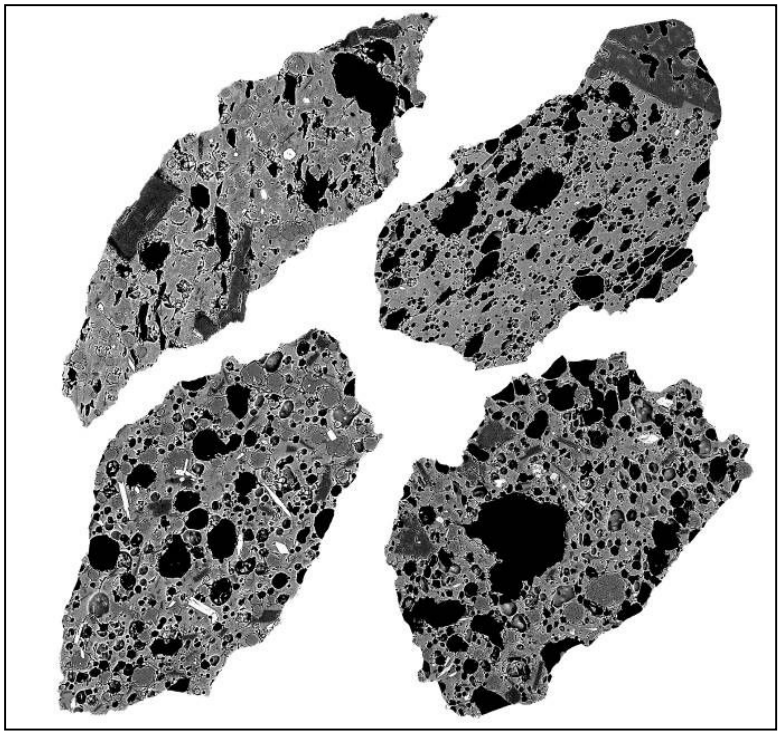

Fig.4.21 Selected PVG fragments in the size range of 1-0.5 mm..

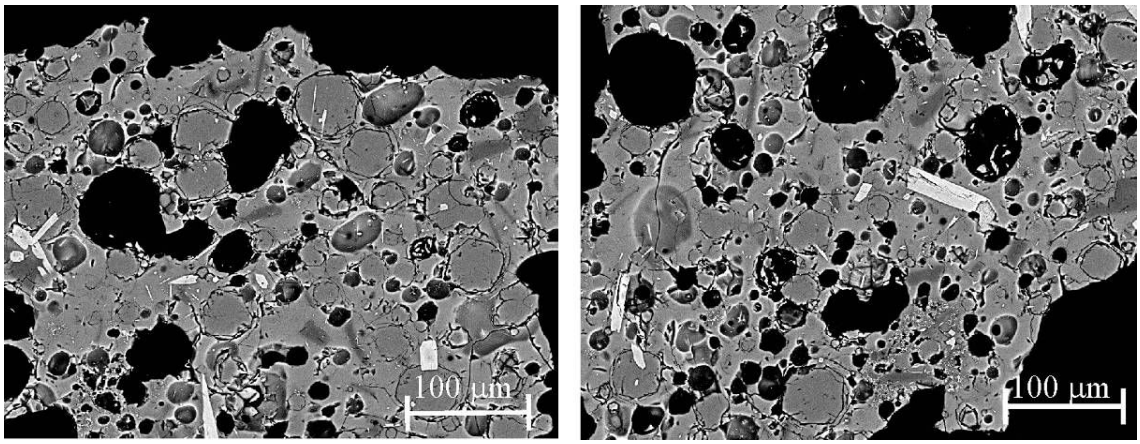

Fig.4.22 Selected groundmass textures from PVG fragments.

Along the sequence the different groups of fragments change in abundance (Fig. 4.23). MVG clasts are the most abundant types (48-55%) in all the samples but for the accretionary lapilli layer VSM54, where they are the only 10% of the total. DCR fragments have the same abundance nearly in all the samples (27-28%), while they represent the 47% of the total in VSM54. MVC fragments totally lack at the base of the eruption, while they vary from 18% in VSM51, to 6% in VSM54, to 23% at the top of the succession (VSM56). PVG fragments are present only at the base of the succession (18%) and in the accretionary lapilli layer (38%).

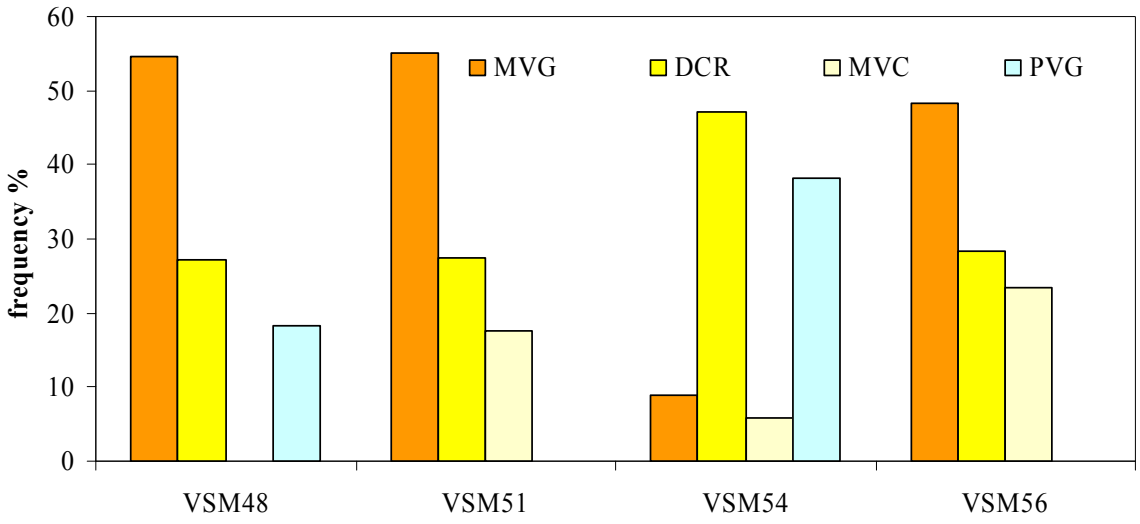

Fig.4.23 Occurrence (%) of the four detected groups of fragments in the different analysed samples.

4.4 Compositional features

Glass composition

Analysis of the glass composition was performed on five ash fragments selected from the MVG, MVC and PVG fragments, as they are representative of the different erupted products. DCR fragments were difficult to analyse for the low quantity of glass between crystals.

Clast-averaged analyses of glasses with related range of variation (1 sigma) are reported in Tab. 4.4.

	VSM48		VSM51		VSM54		VSM56	
	media(n=21)	σ	media(n=14)	σ	media(n=14)	σ	media(n=12)	σ
Na_2O	5.4	0.3	5.9	0.4	5.5	0.5	5.6	0.5
MgO	0.7	0.1	0.8	0.1	0.8	0.1	0.9	0.1
Al_2O_3	20.6	0.2	20.3	0.2	20.1	0.1	20.1	0.3
SiO_2	55.1	0.2	54.6	0.2	54.5	0.1	54.6	0.3
Cl	0.7	0.0	0.7	0.1	0.8	0.1	0.8	0.0
K_2O	7.5	0.5	6.7	0.4	6.9	0.3	6.8	0.5
CaO	4.7	0.2	5.0	0.1	4.9	0.5	4.9	0.2
TiO2	0.6	0.0	0.6	0.0	0.7	0.0	0.7	0.0
MnO	0.1	0.1	0.2	0.1	0.2	0.0	0.2	0.0
FeO	4.6	0.2	5.0	0.3	5.7	0.2	5.4	0.4
ALK	12.8	0.3	12.6	0.4	12.3	0.3	12.6	0.4

Tab.4.4 Averaged glass composition. n= number of analysis; σ = standard deviation.

Samples have a tephritic phonolite composition, with 54.5-55.5 wt % of SiO_2 and 12-13.5 wt % of alkali. Spider diagrams of the major elements versus CaO wt% show that, from the base (VSM48) to the top (VSM56) of the succession, the erupted magma was characterized by a linear trend from more evolved to less evolved terms (Fig. 4.24). Although each sample occupies a peculiar field in the diagrams, the single analyses are widely scattered, indicating inhomogeneities at the millimetric scale, possibly related to different local amount of crystallization of the analysed fragments. Only the sample VSM54 shows a small range of variation, possibly as a consequence of low crystal content of the analyzed (PVG) clasts.

Compositions of minerals were analyzed on the same fragments. Leucite results quasi-stechiometric: SiO_2 range between 56.87 wt% and 56.98 wt%; Al_2O_3 content ranges between 23.12-23.80 wt%, and K_2O content range between 18.49-19.22 wt% (Appendix 2, Tab. 1A). Plagioclase is strongly zoned, and its composition records little variations during the different phases of the eruption. From the base to the top of the succession an increase in Ca content occurs, passing from terms with An_{40-87}-Ab_{10-45}-Or_{1-15} in VSM48, to An_{37-65}-Ab_{30-44}-Or_{5-18} in VSM51 (Appendix 2, Tab. 2A). Clinopyroxene are Ca-Diopside in composition, with $En_{25-38}Wo_{48-51}Fe_{13-22}$, with less Fe content and more Mg content moving toward the top of the succession. Crystals are zoned, and the different zones of growth correspond to variation of

TiO_2, Al_2O_3, FeO and CaO content; in particular, microlites < 20 μm are also zoned with more Fe-rich rims (Appendix 2, Tab. 3A).

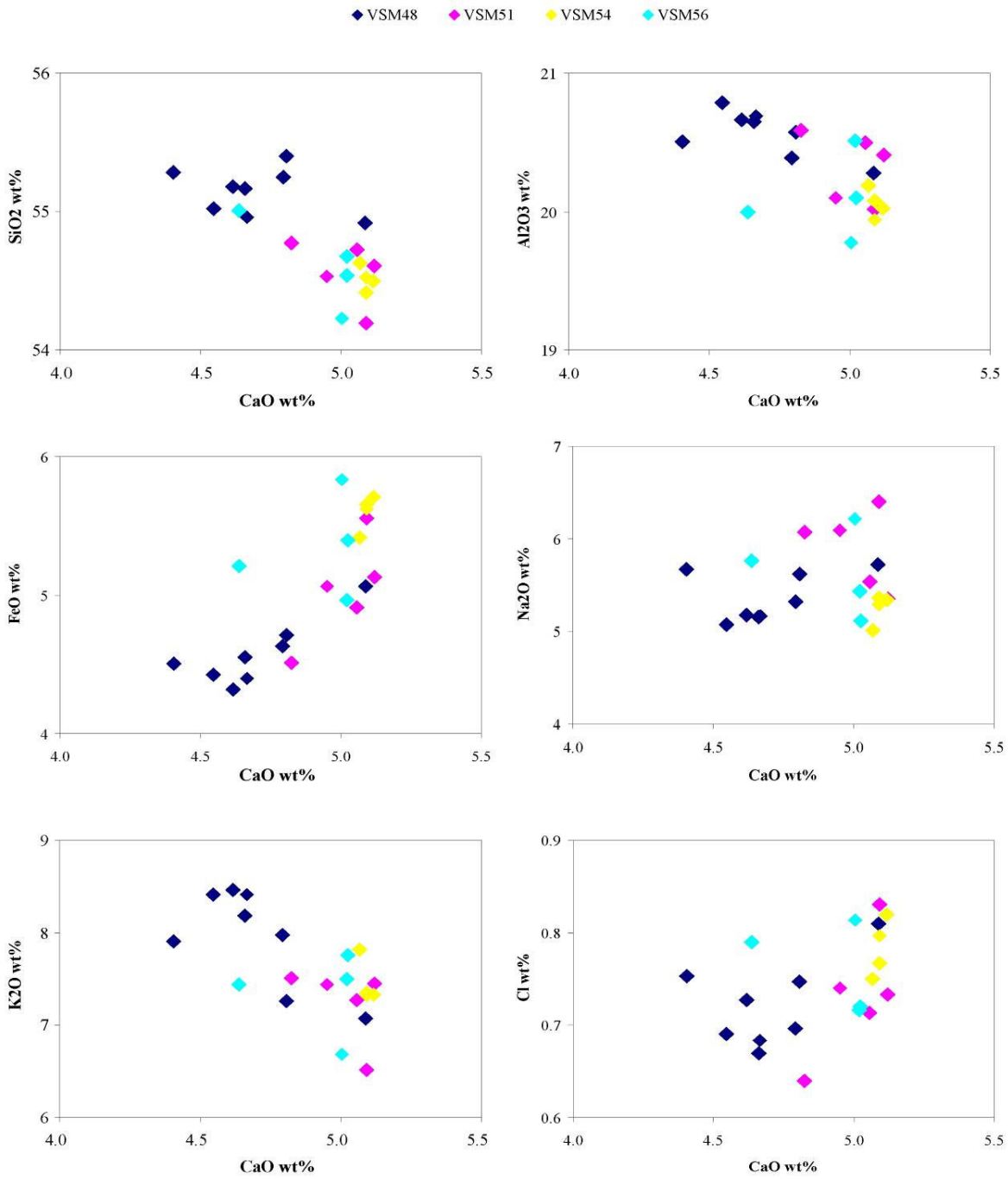

Fig.4.24 Variation diagrams of the principal major elements (oxides wt %) vs CaO wt%.

Trace elements

Trace elements analyses were performed using the LA-ICP-MS facilities at P. Zuddas lab., Earth Science Dept., Univ. of Cagliari. Trace elements concentrations were determined on about 6 ash fragments selected from each sample (Appendix 3, Tab.3.1A, 3.2A, 3.3A, 3.4A). On each fragment a number of 2-3 analyses were performed and the average values were used, although in some cases analyses in two different point of the same fragments resulted very different for the presence of crystals. In that case we consider only those analyses not contaminated (see chapter 2, for details) by partial crystal ablation.

Rare Earth Elements concentrations show similar pattern between the clasts, being the observed variations comparable with the standard deviation bar (Fig. 4.25). The general trend shows a preferential depletion of HREE with respect to LREE, possibly related to clinopyroxene crystallization (Hanson, 1980).

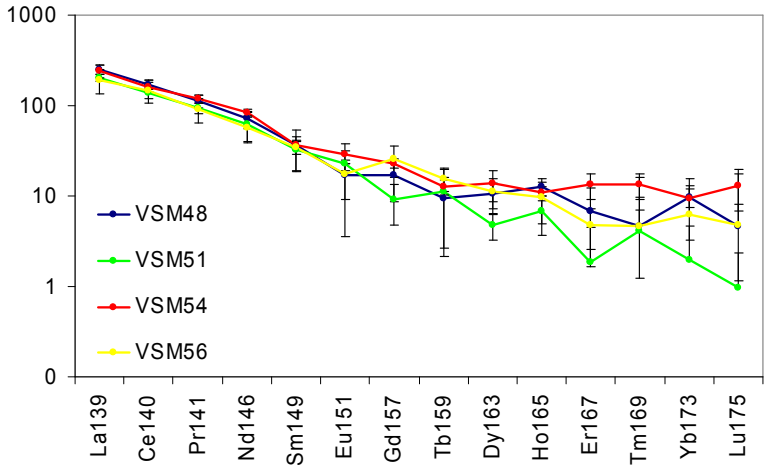

Fig. 4.25 REE pattern of the selected samples.

Trace elements concentration in the residual glass is influenced by the mineralogical phases that occur during melt or fractional crystallization (Hanson, 1980). Indeed, each element is characterized by a partitioning coefficient (D) between two different phases (i.e. phenocryst/melt or phenocryst/glass), on the base of which, it is possible to quantitatively define as incompatible those elements characterized by $D << 1$, and compatible elements those

with D ≥ 1. The magnitude of the effect of a mineral is directly related to both the relative abundance of the mineral and the magnitude of D. D are available for many trace elements in minerals from numerous phenocrysts/melt natural systems (see forex GERM site, http://earthref.org/).

Studies carried out on trachytic and trachyphonolitic obsidians from Campi Flegrei allowed to calculate the partitioning coefficient of trace elements between minerals in natural system similar in composition with the Vesuvian products (Morra et al., 2003) (Tab. 4.6)

elements	plagioclase	pyroxene	leucite	apatite	Ti-magnetite
Sr	5-10.4		0.07-0.0005		
Ba	0.3-2.0		0.07-0.0005		
Rb	0.02		>1		
Pb	0.15-0.22		0.07-0.0005		
Eu	1.37-0.58		0.07-0.0005		
Sc		20	0.07-0.0005		>1
V		3.5	0.07-0.0005		48-52
U			0.07-0.0005		
Th			0.07-0.0005		
Nb			0.07-0.0005		0.24-0.35
Ta			0.07-0.0005		0.25-0.36
Zr			0.07-0.0005		0.08
Y		0.5-4.0	0.07-0.0005	22	
Hf			0.07-0.0005		0.11
La			0.07-0.0005	24	
Lu			0.07-0.0005	7	
Cs			>1		
Ni			0.4-0.1		
Ga			0.4-0.1		
Co			0.4-0.1		

Tab.4.6 Partition coefficients for some trace elements obtained for natural trachitic and trachiphonolitic obsidians of Campi Flegrei (South Italy) (Morra et al, 2003). DCs and DRb of leucite are from Foley and Jenner, (2004).

Results show that DSr and DBa in plagioclase are strongly composition dependent, ranging respectively from 5 to 10.4 and from 0.3 to 2.0. DRb is low (0.02), whereas DPb ranges from 0.15 to 0.22. DREE are < 1, with DEu higher in Na-rich (1.37) than in Ca-rich plagioclase (0.58). For clinopyroxene, Sc and V are the most compatible elements, with D values between about 20 and 3.5, respectively. LILEs are incompatible to strongly incompatible (e.g., U, Th,

Pb). DSr is relatively low and shows a slight increase in Fe-richer crystals. DNb, DTa and DZr are very low; their values tend to increase in Fe-richer crystals. DY is between 0.5 and 4.0. For Ti-magnetite minerals, results indicate that V is strongly partitioned in this phase (DV=48-52), whereas DSc is > 1 only in trachytic melts. DHf and DZr are relatively constant (0.11-0.08) and lower than DNb and DTa (0.24-0.25); these two last elements increase their compatibility in trachyphonolitic melts (0.35-0.36). Finally, DREE and DY for apatite are very high (DLa=24; DLu=7; DY=22). The patterns of DREE is almost flat in the LREE region (DREE between 24 and 30), whereas a strong negative fractionation is observed in the HREE region (DHREE from 35 to 7).

Leucite/melt partition coefficients show values above 1 only for Cs and Rb, whereas values for Ni, Ga and Co are 0.4–0.1. D for most other elements are in the range 0.07–0.0005 (Foley and Jenner, 2004)

Figure 4.26 shows diagrams of variations of single shard LA-ICP-MS analyses for some incompatible (Zr, U, Th) and compatible (Sr, Ba, Rb, Cs, V, Nb) elements. The observed range in compositions from many elements is far larger than any possible analytical errors (see chapter 2, pp.17), and must reflect variation on a small scale within the magma, resulting from a combination of fractional crystallization of mineral phases, causing local compositional variation which persists as a result of low diffusion rates in these viscous magmas (Pearce at al., 2004a).

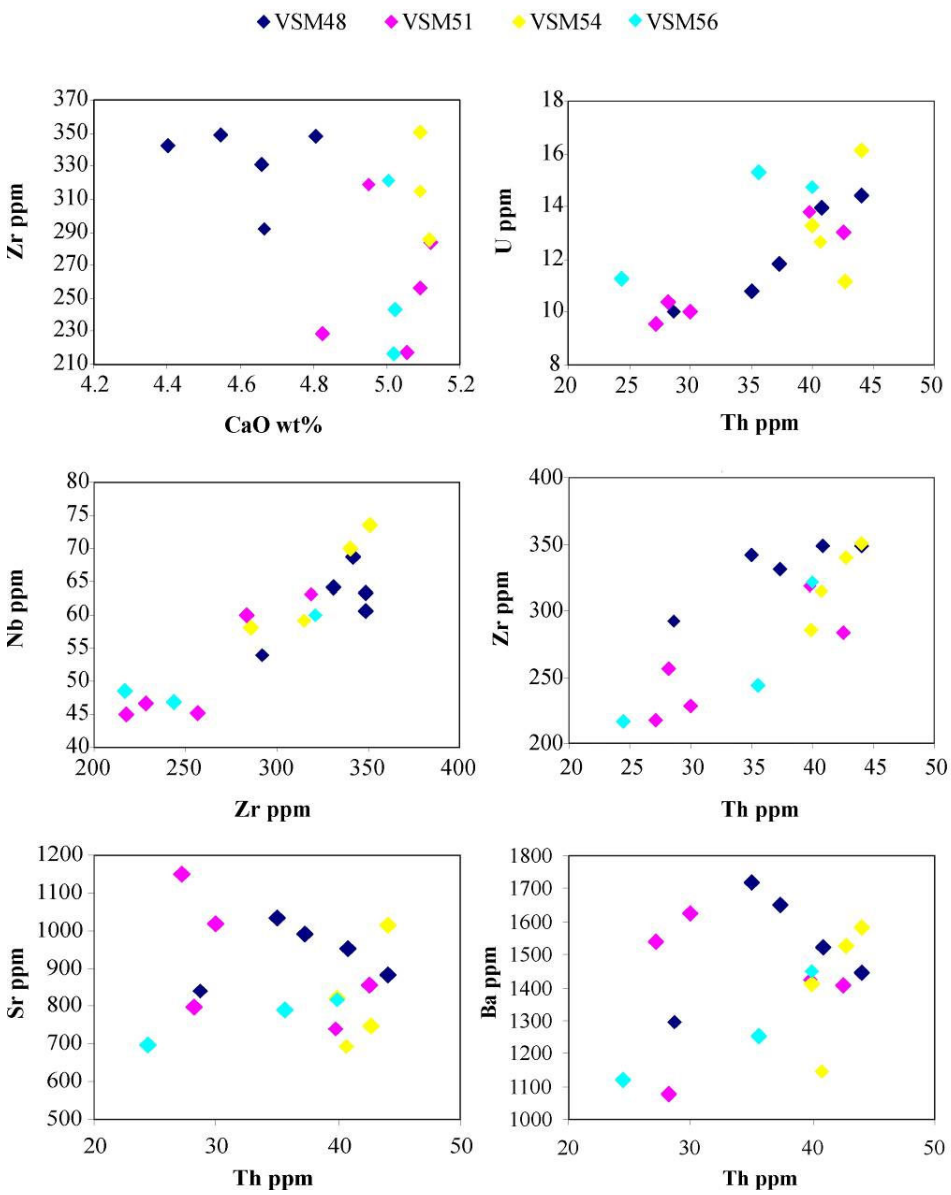
VSM48
VSM51
VSM54
VSM56
Zr ppm
CaO wt%
U ppm
Th ppm
Nb ppm
Zr ppm
Zr ppm
Th ppm
Sr ppm
Th ppm
Ba ppm
Th ppm

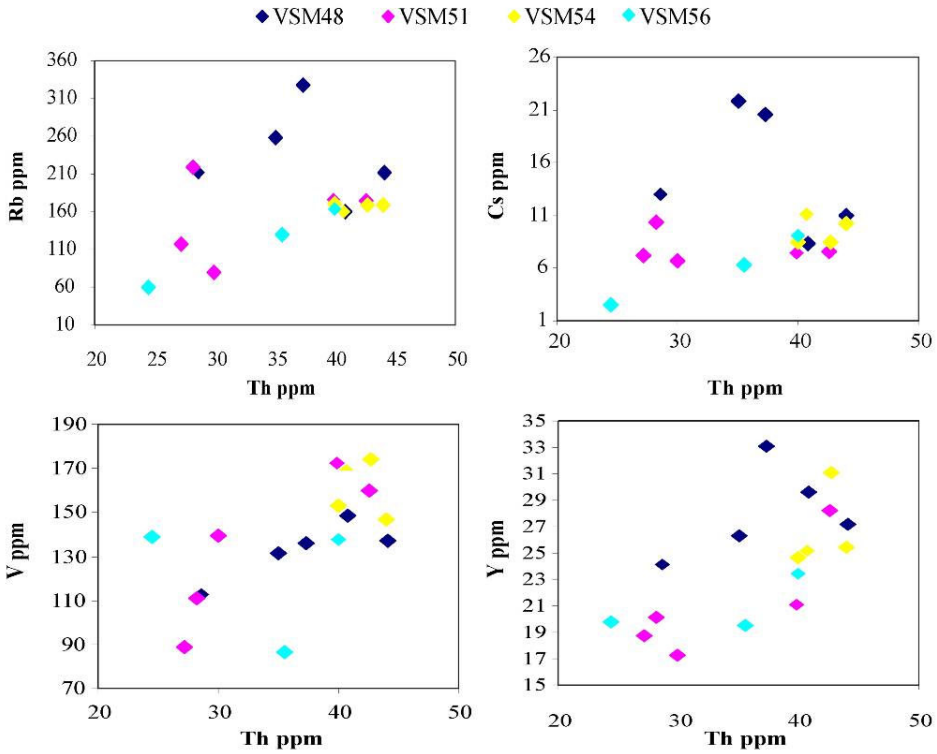

Fig. 4.26 Trace elements variations in AP3 products

The U-Th, Zr-Nb and Zr-Th linear correlation suggest that these elements are incompatible with the mineralogical assemblage of the AP3 products, enriching in the residual melt during the fractional crystallization. For this reason, we choose to plot the compatible elements against Th. As a general rule, the base of the eruption shows the highest concentration with respect to Ba, Rb, Cs and Y, suggesting that a lower degree of crystallization of the minerals that concentrate them. The lapilli rich-layer (VSM51) shows the highest variability for all the selected trace elements, indicating that the products emitted during the strombolian phase of the eruption were highly heterogeneous with respect to the crystallinty. On the other hand, analyses of sample VSM54 result poorly scattered, with high V and Y content (low pyroxene crystallization), and low Rb and Cs (crystallization of leucite). This fact is one again correlated with the relative abundance of PVG fragments in this layer. The top of the eruption is the most

depleted with respect all the trace elements considered, indicating that this phase of the eruption was preceded by an important crystallization.

4.5 Crystal Size Distribution (CSD)

Five clasts were selected from each investigated sample, in order to obtain quantitative information on groundmass texture. We consider only the MVG fragments, which represent the most abundant type in all the investigated samples, except for the VSM54.

Plagioclase is the unique mineralogical phase considered for this textural study. Tab. 4.7 summarizes the main 2D and 3D textural data. Leucite was excluded for its hard identification, due to the similar grey tone with the matrix glass.

		VSM48	VSM51	VSM54	VSM56
	Total Area (mm^2)	2.5	1.3	1.7	3.3
	Bubbles vol%	49%	54%	40%	54%
Plagioclase	Φ vol%	1%	3%	6%	6%
	aspect ratio	1:4:4	1:5:5	1:5:5	1:6:8
	3Gt (1) micron	68	25.0	45.0	53.0
	N_A (mm^{-2})	7.2E+01	5.2E+02	3.9E+02	7.0E+02
	$n°_{(1)}$ mm^{-4}	1.2E+06	8.7E+06	3.3E+06	6.6E+06
	3Gt (2) micron	22.0	_	_	_
	$n°_{(2)}$ mm^{-4}	6.0E+04	_	_	_

Tab.4.7 Plagioclase parameters derived from the crystals size distributions analyses. Φ= fraction of microlites (vol%), G = Average growth rate (mm/sec); τ = time for crystals growth (sec); 3G τ = crystals average dominant size (Cashman, 1992); N_A= number of microlites per unit area (mm^{-2}); n°= nuclei number density (mm^{-4}).

In Fig. 4.27a-d are shown, for each sample, the sums of all microlites of plagioclase detected in the analysed images. For representation, microlites were randomly arranged in a fixed area, proportional to the total investigated area (vesicles-free), with the only scope of visualizing the dimensional relationships and the relative abundance of microlites in a sample with respect to the others, so that they have not significance of spatial distributions of the

crystals. The investigated areal of particles for each sample ranges from 1.3 mm^2 to 3.3 mm^2. We have considered fragments with vesicularity index ranging between 40 vol% and 54 vol% (Tab. 4.7).

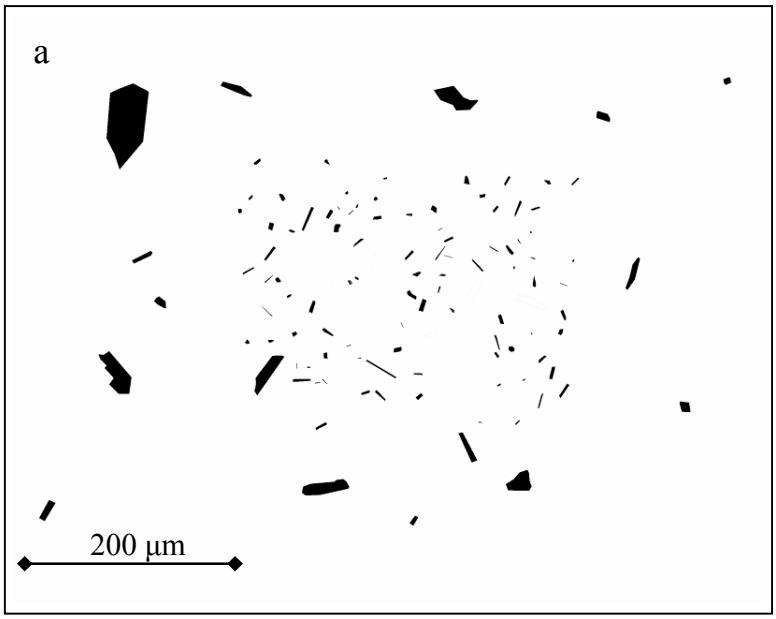

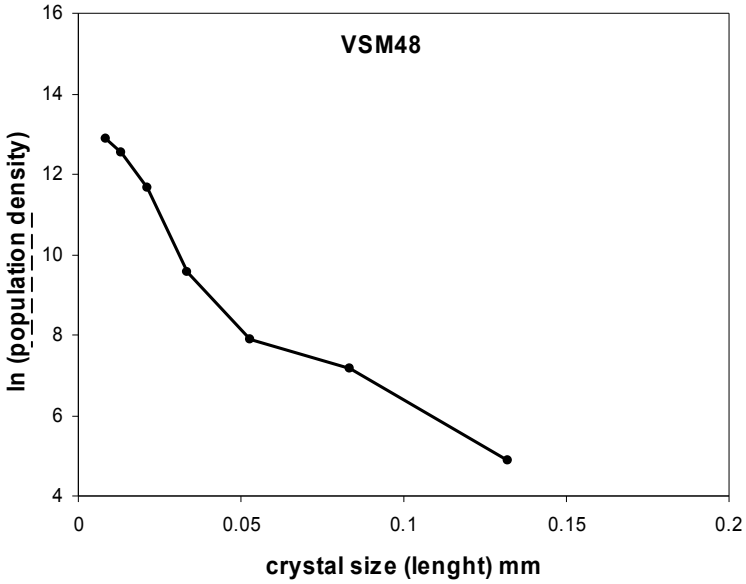

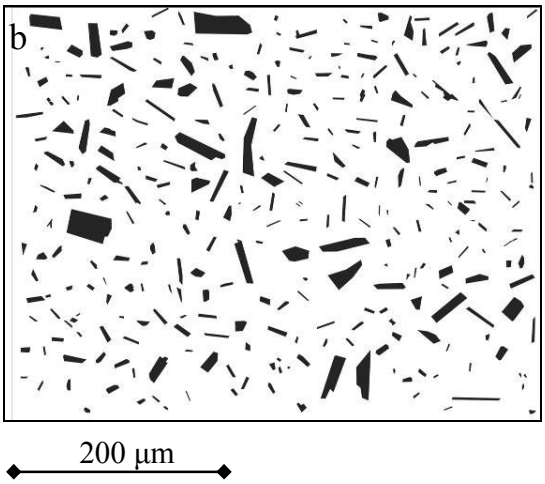
b
200 μm

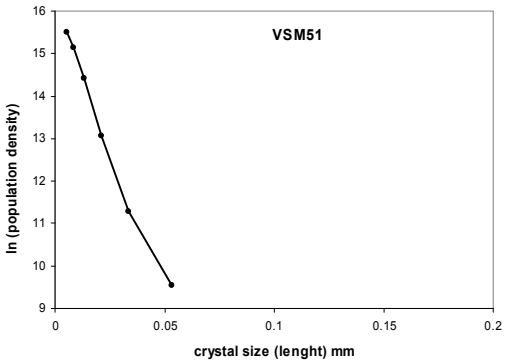
VSM51
ln (population density)
crystal size (lenght) mm
16
15
14
13
12
11
10
9
0
0.05
0.1
0.15
0.2

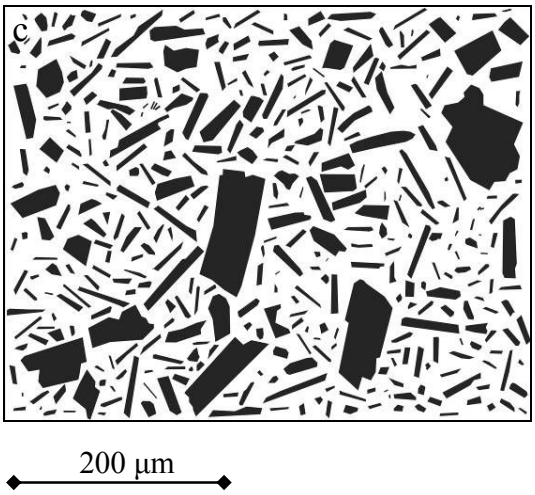
c
200 μm

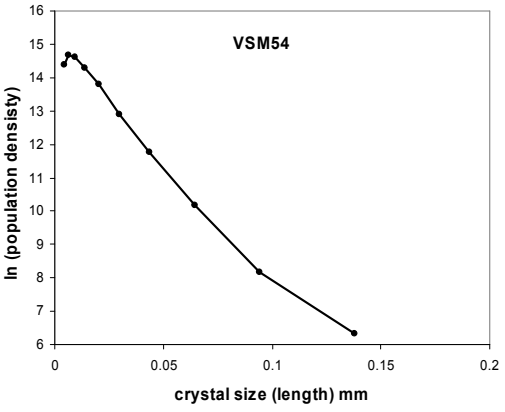
VSM54
ln (population densisty)
crystal size (length) mm
16
15
14
13
12
11
10
9
8
7
6
0
0.05
0.1
0.15
0.2

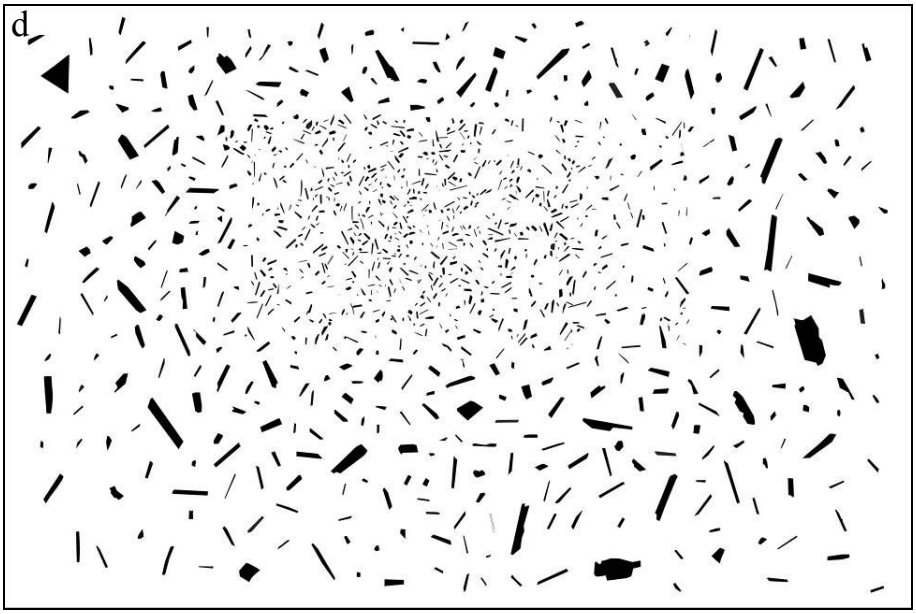

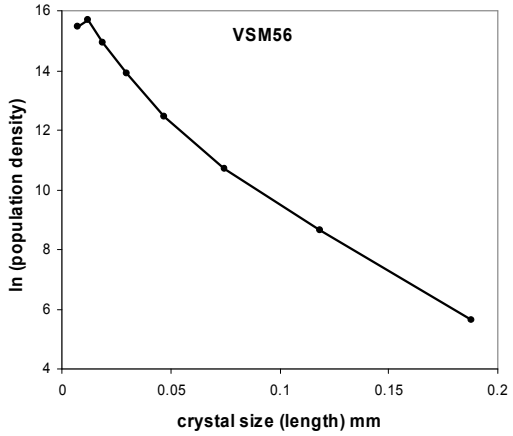

Fig.4.27 All crystals counted and relative CSD, for sample VSM48 (a); VSM51 (b); VSM54 (c); VSM56 (d).

From the base to the top of the succession it is evident that an order of magnitude increase of the abundance of crystals (N_A) occurs, from 7.2E+01 mm^{-2} to 7.0E+02 mm^{-2} (Tab. 4.6). Conversion from 2D to 3D data (Higgins, 1994) suggests a tablet shape for plagioclase

microlites, with aspect ratio ranging from 1:4:4 in VSM48 to 1:6:8 in VSM56. Plagioclase microlite morphology, aspect ratio, abundance and size reflect the degree and timing of imposed supersaturation and the duration of the crystallization interval. In particular, the tendency to form more elongated crystals increases with the increasing of the undercooling (Hammer, 2002), so suggesting an increasing undercooling toward the top of the sequence.

Crystal size distributions of samples in the lower part of the succession (Fig. 4.28 a) show a complex shape, characterised by at least two different segments, divided by the dashed line, with size (length) of 0.132-0.053 mm and 0.053-0.010 mm respectively. Each segment is characterized by its slope ($-1/G\tau$, where G is the crystal growth rate and τ a characteristic time) and by an intercept (n°, nuclei number density, Marsh (1988)). The first crystal size population to crystallize, the larger one, is characterised by $3G\tau = 68$ μm and $n° = 6x10^4$ mm^{-4}, together with a low N_A value (3 mm^{-2}). The smallest size population of this sample is characterised by $3G\tau = 22$ μm and $n° = 1.2x10^6$ mm^{-4}, together with a N_A value of 66 mm^{-2}.

Samples VSM51-54-56 are well described by a single linear segments.

In particular, the CSD plot of sample VSM51 shows a crystal population with $3G\tau = 25$ μm and $n° = 8.7x10^6$ mm^{-4}. As the eruption proceeds, an increase of the average crystal size is recorded by the CSD of the sample VSM54 ($3G\tau = 45$ μm), associated with a low number of nuclei of crystals ($n° = 3.3x10^6$ mm^{-4}), together with a slightly decrease of the N_A, from $5.2x10^2$ in VSM51 to $3.9x10^2$ in VSM54, indicating that the number of crystals on the reference area does not significantly vary. This change in CSD is associated with an increase of the crystal content (vol %) from 3% in VSM51 to 6% in VSM54, suggesting that the early single crystal size population continued to growth with time.

CSD plot of sample VSM56 records a shift toward greater crystals size ($3G\tau = 53$ μm) associated with an increase of the nuclei of crystals ($n° = 6.6x10^6$ mm^{-4}). Plagioclase crystal content remains constant at 6 vol %, while N_A sharply increases to $7x10^2$ mm^{-2}, suggesting a new event of nucleation together with the continuous growth of the pre-existing crystals.

5. DISCUSSION

AP3 eruption was characterized by two contrasting styles of activity, each repeated during the eruption at least two times: 1) emplacement of a fine grained, massive, accretionary lapilli-bearing ash. This activity dominated both the first phase of the eruption (Bed A) and the central part of the eruption (Bed C); and 2) deposition of well sorted lapilli-rich layer, present in the lower part (Bed B) and at the top of the sequence (Bed C_t, sample VSM56). The AP3 juvenile fraction shows largely heterogeneous morphological, textural and compositional features; we correlate and interprete these variations in terms of: 1) mechanism of magma fragmentation; 2) role of external water; 3) syn-eruptive magma crystallization.

Fragmentation processes

The study of external morphology, external outline and groundmass texture of ash fragments allowed to make hypotheses about the fragmentation processes responsible of the ash generation. For simplicity, the different ash layers and lapilli-rich layers are discussed separately, due to their intrinsic differences.

Ash-rich layers. Deposits of this phase of the eruption consist of massive, centimeter thick, fine ash-rich layers, and are characterized by features such as accretionary lapilli and vesiculated tuff, typical of deposition from a "wet" system. Results on external morphology of the juvenile clasts indicate that ash fragments have blocky and platy shapes, with diffuse superficial pitting and adhering of small particles, together with hydration and contraction cracks. Investigation of the particle outlines has evidenced the occurrence of different types of particles, coexisting within the same stratigraphic layer. Anyway, the majority of the fragments (67% of bed A, and 46% of bed C) show a low sphericity external shape, and smooth, not ragged external surface, while very angular fragments, with irregular outlines, are scarcely represented (5% in bed A, and 20 % in bed C). In addition, groundmass characterization of the ash evidenced the presence of poorly vesicular, poorly crystalline glassy fragments (PVG), together with dense, microlite-rich fragments in samples VSM48 (Bed A) and VSM54 (Bed C).

These features have been associated with phreatomagmatic explosions, in which the explosive vaporization of external water results in the fragmentation and quenching of the magma (Wholetz, 1986; Buttner et al., 1999). The curvilinear fractures that commonly bound the Leucite phenocrysts, probably reflect a differential contraction of the glass with respect to the mineral, which undergoes a second order phase transition (from cubic to tetragonal) during cooling, associated with a marked volume decrease (about 6%; Henderson 1984). This process, possibly emphasized by the rapid quenching following magma–water interaction, is the main cause of the very high quantity of loose, glass-free Leucite crystals that commonly characterize Leucite-bearing pyroclastic deposits. All these features are suggestive of a fragmentation involving the physical interaction of magma an external water (Buttner et al., 1999; Morrissey et al., 2000; Andronico and Cioni, 2002; Taddeucci et al., 2002).

The ubiquitous and large occurrence of moderately vesicular, glassy fragments, on the other hand, suggests that external water only acted to increase the intensity of a fragmentation process, which was primarily driven by the gas bubbles explosions. According to this hypothesis, interaction of external water with the magma caused an increase of mixture pressure, favoring the fragmentation of the poorly vesicular portions of the magma.

Lapilli-rich layers. Bed B, representative of violent strombolian episodes, has abundant scoria with large spherical to ovoid vesicles, separated by thick septa. The external surface of the clasts is interested by minor pitting and very minor occurrence of small adhering particles. The study of particles outlines records an increase of very angular (VA) fragments, with bubble-wall-controlled contours, (33 % in bed B and 26 % in Bed C_T). Groundmass analyses highlighted that moderately vesicular, glassy fragments (MVG) represent the most abundant (more than 50%) type of ash emitted during these phases of activity, associated with dense, crystal-rich (DCR) and moderately vesicular, crystal-rich (MVC) fragments. These features are indicative of efficient magma degassing at fragmentation in fully magmatic Strombolian activity (Heiken and Wohletz, 1985). Moderately vesicular clasts with an almost completely crystalline groundmass (MVC) are already present in this beds, suggesting an extreme pressurization caused by microlite growth (Sparks, 1997; Gardner and et al., 1998). These fragments possibly represent the

shattering of magma lining the external portions of the conduit, crystallized for the dual effects of degassing and cooling.

Syn-eruptive magma crystallization

Image analysis of AP3 products has shown that, in bed A (sample VSM48), ash fragments were characterized by low plagioclase content (1 vol %), and a strongly non-log-linear CSD (Fig. 7.2). Marsh, (1998) interpreted this type of CSD curve as derived from two principal separated sources, reflecting local crystal fractionation and mainly due to cooling. One source is represented by crystals nucleated and grown at the present location of the magma. These crystals are almost always associated with solidification and are available for sorting in the magma only up to crystallinities of ~25% (e.g. Marsh, 1996). These crystals will always be small (Zone 1, Fig. 7.2). The second source of crystals is cumulate beds of previously grown crystals incorporated into the magma during transport and emplacement. These are the so-called 'tramp' crystals, which may have resided for some time in the feeding conduit system and annealed or ripened (Zone 2; Fig. 7.2). Because the eruption event involves decompression and possibly degassing, a burst of nucleation will probably be the final event recorded by the CSD.

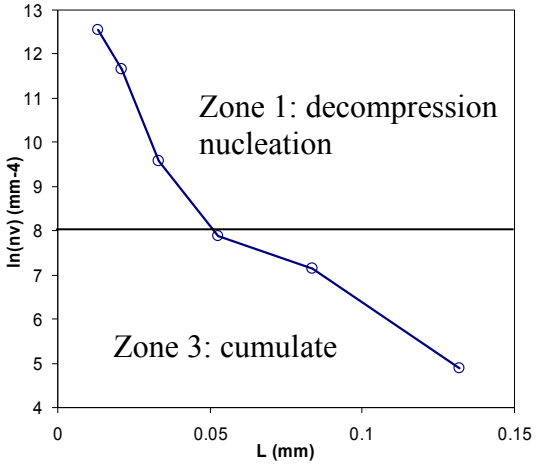

Fig.7.2 CSD plot of sample VSM48

This conclusion is also in agreement with the compositional variations recorded by plagioclase analyzed in sample VSM48. In fact, we find two types of crystals: large, zoned plagioclase, with less evolved cores (SiO_2 45.3 wt% and CaO 17.68 wt%) and more evolved rims (SiO_2 56.5 wt% and CaO 8.24 wt%), and small crystals with an average composition similar to the rims of large crystals (SiO_2 55.03 wt % and CaO 9.86 wt%). The aspect ratio of the two population of crystals slightly varies from tabular (1:3:5) for the larger crystals, to platy (1:4:4) forthe smaller crystals. This can be correlated with nucleation and growth rate pattern. Hammer (2002) found, for single step decompression experiments, that platy shapes forms at high nucleation rate, while more elongated shapes are related to high growth rate. Assuming that plagioclase in AP3 grew at depth in the magma chamber/conduit and had a growth rate of 10^{-7}-10^{-8} mm s^{-1} (Fenn, 1977; Hammer, 1999; Cashman and Blundy, 2000), the residence time for these two populations of crystals result of 3-26 days and 1-8/9 days, respectively for the largest and the smaller populations.

Transition to strombolian activity (VSM51) is recorded by a CSD plot characterized by a single straight line, parallel to the steeper segment of the VSM48 CSD plot (Fig. 7.3a), associated with a reduction of the maximum crystal size, and with an increase of the crystal content (3 vol %) and nucleation density (the intercept of the curve). This behavior can be interpreted considering a batch crystallization model (Marsh, 1998), in which the increase of the nucleation density is produced by an increase of undercooling, possibly related to a higher decompression rate leading to the magma explosion (Hammer, 2002; Cashman and Blundy, 2000; Taddeucci et al., 2004).

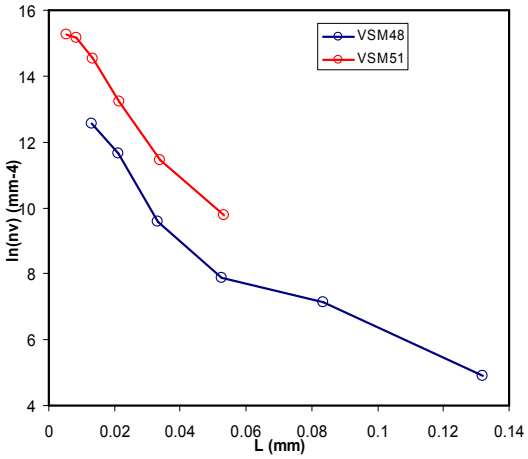

Fig. 7.3 a) CSD plot of sample VSM48 and VSM51;

The CSD plot of the sample from the base of bed C (sample VSM54) again corresponds to a single straight line (Fig. 7. 4a), characterized by increase of crystal size associated with an increase of crystal content (up 6 vol %), and a decrease of the nuclei density (Tab. 6.6). This situation has been generally discussed in terms of coarsening (Higgins, 1996, 2000; Marsh, 1998). Coarsening in an igneous context is a process by which small crystals are resorbed while the larger crystals grow so that the total surface energy is minimized. It occurs when magmas are held near their liquidus temperature for a long period. Fig. 7.4b shows theoretical CSDs for magma that is experiencing coarsening following the Communicating Neighbours model of Dehoff (1991). The turn down of the left side of the CSD curve represents the disappearance of the small crystals, whereas the right side of the CSD flattens during textural coarsening indicating that the growth rate of crystals increases to a maximum with grain size (Higgins, 1998). Thus, both the slope and intercept of the CSD diminish during this process.

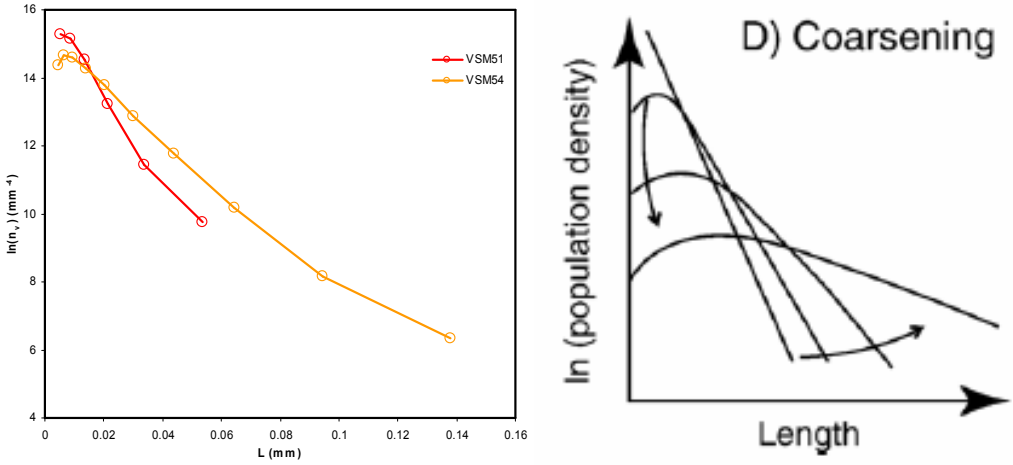

Fig.7.4 a) CSD plot of samples VSM51 and VSM54; b) Theoretical CSDs for magma that is experiencing coarsening following the Communicating Neighbours model of Dehoff (1991).

The CSD plot of the second lapilli-rich layer (Bed C_T , sample VSM56; Fig. 7.5) is characterized by a single straight line, with higher intercept and higher maximum crystal size, but same slope with respect to the base of bed C. This situation is well explained with an increase of the nucleation rate with time, due to rapid undercooling and depressurization of the system (Higgins, 1996).

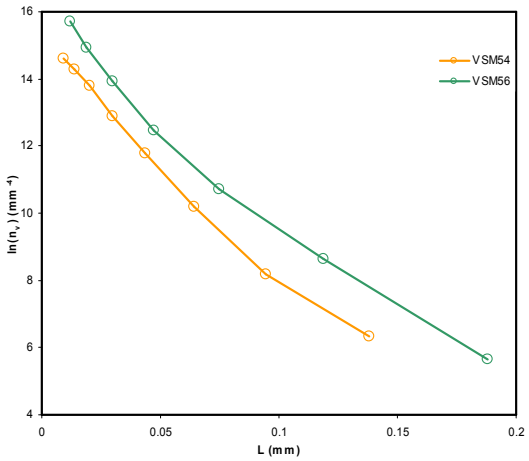

Fig.7.5 CSD plot of sample VSM54 and VSM56

Dynamic model of the AP3 eruption

Stratigraphic evidence suggests that AP3 eruption coincided with the shift of the vent position from Piano delle Ginestre (AP1-AP2) to the present vent area (Andronico and Cioni, 2002). This fact possibly produced a sharp difference in the eruption dynamics and a shift towards more mafic magma compositions, which persisted up to the AP6 eruption. The compositional change, which reflected also in a lowering of melt viscosity, might have favoured the lower intensity observed for the AP3–AP6 eruptions (Andronico and Cioni, 2002). The continuous feeding of the system through mafic magma batches allowed the chamber to grow laterally (Cioni et al., 1997). The opening of new eruptive fractures in a central position with respect to the volcano resulted in the withdrawal of magma from a more lateral position in the reservoir, tapping the deeper, less evolved melts of its lower portion. Glass composition, as major and trace elements, varies accordingly with the textural differences of the ash fragments during the eruption. Indeed, from the base to the top, CSD of plagioclase records an increase of the magma crystallinity, associated with an increase of the maximum size of the crystals, and thus of the time of magma residence (from 10 to 20 days). This behaviour is peculiar of a batch system, which experienced an exponential increase of the nucleation rate with time. The role of external water is the principal cause of magma fragmentation only at the base of bed C, while in the other

phases of the eruptions, it possibly acted only to increase the fragmentation energy of the magmatic explosions.

6. AS1a ERUPTION

6.1 General settings

The stratigraphic and sedimentological features of AS1a Member has been described at 5 outcrops, located toward East respect to the vent, according to the dominant wind direction during the eruption (see chapter 3, pp. 38). The most distal outcrop is located at about 10 km from the vent, where the deposits reach a thickness of 5 cm, while the most proximal outcrops have been detected at 3 km from the vent, where this unit reaches a thickness of 35 cm. The stratigraphic features of the AS1a deposit are well exposed at the Crossodromo quarry (S5), our reference section, where it reaches the maximum thickness (chapter 3, Fig. 3.9).

AS1a Member lies here on a partially eroded, reworked, brown ash layer which represents the top of the 512 AD deposit. AS1a Member shows a peculiar stratigraphy that can be followed up to 10 Km from the vent, so being a good marker for the succession of the deposits of the Middle Age activity.

The stratigraphic succession was subdivided in 5 beds characterised by different grain size and colours, with flat top upper surfaces (Fig. 6.1).

Bed 1 is formed by 4 layers, with a total thickness of 12 cm (Fig. 6.2). The basal layer (1), reaching a maximum thickness of 6 cm, is normally graded and mostly made of yellow, highly vesicular lapilli. It lies on the erosive surface present at the top of the AD 512 deposit, and shows a flat upper surface. In the topographic lows, lapilli are amalgamated in a laterally discontinuous, massive and poorly sorted, black ash layer. The following layer 2 is 4 cm thick, and consists of an alternation of massive, coarse ash and poorly sorted ash. This was followed by 3 cm of a laminated, coarse and fine ash layer (3). At the top, a centimetric, slightly hardened, yellow layer, laterally discontinuous, is presents (bed 4).

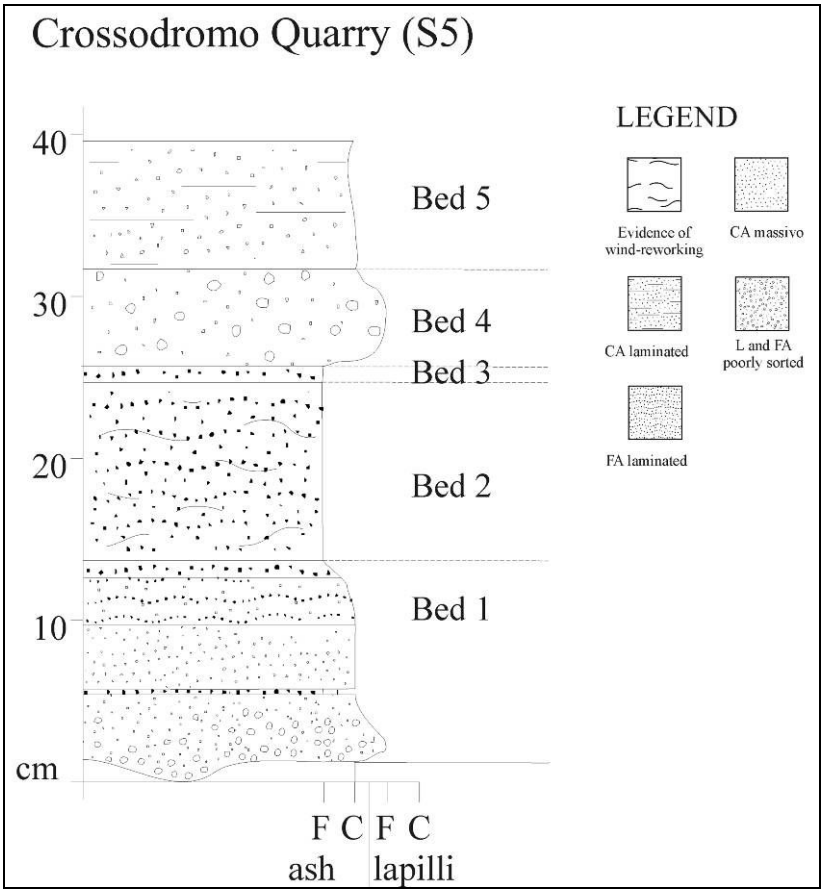

Fig. 6.1 Stratigraphic section of AS1a eruption

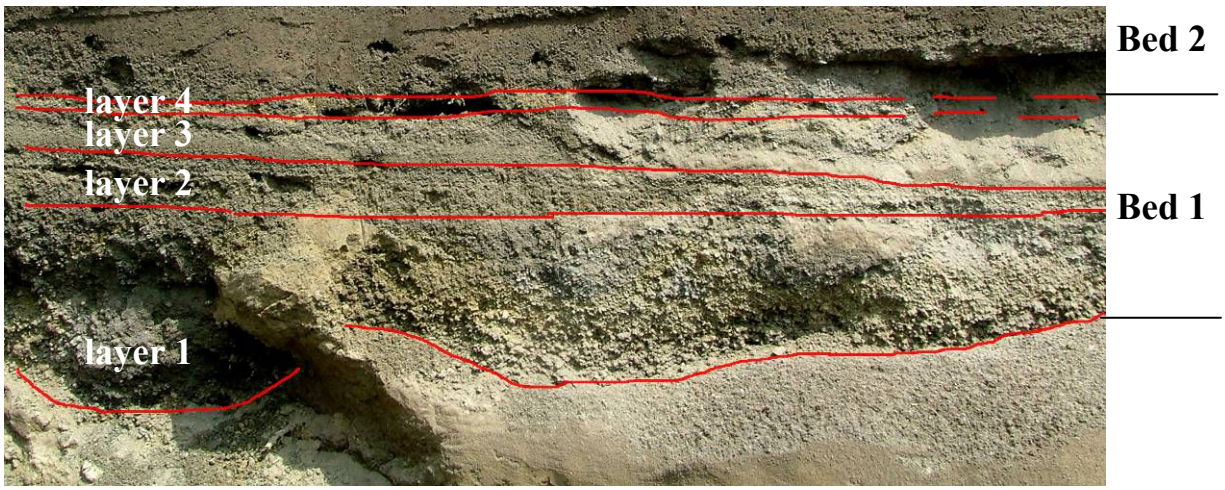

Fig.6.2 AS1a bed 1

Bed 2 is 11 cm thick, and consists of brown, fine and laminated ash. The different laminae are recognized by colour banding, varying form dark to light brown, showing in some parts, a wavy-like shape, possibly due to bioturbation.

Bed 3 consists of a laterally continuous, 1 cm thick, yellow and hardened layer, mainly constituted by accretionary lapilli.

Bed 4 is a massive, poorly sorted bed with a thickness of 6 cm, formed by fine, scoriaceous lapilli and coarse ash.

Bed 5 is formed by laminated, coarse ash, interlayered with minor fine ash, with evidence of wind reworking at top. Total thickness is 8 cm.

Products are largely juvenile, and are mostly made of pumice and scoria, and minor dense, glassy fragments. Crystals of biotite, dark and green pyroxene, and leucite are present as loose crystals within the deposits. The rare lithic clasts are represented by altered fragments of leucite and clinopyroxene-bearing lavas and tuffs.

Lateral variations

Bed 1 is present in all the studied proximal sections, with a thickness ranging between 10 cm and 2 cm. It completely lacks in distal outcrop (Raggi, S9), where the AS1a sequence is characterised by a 5 cm thick of coarse ash and fine scoria lapilli layer, possibly related to Bed 4.

The sequence from *Bed 2* to *Bed 5* show a constant thickness in all the studied stratigraphic sections, except for *Bed 2*, that lacks in sections S3 and S4. All these features indicate that section S1 is located along the dispersal axis of this eruption (chapter 3, figure 9).

6.2 Collected samples and grain size analyses

For the characterisation of the juvenile material, we collected five samples at different stratigraphic heights in the type section (S5), progressively named EP8 – EP2, from the base to the top of the succession (Fig. 6.3). Bed 1 was excluded from these investigations, as it shows a complex inner structures not easy to follow laterally.

Grain size distributions (Fig. 6.4; Tab. 6.1) show that, as a general feature, ash layers (EP2, EP6 and EP8) are very poorly sorted, with a variable mode, that shifts from 1 to 8 Φ

at the base of the eruption, to 2 Φ at the top. Sample EP8 is characterised by very negative, skewed curves, related to the abundance of coarse ash particles, while EP6 show a very positive, fine-tailed, skewed distribution. In sample EP2, grain size distribution is negative, coarse-tailed, skewed, due to the presence of coarsest material. The lapilli-rich layer (EP4) is a poorly sorted, negative (coarse) skewed bed, with a mode at 0 Φ, as we will expected from the deposition by a strombolian activity. The bad sorting of the whole deposit, instead, is a possible consequence of the turbulent character of the weak plumes generated by this type of activity (Bonadonna et al., 2005).

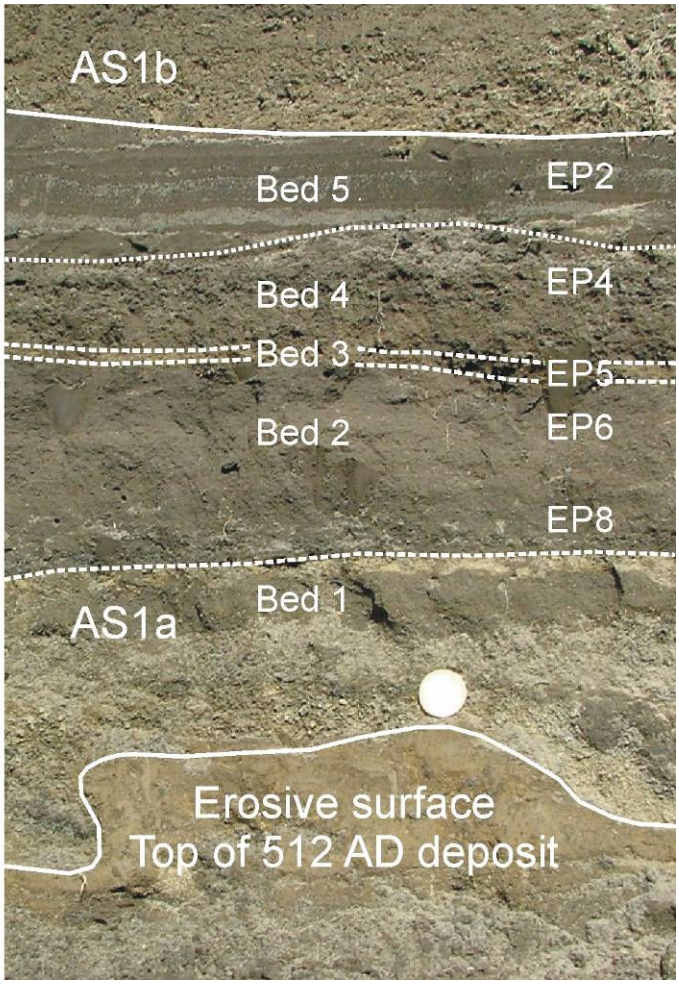

Fig.6.3 AS1a sequence at the Crossodromo quarry (S5). Collected samples are indicated.

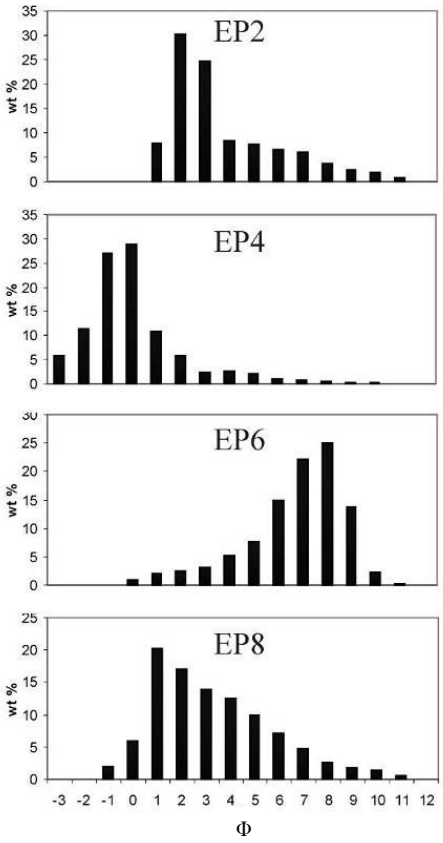

Fig.6.4 Grain size distributions of the collected samples, from the base (EP8) to the top (EP2) at S5. $\Phi = -\log_2(d)$, where d is the diameter of the particle.

Sample	Bed	Φ_5	Φ_{16}	Φ_{25}	Φ_{75}	Φ_{84}	Φ_{95}	MdΦ	$\sigma\Phi$	$\alpha\Phi$
EP2	5	0.63	1.26	1.56	4.51	5.81	8.04	2.48	2.31	0.47
EP4	4	-3.15	-2.11	-1.71	0.16	0.99	4.05	-0.80	1.55	0.16
EP6	2 (top)	1.79	4.28	5.23	7.65	8.01	8.81	6.61	1.87	-0.25
EP8	2 (base)	-0.49	0.4	0.84	4.34	5.35	7.60	2.34	2.47	0.22

Tab.6.1 Grain-size parameters of the AP3 beds. Φn = size (in Φ units) corresponding to the n cumulative percent. $Md\Phi$, $\sigma\Phi$ and $\alpha\Phi$ correspond respectively to the values of the median diameter, sorting (graphic standard deviation) and skewness of the grain size distribution, as defined by Inmann (1952).

6.3 Characterization of the juvenile material

Under the stereomicroscope, the AS1a juvenile products appear highly heterogeneous, showing textural and morphological features varying between two end-members: 1) light-brown, highly to moderately vesicular, sub-aphiric pumice with frequent pseudofluidal structure of the bubbles, and irregular external shape (Fig. 6.5a); and 2) dense, black to dark grey, highly crystalline scoria, sometimes showing glass rims, very poorly to moderately vesicular, with several rounded bubbles, with flat or rounded external shape and a completely oxidised groundmass (Fig. 6.5b). Fragments with textural features intermediate between these two end-members are very frequent (Fig. 6.5c). Sometimes, portions of black scoria are inceluded in the highly vesicular, glassy fragments (Fig. 6.5d).

The dense fragments are more abundant in the lower part of the sequence (EP8-EP6), while in the upper part (EP2) they are subordinated to the pumiceous clasts. Sample EP4 is more homogeneous, with the juvenile fraction mainly constituted by black, porphyritic to sub-aphyric scoria, poorly to moderately vesicular, generally showing flat external morphology and pseudo-fluidal structure of the bubbles. The features of the fragments are strictly related with the grain size, dense clasts being more abundant in the finer-grained portions.

As a general rule, fragments with different textures share a similar porphiritic index, with 5-7% of phenocrysts of leucite, clinopyroxene and phlogopite.

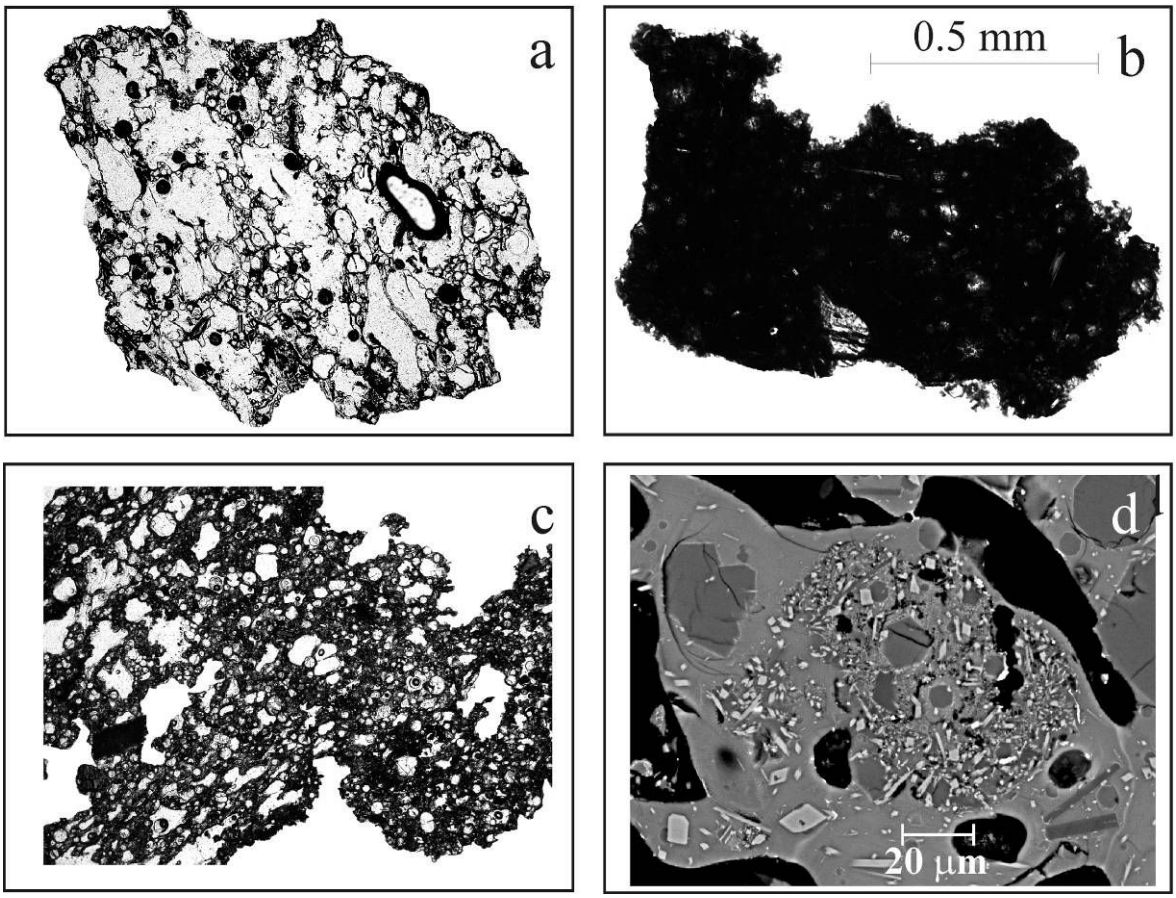

Fig.6.5 Microscope images of the different juvenile fragments obtained at the optical microscope (a, b, c) and at SEM (d): a) highly vesicular, poorly crystallised clast; b) poorly vesicular, crystal-rich clast, with oxidized groundmass; c) moderately vesicular, crystal-rich clast; d) dense portion of magma included in the highly vesicular portion. Optical microscope images have the same size bar of picture b.

Detailed investigation of single ash grains was performed on about 30 fragments, selected for each layer, in the size range of 0.5-1mm. This size class represents a compromise between sample representativeness and suitability of performing reliable analytical work on the single grains. We consider that a sample of 30 fragments is statistically representative of the whole variability of the juvenile population.

6.3.1 External morphology

Description of external morphology was based on the classical methods used in sedimentology for the characterisation of the surface features of a clast. Fragments were characterised looking at: i) shape, content and size of the bubbles exposed on the surface; ii) roundness; iii) shape of the clasts, (the measure of the existent relationships between the three dimensions of an object).

At least three different types of clasts were recognized, by applying the classical descriptive morphological terms described by Heiken and Wohletz (1985) for the juvenile fragments.

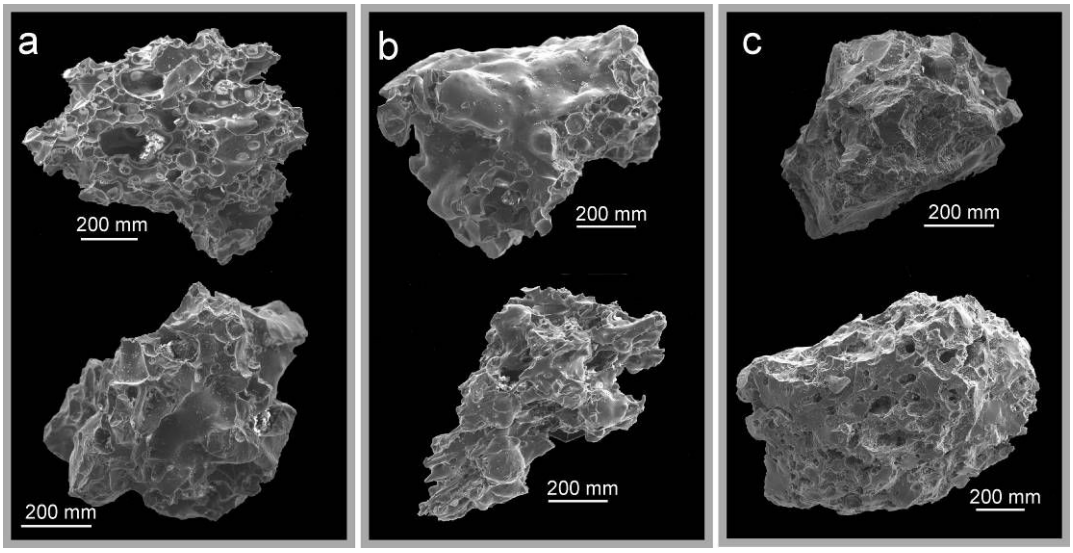

Fig.6.6 Secondary images of the external morphology of the AS1a products: a) spongy fragments, moderately and highly vesicular clasts, respectively in the highest part and in the lower part; b) fused fragments, with glassy and smooth external surface and pseudofluidal structure; c) blocky fragments, non and low vesiculated fragments.

-Spongy clasts. They consist of vesicular fragments, with nearly spherical bubbles of similar size intersecting the external surfaces of the clast (Fig. 6.6a). Clasts vary from highly vesicular, with large coalescent bubbles and thin walls, to moderately vesicular, with less marked coalescence and thicker walls.

-Fused clasts. The fragments are irregularly shaped and show smooth glassy surfaces (Fig. 6.6b). Vesicles, from sub-spherical to elongated in shape, are heterogeneously distributed within the clast, and generally not exposed on the external surface. A particular

type is represented by drop like clasts with fused surfaces and fluidal forms ("achneliths" according to Walker and Croasdale, 1971; or "droplets" according to Heiken, 1971).

-**Blocky clasts.** Their overall shape is determined by planar or curviplanar, glassy to microcrystalline surfaces (Heiken and Wohletz, 1985) intersecting few vesicles (fig.6.6c). They have a nearly isometric form (equant to sub-equant grains). Vesicle shape is largely variable, from irregularly shaped to sub-spherical. Clasts vary from moderately to poorly vesicular.

These three types of fragments are present in all the analysed samples, with variable abundance along the succession. Blocky clasts are the most abundant fragments (36 vol % of the total); they represent the 56 vol % of bed 3, while in the other beds their abundance vary from 26 to 39 vol %. Spongy clasts represent the 32 vol % of the total, and range from 19 vol % in bed 3 to 52 vol % in bed 5. The larger variability is shown by fused clasts, that represent the majority (45 vol %) of bed 4.

6.3.2 Particle outline

Particle outline is represented by the projection of the particle 3D contour on the horizontal plane. On each outline, filled and converted into a binary image, we calculated the rectangularity, compactness, elongation and circularity. Results indicate that the analysed particles show apparently a small range of variability of this shape parameters (Tab. 6.2; in Appendix 1 are reported the results obtained on each single analyzed fragment).

Sample	Bed	Rectangularity	Compactness	Elongation	Circularity
EP2	5	0.990 (0.061)	0.652 (0.064)	2.078 (0.248)	1.395 (0.129)
EP4	4	0.994 (0.082)	0.656 (0.054)	2.138 (0.361)	1.397 (0.131)
EP5	3	0.995 (0.080)	0.668 (0.066)	2.057 (0.436)	1.384 (0.150)
EP6	2 (top)	0.974 (0.050)	0.663 (0.065)	2.054 (0.353)	1.364 (0.111)
EP8	2 (base)	1.071 (0.074)	0.673 (0.034)	1.997 (0.257)	1.484 (0.104)

Tab.6.2 Average value of the shape parameters for the selected fragments of each sample.

The critical analysis of the average value of the single parameter for each sample shows that the differences between samples are small, all the data being within the range of

variability calculated for each clast. Exception is sample EP8, in which the fragments have a high rectangularity value, and are more compact and less elongated than other samples. This suggests that at the onset of the eruption magma fragmentation possibly occurred in a fragile regime.

Plotting the data in frequency histograms (Fig. 6.7), it is evident that, within the same layer, there is the contemporaneous occurrence of clasts with different external shape, and these differences are common to all layers.

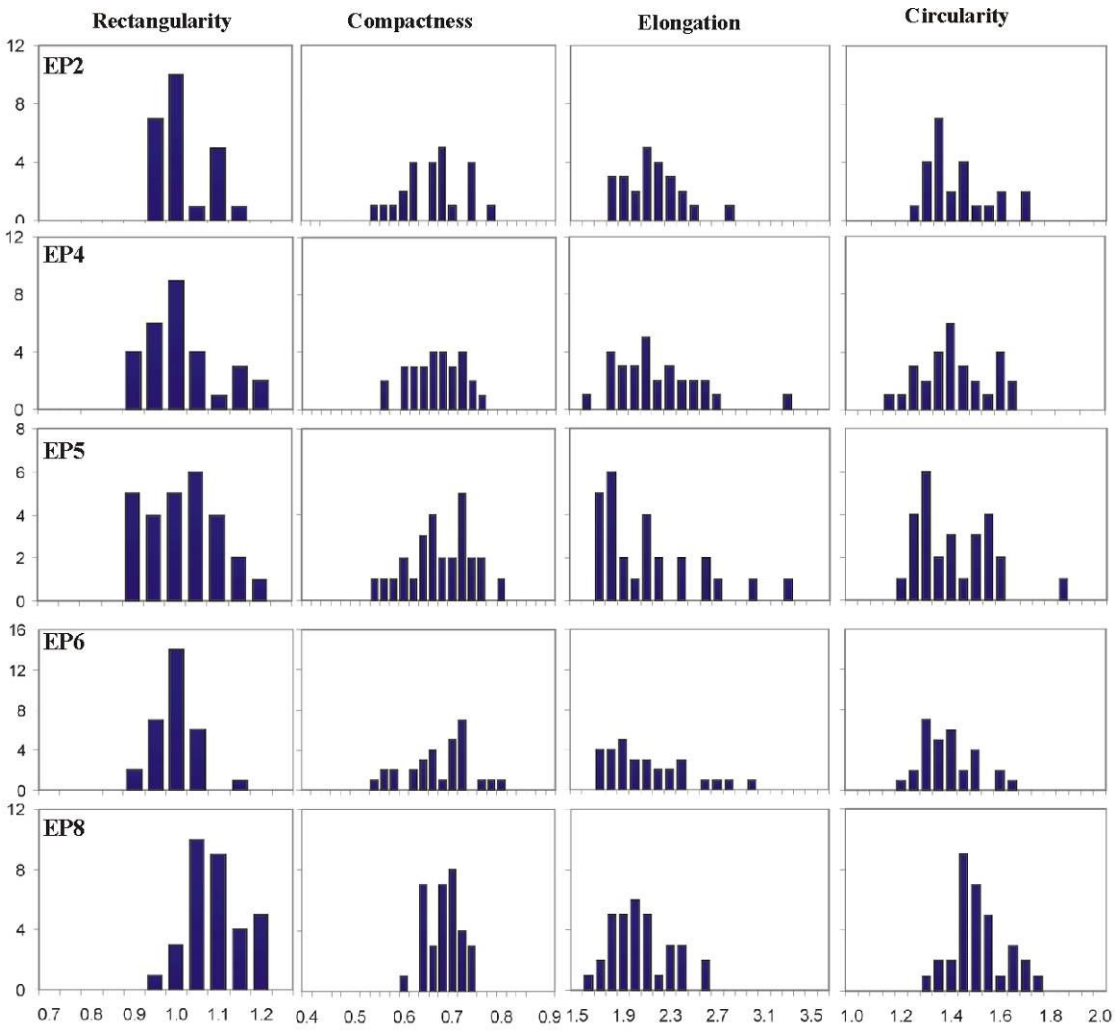

Fig.6.7 Histograms of frequency of the four measured shape parameters for each layer.

6.3.2.1 Principal Component Analysis

To identify what are the most common external morphologies characteristic of the ash, we applied the Principal Component Analyses (PCA) to the shape parameters. The method evidenced two principal components that explain the 97.2% of the total variance of the system (Tab. 6.3). This means that data are widely scattered in the plain defined by this two components (Fig. 6.8).

Variables	Eigenvalue	F1	F2	F3	F4
1	2.5799	-0.42974	-0.70649	-0.070034	-0.55794
2	0.96694	0.48053	-0.51128	-0.61787	0.35486
3	0.30163	-0.49045	0.41945	-0.7617	-0.057765
4	8.97E-03	-0.58641	-0.25204	0.18207	0.74796
tot.var%		**66.881**	**25.067**	7.8194	0.23244

Tab.6.3 Results of the Principal Component Analyses

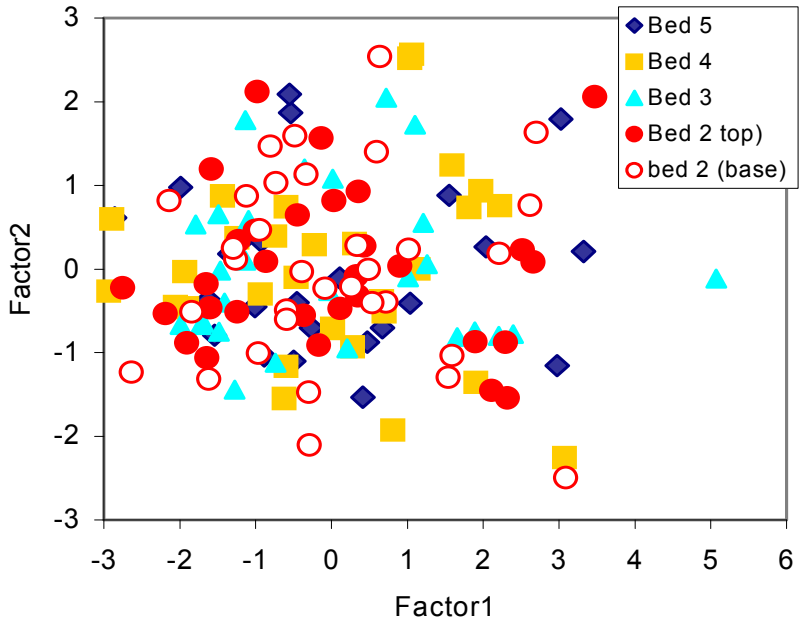

Fig.6.8 Binary plot of scores produced by principal components analysis

In the plot, the clasts are arranged according to the following scheme: 1) clasts plotting on the left side of the diagram are characterised by high compactness and low value of the other shape parameters; 2) clasts plotting on the upper part are characterised by low elongation and high value of the other shape parameters; 3) clasts plotting on the right side

are characterised by low compactness, and by high value of the other shape parameters; 4) clasts plotting in the lowest part of the diagram are characterised by high elongation and by low value of the other shape parameters (Fig. 6.9).

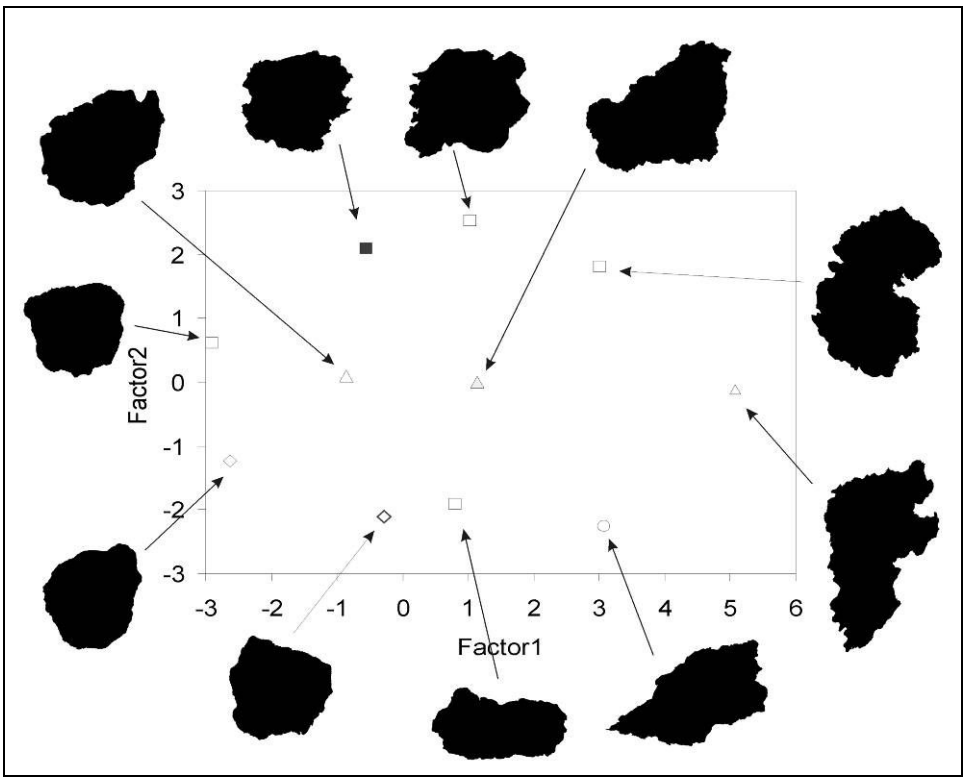

Fig.6.9 Discriminating diagram obtained from PCA of particles outlines on selected particles. Miniature of particles contours are insert for visualization.

The information contained in this plot is that in the five analysed samples, fragments with different external features coexist, and that the majority of the fragments, that fall on the central-left side of the diagram, are characterised by high compactness and variable elongation.

To define what are the most common shapes, we applied a cluster analysis using the first two principal components obtained by the multivariate analysis.

Each sample is represented by an horizontal line and it is joined to its nearest neighbour by a vertical line. The Euclidean Distance scale at the top of the diagram shows the degree of similarity or correlation between particles within a cluster or between clusters. Particles within a cluster that extends to a low value of Euclidean distance are more highly correlated with one another than particles within a cluster that extends to a higher value.

Assembling the particle images in accordance with the cluster tree (Fig. 6.10) is useful for visually assessing the grouping of shapes dictated by the model.

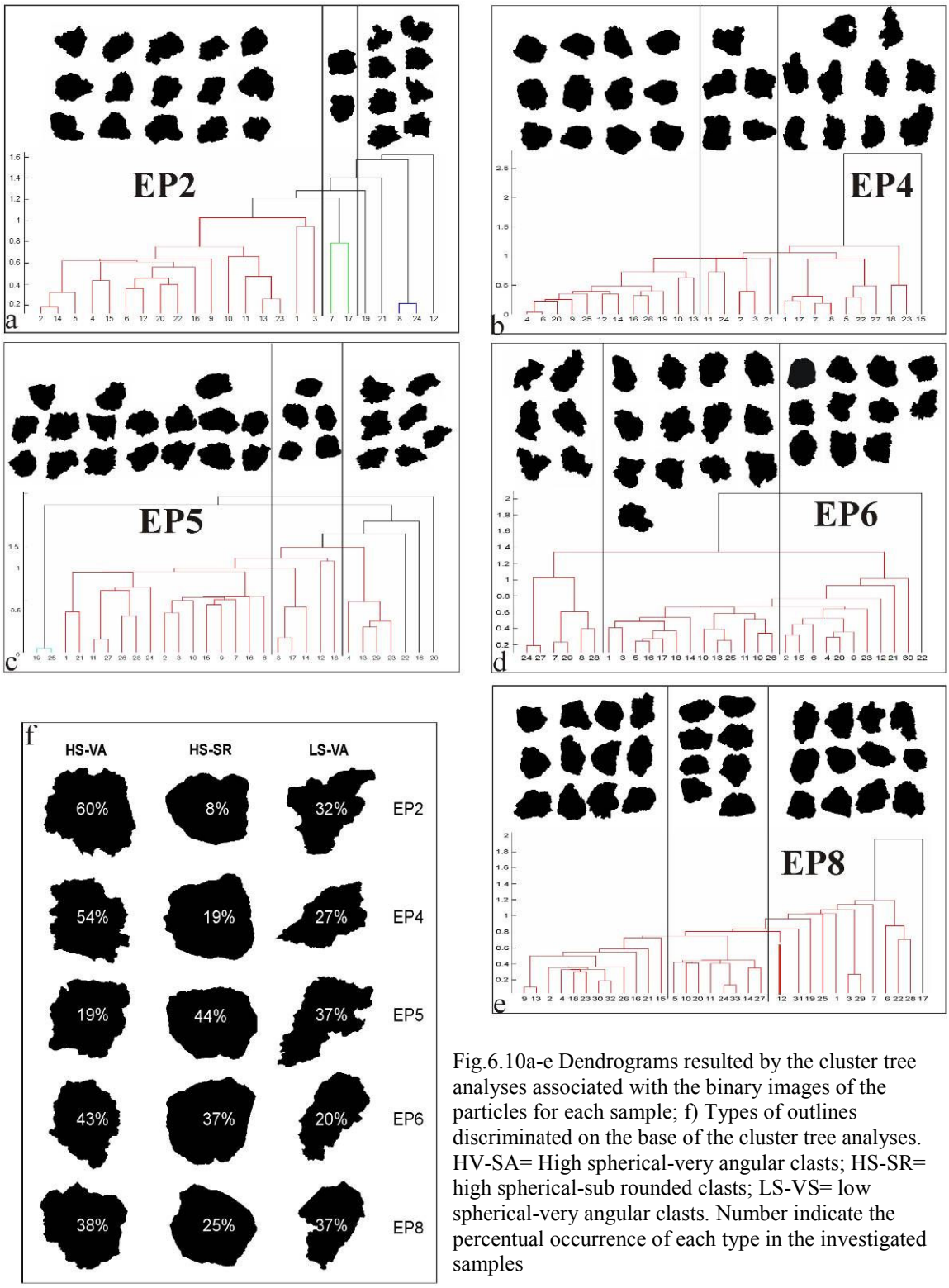

Fig.6.10a-e Dendrograms resulted by the cluster tree analyses associated with the binary images of the particles for each sample; f) Types of outlines discriminated on the base of the cluster tree analyses. HV-SA= High spherical-very angular clasts; HS-SR= high spherical-sub rounded clasts; LS-VS= low spherical-very angular clasts. Number indicate the percentual occurrence of each type in the investigated samples

In Fig. 6.10, the external outline representative of the recognized groups, and the percentage of each group in the different samples, are shown. Three groups of clasts include all the particles and can be described in terms of the classical grain shape parameters used in sedimentary petrology. According to this terminology, each group can be identified in terms of sphericity and roundness of the clasts (Blatt et al., 1980). The first group consists of equidimensional (High Sphericity) clasts with uneven outline (Very Angular) (HS-VA). This is the most abundant type, forming the 42 vol % of the analysed fragments. It always represents the majority of the juvenile fragments also in the single samples, ranging between 38 and 60 vol % in almost all analysed samples, except in bed 3 (sample EP5) (19 vol%). The second group (HS-SR) contains equidimensional (High Sphericity) particles with smooth outline (Sub-Rounded), and represents the 27 vol % of the total. It reaches the maximum value (44 vol %) in sample bed 3 (sample EP5), decreasing until 8 vol % at the top of the succession (sample EP2). Particles of the third group (LS-VA) are elongated (Low Sphericity) fragments with uneven outline (Very Angular), and represent the 31 vol % of the total fragments, showing a quite constant abundance (27-37 vol %) along the succession.

6.3.3 Groundmass texture

Heterogeneities between the clasts are also shown by the groundmass texture, which varies from nearly glassy in the pumice, to holocrystalline in the scoria clasts. Microlites and microphenocrysts of leucite, pyroxene and plagioclase are the main mineral phases, with only minor Fe-Ti-oxide and apatite, occurring in the most crystalline products. Leucite is present as isotropic crystals, sometimes formed by clustering of microlites < 20 μm. In the whole range of size, pyroxene crystals are zoned, with more complex zoning in large crystals. Sometimes, small crystals of leucite grow along the rim of cpx phenocrysts. Plagioclase crystals generally occur as elongated laths, with an average 2D aspect ratio of about 1:10.

A large variability in vesicle size, shape and content and crystal content in the ash is observed. On the base of the vesicularity index (Houghton and Wilson, 1989) (vesicles content vol %) and crystal content (crystal content vol %, vesicles free), three different groups of fragments were recognized in all the samples, occurring at different stratigraphic

position with variable abundances (in Appendix 1 are reported the textural features analyzed for each single fragments in all the investigated sample).

-Moderately Vesicular, Glassy clasts (**MVG**) are characterised by a vesicularity index ranging between 35 and 50 vol % (Fig. 6.11). The mean diameter of the vesicles ranges between 40 and 90 μm in bed 2 (base) (sample EP8) and regularly decreases toward the top of the sequence, between 20 and 45 μm (bed 5). Bubbles have a complex lobate shape, with rounded outlines, and show evidences of coalescence; in some clasts flattening of bubbles results in a pseudo-fluidal structure.

Cumulative size population density of all the measured vesicles has a bell-shaped distribution skewed toward the largest vesicles (Fig. 6.12). Small, rounded vesicles are also present, recorded by the fine grained tail in of the vesicle the distribution.

The crystal content is largely variable, ranging between 33 and 80 vol %, with the most frequent values around 55-75 vol % (Fig. 6.13).

MVG clasts are the most abundant type of fragments, representing the 44 vol % of the whole dataset, ranging between 30 vol % in bed 3 to 70 vol % in bed 4.

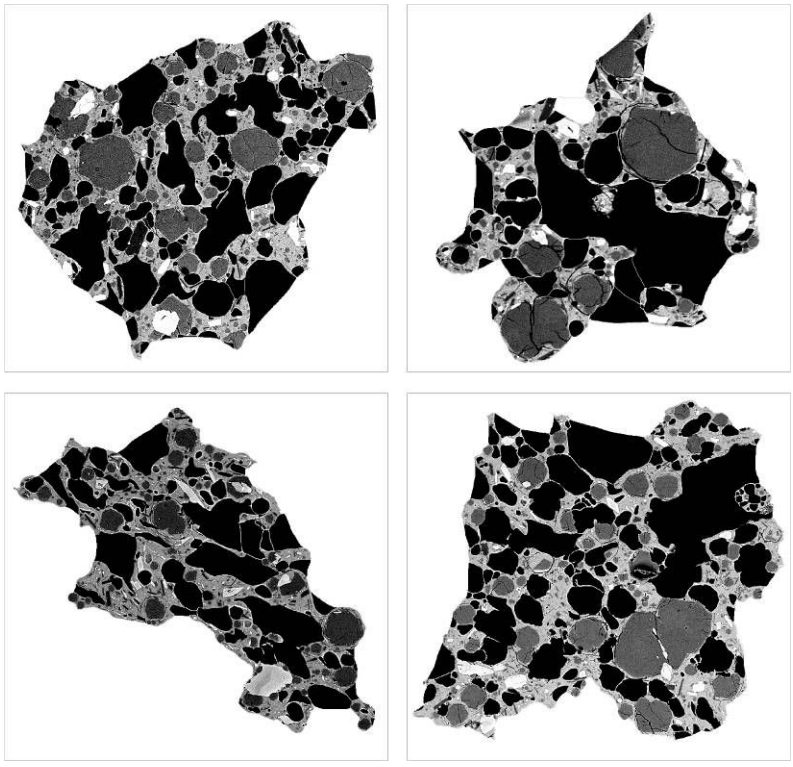

Fig.6.11 BSE image of selected MVG clasts. Clasts were selected from the grain size between 1-0,5 mm.

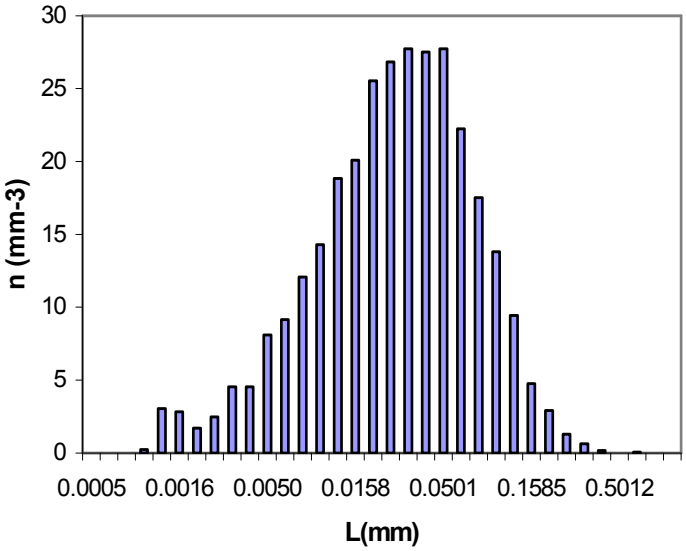

Fig.6.12 MVG cumulative size population density of vesicles.

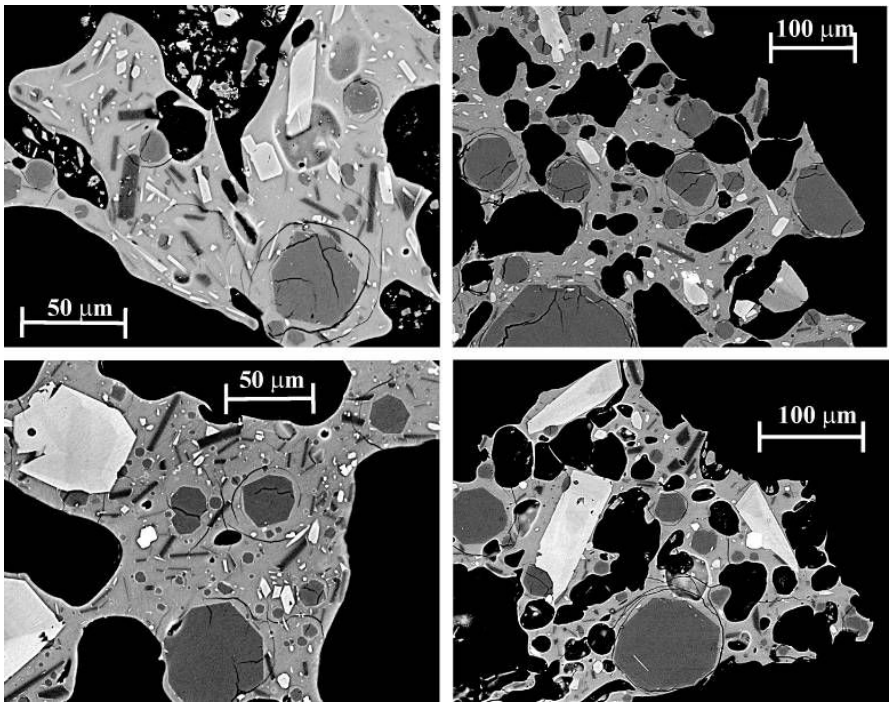

Fig.6.13 MVG groundmass texture of selected clasts.

-Poorly Vesicular, Glassy clasts (**PVG**) are characterized by a vesicularity index ranging between 15-30 vol % (Fig. 6.14).

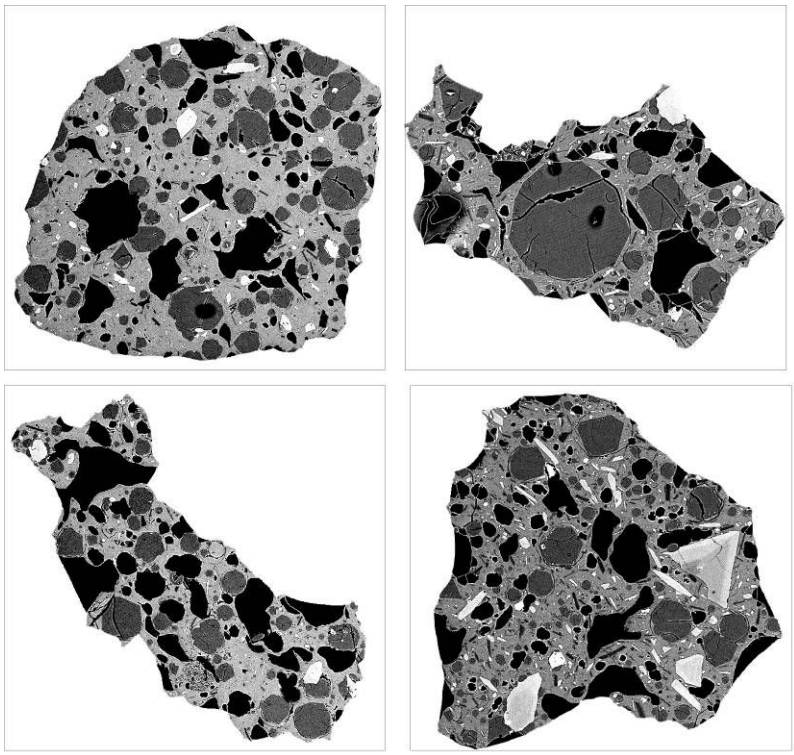

Fig.6.14 BSE image of selected PVG clasts. Grain size in the 1-0.5 mm range.

The mean vesicle diameter ranges between 35 and 75 μm in bed 2 (base), decreasing to 20-35 μm in bed 5. Bubbles are nearly spherical, and do not evidence incipient coalescence. In some fragments collapsed bubbles, characterised by amoeboid shape, are present.

The generally smaller dimension of bubbles with respect to MVG clasts reflects in a size population density distribution more symmetrical and peaked at a smaller size (Fig. 6.15).

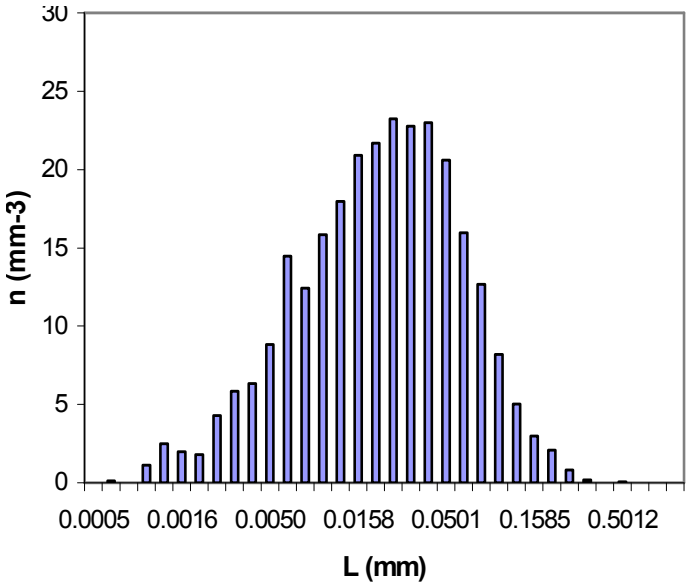

Fig.6.15 Cumulative size population density of vesicles

Crystal content ranges between 55-85 vol %, as the MVG clasts (Fig. 6.16).

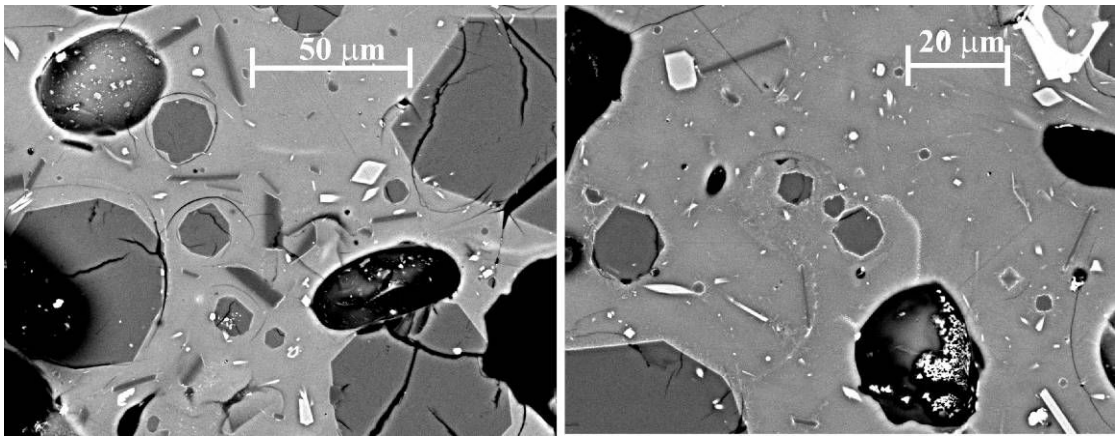

Fig.6.16 Selected groundmass textures images of PVG clasts.

PVG clasts represent the 35 vol % of the total fragments; they are the most abundant type of fragments at the base of the sequence, regularly decreasing fro m 54 vol % to 20 vol % at top of the sequence.

-Dense, Crystal-Rich clasts (DCR) are characterized by vesicularity lower than 30 vol %, similar to that shown by PVG fragments (Fig. 6.17).

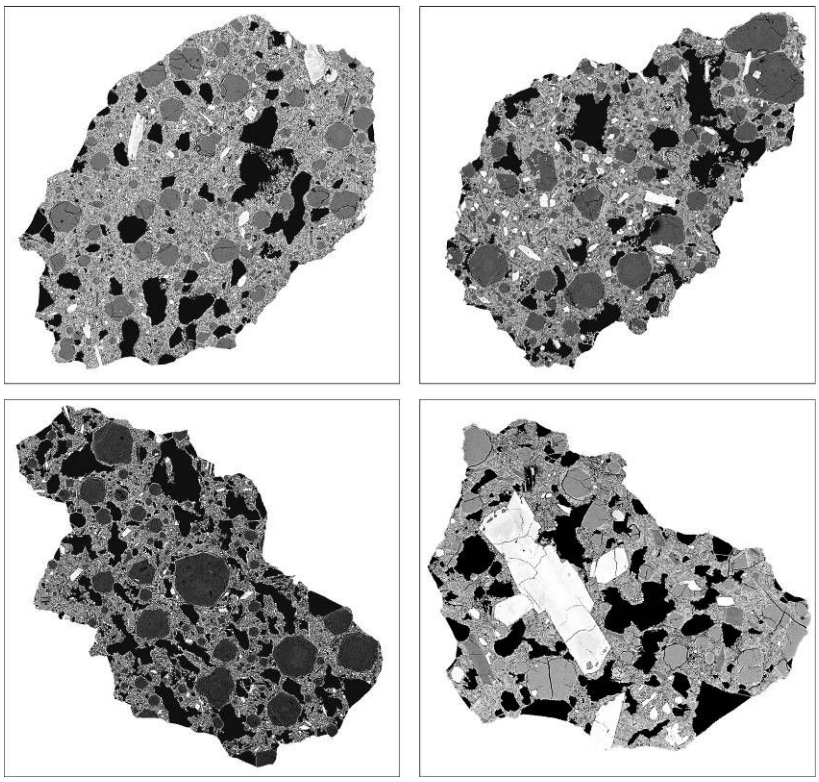

Fig.6.17 BSE image of a DCR clasts. Grain size in the 1-0.5 mm range.

Vesicle diameter ranges between 20 and 65 μm, increasing toward the top of the sequence. Bubbles are irregularly shaped, reflecting crystal growth on the bubble walls, and show evidence of coalescence, sometimes along a preferential directions.

Population density of bubbles lacks the very pronounced modes of MVG and PVG clasts, showing a platykurtic distribution and a dimensional range of the vesicles similar to the other two clast types (Fig. 6.18).

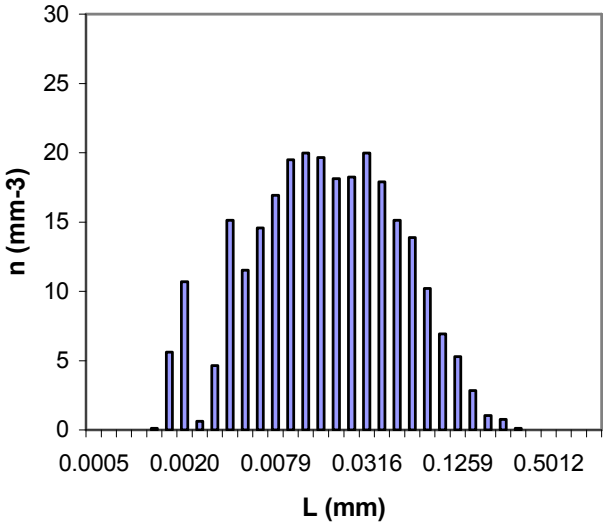

Fig.6.18 Cumulative size population density of vesicles

Crystal content is > 90 vol %. In the presence of small amount of glass, round vesicles smaller than 5 μm in diameter are present in nearly holocrystalline fragments, suggesting a final vesiculation event possibly forced by extreme crystal nucleation and growth. Mineralogical assemblage includes, in order of abundance, clinopyroxene, leucite, small microlites of oxides and plagioclase (Fig. 6.19).

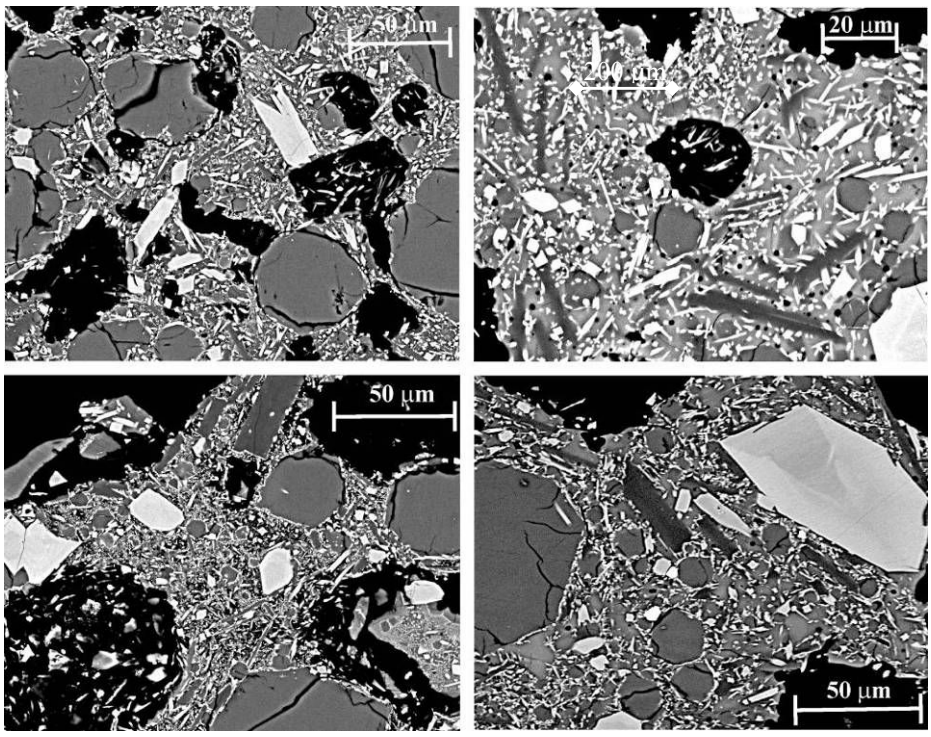

Fig.6.19 Selected groundmass textures of DCR clasts.

DCR clasts are the less abundant type of fragments (20 vol % of the total). They are the most abundant type of fragments in bed 3 (42 vol%), while are poorly represented in the other layers (from 3 to 10 vol%).

6.3.4 Relationships between the different parameters

The discussed morphological and textural features represent a dataset which exhaustively describes the juvenile fraction of each studied sample. While the relative abundance of the different classes described above, recognized for each observed feature (external morphology, particle outline, groundmass composition and texture), is dependent on the grain size selected for the study, these classes well represent the variability of the juvenile material from few millimetres to a hundred microns (fine lapilli to fine ash, according to the grain size terminology introduced by White and Houghton, 2006). Cross-correlation between the different measured parameters is shown in Fig. 6.20 for all the studied samples. Within a same sample, we observe no clear mutual relationships between the different parameters. The main result is that a one-to-one correlation between the parameters does not exist so that, while for example all the DCR clasts of sample EP6 have blocky morphology (Fig. 6.20p), the blocky clasts of the same sample are characterized by variable groundmass texture (Fig. 6.20m). Apparently, the commonly used classification based on external morphology of the clasts (Heiken, 1974) is not suited to differentiate clasts with similar characteristics of the groundmass texture (Fig. 6.20).

In the presented study, for example, while spongy and fused clasts of sample EP2 (bed 5) mainly belong to MVG category, the same fragments of sample EP5 (bed 3) practically cover the whole spectrum of groundmass textures (Fig. 6.20a, i). Surprisingly, the classes of particle outline do not show a correlation with the morphological features of the external surface of the clast (Fig. 6.20e, f, k, o). Similarly, particle outline of the clasts is completely uncorrelated with groundmass texture (Fig. 6.20c, d, j, n). This suggests that the classes of particle outline as derived from the proposed method of cluster analysis represent an additional good descriptor for juvenile particles of the tephra, being completely independent from all the other measured parameters.

Moreover, the variable occurrence of the different classes of clast along the succession indicate that each bed, and then each phase of activity of the AS1a eruption, was

characterised by the emission of products with distinctive features. This means that all the studied morphological and textural parameters, can be utilised to unequivocally identify a single layer.

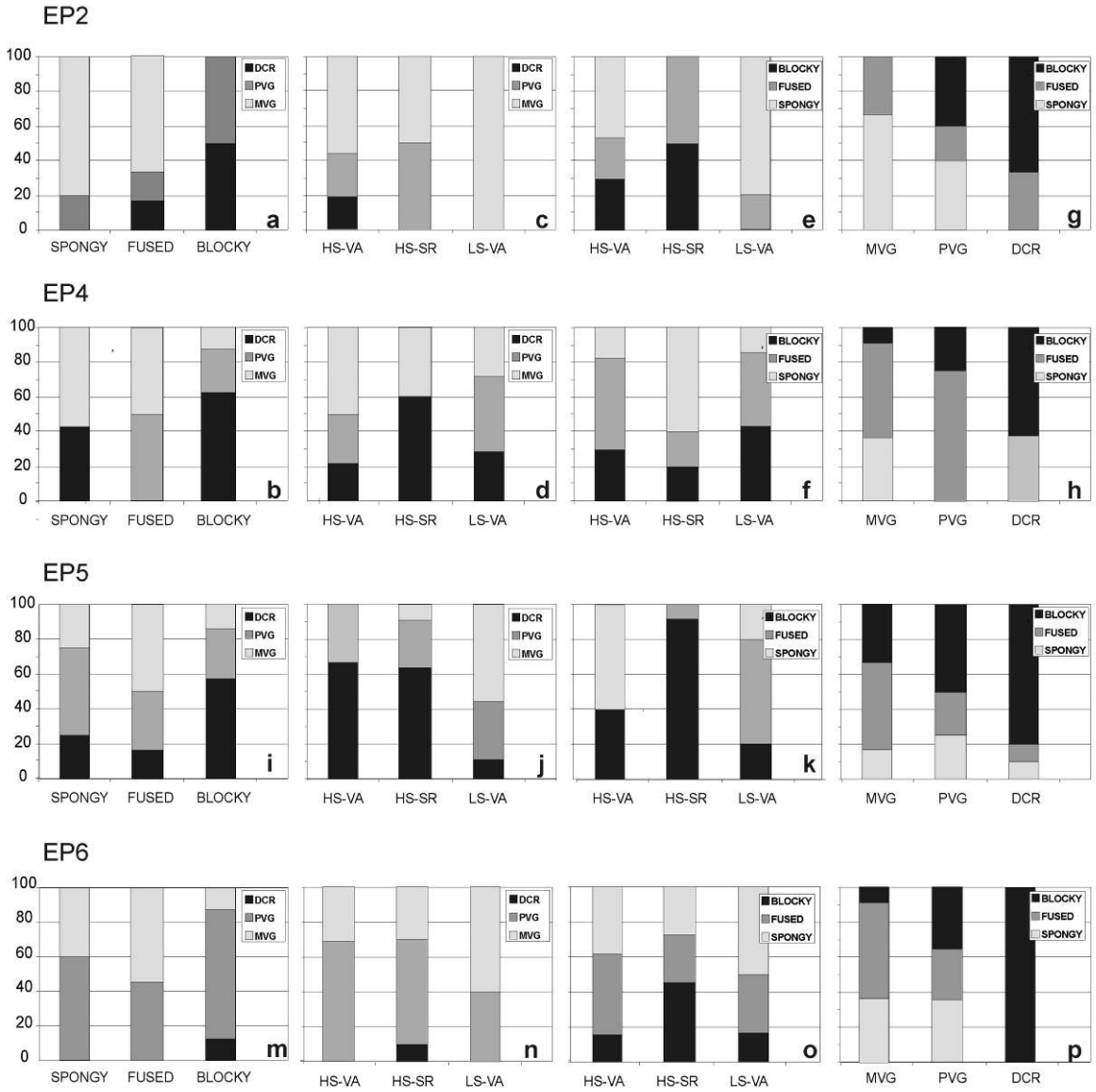

Fig.6.20 Cross-correlation of all studied morphological and textural parameters obtained on each singlefragments, in the investigated layers.

6.4 Compositional features

Bulk rock and glass composition

Bulck rock composition were determined on a scoria from Bed 4, indicating a phonolitic tephrite bulk composition. Matrix glass, as determined from ash fragments from all the main beds, has a foiditic composition, with a lower SiO_2 content and a larger range of alkali than bulk rock (Tab. 6.4).

	Bulk rock	***Glass composition***							
Sample	**VS97-723**	**EP2** ***(Bed 5)***				**EP4** ***(Bed 4)***			
		MVG		DCR		MVG		DCR	
Elements		Mean (n=15)	σ	Mean (n=3)	σ	Mean (n=14)	σ	Mean (n=11)	σ
SiO_2	51.16	47.82	0.29	47.95	0.50	47.59	0.30	48.07	0.96
TiO_2	0.78	0.96	0.09	0.98	0.08	0.92	0.06	0.85	0.09
Al_2O_3	19.43	20.14	0.19	19.95	0.56	20.15	0.19	20.43	0.83
FeO	7.4	8.30	0.20	9.09	0.25	8.21	0.31	8.50	1.50
MnO	0.15	0.24	0.07	0.40	0.11	0.24	0.08	0.32	0.10
MgO	2.24	1.35	0.11	0.67	0.03	1.39	0.08	1.04	0.34
CaO	7.04	7.78	0.45	4.54	0.60	7.95	0.47	6.27	1.62
Na_2O	3.47	6.84	0.60	9.93	0.80	6.57	0.30	7.69	1.47
K_2O	7.98	5.30	0.42	5.03	1.29	5.70	0.57	5.49	1.03
P_2O_5	0.36	0.12	0.11	0.00	0.00	0.15	0.06	0.04	0.10
Cl	0.00	1.16	0.05	1.48	0.12	1.13	0.01	1.30	0.16

	EP5 ***(Bed 3)***				**EP6** ***(Bed 2top)***				**EP8** ***(Bed 2base)***		
	MVG		DCR		MVG		DCR		MVG		DCR
Elements	Mean (n=18)	σ	Mean (n=2)	σ	Mean (n=15)	σ	Mean (n=8)	σ	Mean (n=15)	σ	n=1
SiO_2	47.49	0.34	47.58	0.21	48.05	0.32	47.90	0.94	47.85	0.53	45.81
TiO_2	1.00	0.05	0.77	0.11	0.91	0.08	0.93	0.17	0.91	0.10	1.44
Al_2O_3	20.03	0.31	20.16	0.13	20.29	0.25	20.52	0.58	20.21	0.33	19.65
FeO	8.54	0.35	9.95	0.26	8.42	0.29	9.05	1.41	8.29	0.33	11.21
MnO	0.26	0.08	0.36	0.06	0.27	0.08	0.29	0.09	0.32	0.10	0.31
MgO	1.33	0.16	0.84	0.05	1.22	0.09	1.05	0.25	1.23	0.11	1.00
CaO	8.13	0.31	6.44	0.16	7.68	0.27	6.33	1.40	7.74	0.40	5.44
Na_2O	6.74	0.46	7.64	0.09	6.64	0.45	7.83	1.10	6.77	0.77	9.23
K_2O	5.12	0.47	4.93	0.03	5.25	0.34	4.87	0.23	5.42	0.24	4.66
P_2O_5	0.16	0.02	0.18	0.12	0.08	0.06	0.00	0.00	0.05	0.05	0.11
Cl	1.19	0.08	1.20	0.02	1.18	0.05	1.24	0.05	1.20	0.06	1.13

Tab.6.4 Bulk rock composition and average glass composition for MVG and DCR clasts. n= number of point analysis; σ = standard deviation.

Scatter plots of the most significant major elements (SiO_2, Al_2O_3, MgO, FeO, Na_2O, K_2O and Cl) versus CaO wt% are shown in Fig. 6.21.

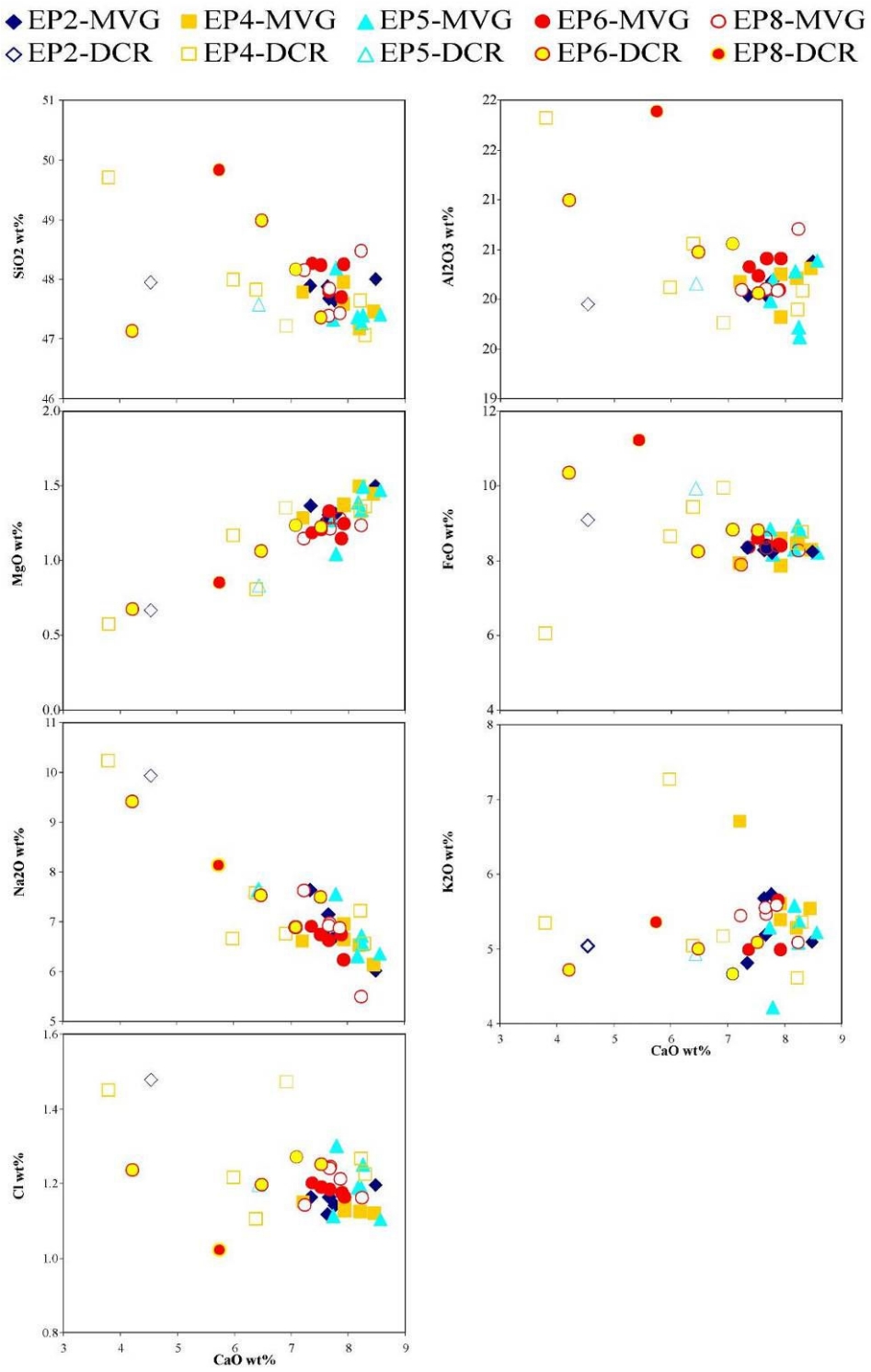

Fig.6.21 Variation diagrams of the major elements (as oxides wt%) versus CaO wt%.

The rather scattering of glass composition can be discussed by discriminating between MVG and DCR fragments. PVG glass compositions are homogeneous, being very similar to that of the MVG clasts, then, for the sake of simplicity, they were grouped with the MVG fragments in the diagrams. We find that a clear correlation exists between categories of groundmass texture and composition of the residual glass.

MVG and PVG glass compositions are homogeneous both at the scale of a single fragment (Tab. 6.4) and between the different fragments of this type. This possibly reflects the similar crystal content of the two types of fragments. On the other hand, DCR glass compositions are largely variable between the different samples, showing different concentrations of some oxides with respect to MVG and PVG clasts. In particular, they are depleted in CaO and MgO, while FeO_2 and K_2O remain quite similar. Moreover an enrichment in SiO_2, Al_2O_3 and Na_2O is observed. All this features indicate that the differences between the two types of fragments, MVG and DCR, are related to the crystallization of a Ca-rich pyroxene.

The correlations between groundmass textures and composition should be taken in account when trying to describe the whole compositional spectrum typical of a given tephra bed. Indeed, these compositional features are very common in the products of violent strombolian and ash emission activity of Vesuvius (Santacroce et al., 1993; Marianelli et al., 1999; Andronico and Cioni, 2002). The compositional range of the oxides of the major elements in groundmass glass is fully comparable with the compositional range shown by the 472 AD (Santacroce et al., 2007), and partially overlaps the composition of 512 AD (Fig. 6.22), being not easily distinguishable from them only on the base of glass composition.

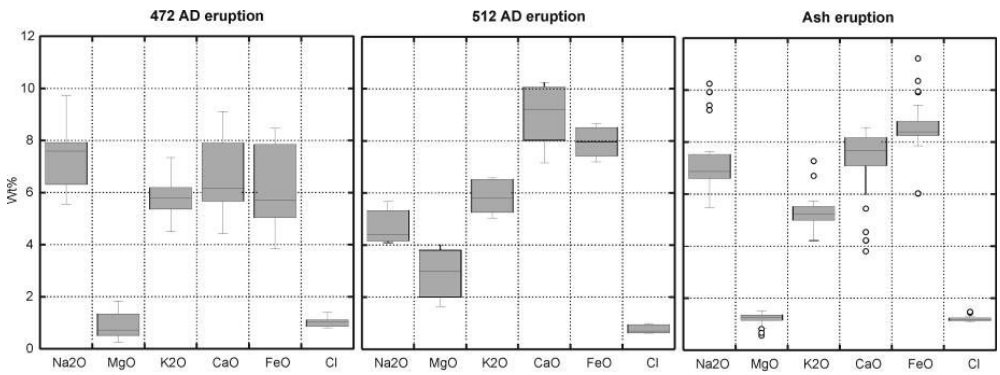

Fig.6.22 Box and whisker plots of selected major oxides for the 472AD, 512 AD and AS1a eruption.

A striking feature of the products of AS1a eruption is the very high chlorine concentration in matrix glass, ranging between 1.10 and 1.49 wt%, with the highest values corresponding to the denser, highly evolved products. When compared to the Chlorine content of historical Plinian and Sub-Plinian eruptions of Vesuvius, the products of AS1a result the most Cl-enriched. This can be related to the development in the magma of a permeability network at low pressure, favouring the rapid loss of those volatile phases characterised by the highest diffusivity coefficients, like water. Indeed, Gardner et al. (2006) experimentally demonstrate that the partitioning coefficient of Cl between melt and gas decrease at lower pressure, for low permeable magma, with no fluid surrounding the melt.

Trace elements

Trace elements concentrations were determined using the Laser Ablation ICP-MS device, installed Earth Science Dept., Univ. of Cagliari (see chapter 2). About 10 ash fragments from each sample were analysed, selected within the MGV and PVG types (Appendix 3, Tab. 3.5A, 3.6A, 3.7A, 3.8A, 3.9A). On each fragment a number of 2-3 analyses was performed and the average values were plotted in the classifications diagrams, although in some cases analyses of two different points of the same fragments resulted very different for the partial ablation of microlites. Detection of microlite ablation was made basing on the critical inspection of time-resolved spectra of selected elements with a large partition coefficient for the mineral. In that case we only considered the analyses not contaminated.

Rare Earth pattern indicates that the different samples have an homogeneous composition, being the observed variations within the standard deviation (Fig. 6.23). The fact that we do not observe Eu anomaly, although the plagioclase is present in this products, suggest that plagioclase crystallization possibly occurred at high oxygen fugacity, so the Eu remains in a 3+ state (White, 2007).

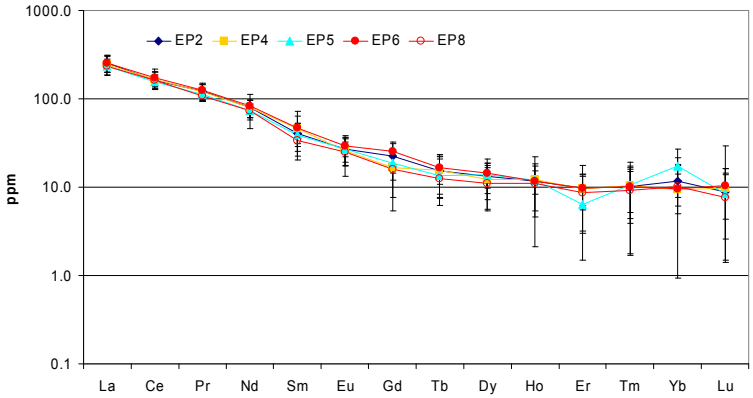

Fig.6.23 Average value and error bar (standard deviation) of Rare Earth pattern.

As explained in the compositional section of chapter 4, trace elements that give information about variations of crystal content between the different samples, are those elements compatible with the principal mineralogical phases of the eruption (Tab. 6.5). In Fig. 6.24 the scatter plots of incompatible elements (U, Nb, Th) and compatible elements (Sr, Ba, Rb, Sc, V, Nb, Y, Cs) vs. Th are shown.

elements	plagioclase	pyroxene	leucite	apatite	Ti-magnetite
Sr	5-10.4		0.07-0.0005		
Ba	0.3-2.0		0.07-0.0005		
Rb	0.02		>1		
Pb	0.15-0.22		0.07-0.0005		
Eu	1.37-0.58		0.07-0.0005		
Sc		20	0.07-0.0005		>1
V		3.5	0.07-0.0005		48-52
U			0.07-0.0005		
Th			0.07-0.0005		
Nb			0.07-0.0005		0.24-0.35
Ta			0.07-0.0005		0.25-0.36
Zr			0.07-0.0005		0.08
Y		0.5-4.0	0.07-0.0005	22	
Hf			0.07-0.0005		0.11
La			0.07-0.0005	24	
Lu			0.07-0.0005	7	
Cs			>1		
Ni			0.4-0.1		
Ga			0.4-0.1		
Co			0.4-0.1		

Table 6.5 Partition coefficients for some trace elements obtained for natural trachitic and trachiphonolitic obsidians of Campi Flegrei (South Italy) (Morra et al, 2003). DCs and DRb of leucite are from Foley and Jenner, 2004.

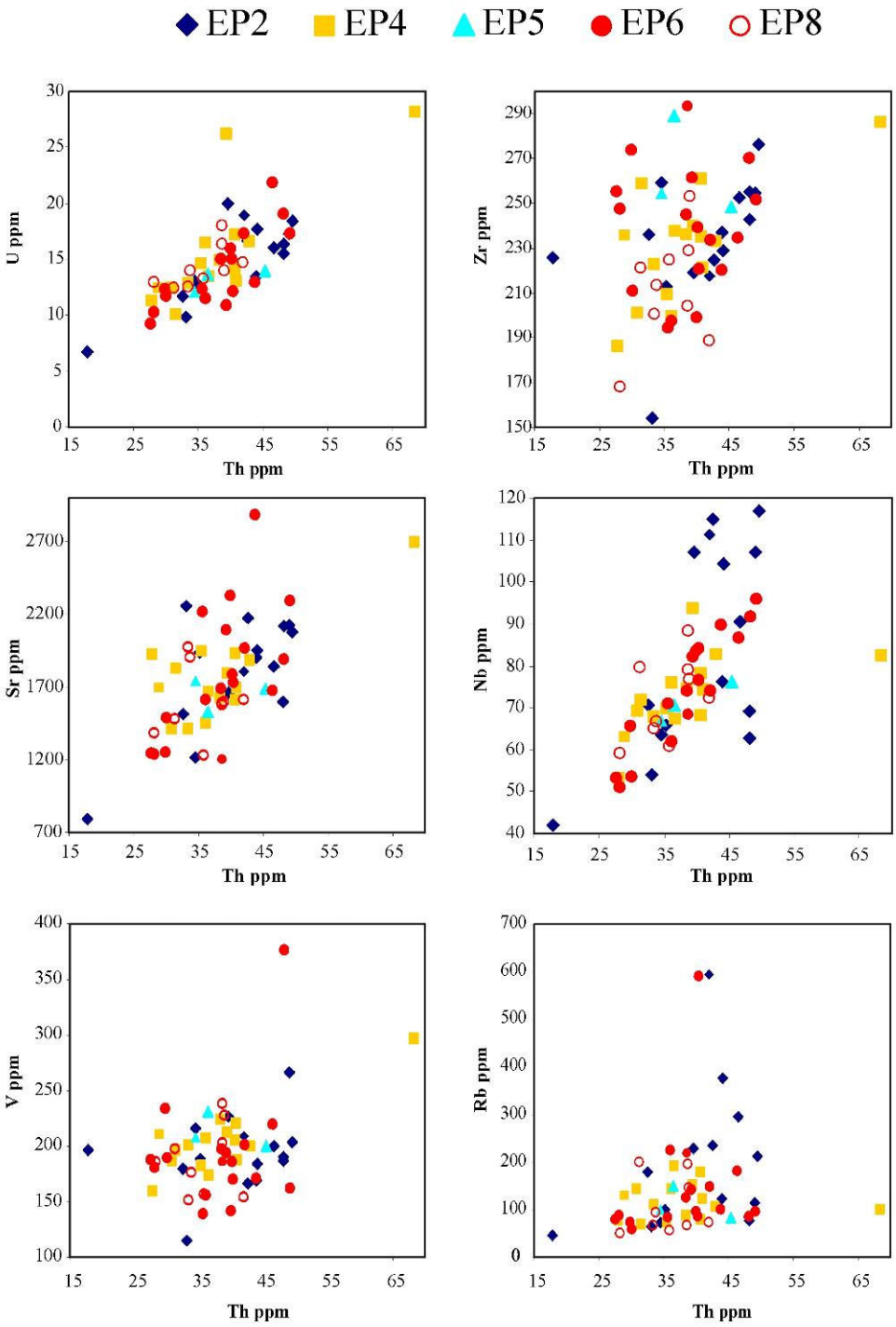
EP2
EP4
EP5
EP6
EP8
U ppm
Th ppm
Zr ppm
Th ppm
Sr ppm
Th ppm
Nb ppm
Th ppm
V ppm
Th ppm
Rb ppm
Th ppm

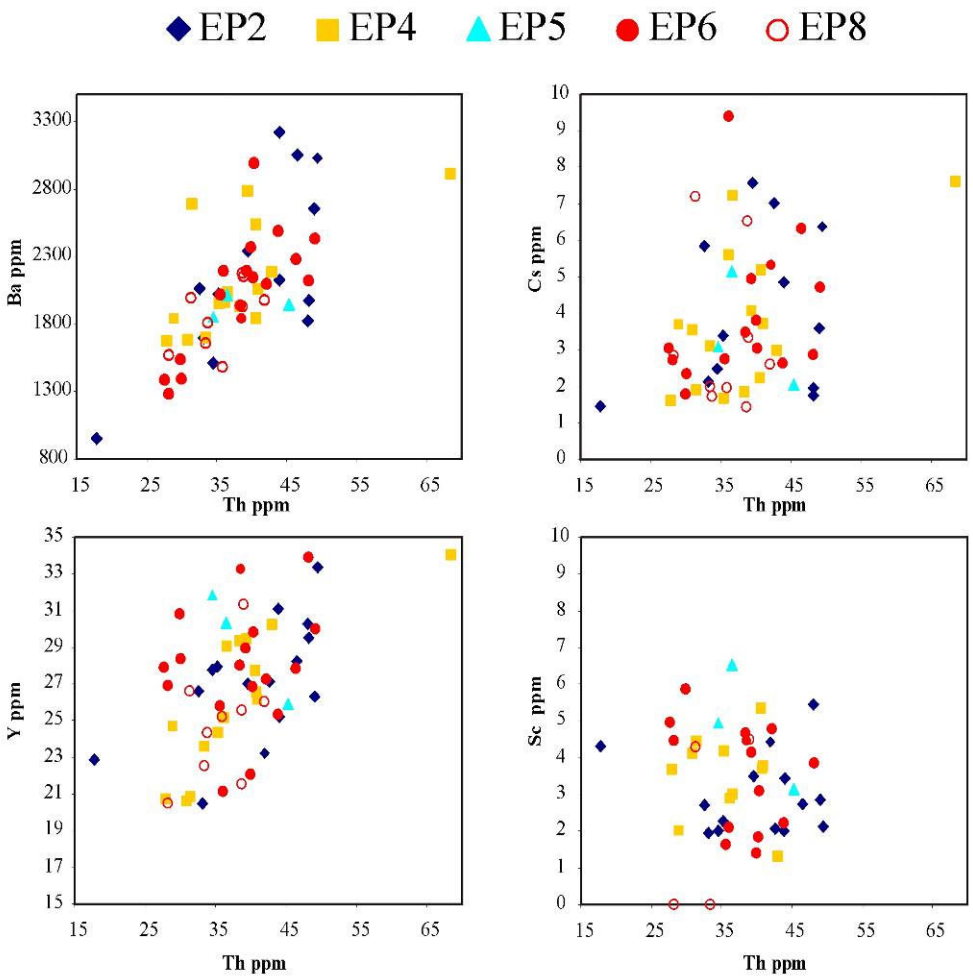

Fig.6.24 Spider diagrams of incompatible elements against compatible elements.

Glass analyses from single shards cover a wide range of composition in the studied samples. The reproducibility of the LA-ICP-MS technique is typically 5% on repeated analyses of the same, homogeneous material (such as the calibration standard NIST612, see chapter 2). Clearly the fields of data from the individual shards within each sample spread across a range considerably wider than the 5% of the average bulk sample value. These fields thus represent real within-sample, inter-shard variation in trace element composition.

Results show that for these products, Zr is a semi compatible elements, while Nb, Th and U result well correlated between them, suggesting a similar incompatible behaviour.

With respect to the other considered trace elements, samples show large variations, with the exception of base of the eruption that results more homogeneous.

The REE data can be presented as the chondrite normalised slope of the REEs Ce_N/Yb_N plotted against the size of the Eu anomaly (Eu/Eu*). The majority of samples show small negative Eu anomalies Eu/Eu* < 1 whilst some shards from this sample show positive Eu anomaly, possibly related to contamination of the analyses with microlites of plagioclase (Fig. 6.25).

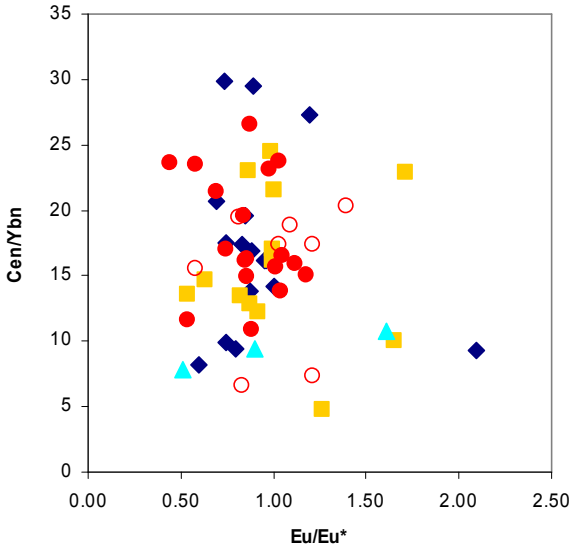

Fig.6.25 Eu anomaly

Minerals

Mineral compositions were analysed for the principal phases crystallized in the groundmass, and for the accessory minerals.

- Leucite composition is quasi-stechiometric: silica ranges between 55.5 wt% and 54.6 wt%, regularly decreasing toward the top of the sequence; alumina content ranges between 23.8-24 wt%, and K_2O content shows a little increase from the base (18.8 wt%) to the top of the sequence (20.2 wt%). Some large crystals have a rim of 10 μm, which shows little variation of the silica and iron content (Appendix 2, Tab. 4A, 5A).

- Plagioclase composition records little variations in the melt during the different phases of the eruption. From the base to the top of the succession a decrease in Ca content occurs, passing from terms with An_{58-73}-Ab_{24-34}-Or_{1-10} in bed 2, to An_{51-74}-Ab_{23-40}-Or_{3-16} in bed 5. Plagioclase in sample EP4 (bed 4) are An_{41-74}-Ab_{24-42}-Or_{3-18} in composition, showing the largest compositional range in term of Ca content (Appendix 2, Tab. 6A, 7A, 8A, 9A).

- Clinopyroxene is a Diopside with $En_{22-35}Wo_{49-54}Fe_{14-26}$. The different growth zones correspond to variation of TiO_2, Al_2O_3, FeO and CaO contents. Microlites < 20 μm are also zoned, with more Fe-rich rims (Appendix 2, Tab. 11A, 12A, 13A).

Ca-Amphibole (from Edenite to Fe-Edenite, to Fe-Pargasite to Pargasite), Fl-Apatite, Scapolite and Cancrinite crystallize as accessory minerals, forming laths < 10 μm in size (Appendix 2, Tab. 14A).

Glass composition and groundmass texture

Chemical variations of the matrix glass in the analysed ashes is well correlated with groundmass texture. In detail, moderately vesicular and glassy fragments show small variations of the major elements contents, recording the same degree of crystallization (35-55 vol%). Dense, crystal-rich clasts represent a more advanced state of crystallization, where microlites form a tight network that prevents the movement and re-homogenization of the melt, and promote strong local compositional differences. Thus, glass of DCR fragments would be the result of confined (at micrometer scale) conditions of crystallization, controlled by local enrichment-depletion of elements that are included/discharged by adjacent precipitating minerals. The variations of trace elements concentrations in glasses of MVG and PVG clasts, on the other hand, reflect the differences of the 25-30% of crystal contents between fragments of the same type. The crystal content and (local or not) crystallization-related compositional changes have a large effect on the physical properties that control eruptive style. Indeed, increase of the crystal content results in an increase of the viscosity of the magma, which affect the fragmentation processes (Cashman et al., 2000).

6.5 Crystal Size Distribution (CSD)

Five clasts were selected from different stratigraphic levels for quantitative observations of the groundmass. Due to the large variability of clast types, we preferred to analyse only MVG clasts, which represent the most abundant type in all the studied samples, and so they represent the majority of the erupted magma.

Leucite, Plagioclase and Pyroxene were considered for this textural study, yielding the CSD plots shown in Fig. 6.26, 6.27, 6.28. Tab. 6.6 summarizes the main 2D and 3D textural data.

		Bed 5 (EP2)	Bed 4 (EP4)	Bed 3 (EP5)	Bed 2 (top) (EP6)	Bed 2 (base) (EP8)
	Total Area (mm2)	1.28	1.64	1.57	1.43	1.94
	Bubbles vol%	43%	39%	46%	32%	45%
Leucite	φ	63%	22%	30%	28%	29%
	aspect ratio	1:1:1	1:1:1	1:1:1	1:1:1	1:1:1
	3Gτ (1) micron	120	60.3	79.5	85.8	109
	3Gτ (2) micron	51	_	31.1	31	40.9
	3Gτt (3) micron	11	11	9	9	10
	N_A (n/mm^2)	1.40E+03	3.04E+03	9.90E+02	7.21E+02	1.07E+03
	n°(1) mm^{-4}	8.56E+04	9.93E+05	4.29E+05	2.67E+05	9.34E+04
	n°(2) mm^{-4}	1.63E+06	_	8.42E+06	7.54E+06	5.29E+06
	n°(3) mm^{-4}	1.81E+08	1.59E+08	2.68E+08	2.04E+08	1.32E+08
Plagioclase	φ	4%	2%	3%	5%	5%
	aspect ratio	1:6:6	1:6:8	1:7:8	1:6:6	1:5:6
	3Gτ (1) micron	_	68	_	_	_
	3Gτ (2) micron	24	27	32	24	26
	N_A (n/mm^2)	1.59E+03	6.18E+02	9.56E+02	1.61E+03	1.11E+03
	n°(1) mm^{-4}	2.05E+07	4.42E+05	3.83E+07	6.51E+07	5.71E+07
	n°(2) mm^{-4}		3.33E+07	_	_	_
Pyroxene	φ	11%	5%	7%	10%	3%
	aspect ratio	1:3:3	1:3:3	1:2:4	1:2:3	1:2:3
	3Gτ (1)	_		87	144	92
	3Gτ (2)	98	49	24.4	64.5	38
	3Gτ (3)	19.7	11.43	11.1	18.5	14.5
	N_A (n/mm^2)	1.17E+03	1.22E+03	1.67E+03	1.62E+03	1.68E+03
	n°(1) mm^{-4}	_		7.06E+05	9.76E+04	1.60E+05
	n°(2) mm^{-4}	1.32E+05	1.92E+06	7.36E+07	2.11E+06	6.99E+06
	n°(3) mm^{-4}	5.57E+07	2.75E+08	7.13E+08	2.32E+08	3.19E+08

Tab. 6.6 Leucite, Plagioclase and Pyroxene parameters derived from the crystals size distributions analyses. Φ= fraction of microlites (vol%), G = Average growth rate (mm/sec); τ = time for crystals growth (sec); 3Gτ = crystals average dominant size (Cashman 1992); N_A= number of microlites per unit area (mm^{-2}); n° = nuclei number density (mm^{-4}).

- LEUCITE - CSD plots of leucite crystals are very similar in all the analysed samples. They are characterized by exponential trends, differing only for the maximum crystal size, that increase toward the top of the succession (Fig. 6.26). The pronounced upward concavity in the CSD suggests a multistage CSD history (Marsh 1998). Crystals may have been added to ascending magma from other local crystallization regimes or may reflect a long and varied, but continuous and batch-like, evolution for the ascending magma where changing thermal regimes induce different nucleation regimes. In the former instance, the CSD may be piecewise continuous, being a collection of linear CSD, and in the latter, the CSD may show continuous curvature. In our case, three straight lines well fit with the CSD curves, indicating the first interpretation as the most probable. These three linear CSD could thus reflect a deep cumulate phase (largest crystal size), nucleation during continued ascent, and finally strong nucleation attending eruption (smallest crystal size).

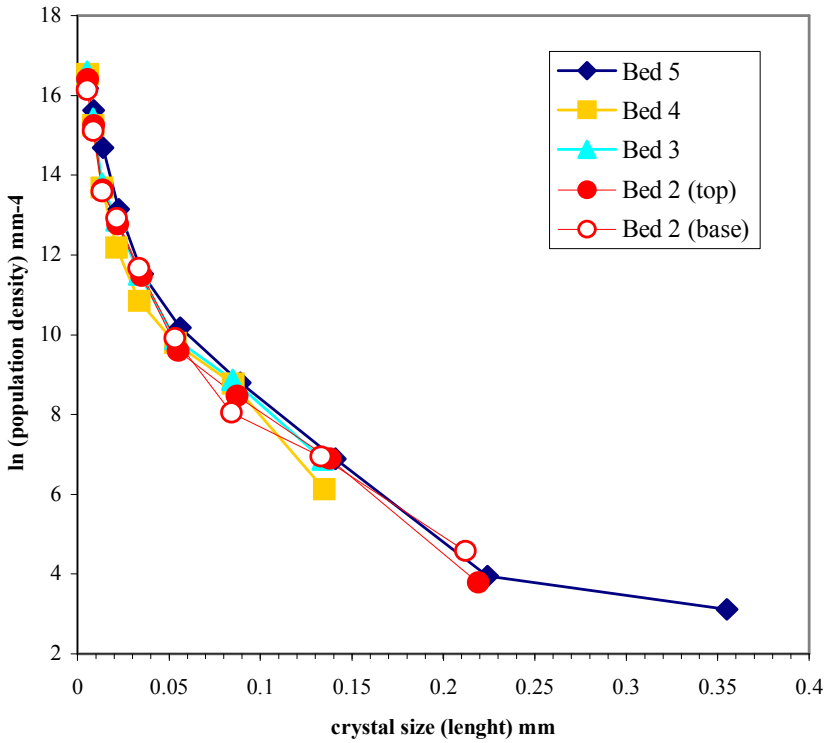

Fig.6.26 CSD plots of Leucite crystals.

- PLAGIOCLASE - Conversion from 2D to 3D data (Higgins 1994) suggests a microphenocryst tablet shape, with a quite invariant aspect ratio from 1:5:6 to 1:7:8. Crystal size distributions of samples from the lower part (bed 2 and bed 3) of the succession are well described by a linear segment for the 10 – 100 μm population (Fig. 6.27). Bed 5 and bed 4 show a second, less steep segment for crystal sizes larger than 100 μm (Fig. 6.27). CSD plots show a clear shift from a single crystal population at the base ($3G\tau$ = 26-32 μm; n° = 3.8-6.5x10^7 mm^{-4}) to a double population at the top. The smallest size population in bed 4 is characterised by a $3G\tau$ of 27 μm and an intercept of 3.3x10^7 mm^{-4}, and by an average dominant size of the largest population of 68 μm and an intercept of 4x10^5 mm^{-4}. This suggests the occurrence of at least two events of crystal nucleation (Marsh, 1988). This change in CSD is not associated with an increase of the crystal content (vol %) nor with a large variation of the N_A, that slightly decreases from 1.1x10^3 mm^{-2} in bed 2(base) to 6.2x10^2 mm^{-2} in bed 4 (Tab. 6.6).

From bed 4 (sample EP4) to bed 5 (sample EP2) a further growth of crystals occurs. CSD plot of EP2 shows a first size population characterised by an average maximum size of 130 μm and intercept of 5x10^4 mm^{-1}, and a second population with $3G\tau$ = 29 μm and n° = 3x10^7 mm^{-4}, identical to the smaller population of EP4. In this sample an abrupt increase in the plagioclase crystal content occurs, from 2-5 vol % at the base, to 16 vol % at the top.

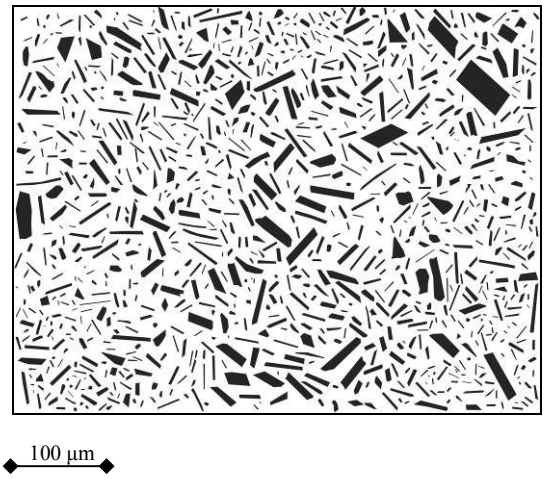

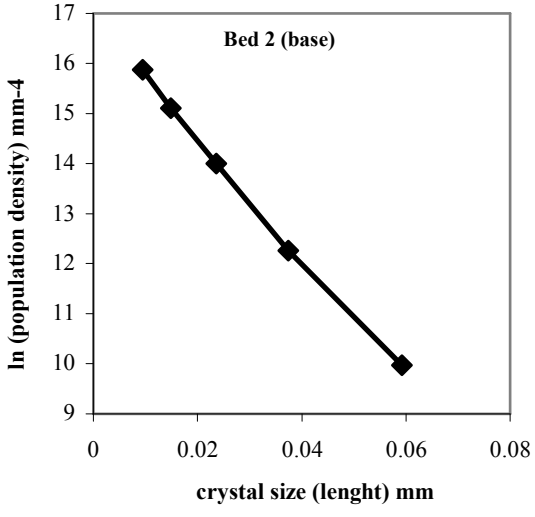

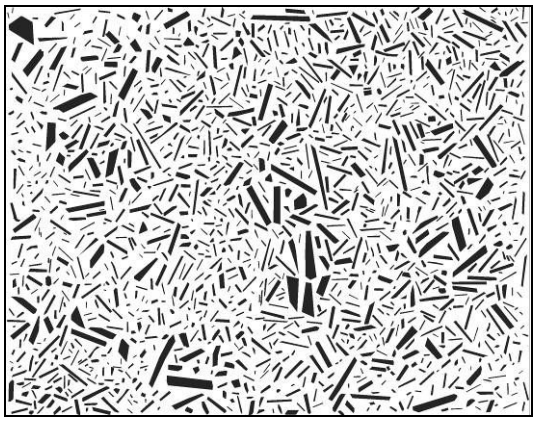

100 µm

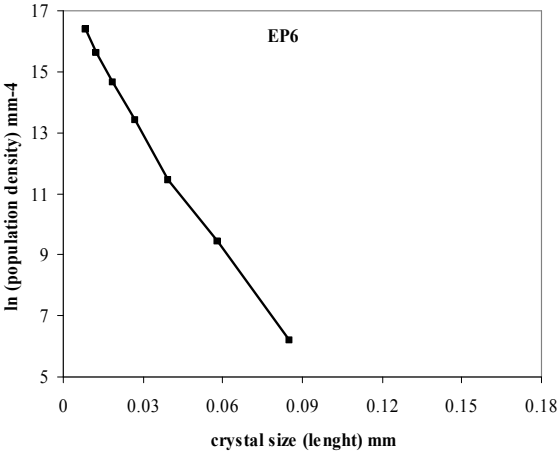

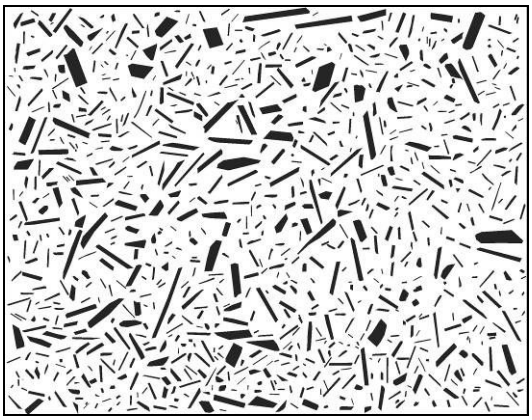

100 µm

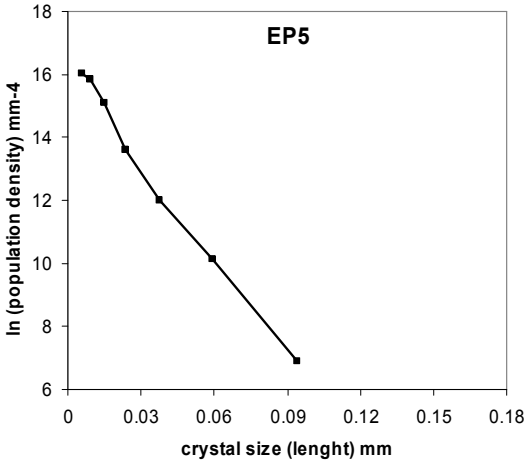

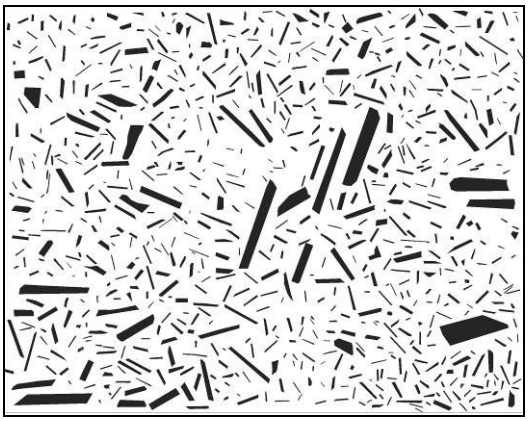

100 µm

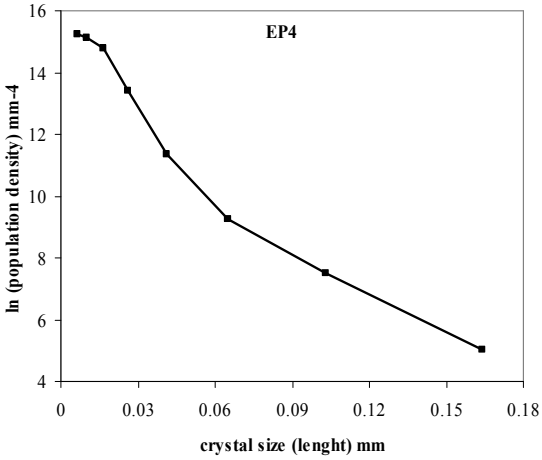

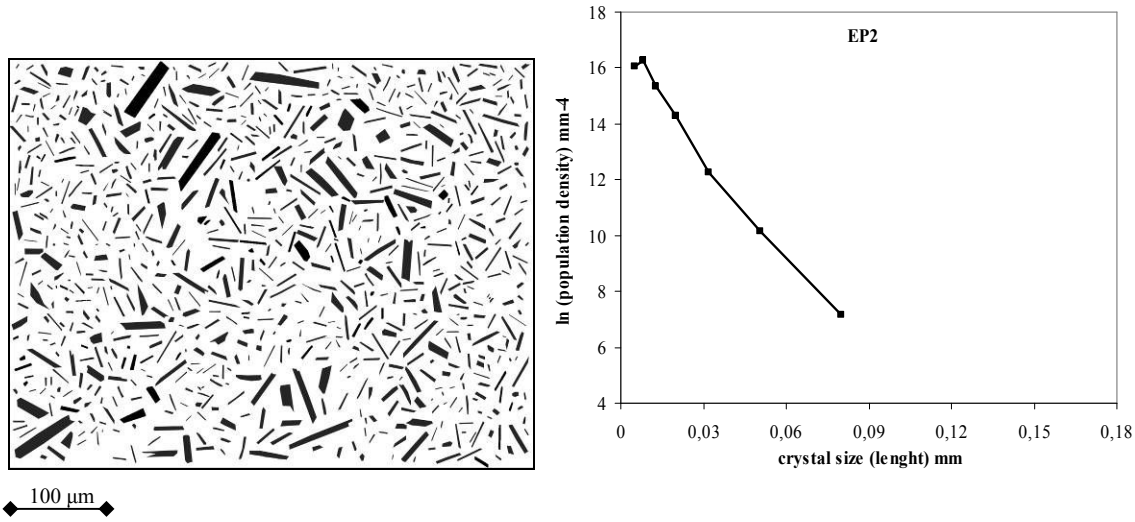

Fig.6.27 Analyzed microlites and CSD plots of Plagioclase crystals in samples EP8, EP6, EP5, EP4 and EP2.

- PYROXENE - The CSD plots of pyroxene crystals, from bed 2 to bed 5, show complex, not linear CSD trends (Fig. 6.28), that fit well (with R^2 =0.99±0.004) with a CSD with a continuous curvature. This CSD may reflect a long and varied, but continuous and batch-like, evolution for the ascending magma where changing thermal regimes induce different nucleation (and possibly growth) regimes (Marsh, 1998). Such conditions also changed during the eruption, and each sample shows a different curvature of the CSD plot. From the base to the top of bed 2, an increase of the nucleation and growth rates is observed, associated to an increase of the maximum size of the crystals and of the crystal content (from 3 to 10 vol%). CSD plot of bed 3 recorded only a decrease of the maximum crystal size. The CSD of bed 4 is characterized by a trend, in which a continuous decrease of the nucleation and crystal growth rates, associated with a decreasing of the maximum crystals size and of the crystal content (Tab. 6.6) occurred. The products of the followed explosion, that emplaced bed 5, show a CSD plot characterized by the increase of the nucleation and growth rate, together with an increase of the maximum crystal size and of the crystal content (11 vol%).

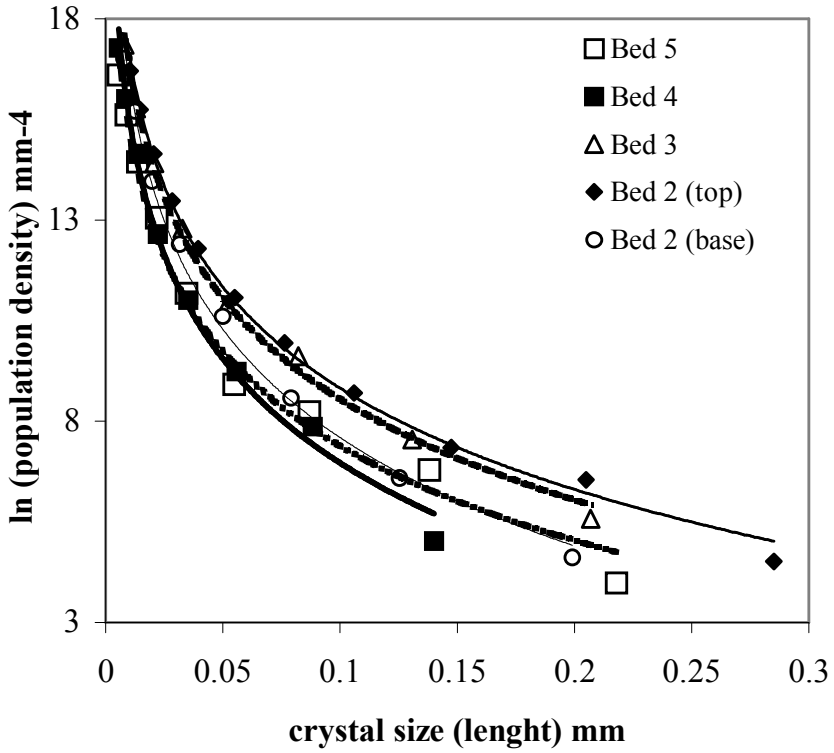

Fig.6.28 CSD plots of Pyroxene crystals in all the analysed samples.

7. DISCUSSION

The AS1a eruption is characterized by the generation of a fallout sequence, in which periods of continuous or pulsating ash emission are alternated with violent strombolian events. During these phases of the eruptions, ejected products are essentially characterized by juvenile material, and show a large variability of their morphological, textural and compositional features. Description and classification of this variability have been performed in order to get information about eruption dynamics and evolution. Results are discussed in terms of: 1) fragmentation processes; 2) eruption dynamics and the role of syn-eruptive crystallization during magma ascent.

Fragmentation processes

Investigations of external morphology and textural features of juvenile fragments give useful indications to the understanding of fragmentation process. These studies have evidenced that different types of fragments coexist in a same stratigraphic level, though with different relative abundance. In particular, fragments with blocky shape are the most abundant component of the ash-rich layers (bed 2, bed 3, Fig. 7.1), while the lapilli-rich layers are largely represented of spongy or fused fragments (bed 4, Fig. 7.1).

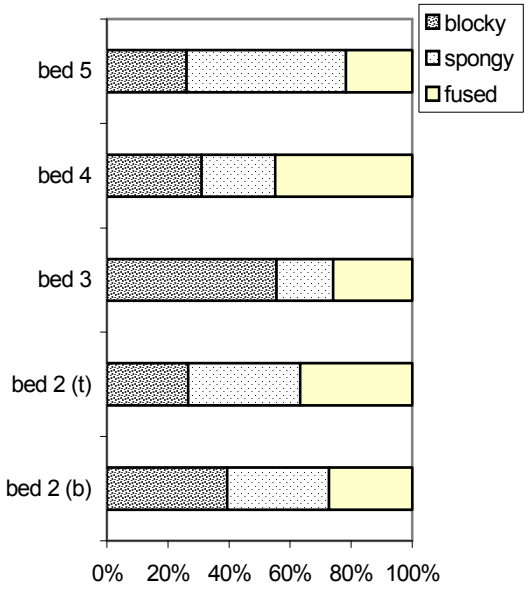

Fig.7.1 Variation of component proportions (external morphology of the particles, %) in the different beds of AS1a Unit.

These features are also peculiar to other ash-dominated eruptions, as shown for example in the case of the 2001 eruption of Mt Etna (Taddeucci et al., 2004), and in the 1994-1997 ash emission activity at Popocatepetl volcano (Mexico) (Martin-Del Pozzo et al., 2007)..

In AS1a eruption, blocky fragments are characterized by low vesicular (15-35 vol%) and highly crystallized (DCR clasts) or glassy (PVG clasts) textures. Conversely, spongy and fused fragments generally show moderately vesicular (35-55 vol%), glassy (MVG) groundmass, and this type of fragments is often characterized by the presence of inclusions of highly crystallized material (DCR fragments). The vesicularity range shown by all the fragments is in agreement with a magmatic fragmentation of low vesicular (< 60%) material by rapid decompression (Cashman at al., 2000). This model was designed to describe volcanic blasts, where the depressurization front is predicted to move downward in the magma, at the sound speed of the magma (from a few to a several tens of meters per second, depending on the physical state of magma mixture). This is supported also by the abundance of very angular fragments (VA) with uneven, irregular external shape, suggestive of fragmentation driven by bubbles explosion.

However, the contemporary occurrence of clasts with different features, and the general abundance of ash in the erupted material (practically more than 95 wt % of the total), imply that fragmentation possibly occurred in a system with a complex distribution of its physical features.

In recent works, the mechanism of fragmentation responsible of ash generations has been investigated, essentially based on experimental data (Zimanowsky, 2003; Taddeucci et al., 2004). This problem was approached from the point of view of the efficiency of conversion of thermal energy into mechanical energy, and of the decompression rate of the magma at the fragmentation surface. Results show that large surface area created by fine fragmentation increases the efficiency and the kinetic of conversion of magma thermal energy into mechanical energy, resulting in high energy explosions Zimanowsky et al. (2003). For viscous, microlite-rich magma, this process has been associated with a fragmentation in a brittle regime, caused by excess strain that exceeds the elastic properties of the viscous magma at fragmentation. In addition, experiments on basalts of Mt Etna evidenced that the fragmentation threshold is inversely proportional to the porosity (Taddeucci et al., 2004), the same behaviour described for products of different texture and composition by Spieler et al. (2004). This implies that the overall resistance of the more

crystalline magma to the inner pressure is related to its porosity and, in particular, to that of its most porous zones. When the pressure differential overcomes the fragmentation threshold of the most porous parts of the more viscous, highly crystallized magma, each of these parts fragments to a degree directly proportional to the local porosity (Spieler et al., 2004a). An implication of the inverse correlation between fragmentation threshold and porosity is that the ΔP needed for magma rupture is nearly the same for vesicularity higher than 20 vol% (and in the order of 2 to 5 MPa).

Such conditions may occur when in a narrow conduit, partially filled by a degassed crystallized magma, gas pressure is increased by the arrival of fresh, gas-charged magma, creating a pressure differential able to fragment material with a large variability of vesicle content. This is supported by the occurrence of blocky ash morphology, not controlled by surface tension, indicating that brittle fragmentation dominated during the ash-emission events, when the relative proportions of newly arrived, gas-charged, fluid magma was low respect to resident, partially degassed, low to mid-vesicularity, rigid magma. Spongy and fused fragments, dominant during violent strombolian events, result on the contrary, from fragmentation in a ductile regime, in which the expansion of gas bubbles within a poor crystalline magma is responsible of the fragmentation. After fragmentation, modification of the fused fragments are suggestive of the still ductile state of the magma.

Role of syn-eruptive crystallization during magma ascent

Crystal size distributions analysis was performed on MVG fragments, generally characterized also by a spongy or fused morphology. For this reason, the interpretation of the obtained results refers to the portion of fresh magma involved in each explosion.

Interpretation of crystal size distributions commonly extensively relies on the CSD theory described in Marsh (1988), Cashman and Marsh (1988), Marsh (1998) and Higgins (2000). This theory allows to define quantitatively, under given conditions, crystallization parameters such as growth and nucleation rates, or times of crystal growth from plots of crystal size vs. natural logarithm of crystal number per unit size.

The different samples of AS1a eruption analyzed for CSD show slight variations of the crystal size distributions, yet all were produced during a single, relatively short eruption. The challenge is to describe the petrological processes which governed the formation of

these materials. Two processes are likely to have generated the petrographycal diversity of AS1a material: (1) simple crystal nucleation and growth, and 2) the occurrence of more than one event of nucleation (Fig. 7.2). These processes can be observed texturally (Higgins, 2000).

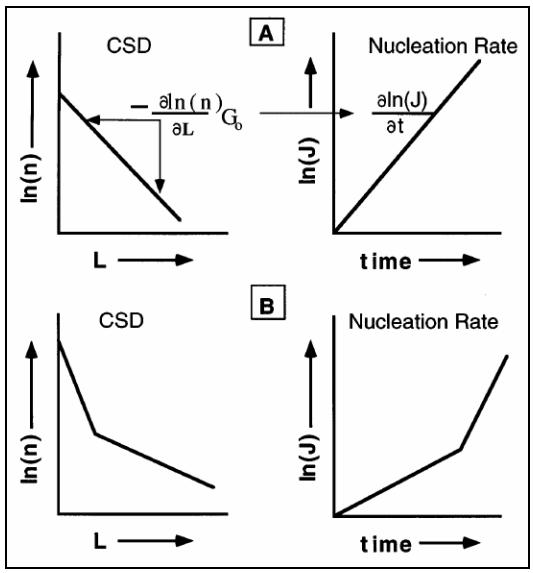

Fig.7.2 The relation of the CSD slope to the time variation in nucleation rate. The upper set describes a single exponential nucleation event and the lower, kinked CSD, reflects a sequence of two nucleation events (from Marsh, 1998).

1) Simple crystal nucleation and growth

Nucleation and growth rates of crystals are controlled by the magnitude of the crystallization driving force, which can be expressed thermally as undercooling or chemically as saturation. Changes in intensive parameters, like temperature and pressure, concur to change the value of the crystallisation driving force. Simple, instantaneous nucleation and subsequent growth of crystals is probably not common. The model elaborated by Marsh (1988) describes the crystal population in a magma chamber that is continuously fed with new magma and drained by eruptions. The CSD in such a magma chamber is characterized by a straight line with negative slope on a graph of ln (population density) versus length. The slope of the CSD curve can generally be equated with −1/ (growth rate*typical crystal residence time) and the intercept is the nucleation density (number of crystal nuclei per unit of volume per unit of length). For constant conditions,

there will only be one CSD. For a similar growth rate, a longer residence time will favour the growth of larger crystals; therefore, it will produce a change in the CSD slope but with the same intercept (Higgins, 2000). A change in the growth rate will produce the same effect. If the crystal growth rate can be established, then residence times can be calculated (Higgins, 1996).

CSD plots of beds 2 (base), 2 (top) , 3 and 5 (samples EP8, EP6, EP5 and EP2) are characterized by single straight lines with slightly different slopes (Fig. 7.3) In particular, from bed 2 (top) to bed 3 we observe a decreasing of the slope associated with an increase of the maximum crystal size, interpreted as a protracted crystallization (increasing of the residence time) of the related magma. As the investigated material is representative of the gas-rich, crystal-poor "fresh magma" driving the explosions (MVG clasts), the slope of the CSD plot can be interpreted as a proxy for the duration of the intervals of time between each explosions. A large range of growth rates for plagioclase is proposed for acid magma. Fenn (1977) measured a growth rate of 10^{-8} mm $s^{-}1$ in feldspar liquids, similar or slightly higher than existing data for dacitic magmas (Cashman and Blundy 2000). Hammer et al. (1999) calculated a growth rate in dacitic magma of 1991 eruption Pinatubo (Philippine) of about 10^{-7} mm s^{-1}. Assuming that plagioclase in AS1a grew at depth in the magma chamber/conduit at a growth rate of 10^{-8}-10^{-7} mm $s^{-}1$, we find that each arrival of fresh magma occurred at intervals of 1-10 days.

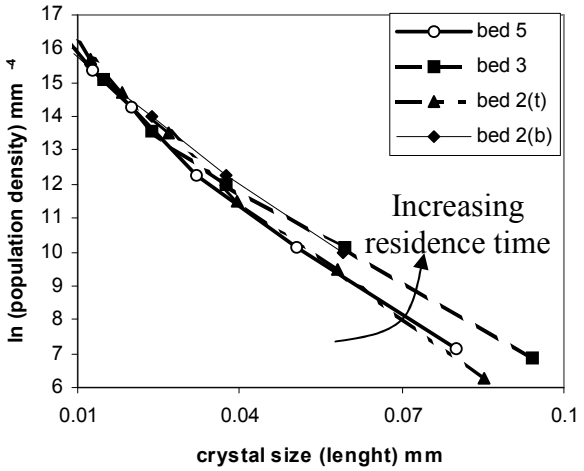

Fig.7.3 CSD plots of MVG fragments from beds 2 (base), 2(top), 3 and 5. We observe a general increase of the CSD slope at a constant nucleation density (intercept of the CSD curve), interpreted as an increase of the residence time under crystallization conditions

2) Occurrence of more than one event of nucleation

The CSD plot of bed 4 (sample EP4) is characterized by a distinct break in slope, marking a different growth history for microlites of small size (L<65 μm) respect to larger size microlites (65<L<164 μm) (Fig. 7.4): Each size range is represented by a straight-line fit, and the CSD is fully defined by two different slopes and intercepts (see chapter 6, Tab. 6.6). The maximum crystal size, estimated from the average of the four largest L values of each CSD is a direct measure of the system age or residence time (Marsh, 1998); results give a residence time of 26 days.

CSD plot of bed 4 is so suggestive of two different events of nucleation (Fig. 7.2), possibly related to a sudden change of nucleation rate. The variation of the rates of nucleation and growth are correlated with the undercooling of the system. In general, highest undercooling is needed for promoting an increase of nucleation respect to the simple coarsening of the crystals. This reflect also in a change of the microlites morphology, from large, faceted crystals to elongated, tabular crystals (Hammer 2002), as we observe passing from the products of beds 2 and 3 to bed 4 (Tab. 6.6, chapter 6). Violent strombolian events (here represented by Bed 4) were so preceded by different conditions of crystallization (and possibly degassing) with respect to the ash-dominated phases of the eruption.

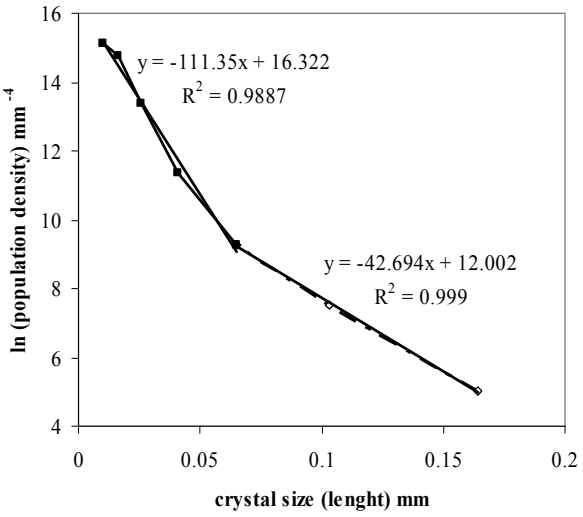

Fig.7.4 CSD plot of MVG fragments from Bed 4. CSD is characterized by two segments.

Eruption dynamics

All the data discussed above can be reconciled in a proposed model for an AS1a-type eruption. Crystal-poor, vesicle-rich, glassy fragments showing similar textural features are always present (at different concentrations) in all the analysed samples, indicating that the different phases of AS1a eruption were driven by primary fragmentation of gas-rich magma by explosion of internal gas bubbles. The kinetic of nucleation and growth of plagioclase suggests that the ejected magma experienced a similar decompression history and undercooling rate during each explosion. These features, together with the pulsating character of this eruption, are in agreement with the rising of a crystal-poor, gas-rich magma from a shallow reservoir. The interval between each arrival is estimated around 1-10 days for the stratified ash layers, possibly produced by several explosions of this type, occurring at shorter time intervals.

The dense, crystal-rich, blocky fragments, abundant in this type of deposits, could represent those portions of the magma remained in the conduit after the preceding explosions, which continued to degas increasing their crystallinity. When fresh magma raised along this partially filled, narrow conduit, this highly viscous magma was passively fragmented at a same overpressure than vesicle-rich magma. In this case, being this crystal-rich material passively fragmented by “fresh”, newly arrived magma, only the fine-grained portions of this material were transported in the ascending magma mixture. Coarse material was possibly recycled inside the crater.

The strombolian events, characterized by discrete, coarsest beds with respect to the ash layers, should be correlated with the arrival of a larger volume of gas-rich, “fresh” magma, as also indicated by the lower relative proportions of crystal-rich fragments derived from degassed magma still resident in the conduit.

8. CONCLUSIONS

The proposed methodology of physical and compositional fingerprinting of ash particles and related deposits includes a set of parameters that can be used as a collective, unequivocal descriptor of the juvenile material. The acquisition of the whole spectrum of information (external morphology, particle outline, groundmass texture, glass composition) has revealed very useful to deriving information about the dynamics of magma ascent, fragmentation, transport and depositional processes, and the timing of the eruptions. The methodology adopted for the study of ash fragments, partially developed during this work, represents an important tool for investigating different aspects associated with tephra studies, from physical volcanology to tephrostratigraphy.

In particular, for the studied eruptions, AP3 and AS1a, considered as end-members of the whole spectrum of variability of ash emission activity at Vesuvius, the following conclusions were reached as a result of this study:

1. Both eruptions were produced during discontinuous, explosive events (pulsating activity).
2. Fragments of gas-rich, crystal-poor, juvenile magma, represented by spongy and fused clasts with moderate to high vesicularity and glassy groundmass, are always presents, indicating that, in both the eruptions, the fragmentation process was mainly driven by magmatic explosivity.
3. The discontinuous arrivals, from a shallow reservoir, of the fresh, gas-charged, magma, provided the necessary energy to the explosive fragmentation of the system.
4. The denser, more crystallized, moderately to low vesicularity, degassed magma, filling the conduit, was passively fragmented and transported into the atmosphere by streaming of gas mainly derived from the newly arrived magma.
5. The interaction of magma with external water, (phreatomagmatic eruptions), occurred only during the AP3 eruption. This process acted to increase (and not to trigger) the explosive fragmentation of the magma, due to its the vaporization.

6. During the violent strombolian phases which characterized both the types of eruptions, a larger volume of gas-rich magma was involved in the eruptions, generating coarser-grained products and discrete depositional beds.
7. Each batch of magma experienced a similar degree of syn- or intra-eruptive volatile loss, indicating that magma in the conduit consistently equilibrated.
8. Observed groundmass crystallization was probably primarily a response to volatile loss rather than cooling of magma in the conduit.
9. Groundmass crystallization accompanied the course of the eruptions, and possibly occurred in a shallow reservoir or in the conduit system. The intervals between each explosion were estimated, on the basis of microlite growth, in the order of 1-10 days.
10. The relative long lasting of these ash emission eruptions pose important implications for the hazard mitigation and the emergency plans.

The methodological results presented in this work can also be useful for tephrostratigraphic purposes. In general, ash fragments were studied trying to associate the external features with the internal texture and geochemistry of single fragments. To date, correlations between proximal and distal tephra beds in tephrostratigraphic studies mainly rely on the comparison (sometimes poorly representative on a statistical basis) of the composition of a distal tephra bed with the existing dataset of selected possible sources. This can reveal an important pitfall, because the detailed study of randomly selected juvenile fragments also from single beds of a pyroclastic deposit has highlighted the large variability in terms of clast shape, external surface, groundmass texture and composition (Cioni et al., 2007). This variability is strongly present in small-scale, sub plinian to violent strombolian to ash-dominated eruptions, which often lack a largely predominant type of juvenile material, in terms of physical and compositional features, and all the different types of fragments are unevenly distributed along the succession of the deposits. The presence of different types of juvenile fragments in a tephra bed introduces an inherent uncertainty when correlations are only based on glass composition of not clearly identified juvenile fragments. Conversely, this variability represents an additional feature to be used for a more in-depth characterization of the tephra bed and, if opportunely described and

quantified, can represent a decisive clue for the correct identification and correlation of the tephra bed.

Appendix 1:

Measured parameters (mean and standard deviation) of each analysed particle for AS1a eruption: Rectangularity, Compactness, Elongation, Circularity, Vesicularity (%), crystal content (%), particle outline, external morphology, groundmass texture.

SAMPLE	Rect.	Compact.	Elong.	Circ.	%ves.	%crs
EP2_1	0.938	0.776	1.720	1.205	15	60
EP2_2	0.983	0.731	2.059	1.301	40	68
EP2_3	0.981	0.766	1.830	1.267	30	69
EP2_4	0.930	0.688	1.906	1.265	49	46
EP2_5	0.956	0.661	1.706	1.329	42	61
EP2_6	0.961	0.652	2.061	1.345	36	85
EP2_7	1.068	0.613	2.084	1.548	45	81
EP2_8	1.059	0.727	1.811	1.408	51	74
EP2_9	0.995	0.679	2.274	1.368	46	58
EP2_10	0.937	0.613	2.402	1.364	/	/
EP2_11	0.998	0.594	2.185	1.466	/	/
EP2_12	1.147	0.597	2.171	1.682	39	64
EP2_13	0.965	0.610	2.231	1.400	44	69
EP2_14	0.977	0.679	1.865	1.345	17	95
EP2_15	0.910	0.656	1.874	1.274	23	95
EP2_16	0.940	0.662	1.958	1.316	24	87
EP2_17	1.056	0.605	2.333	1.552	48	49
EP2_18	0.954	0.640	2.137	1.346	18	65
EP2_19	1.079	0.525	2.297	1.681	53	33
EP2_20	0.920	0.655	2.114	1.296	43	61
EP2_21	1.023	0.550	2.701	1.559	41	59
EP2_22	0.936	0.676	2.349	1.290	26	95
EP2_23	0.971	0.575	2.064	1.450	41	61
EP2_24	1.067	0.721	1.726	1.419	70	69
mean	0.990	0.652	2.078	1.395	38	68
st. dev.	0.061	0.064	0.248	0.129	14	16

SAMPLE	Rect.	Compact.	Elong.	Circ.	%ves.	%crs
EP4_1	0.883	0.598	2.063	1.290		
EP4_2	1.009	0.699	1.980	1.376	41	67
EP4_3	0.984	0.667	1.808	1.360	29	95
EP4_4	1.117	0.652	2.254	1.561	45	64
EP4_5	0.973	0.682	2.227	1.337	29	61
EP4_10	1.017	0.646	2.076	1.433	48	71
EP4_11	0.938	0.647	1.843	1.321	55	83
EP4_12	0.892	0.682	1.754	1.220	31	47
EP4_13	1.001	0.670	2.071	1.382	52	57
EP4_14	0.966	0.710	1.956	1.310	28	95
EP4_15	0.999	0.650	2.515	1.406	43	95
EP4_16	0.873	0.738	1.787	1.149	19	54
EP4_17	1.104	0.606	2.127	1.607	44	69
EP4_18	0.922	0.707	1.840	1.238	40	68
EP4_19	0.980	0.557	2.593	1.497	/	/
EP4_20	0.987	0.711	1.711	1.321	19	95
EP4_21	0.896	0.673	1.745	1.234	36	95
EP4_22	0.919	0.750	1.561	1.198	35	95
EP4_23	1.171	0.723	2.119	1.557	31	65
EP4_24	0.976	0.545	3.281	1.525	27	56
EP4_25	0.907	0.666	2.443	1.285	23	95
EP4_26	0.919	0.582	2.620	1.363	37	84
EP4_27	1.108	0.612	2.346	1.604	23	63
EP4_28	1.035	0.634	2.422	1.469	41	70
EP4_29	1.172	0.717	2.059	1.569	/	/
EP4_30	0.947	0.612	2.260	1.383	49	59
EP4_31	0.988	0.629	2.396	1.421	30	45
EP4_32	0.948	0.605	2.023	1.382	48	68
EP4_33	1.085	0.593	2.041	1.597	58	90
mean	0.990	0.654	2.135	1.393	37	73
st. dev.	0.083	0.054	0.355	0.131	11	17

SAMPLE	Rect.	Compact.	Elong.	Circ.	%ves.	%crs
EP5_1	1.016	0.574	2.531	1.516	31	70
EP5_2	1.052	0.747	2.016	1.374	36	95
EP5_3	1.054	0.705	1.912	1.419	35	95
EP5_4	0.894	0.689	1.759	1.216	23	79
EP5_5	1.020	0.611	2.139	1.474	/	/
EP5_6	0.889	0.674	1.633	1.223	16	95
EP5_7	1.021	0.557	2.548	1.551	32	78
EP5_8	1.036	0.594	2.928	1.536	43	64
EP5_9	0.881	0.701	1.727	1.192	16	95
EP5_10	0.861	0.624	1.796	1.233	/	/
EP5_11	0.974	0.657	2.092	1.370	17	74
EP5_12	0.956	0.701	1.786	1.290	32	95
EP5_13	0.903	0.643	2.052	1.274	21	92
EP5_14	0.938	0.718	1.810	1.255	55	66
EP5_15	1.160	0.522	3.260	1.813	44	69
EP5_16	0.956	0.744	1.623	1.251	17	95
EP5_17	1.008	0.591	2.604	1.480	39	73
EP5_19	1.122	0.653	1.702	1.567	22	66
EP5_20	0.983	0.713	1.673	1.318	13	91
EP5_21	0.894	0.662	1.693	1.240	45	95
EP5_22	1.053	0.796	1.772	1.340	16	95
EP5_23	1.041	0.629	2.325	1.486	27	95
EP5_24	1.136	0.732	2.017	1.505	44	67
EP5_25	0.949	0.629	2.302	1.351	19	82
EP5_26	0.917	0.692	1.803	1.251	22	95
EP5_27	0.973	0.740	1.665	1.283	26	95
EP5_28	1.066	0.642	2.190	1.504	55	59
mean	1.065	0.678	2.032	1.472	30	83
st. dev.	0.059	0.037	0.296	0.096	13	13

SAMPLE	Rect.	Compact.	Elong.	Circ.	%ves.	%crs
EP6_1	0.945	0.640	1.966	1.334	18	57
EP6_2	0.895	0.651	1.717	1.253	18	75
EP6_3	0.939	0.705	2.587	1.308	30	63
EP6_4	0.922	0.693	1.814	1.251	24	87
EP6_5	0.966	0.610	1.944	1.397	27	83
EP6_6	0.904	0.698	1.640	1.222	35	58
EP6_7	0.966	0.572	2.762	1.461	13	79
EP6_8	0.991	0.629	2.987	1.477	41	78
EP6_9	0.928	0.706	2.041	1.267	34	82
EP6_10	0.962	0.703	1.980	1.296	21	57
EP6_11	0.993	0.713	2.012	1.329	47	63
EP6_12	1.032	0.712	1.795	1.382	49	66
EP6_13	0.961	0.710	1.791	1.288	39	78
EP6_14	0.997	0.653	2.329	1.412	29	74
EP6_15	0.899	0.694	1.852	1.222	48	79
EP6_16	0.980	0.649	2.126	1.378	41	66
EP6_17	0.959	0.656	2.222	1.356	40	78
EP6_18	0.990	0.622	1.847	1.417	27	82
EP6_19	1.019	0.686	2.027	1.398	30	68
EP6_20	0.929	0.687	1.646	1.266	21	62
EP6_21	0.987	0.791	1.883	1.270	19	95
EP6_22	1.129	0.616	2.350	1.625	45	68
EP6_23	0.905	0.747	1.640	1.183	32	75
EP6_24	1.026	0.541	2.193	1.574	/	/
EP6_25	0.970	0.701	1.770	1.310	34	90
EP6_26	1.005	0.674	1.861	1.387	25	81
EP6_27	1.032	0.563	2.254	1.553	41	72
EP6_28	0.978	0.559	2.378	1.484	40	59
EP6_29	0.963	0.534	2.613	1.491	26	71
EP6_30	1.035	0.762	1.605	1.338	56	54
mean	0.957	0.668	2.078	1.336	32	72
st. dev.	0.038	0.042	0.371	0.079	11	10

SAMPLE	Rect.	Compact.	Elong.	Circ.
EP8_1	0.966	0.723	1.768	1.283
EP8_2	1.071	0.669	1.871	1.485
EP8_3	1.172	0.691	1.900	1.601
EP8_4	1.077	0.699	2.361	1.493
EP8_5	0.998	0.643	1.977	1.408
EP8_6	1.167	0.638	2.521	1.677
EP8_7	1.046	0.623	2.564	1.524
EP8_9	1.088	0.708	1.734	1.462
EP8_10	1.053	0.688	1.902	1.439
EP8_11	1.030	0.625	1.975	1.474
EP8_12	1.018	0.670	2.082	1.404
EP8_13	1.102	0.721	1.610	1.465
EP8_14	1.057	0.720	2.149	1.417
EP8_15	1.018	0.638	2.262	1.439
EP8_16	1.017	0.694	1.559	1.379
EP8_17	1.046	0.697	1.759	1.414
EP8_18	1.284	0.729	1.817	1.697
EP8_19	1.097	0.664	1.962	1.521
EP8_20	1.075	0.649	2.373	1.512
EP8_21	1.009	0.673	2.326	1.421
EP8_22	1.111	0.686	2.279	1.552
EP8_23	1.177	0.599	1.829	1.718
EP8_24	1.086	0.703	2.207	1.490
EP8_25	1.004	0.639	1.638	1.418
EP8_26	0.947	0.631	1.765	1.346
EP8_27	1.053	0.666	1.896	1.460
EP8_28	1.001	0.623	2.049	1.434
EP8_30	1.179	0.653	2.076	1.648
EP8_31	1.175	0.681	1.706	1.609
EP8_32	1.116	0.692	2.082	1.527
EP8_33	0.991	0.704	1.938	1.339
EP8_34	1.108	0.678	1.941	1.522
EP8_35	1.001	0.677	2.026	1.386
mean	1.071	0.673	1.997	1.484
st. dev.	0.074	0.034	0.257	0.104

Appendix 2: Minerals compositions

Tab.2.1A EPMA- SEM compositions of Leucite in AP3 products

	VSM48		VSM51	
	Leucite 1	**Leucite 2**	**Leucite 3**	**Leucite 4**
SiO_2	56.85	56.87	56.98	56.94
Al_2O_3	23.36	23.12	23.80	23.16
FeO	0.55	0.60	0.46	0.68
Na_2O	0.58	0.50	0.00	0.00
K_2O	18.59	18.91	18.75	19.22

Tab. 2.2A EPMA-SEM compositions of phenocrystals and microlites of plagioclase in AP3 products

	VSM48				VSM51							
	Plg1 (core)	**Plg1 (rim)**	**Plg2 (pheno)**	**Plg3 (micro)**	**Plg1-1**	**Plg1-2**	**Plg2**	**Plg3**	**Plg4**	**Plg5**	**Plg6**	**Plg7**
SiO_2	45.13	56.55	45.44	55.03	51.20	51.22	55.76	56.90	51.63	52.95	50.80	54.70
Al_2O_3	35.09	26.44	34.70	28.05	30.59	30.50	26.09	23.65	30.29	29.14	31.03	27.45
FeO	0.61	1.07	0.64	0.75	0.70	00.88	1.53	2.28	0.61	0.69	0.62	1.06
CaO	17.68	8.24	17.69	9.86	13.01	12.28	8.16	7.96	12.92	11.11	13.13	9.49
Na_2O	1.28	5.10	1.16	3.77	3.44	3.54	4.80	5.19	3.47	3.76	3.29	4.49
K_2O	0.20	2.59	0.37	2.54	1.06	1.02	2.88	3.23	1.08	1.90	0.91	2.08
Si	8.34	10.27	8.40	10.00	9.36	9.40	10.25	10.52	9.43	9.70	9.30	10.02
Al	7.64	5.66	7.56	6.01	6.59	6.60	5.65	5.15	6.52	6.29	6.69	5.93
Fe(ii)	0.09	0.16	0.10	0.11	0.11	0.14	0.24	0.35	0.09	0.11	0.09	0.16
Ca	3.50	1.60	3.50	1.92	2.55	2.41	1.61	1.58	2.53	2.18	2.57	1.89
Na	0.46	1.80	0.42	1.33	1.22	1.26	1.71	1.86	1.23	1.33	1.17	1.59
K	0.05	0.60	0.09	0.59	0.25	0.24	0.68	0.76	0.25	0.44	0.21	0.49
An	87.38	40.09	87.45	50.03	63.47	61.71	40.25	37.55	63.07	55.06	65.11	47.23
Ab	11.45	44.90	10.38	34.62	30.37	32.19	42.84	44.31	30.65	33.72	29.52	40.44
Or	1.18	15.00	2.18	15.35	6.16	6.10	16.91	18.14	6.28	11.21	5.37	12.33

Tab.2.3A EPMA-SEM compositions of pyroxene in AP3 products

	VSM48		VSM51				
	Cpx1	**Cpx2**	**Cpx3**	**Cpx4**	**Cpx5**	**Cpx6**	**Cpx7**
SiO_2	45.99	42.36	46.68	48.02	43.11	45.39	47.52
TiO_2	1.15	2.42	1.08	1.31	2.28	1.64	0.84
Al_2O_3	7.18	10.88	6.89	7.00	10.62	7.71	6.45
FeO	13.00	12.98	11.43	8.04	12.82	11.51	10.49
MgO	8.91	8.12	10.17	12.70	7.97	10.11	11.02
CaO	23.39	22.75	23.44	22.68	22.74	23.18	23.35
Na_2O	0.39	0.49	0.31	0.25	0.46	0.46	0.34
Si	1.75	1.61	1.76	1.78	1.64	1.71	1.78
Ti	0.03	0.07	0.03	0.04	0.07	0.05	0.02
Al	0.32	0.49	0.31	0.31	0.48	0.34	0.29
Fe(ii)	0.41	0.41	0.36	0.25	0.41	0.36	0.33
Mg	0.50	0.46	0.57	0.70	0.45	0.57	0.62
Ca	0.95	0.93	0.95	0.90	0.93	0.94	0.94
Na	0.03	0.04	0.02	0.02	0.03	0.03	0.02
Wo	50.28	50.66	49.90	48.21	51.05	49.39	49.29
En	26.65	25.16	30.13	37.57	24.90	29.98	32.35
Fs	21.55	22.20	18.78	13.26	22.18	18.86	17.09

Tab.2.4A EPMA- SEM compositions of Leucite in samples EP6 (bed 2 top) and EP8 (bed 2 base) in AS1a products

	EP6_14			EP6_16	EP6_20		EP8_16		EP8_18	EP8_19
	lct1_core	**lct1_rim**	**lct1_rim**	**lct1**	**lct1**	**lct2**	**lct1**	**lct2**	**lct1**	**lct1**
SiO_2	54.87	55.37	54.95	54.97	55.01	54.16	55.81	55.3	55.32	55.89
Al_2O_3	24.13	23.85	24.23	23.91	23.9	23.52	23.94	24.05	23.9	24.15
FeO	0.53	0.56	0.59	0.61	0.49	0.74	0.56	0.53	0.5	0.52
Na_2O	0.59	0.56	0.68	0.55	0.57	0.72	0.73	0.69	0.62	0.73
K_2O	19.54	19.43	19.35	19.6	19.7	20.35	18.65	19.11	19.23	18.3
BaO	0.35	0.24	0.2	0.36	0.33	0.5	0.31	0.33	0.43	0.4

Tab.2.5A EPMA- SEM compositions of Leucite in samples EP2 (bed 5) in AS1a products

	EP2_9						EP2_18				EP2_19			
	lct1	**lct2**	**lct3_core**	**lct3_int**	**lct3_rim**	**lct4**	**lct1_1**	**lct1_2**	**lct2**	**lct3**	**lct1_core**	**lct1_rim**	**lct2_core**	**lct_rim**
SiO_2	55.05	54.6	54.05	54.21	54.28	54.22	55.18	55.13	54.8	54.6	54.27	54.18	54.78	55.35
Al_2O_3	23.9	24.11	23.81	23.53	23.53	23.6	23.86	23.84	23.94	23.74	23.64	23.76	24.01	23.86
FeO	0.64	0.77	0.32	0.66	1.12	0.86	0.36	1.05	0.53	0.55	0.49	0.56	1.45	3.47
Na_2O	0.24	0.28	0.26	0.31	0.75	0.33	0.37	0.52	0.46	0.42	0.98	0.75	0.71	1.67
K_2O	19.95	19.75	21.16	21.12	19.85	20.82	20	19.12	19.97	20.69	20.26	20.48	18.63	15.4
BaO	0.22	0.47	0.39	0.17	0.48	0.16	0.23	0.34	0.3	0	0.36	0.26	0.43	0.25

Tab.2.6A EPMA-SEM compositions of plagioclase in sample EP8 (bed 2 base) in AS1a products

Ash fragment	EP8_3		EP8_16		EP8_17		EP8_18		EP8_19	
	plg1	**plg2**	**plg1**	**plg2**	**plg1**	**plg2**	**plg1**	**plg2**	**plg1**	**plg2**
SiO_2	49.30	49.11	49.29	50.08	49.24	49.19	50.79	50.01	49.76	49.11
Al_2O_3	30.54	32.54	31.97	30.29	32.05	31.85	30.17	30.93	30.88	31.80
Fe_2O_3	2.15	0.94	0.89	1.84	1.16	1.16	1.42	1.24	1.28	1.00
CaO	12.51	14.03	13.94	13.10	14.09	13.80	12.32	13.39	13.48	14.00
Na_2O	3.38	2.65	2.83	3.23	2.76	2.84	3.66	3.28	3.15	2.89
K_2O	1.31	0.55	0.61	1.29	0.52	0.55	1.07	0.86	0.74	0.64
BaO	0.81	0.17	0.48	0.18	0.18	0.60	0.56	0.29	0.71	0.56
Si	2.29	2.25	2.26	2.31	2.26	2.26	2.34	2.30	2.30	2.26
Al	1.67	1.76	1.73	1.65	1.73	1.73	1.64	1.68	1.68	1.73
Fe	0.08	0.04	0.03	0.07	0.04	0.04	0.05	0.05	0.05	0.04
Ca	0.62	0.69	0.69	0.65	0.69	0.68	0.61	0.66	0.67	0.69
Na	0.30	0.24	0.25	0.29	0.25	0.25	0.33	0.29	0.28	0.26
K	0.08	0.03	0.04	0.08	0.03	0.03	0.06	0.05	0.04	0.04
Sr	0.00	0.00	0.00	0.00	0.00	0.00	0.00	0.00	0.00	0.00
Ba	0.01	0.00	0.01	0.00	0.00	0.01	0.01	0.01	0.01	0.01
An	61.97	72.02	70.45	63.96	71.51	70.43	60.94	65.80	67.19	70.03
Ab	30.30	24.62	25.88	28.54	25.35	26.23	32.76	29.17	28.41	26.16
Or	7.73	3.36	3.67	7.50	3.14	3.34	6.30	5.03	4.39	3.81

Tab.2.7A EPMA-SEM compositions of plagioclase in sample EP6 (bed 2 top) in AS1a products

Ash fragment	EP6_14			EP6_16		EP6_20		EP6_28		EP6_29		
	plg1	**plg2**	**plg3**	**plg1**	**plg2**	**plg1**	**plg2**	**plg1**	**plg2**	**plg1_1**	**plg1_2**	**plg3**
SiO_2	50.84	49.61	50.32	49.96	49.08	50.48	57.52	50.44	50.11	48.41	48.91	50.30
Al_2O_3	30.42	31.94	30.85	31.25	32.23	29.97	28.80	30.50	30.07	32.57	32.52	29.43
Fe_2O_3	1.08	0.73	1.18	1.25	0.90	1.44	2.70	1.33	2.13	0.95	0.80	2.14
CaO	12.75	13.71	12.66	13.23	14.21	12.68	12.06	12.92	12.96	14.27	14.32	12.67
Na_2O	3.79	2.93	3.55	3.24	2.95	3.40	3.66	3.51	3.30	2.64	2.78	3.42
K_2O	0.69	0.54	1.04	0.88	0.14	1.10	1.63	0.79	1.13	0.52	0.50	1.70
BaO	0.43	0.55	0.39	0.18	0.49	0.93	0.93	0.50	0.29	0.64	0.17	0.35
Si	2.33	2.28	2.31	2.29	2.25	2.33	2.47	2.32	2.32	2.23	2.24	2.33
Al	1.65	1.73	1.67	1.69	1.74	1.63	1.46	1.65	1.64	1.77	1.76	1.61
Fe	0.04	0.03	0.05	0.05	0.03	0.06	0.10	0.05	0.08	0.04	0.03	0.08
Ca	0.63	0.67	0.62	0.65	0.70	0.63	0.56	0.64	0.64	0.70	0.70	0.63
Na	0.34	0.26	0.32	0.29	0.26	0.30	0.31	0.31	0.30	0.24	0.25	0.31
K	0.04	0.03	0.06	0.05	0.01	0.06	0.09	0.05	0.07	0.03	0.03	0.10
Sr	0.00	0.00	0.00	0.00	0.00	0.00	0.00	0.00	0.00	0.00	0.00	0.00
Ba	0.01	0.01	0.01	0.00	0.01	0.02	0.02	0.01	0.01	0.01	0.00	0.01
An	62.41	69.75	62.30	65.69	72.08	62.95	58.48	63.92	63.91	72.56	71.79	60.67
Ab	33.57	26.98	31.61	29.11	27.08	30.55	32.11	31.43	29.45	24.29	25.22	29.64
Or	4.02	3.27	6.09	5.20	0.85	6.50	9.41	4.65	6.64	3.15	2.98	9.69

Tab.2.8A EPMA-SEM compositions of plagioclase in sample EP4 (bed 4) in AS1a products

Ash fragment	EP4_2										
	plg1core	**plg1 rim**	**plg3core**	**plg3 rim**	**plg2core**	**plg4 core**	**plg4 rim**	**plg5 core**	**plg5 rim**	**plg6 core**	**plg6 rim**
SiO_2	49.92	50.01	50.16	51.66	50.57	50.65	50.35	51.36	50.66	50.60	51.72
Al_2O_3	28.79	29.12	29.45	26.33	24.25	27.86	23.68	28.47	26.78	31.33	28.13
Fe_2O_3	2.65	2.36	1.88	3.38	5.84	2.95	5.85	1.97	4.05	0.96	2.09
CaO	12.25	12.50	12.96	10.86	9.61	11.79	9.75	11.83	10.38	12.92	11.75
Na_2O	3.75	3.75	3.61	4.61	4.97	4.05	5.38	4.05	4.66	3.26	4.23
K_2O	1.87	1.46	1.42	2.14	3.41	1.91	3.45	1.51	2.49	0.61	1.29
BaO	0.78	0.80	0.52	1.02	1.36	0.80	1.54	0.80	0.99	0.33	0.79
Si	2.33	2.33	2.33	2.42	2.43	2.37	2.43	2.38	2.39	2.31	2.40
Al	1.59	1.60	1.61	1.46	1.37	1.54	1.35	1.56	1.49	1.69	1.54
Fe	0.10	0.09	0.07	0.13	0.23	0.12	0.24	0.08	0.16	0.04	0.08
Ca	0.61	0.62	0.64	0.55	0.49	0.59	0.50	0.59	0.52	0.63	0.58
Na	0.34	0.34	0.32	0.42	0.46	0.37	0.50	0.36	0.43	0.29	0.38
K	0.11	0.09	0.08	0.13	0.21	0.11	0.21	0.09	0.15	0.04	0.08
Sr	0.00	0.00	0.00	0.00	0.00	0.00	0.00	0.00	0.00	0.00	0.00
Ba	0.01	0.01	0.01	0.02	0.03	0.01	0.03	0.01	0.02	0.01	0.01
An	57.61	59.45	61.18	49.93	42.40	55.11	41.32	56.45	47.66	66.10	56.11
Ab	31.92	32.28	30.84	38.35	39.68	34.26	41.26	34.97	38.72	30.18	36.55
Or	10.47	8.27	7.98	11.71	17.91	10.63	17.41	8.58	13.61	3.72	7.33

Tab.2.8A *continue*

Ash fragment	EP4_11							
	plg1 core	**plg1 rim**	**plg2 core**	**plg3core**	**plg3 rim**	**plg4 core**	**plg4 rim**	**plg5 core**
SiO_2	50.54	50.43	50.93	49.66	50.08	50.61	50.66	50.77
Al_2O_3	29.79	28.85	29.62	28.46	27.41	30.91	31.00	27.28
Fe_2O_3	1.51	2.26	1.30	3.17	3.86	0.96	0.78	3.33
CaO	12.11	12.89	12.78	11.93	11.38	12.99	13.21	10.98
Na_2O	4.04	3.73	3.69	3.80	4.06	3.47	3.31	4.50
K_2O	1.34	1.48	1.23	2.31	2.66	0.63	0.82	2.35
BaO	0.67	0.36	0.47	0.67	0.55	0.43	0.24	0.78
Si	2.34	2.34	2.35	2.33	2.36	2.32	2.32	2.38
Al	1.62	1.58	1.61	1.57	1.52	1.67	1.67	1.51
Fe	0.06	0.09	0.05	0.12	0.15	0.04	0.03	0.13
Ca	0.60	0.64	0.63	0.60	0.57	0.64	0.65	0.55
Na	0.36	0.34	0.33	0.35	0.37	0.31	0.29	0.41
K	0.08	0.09	0.07	0.14	0.16	0.04	0.05	0.14
Sr	0.00	0.00	0.00	0.00	0.00	0.00	0.00	0.00
Ba	0.01	0.01	0.01	0.01	0.01	0.01	0.00	0.01
An	57.62	60.23	61.08	55.34	51.98	64.89	65.47	50.09
Ab	34.79	31.54	31.92	31.90	33.56	31.37	29.69	37.15
Or	7.59	8.23	7.00	12.76	14.47	3.75	4.84	12.76

Tab.2.8A *continue*

Ash fragment	EP4_19						EP4_12				
	plg1 core	**plg2 core**	**plg3 core**	**plg3 rim**	**plg4 core**	**plg5 core**	**plg1 core**	**plg2 core**	**plg3 core**	**plg4 core**	**plg5 core**
SiO_2	51.15	50.11	48.51	51.01	48.73	50.06	50.20	49.54	50.65	50.57	49.10
Al_2O_3	28.75	29.51	32.62	30.35	31.95	28.85	30.32	27.68	26.94	30.67	29.47
Fe_2O_3	1.92	1.79	0.96	1.17	1.00	2.36	1.85	3.62	3.28	1.06	2.77
CaO	11.95	13.07	14.70	12.66	14.42	12.35	12.57	13.31	11.27	13.33	12.74
Na_2O	3.90	3.50	2.60	3.53	2.90	3.82	3.42	3.44	4.43	3.28	3.35
K_2O	1.54	1.18	0.49	1.02	0.56	1.71	1.22	1.53	2.22	0.76	1.91
BaO	0.78	0.84	0.11	0.26	0.45	0.85	0.42	0.88	1.21	0.34	0.66
Si	2.37	2.33	2.23	2.34	2.25	2.34	2.32	2.33	2.38	2.32	2.30
Al	1.57	1.61	1.77	1.64	1.74	1.59	1.65	1.54	1.50	1.66	1.63
Fe	0.07	0.07	0.04	0.04	0.04	0.09	0.07	0.14	0.13	0.04	0.11
Ca	0.59	0.65	0.72	0.62	0.71	0.62	0.62	0.67	0.57	0.66	0.64
Na	0.35	0.31	0.23	0.31	0.26	0.35	0.31	0.31	0.40	0.29	0.30
K	0.09	0.07	0.03	0.06	0.03	0.10	0.07	0.09	0.13	0.04	0.11
Sr	0.00	0.00	0.00	0.00	0.00	0.00	0.00	0.00	0.00	0.00	0.00
Ba	0.01	0.02	0.00	0.00	0.01	0.02	0.01	0.02	0.02	0.01	0.01
An	57.34	62.81	73.54	62.48	70.91	57.98	62.19	62.32	51.39	66.09	60.45
Ab	33.86	30.44	23.54	31.53	25.81	32.46	30.62	29.15	36.56	29.43	28.76
Or	8.80	6.75	2.92	5.99	3.28	9.56	7.19	8.53	12.05	4.49	10.79

Tab.2.8A *continue*

Ash fragment	EP4_28												
	plg1 core	**plg1 rim**	**plg2 core**	**plg2 rim**	**plg3 core**	**plg3 rim**	**plg3 rim2**	**plg5 core**	**plg5 rim**	**plg6 core**	**plg6 rim**	**plg7 core**	**plg7 rim**
SiO_2	49.80	50.61	51.17	50.46	49.19	50.08	50.83	50.53	50.70	49.97	49.93	51.72	48.21
Al_2O_3	31.69	28.61	28.43	24.67	26.00	24.07	30.32	27.16	26.58	28.25	31.14	29.57	21.23
Fe_2O_3	1.13	3.08	2.73	6.12	5.24	6.35	1.16	3.34	3.64	3.48	0.97	1.19	9.80
CaO	13.60	12.68	11.76	11.29	11.19	10.24	12.85	11.26	10.78	12.09	13.33	12.17	9.96
Na_2O	3.02	3.62	4.00	4.61	4.15	5.06	3.43	4.42	4.59	3.72	3.47	3.76	5.59
K_2O	0.77	1.40	1.90	2.84	3.11	3.14	0.87	2.29	2.70	2.04	0.82	0.78	3.56
BaO					1.12	1.05	0.55	1.01	1.00	0.45	0.34	0.82	1.66
Si	2.28	2.35	2.37	2.40	2.35	2.41	2.34	2.38	2.39	2.34	2.30	2.37	2.39
Al	1.71	1.57	1.55	1.38	1.47	1.36	1.64	1.51	1.48	1.56	1.69	1.60	1.24
Fe	0.04	0.12	0.11	0.24	0.21	0.26	0.04	0.13	0.14	0.14	0.04	0.05	0.41
Ca	0.67	0.63	0.58	0.58	0.57	0.53	0.63	0.57	0.54	0.61	0.66	0.60	0.53
Na	0.27	0.33	0.36	0.43	0.39	0.47	0.31	0.40	0.42	0.34	0.31	0.33	0.54
K	0.05	0.08	0.11	0.17	0.19	0.19	0.05	0.14	0.16	0.12	0.05	0.05	0.23
Sr	0.00	0.00	0.00	0.00	0.00	0.00	0.00	0.00	0.00	0.00	0.00	0.00	0.00
Ba	0.00	0.00	0.00	0.00	0.02	0.02	0.01	0.02	0.02	0.01	0.01	0.01	0.03
An	68.06	60.68	55.31	49.06	49.95	44.26	63.95	51.22	48.34	56.89	64.75	61.15	40.96
Ab	27.35	31.35	34.05	36.25	33.52	39.58	30.89	36.38	37.25	31.68	30.50	34.19	41.60
Or	4.59	7.98	10.64	14.69	16.53	16.16	5.16	12.40	14.42	11.43	4.74	4.67	17.43

Tab.2.9A EPMA-SEM compositions of plagioclase in sample EP2 (bed 5) in AS1a products

Ash fragment	EP2_9					EP2_18						EP2_22			
	plg1	**plg2**	**plg3**	**plg4**	**plg5**	**plg1**	**plg2**	**plg3**	**plg4_1**	**plg4_2**	**plg5**	**plg1**	**plg2**	**plg3core**	**plg3rim**
SiO_2	50.55	50.32	49.73	49.68	49.51	48.33	50.02	52.13	49.46	52.29	49.50	49.52	51.12	49.85	51.85
Al_2O_3	30.57	29.83	31.11	29.93	30.08	32.53	31.13	28.31	31.84	23.62	31.32	31.94	29.03	31.05	27.04
Fe_2O_3	1.19	2.16	1.11	2.06	1.95	0.94	1.06	1.51	1.15	5.79	0.93	0.83	1.74	1.14	2.92
CaO	12.94	12.02	13.44	13.07	13.67	14.77	13.53	11.90	14.12	10.81	14.12	14.29	11.15	13.49	11.21
Na_2O	3.40	3.73	3.04	3.42	3.02	2.50	3.08	4.28	2.74	4.57	2.96	2.83	3.50	3.11	4.78
K_2O	0.93	1.52	0.86	1.35	1.16	0.47	0.75	1.11	0.69	1.76	0.63	0.59	2.74	0.79	1.54
BaO	0.43	0.41	0.7	0.49	0.62	0.46	0.43	0.75	0	1.15	0.54	0	0.71	0.56	0.67
Si	2.32	2.33	2.29	2.31	2.30	2.23	2.30	2.40	2.27	2.48	2.28	2.27	2.37	2.30	2.41
Al	1.66	1.63	1.69	1.64	1.65	1.77	1.69	1.54	1.72	1.32	1.70	1.72	1.59	1.69	1.48
Fe	0.05	0.08	0.04	0.08	0.08	0.04	0.04	0.06	0.04	0.23	0.04	0.03	0.07	0.04	0.11
Ca	0.64	0.60	0.66	0.65	0.68	0.73	0.67	0.59	0.69	0.55	0.70	0.70	0.55	0.67	0.56
Na	0.30	0.33	0.27	0.31	0.27	0.22	0.27	0.38	0.24	0.42	0.26	0.25	0.31	0.28	0.43
K	0.05	0.09	0.05	0.08	0.07	0.03	0.04	0.07	0.04	0.11	0.04	0.03	0.16	0.05	0.09
Sr	0.00	0.00	0.00	0.00	0.00	0.00	0.00	0.00	0.00	0.00	0.00	0.00	0.00	0.00	0.00
Ba	0.01	0.01	0.01	0.01	0.01	0.01	0.01	0.01	0.00	0.02	0.01	0.00	0.01	0.01	0.01
An	64.06	58.41	67.32	62.64	66.63	74.39	67.66	56.76	70.96	51.05	69.81	71.05	53.75	67.25	51.67
Ab	30.46	32.80	27.55	29.66	26.64	22.79	27.87	36.94	24.92	39.05	26.48	25.46	30.53	28.06	39.87
Or	5.48	8.79	5.13	7.70	6.73	2.82	4.47	6.30	4.13	9.90	3.71	3.49	15.73	4.69	8.45

Tab.2.10A EPMA-SEM compositions of pyroxene in sample EP8 (bed 2 base) in AS1a products

	EP8_3					EP8_10		EP8_16				
Ash fragment	**cpx1_1**	**cpx1_2**	**cpx2_1**	**cpx2_2**	**cpx3**	**cpx1**	**cpx2**	**cpx1_1**	**cpx1_2**	**cpx2**	**cpx3 light-zone**	**cpx3 dark-zone**
SiO_2	39.37	42.34	43.97	46.48	42.44	44.49	45.78	40.86	40.09	42.63	39.87	43.63
TiO_2	2.94	2.32	1.83	1.34	2.22	1.74	1.15	2.67	2.92	1.91	2.83	1.55
Al_2O_3	13.08	9.91	9.91	8.87	9.89	9.47	9.05	12.84	12.79	10.16	13.61	9.00
FeO	12.56	12.11	12.59	11.71	14.45	9.08	8.40	12.09	12.35	12.37	12.83	12.16
MnO	0.05	0.14	0.40	0.22	0.23	0.07	0.05	0.37	0.20	0.19	0.11	0.11
MgO	7.74	9.19	7.54	9.14	7.26	10.61	11.05	7.66	7.89	8.95	7.41	9.53
CaO	23.82	23.53	22.41	21.20	22.79	24.06	24.06	22.98	23.28	23.44	22.70	23.71
Na_2O	0.44	0.45	1.34	1.04	0.72	0.49	0.45	0.52	0.47	0.35	0.65	0.31
Si	1.49	1.60	1.66	1.75	1.62	1.66	1.70	1.55	1.52	1.61	1.51	1.65
Ti	0.08	0.07	0.05	0.04	0.06	0.05	0.03	0.08	0.08	0.05	0.08	0.04
Al	0.58	0.44	0.44	0.39	0.45	0.42	0.40	0.57	0.57	0.45	0.61	0.40
Fe	0.40	0.38	0.40	0.37	0.46	0.28	0.26	0.38	0.39	0.39	0.41	0.38
Mn	0.00	0.00	0.01	0.01	0.01	0.00	0.00	0.01	0.01	0.01	0.00	0.00
Mg	0.44	0.52	0.43	0.51	0.41	0.59	0.61	0.43	0.45	0.51	0.42	0.54
Ca	0.97	0.95	0.91	0.85	0.93	0.96	0.96	0.93	0.95	0.95	0.92	0.96
Na	0.03	0.03	0.10	0.08	0.05	0.04	0.03	0.04	0.03	0.03	0.05	0.02
Wo	53.61	51.28	52.06	49.04	51.38	52.34	52.27	52.99	52.84	51.29	52.65	50.93
En	24.24	27.87	24.38	29.42	22.78	32.12	33.40	24.58	24.92	27.25	23.92	28.49
Fs	22.15	20.84	23.56	21.54	25.84	15.54	14.33	22.43	22.24	21.46	23.43	20.58

Tab.2.10A *continue*

	EP8_17				EP8_18					EP8_19					
Ash fragment	**cpx1**	**cpx2_1**	**cpx2_2**	**cpx3**	**cpx1**	**cpx2**	**cpx3_1**	**cpx3_2**	**cpx3_3**	**cpx1_core**	**cpx2**	**cpx3**	**cpx4**	**cpx3 light-zone**	**cpx3 dark-zone**
SiO_2	38.53	44.59	41.02	39.77	43.75	40.46	45.60	44.05	40.18	40.94	44.74	39.78	44.47	40.15	44.21
TiO_2	3.59	1.43	2.10	3.24	1.59	2.79	1.33	1.25	2.81	2.65	1.72	3.01	1.51	3.17	1.63
Al_2O_3	13.74	8.00	12.23	13.34	8.71	13.44	7.59	9.58	12.38	13.81	8.98	13.70	8.88	13.23	9.11
FeO	12.77	11.16	11.83	12.13	11.92	12.11	10.34	11.67	12.05	12.20	11.74	12.61	11.27	12.34	11.89
MnO	0.16	0.15	0.05	0.26	0.17	0.20	0.12	0.13	0.12	0.55	0.22	0.38	0.13	0.09	0.15
MgO	7.46	10.34	8.32	7.66	9.53	8.10	10.95	9.34	8.35	7.28	9.10	7.31	9.79	7.84	9.57
CaO	23.27	23.94	23.82	23.17	24.03	22.38	23.63	23.66	23.66	21.63	22.88	22.55	23.37	22.74	23.13
Na_2O	0.49	0.38	0.64	0.42	0.29	0.52	0.46	0.31	0.44	0.94	0.62	0.66	0.58	0.45	0.31
Si	1.46	1.68	1.55	1.51	1.65	1.53	1.71	1.66	1.52	1.55	1.69	1.51	1.67	1.52	1.67
Ti	0.10	0.04	0.06	0.09	0.05	0.08	0.04	0.04	0.08	0.08	0.05	0.09	0.04	0.09	0.05
Al	0.62	0.35	0.54	0.60	0.39	0.60	0.34	0.43	0.55	0.62	0.40	0.61	0.39	0.59	0.41
Fe	0.41	0.35	0.37	0.39	0.38	0.38	0.32	0.37	0.38	0.39	0.37	0.40	0.35	0.39	0.38
Mn	0.01	0.00	0.00	0.01	0.01	0.01	0.00	0.00	0.00	0.02	0.01	0.01	0.00	0.00	0.00
Mg	0.42	0.58	0.47	0.43	0.54	0.46	0.61	0.53	0.47	0.41	0.51	0.41	0.55	0.44	0.54
Ca	0.95	0.96	0.96	0.94	0.97	0.91	0.95	0.96	0.96	0.88	0.93	0.92	0.94	0.92	0.94
Na	0.04	0.03	0.05	0.03	0.02	0.04	0.03	0.02	0.03	0.07	0.05	0.05	0.04	0.03	0.02
Wo	53.19	50.77	53.32	53.26	51.42	51.73	50.24	51.58	52.84	51.85	50.98	52.61	50.92	52.45	50.45
En	23.73	30.51	25.92	24.50	28.38	26.05	32.40	28.34	25.95	24.28	28.22	23.73	29.69	25.17	29.05
Fs	23.07	18.72	20.76	22.24	20.20	22.21	17.36	20.08	21.22	23.87	20.80	23.66	19.39	22.38	20.50

Tab.2.11A EPMA-SEM compositions of pyroxene in sample EP6 (bed 2 top) in AS1a products

	EP6_14			EP6_16				EP6_20			EP6_28		EP6_29		
Ash fragment	**cpx1 core**	**cpx1 rim**	**cpx2**	**cpx1 light**	**cpx1 dark**	**cpx2**	**cpx3**	**cpx1 light**	**cpx1 dark**	**cpx1 light**	**cpx1**	**cpx2**	**cpx1**	**cpx2_1**	**cpx2_2**
SiO_2	43.81	38.44	43.79	38.98	45.16	42.84	39.01	39.23	41.30	46.85	39.42	43.35	43.51	40.24	37.94
TiO_2	1.75	3.56	1.66	3.54	1.43	1.82	3.51	2.97	2.74	1.32	3.25	1.84	1.83	2.74	3.90
Al_2O_3	9.06	14.06	9.34	13.63	8.27	10.33	13.77	13.07	12.08	8.86	13.48	9.48	9.13	12.86	14.45
FeO	11.86	12.93	12.20	12.36	10.62	12.19	12.62	12.83	12.28	10.89	12.12	12.33	11.98	12.22	13.18
MnO	0.10	0.09	0.18	0.14	0.22	0.20	0.08	0.07	0.49	0.91	0.19	0.17	0.22	0.10	0.13
MgO	9.42	7.26	9.22	7.48	10.17	9.11	7.55	7.43	7.82	9.25	7.84	9.38	9.65	8.09	6.95
CaO	23.59	23.21	23.13	23.34	23.67	22.93	22.82	23.91	22.59	21.04	23.23	23.06	23.17	23.32	22.93
Na_2O	0.41	0.46	0.48	0.53	0.46	0.58	0.64	0.49	0.72	0.89	0.46	0.39	0.52	0.43	0.53
Si	1.65	1.46	1.65	1.48	1.70	1.62	1.48	1.49	1.57	1.76	1.49	1.64	1.64	1.52	1.45
Ti	0.05	0.10	0.05	0.10	0.04	0.05	0.10	0.08	0.08	0.04	0.09	0.05	0.05	0.08	0.11
Al	0.40	0.63	0.42	0.61	0.37	0.46	0.62	0.59	0.54	0.39	0.60	0.42	0.41	0.57	0.65
Fe	0.37	0.41	0.39	0.39	0.33	0.38	0.40	0.41	0.39	0.34	0.38	0.39	0.38	0.39	0.42
Mn	0.00	0.00	0.01	0.00	0.01	0.01	0.00	0.00	0.02	0.03	0.01	0.01	0.01	0.00	0.00
Mg	0.53	0.41	0.52	0.42	0.57	0.51	0.43	0.42	0.44	0.52	0.44	0.53	0.54	0.46	0.39
Ca	0.95	0.95	0.94	0.95	0.95	0.93	0.93	0.97	0.92	0.85	0.94	0.93	0.94	0.95	0.94
Na	0.03	0.03	0.04	0.04	0.03	0.04	0.05	0.04	0.05	0.06	0.03	0.03	0.04	0.03	0.04
Wo	51.24	53.39	50.70	53.65	51.14	50.64	52.78	53.95	52.00	48.78	53.10	50.27	50.24	52.77	53.34
En	28.48	23.24	28.12	23.92	30.58	28.00	24.30	23.33	25.05	29.84	24.94	28.46	29.11	25.47	22.50
Fs	20.28	23.38	21.18	22.43	18.28	21.36	22.93	22.72	22.95	21.37	21.97	21.27	20.65	21.76	24.17

Tab.2.12A EPMA-SEM compositions of pyroxene in sample EP4 (bed 4) in AS1a products

	EP4_2				EP4_11				EP4_12			EP4_19				
Ash fragment	**cpx1**	**cpx2**	**cpx3**	**cpx4**	**cpx1 core**	**cpx2_1**	**cpx2_2**	**cpx3_1**	**cpx1_1**	**cpx2**	**cpx3**	**cpx1_ core**	**cpx1_ rim**	**cpx2_1**	**cpx2_2**	**cpx3_1**
SiO_2	40.64	41.60	41.31	42.60	43.48	41.46	40.96	44.99	43.48	39.06	41.90	44.23	42.56	44.91	40.93	43.21
TiO_2	2.82	3.05	2.90	2.46	1.84	3.66	3.33	1.62	1.93	2.80	2.72	1.78	2.59	1.52	2.56	1.99
Al_2O_3	12.68	14.61	13.44	10.53	9.58	13.32	13.68	9.55	9.90	13.84	13.40	8.96	12.81	8.42	12.63	10.14
FeO	11.87	11.88	11.62	11.61	12.02	9.27	11.12	11.33	11.86	12.89	11.86	11.85	11.90	11.23	12.06	11.47
MnO	0.00	0.00	0.00	0.00	0.00	0.00	0.00	0.00	0.00	0.00	0.00	0.00	0.00	0.00	0.00	0.00
MgO	8.29	7.45	8.23	9.60	9.52	9.42	8.33	9.31	9.40	7.62	7.66	9.79	7.44	9.97	8.16	9.83
CaO	23.24	20.60	21.85	22.95	23.10	22.26	22.08	22.75	23.02	23.34	21.75	23.08	21.84	23.50	23.08	22.78
Na_2O	0.46	0.82	0.65	0.25	0.46	0.62	0.50	0.47	0.40	0.45	0.71	0.32	0.86	0.44	0.58	0.58
Si	1.54	1.57	1.56	1.61	1.64	1.55	1.55	1.70	1.64	1.48	1.58	1.67	1.61	1.69	1.55	1.62
Ti	0.08	0.09	0.08	0.07	0.05	0.10	0.09	0.05	0.05	0.08	0.08	0.05	0.07	0.04	0.07	0.06
Al	0.57	0.65	0.60	0.47	0.43	0.59	0.61	0.42	0.44	0.62	0.60	0.40	0.57	0.37	0.56	0.45
Fe	0.38	0.38	0.37	0.37	0.38	0.29	0.35	0.36	0.37	0.41	0.38	0.37	0.38	0.35	0.38	0.36
Mn	0.00	0.00	0.00	0.00	0.00	0.00	0.00	0.00	0.00	0.00	0.00	0.00	0.00	0.00	0.00	0.00
Mg	0.47	0.42	0.46	0.54	0.54	0.53	0.47	0.52	0.53	0.43	0.43	0.55	0.42	0.56	0.46	0.55
Ca	0.94	0.83	0.88	0.93	0.93	0.89	0.89	0.92	0.93	0.95	0.88	0.93	0.89	0.95	0.93	0.92
Na	0.03	0.06	0.05	0.02	0.03	0.05	0.04	0.03	0.03	0.03	0.05	0.02	0.06	0.03	0.04	0.04
Wo	52.77	51.19	51.57	50.58	50.51	52.25	52.14	51.07	50.75	53.04	52.20	50.23	52.65	50.93	52.64	50.16
En	26.19	25.76	27.03	29.44	28.97	30.77	27.37	29.08	28.84	24.10	25.58	29.65	24.96	30.07	25.90	30.12
Fs	21.04	23.04	21.40	19.97	20.52	16.98	20.49	19.85	20.41	22.86	22.22	20.13	22.39	19.00	21.47	19.71

Tab.2.13A EPMA-SEM compositions of pyroxene in sample EP2 (bed 5) in AS1a products

	EP2_9			EP2_18								
Ash fragment	**cpx1_rim**	**cpx2_core**	**cpx2_rim**	**cpx1_core**	**cpx1_rim**	**cpx3**	**cpx2_core**	**cpx2_int**	**cpx2rim**	**cpx4**	**cpx5**	**cpx6**
SiO_2	39.12	43.51	43.80	43.96	40.19	44.08	43.26	40.09	41.92	40.30	44.75	42.79
TiO_2	3.37	1.71	1.84	1.64	2.75	1.56	1.56	2.86	1.99	2.91	1.73	2.14
Al_2O_3	13.09	11.10	10.51	9.57	12.52	8.64	8.91	12.69	12.23	13.72	9.87	9.73
FeO	12.51	12.10	12.28	9.64	11.41	11.72	12.84	11.91	11.71	12.07	11.11	12.33
MnO	0.00	0.00	0.00	0.00	0.00	0.00	0.00	0.00	0.00	0.00	0.00	0.00
MgO	7.91	8.69	8.73	10.47	8.57	9.79	9.03	8.19	8.47	7.68	9.42	8.92
CaO	23.61	22.61	22.43	24.41	23.96	23.69	23.78	23.79	22.72	22.16	21.86	23.24
Na_2O	0.40	0.28	0.40	0.31	0.52	0.41	0.48	0.44	0.68	0.81	0.74	0.60
Si	1.48	1.65	1.66	1.64	1.52	1.66	1.64	1.52	1.58	1.53	1.69	1.62
Ti	0.10	0.05	0.05	0.05	0.08	0.04	0.04	0.08	0.06	0.08	0.05	0.06
Al	0.59	0.50	0.47	0.42	0.56	0.38	0.40	0.57	0.54	0.61	0.44	0.43
Fe	0.40	0.38	0.39	0.30	0.36	0.37	0.41	0.38	0.37	0.38	0.35	0.39
Mn	0.00	0.00	0.00	0.00	0.00	0.00	0.00	0.00	0.00	0.00	0.00	0.00
Mg	0.45	0.49	0.49	0.58	0.48	0.55	0.51	0.46	0.48	0.43	0.53	0.50
Ca	0.96	0.92	0.91	0.98	0.97	0.96	0.97	0.96	0.92	0.90	0.88	0.94
Na	0.03	0.02	0.03	0.02	0.04	0.03	0.04	0.03	0.05	0.06	0.05	0.04
Wo	53.20	51.22	50.79	52.49	53.49	50.99	51.29	53.48	52.05	52.43	50.09	51.33
En	24.80	27.39	27.51	31.33	26.62	29.32	27.10	25.62	27.00	25.28	30.04	27.42
Fs	22.00	21.39	21.70	16.18	19.88	19.69	21.61	20.90	20.94	22.29	19.87	21.26

Tab.2.13A *continue*

	EP2_19		EP2_22			
Ash fragment	**cpx1_core**	**cpx1_rim**	**cpx1_core**	**cpx1_rim**	**cpx2_1**	**cpx2_2**
SiO_2	43.93	40.73	43.88	39.31	45.07	40.62
TiO_2	1.85	2.78	1.57	3.07	2.30	3.55
Al_2O_3	9.72	14.07	8.72	14.19	8.43	14.04
FeO	11.64	12.20	11.89	12.34	9.23	10.35
MnO	0.00	0.00	0.00	0.00	0.00	0.00
MgO	9.27	7.00	9.71	7.42	11.05	8.29
CaO	22.93	21.31	23.58	22.86	23.30	20.78
Na_2O	0.45	0.92	0.57	0.66	0.46	0.82
Si	1.66	1.56	1.65	1.49	1.69	1.55
Ti	0.05	0.08	0.04	0.09	0.06	0.10
Al	0.43	0.63	0.39	0.63	0.37	0.63
Fe	0.37	0.39	0.37	0.39	0.29	0.33
Mn	0.00	0.00	0.00	0.00	0.00	0.00
Mg	0.52	0.40	0.55	0.42	0.62	0.47
Ca	0.93	0.87	0.95	0.93	0.94	0.85
Na	0.03	0.07	0.04	0.05	0.03	0.06
Wo	51.05	52.52	50.85	53.39	50.78	51.44
En	28.72	24.01	29.14	24.12	33.51	28.56
Fs	20.23	23.47	20.01	22.49	15.70	20.00

Appendix 3 : Laser Ablation ICP-MS Trace elements compositions of groundmass glasses

Tab. 3.1A Average concentration of single glass shards

AP3	VSM48						
Fragments	A	D	E	F	G	mean	σ
Li7	49.52	70.39	42.43	28.36	65.68	51.27	17.17
B11	100.54	69.24	96.82	80.29	30.19	75.42	28.27
Na23	34632.38	46129.93	45356.10	47739.60	48933.64	44558.33	5720.46
Mg25	4132.59	5746.84	6439.22	5509.47	4252.36	5216.09	995.81
Si29	201434.69	272166.44	232563.36	268055.31	258333.89	246510.74	29531.97
Ca43	35735.05	35735.05	35735.05	35735.05	35735.05	35735.05	0.00
Ti49	3206.66	3979.79	4397.03	3907.03	4480.76	3994.25	506.71
V51	112.76	135.92	148.74	131.63	137.00	133.21	13.07
Co59	74.68	11.85	15.29	9.56	7.50	23.78	28.60
Zn66	58.66	121.04	97.29	110.46	128.41	103.17	27.50
Rb85	211.80	327.40	160.31	257.79	212.25	233.91	62.62
Sr88	840.85	990.98	951.46	1032.20	881.58	939.41	78.22
Y89	24.17	33.05	29.64	26.26	27.18	28.06	3.41
Zr90	292.05	331.12	348.30	342.14	348.49	332.42	23.65
Nb93	53.95	64.14	60.69	68.73	63.36	62.17	5.43
Cs133	13.01	20.58	8.33	21.81	10.99	14.94	5.96
Ba137	1295.70	1649.81	1520.62	1719.94	1445.36	1526.28	167.71
La139	77.79	95.25	97.06	90.28	98.36	91.74	8.38
Ce140	135.49	162.99	173.55	165.36	183.76	164.23	18.01
Pr141	12.73	17.57	17.36	14.01	17.62	15.86	2.32
Nd146	35.88	60.18	55.14	49.43	65.91	53.31	11.49
Sm149	5.75	3.30	12.06	8.96	9.58	7.93	3.43
Eu151	1.28	-	2.19	1.23	1.96	1.67	0.49
Gd157	4.21	3.01	6.41	12.24	4.58	6.09	3.65
Tb159	0.65	-	0.45	0.42	1.12	0.66	0.33
Dy163	5.93	4.79	3.85	3.42	11.81	5.96	3.41
Ho165	0.98	-	1.00	0.90	1.70	1.14	0.37
Er167	2.01	1.04	1.71	3.17	-	1.98	0.89
Tm169	0.21	0.30	0.17	0.20	0.17	0.21	0.05
Yb173	2.03	5.60	2.81	3.01	2.71	3.23	1.37
Lu175	0.47	0.50	0.31	0.48	-	0.44	0.09
Hf177	4.09	7.59	4.50	6.22	7.54	5.99	1.64
Ta181	1.50	1.79	2.34	2.91	1.63	2.03	0.58
Pb208	47.87	52.07	59.54	57.47	63.92	56.17	6.30
Th232	28.64	37.32	40.83	35.05	44.06	37.18	5.88
U238	10.01	11.85	13.98	10.81	14.43	12.22	1.93

Tab. 3.2A Average concentration of single glass shards

AP3	VSM51						
Fragments	A	B	D	E	F	mean	σ
Li7	63.65	19.88	33.29	61.33	33.60	42.35	19.22
B11	196.32	92.67	67.27	54.25	103.07	102.72	55.83
Na23	51236.63	33711.97	30883.40	38173.29	43826.04	39566.26	8153.96
Mg25	7183.83	5338.73	5171.50	4504.62	6499.31	5739.60	1080.69
Si29	255447.29	197978.23	195268.86	189780.23	236687.14	215032.35	29246.39
Ca43	35735.04	35735.04	35735.04	35735.04	35735.04	35735.04	0.00
Ti49	4811.32	3412.21	3322.05	2866.39	4258.79	3734.15	784.54
V51	172.48	139.65	111.13	88.96	159.91	134.43	34.41
Co59	18.91	12.60	34.15	9.29	21.65	19.32	9.63
Zn66	42.45	41.54	48.93	56.05	49.48	47.69	5.91
Rb85	175.96	79.06	219.19	116.86	174.33	153.08	55.08
Sr88	740.31	1019.71	799.23	1149.79	855.56	912.92	168.46
Y89	21.12	17.23	20.16	18.77	28.26	21.11	4.26
Zr90	318.67	228.28	256.36	217.37	283.71	260.88	41.34
Nb93	63.15	46.71	45.13	45.10	59.96	52.01	8.81
Cs133	7.47	6.69	10.35	7.16	7.61	7.86	1.44
Ba137	1425.31	1626.57	1075.08	1537.35	1405.46	1413.95	209.45
La139	96.49	71.56	66.29	70.26	84.54	77.83	12.48
Ce140	157.74	124.19	119.86	118.25	140.13	132.03	16.78
Pr141	14.61	13.28	11.56	11.72	15.21	13.27	1.65
Nd146	50.37	43.69	44.17	33.16	60.70	46.42	10.10
Sm149	11.19	6.83	10.19	14.46	4.22	9.38	3.96
Eu151	2.10	2.19	0.40	2.97	1.00	1.73	1.02
Gd157	-	4.87	3.64	2.77	4.52	3.95	0.94
Tb159	0.99	0.84	0.87	1.04	1.18	0.98	0.14
Dy163	2.18	2.11	2.80	2.21	2.68	2.40	0.32
Ho165	-	0.92	0.73	0.58	0.62	0.71	0.15
Er167	4.68	-	3.40	1.39	2.46	2.98	1.40
Tm169	0.53	0.21	-	0.22	0.40	0.34	0.15
Yb173	1.95	2.89	-	-	6.10	3.65	2.18
Lu175	0.33	0.22	0.51	-	0.32	0.35	0.12
Hf177	7.88	4.03	7.21	5.64	3.00	5.55	2.06
Ta181	2.77	2.01	1.87	1.53	3.03	2.24	0.63
Pb208	53.30	42.54	39.63	50.33	55.43	48.24	6.86
Th232	39.83	29.95	28.19	27.15	42.54	33.53	7.12
U238	13.79	10.02	10.36	9.58	13.05	11.36	1.92

Tab. 3.3A Average concentration of single glass shards

AP3	VSM54					
Fragments	2	3	4	5	mean	σ
Li7	34.62	37.12	64.33	64.74	50.20	16.58
B11	78.88	106.51	99.63		95.00	14.38
Na23	34952.23	39692.12	43911.88	44407.52	40740.93	4401.06
Mg25	7939.07	7146.74	8097.81	6591.41	7443.76	704.23
Si29	208744.18	239809.35	258847.66	266521.36	243480.63	25736.62
Ca43	36378.29	36378.28	36378.28	36378.28	36378.28	0.00
Ti49	4378.12	4126.65	5031.23	4374.48	4477.62	387.39
V51	169.15	152.81	174.21	147.06	160.81	12.94
Co59	23.70	11.39	14.82	10.11	15.00	6.13
Zn66	43.01	76.89	89.00	66.81	68.93	19.52
Rb85	159.48	170.51	169.14	169.21	167.08	5.11
Sr88	695.12	822.88	747.54	1015.34	820.22	140.25
Y89	25.16	24.65	31.05	25.41	26.57	3.01
Zr90	314.90	285.77	339.95	350.60	322.80	28.87
Nb93	59.27	58.13	70.07	73.59	65.26	7.73
Cs133	11.08	8.39	8.51	10.23	9.55	1.32
Ba137	1145.13	1409.53	1525.82	1583.58	1416.01	194.56
La139	79.21	87.98	109.84	98.01	93.76	13.19
Ce140	154.54	150.22	180.06	170.32	163.79	13.87
Pr141	15.86	14.80	18.85	18.37	16.97	1.95
Nd146	56.37	55.16	68.28	73.06	63.22	8.84
Sm149	7.48	7.85	9.91	12.09	9.33	2.13
Eu151	1.80	3.13	3.28	2.31	2.63	0.70
Gd157	6.19	6.68	7.91	9.35	7.53	1.41
Tb159	0.67	1.11	0.94	0.79	0.88	0.19
Dy163	5.44	7.57	5.25	3.16	5.35	1.80
Ho165	1.11	1.01	0.82	0.88	0.95	0.13
Er167	4.53	4.45	3.78	4.83	4.40	0.44
Tm169	0.56	0.68	0.42	0.91	0.64	0.21
Yb173	4.41	3.61	1.95	3.43	3.35	1.03
Lu175	0.78	0.44	0.89	0.31	0.60	0.27
Hf177	4.84	6.03	3.72	13.57	7.04	4.45
Ta181	1.24	2.53	2.66	3.06	2.37	0.79
Pb208	54.31	61.19	79.98	68.87	66.09	11.01
Th232	40.70	39.95	42.73	44.02	41.85	1.86
U238	12.66	13.29	11.14	16.16	13.31	2.10

Tab. 3.4A Average concentration of single glass shards

AP3	VSM56				
Fragments	1	3	4	mean	σ
Li7	33.87	42.96	43.69	40.17	5.47
B11	68.24	50.80	45.26	54.77	11.99
Na23	36668.80	37371.02	40416.31	38152.04	1992.09
Mg25	7487.09	6164.56	7638.07	7096.57	810.66
Si29	220738.39	178475.31	230787.83	210000.51	27760.16
Ca43	35163.28	35163.29	35163.29	35163.29	0.005
Ti49	4014.52	3320.91	2955.17	3430.20	538.06
V51	137.75	138.55	86.53	120.94	29.80
Co59	10.94	9.80	88.50	36.41	45.11
Zn66	84.42	71.38	65.43	73.74	9.71
Rb85	164.44	60.81	129.51	118.25	52.72
Sr88	818.21	697.51	788.40	768.04	62.87
Y89	23.43	19.79	19.49	20.90	2.19
Zr90	321.27	216.52	243.68	260.49	54.36
Nb93	59.93	48.57	46.82	51.77	7.11
Cs133	9.07	2.48	6.36	5.97	3.31
Ba137	1450.18	1119.82	1253.92	1274.64	166.15
La139	92.83	70.70	67.93	77.15	13.64
Ce140	161.10	141.05	126.90	143.02	17.18
Pr141	16.41	12.50	14.64	14.52	1.96
Nd146	56.89	41.13	41.11	46.38	9.10
Sm149	7.88	7.94	8.62	8.15	0.41
Eu151	2.09	1.54	3.85	2.49	1.20
Gd157	8.87	7.95	4.37	7.06	2.37
Tb159	0.42	0.91	1.50	0.94	0.54
Dy163	2.68	4.23	3.67	3.53	0.78
Ho165	0.46	0.82	-	0.64	0.25
Er167	-	1.21	-	1.21	--
Tm169	1.03	0.34	1.15	0.84	0.44
Yb173	4.13	3.09	4.27	3.83	0.64
Lu175	-	0.36	-	0.36	--
Hf177	5.40	2.31	2.71	3.47	1.68
Ta181	2.27	1.71	1.17	1.72	0.55
Pb208	55.15	48.71	56.39	53.42	4.12
Th232	39.96	24.43	35.57	33.32	8.005
U238	14.71	11.27	15.33	13.77	2.18

Tab. 3.5A Average concentration of single glass shards

AS1a	EP2							
Fragments	1	23	7	6	4	12	13	14
Li	73.39	38.32	36.16	38.51	32.09	15.34	28.78	38.16
B	156.44	132.03	116.33	110.96	144.90	46.75	99.07	144.69
Na	89779.38	77866.98	90465.61	83817.52	84629.84	30480.13	46100.65	79909.88
Mg	9825.20	11740.73	9330.92	10599.91	10314.07	17180.24	10234.94	11073.36
Si	378707.03	254155.61	321406.16	230608.20	278834.19	119699.10	202384.47	263913.88
Ca43	54617.64	57012.83	57574.45	60338.84	59997.62	57626.79	61326.27	56229.09
Ca44	57176.07	57176.07	57176.07	57176.07	57176.07	57176.07	57176.07	57176.07
Sc	4.44	2.13	3.43	2.85	2.07	4.31	2.00	3.49
Ti	7336.96	7278.62	5858.82	7001.25	5389.23	6482.04	4953.56	6672.59
V	208.90	203.94	184.06	266.71	166.02	196.43	168.87	226.32
Cr	<6.30	8.42	<6.56	<3.40	<6.13	<1.66	<1.84	30.14
Co	27.53	23.32	20.37	22.23	21.88	16.54	18.38	24.74
Ni	7.32	8.34	3.83	1.91	4.32	6.05	3.44	10.46
Zn	194.43	141.45	675.79	128.53	458.94	65.49	90.27	527.77
Rb	593.31	212.00	375.68	114.62	235.17	46.63	122.58	228.20
Sr	1805.18	2077.24	1951.57	2125.85	2176.55	792.58	1900.89	1661.74
Y	23.20	33.39	25.21	26.30	27.10	22.88	31.07	27.04
Zr	217.76	276.39	229.07	254.76	224.59	225.84	237.17	219.05
Nb	111.36	117.00	104.19	106.99	114.86	41.86	76.33	107.22
Cs	32.30	6.36	15.31	3.59	7.02	1.46	4.84	7.57
Ba	3603.23	3029.42	3219.13	2654.91	3523.50	950.16	2124.51	2344.77
La	97.94	121.84	104.07	109.59	118.84	61.17	108.48	100.47
Ce	195.67	198.64	184.09	189.47	179.07	119.15	177.77	184.80
Pr	17.31	24.11	17.71	20.37	17.03	15.37	20.35	19.50
Nd	70.09	73.71	58.81	63.70	50.85	58.60	74.56	60.60
Sm	12.61	9.13	11.09	10.75	10.98	11.57	12.52	8.87
Eu	3.22	2.44	2.07	2.86	2.89	2.69	2.80	2.02
Gd	5.35	8.77	6.66	7.57	9.06	7.61	10.32	5.32
Tb	0.64	1.29	0.96	0.79	1.38	1.04	1.04	0.91
Dy	5.13	6.12	7.15	5.83	5.75	4.33	5.98	5.69
Ho	0.88	0.80	1.00	1.04	0.97	1.08	0.97	0.60
Er	2.90	3.18	2.95	3.03	2.02	2.78	3.36	3.33
Tm	0.46	0.22	0.24	0.38	0.28	0.30	0.42	0.36
Yb	1.93	3.09	1.66	3.17	2.86	2.32	2.74	1.69
Lu	0.40	0.36	0.32	0.34	0.12	0.21	0.50	0.44
Hf	5.52	4.61	2.50	4.32	4.12	6.33	4.01	4.60
Ta	3.57	4.78	4.20	4.31	4.46	2.10	3.43	3.88
Pb	98.63	113.21	81.29	66.40	129.87	26.83	78.03	100.93
Th	42.00	49.48	44.06	49.03	42.59	17.86	43.96	39.56
U	18.95	18.45	17.67	17.28	16.62	6.74	13.44	20.00

Tab. 3.5A Average concentration of single glass shards

AS1a	*continue EP2*						
Fragments	3	2	7	13	17	19	23
Li	38.70	31.52	23.91	34.00	30.76	39.90	35.58
B	103.99	98.63	59.65	45.36	48.44	37.47	56.03
Na	81063.73	66199.82	25452.17	28947.04	32508.29	29225.38	29904.44
Mg	9838.58	12208.13	5361.54	8134.15	8144.67	10754.30	12808.11
Si	277118.03	214586.36	156737.34	184393.47	189971.18	168614.09	169325.32
Ca	62317.03	52213.67	51744.34	51744.34	51744.34	51744.34	51744.34
Sc	2.73	2.71	1.96	2.28		5.44	2.01
Ti	5903.79	5456.47	3219.89	4215.40	4577.47	4691.26	4931.31
V	199.62	179.62	114.74	188.25	190.00	186.79	215.80
Cr	<7.28	<3.54				78.45	
Co	21.17	18.44	12.04	13.92	18.87	16.39	18.23
Ni	3.45	3.27	6.20	12.42	4.11	5.63	2.32
Zn	164.36	98.77	67.07	113.95	81.48	103.72	80.54
Rb	295.10	178.84	63.57	99.35	76.06	84.44	73.31
Sr	1838.30	1511.61	2258.79	1935.22	2120.52	1594.56	1212.18
Y	28.23	26.61	20.51	27.96	29.55	30.26	27.79
Zr	252.37	236.06	154.33	212.74	242.60	254.95	259.54
Nb	90.42	70.51	53.99	65.72	69.08	62.76	63.70
Cs	14.06	5.85	2.13	3.39	1.74	1.96	2.48
Ba	3055.51	2065.03	1695.41	2024.12	1977.60	1824.40	1508.54
La	105.46	88.88	81.45	87.29	90.04	91.38	75.68
Ce	185.10	141.31	129.54	134.25	144.53	146.02	133.43
Pr	19.00	14.94	15.49	14.17	14.75	14.90	14.72
Nd	63.01	58.54	41.08	51.11	49.79	55.49	52.27
Sm	11.89	9.57	9.88	9.48	8.78	4.18	10.33
Eu	2.87	2.41	1.62	2.14	1.65	2.79	2.35
Gd	7.07	7.75	5.12	7.03	7.92	3.92	8.88
Tb	0.86	0.88	0.91	1.16	0.47		1.04
Dy	6.41	5.37	2.27	3.11	6.69	3.98	5.51
Ho	1.07	0.84	0.69	0.88	0.80	1.84	1.26
Er	3.33	2.52	2.76	1.66	3.17		2.63
Tm	0.33	0.29	0.27	0.53	0.64	0.74	0.20
Yb	3.09	1.95	1.69	3.86	4.77	4.21	3.62
Lu	0.22	0.36		0.48	0.42		0.40
Hf	3.17	3.73	2.74	4.46	3.32	12.71	4.86
Ta	4.27	3.12	2.31	2.68	3.80	4.21	2.33
Pb	89.18	63.41	40.62	63.94	59.70	65.05	63.97
Th	46.58	32.60	33.13	35.26	48.17	48.13	34.50
U	16.07	11.64	9.82	12.54	15.52	16.38	12.99

Tab. 3.6A Average concentration of single glass shards

AS1a	EP4								
Fragments	2	4	11	12	16	19	29	2	13
Li	32.48	48.98	52.46	27.56	-	40.36	37.47	46.47	32.37
B	23.98	44.74	26.58	33.98	-	50.11	56.34	20.78	30.97
Na	30298.92	33530.52	36224.23	35021.09	49425.99	32898.12	31439.89	37674.29	34806.46
Mg	12758.48	10392.42	8757.55	10601.35	14449.83	10550.6	10611.36	10462.54	8610.93
Si	198424.7	214355.2	175082.4	197956.48	320992.3	191462.2	191583.5	202076.7	191419.6
Ca43	55603.73	55603.73	55603.73	55603.73	55603.74	55603.74	55603.74	55603.74	55603.74
Sc	2.02	3.76	1.32	2.88	-	5.35	-	-	4.15
Ti	4978.5	4976.57	4830.43	4662.67	6261.65	5227.05	4990.02	5188.23	4634.24
V	210.89	187.21	200.22	206.80	296.55	205.155	200.56	223.81	182.48
Cr			33.57	54.47	-	85.83	-	72.64	-
Co	19.67	18.945	19.26	19.96	-	20.79	19.445	23.725	17.12
Ni	3.595	22.48	1.69	-	83.85	13.4	8.39	-	-
Zn	77.89	154.07	95.105	89.57	-	70.51	96.28	68.19	84.675
Rb	129.25	121.91	106.26	144.16	99.32	78.64	110.145	87.27	73.44
Sr	1692.47	1691.38	1880.39	1449.17	2692.17	1612.16	1406.46	1622.05	1942.69
Y	24.66	26.16	30.24	25.16	33.98	27.7	23.585	29.34	24.34
Zr	235.49	221.35	233.05	199.24	286.08	260.72	222.53	236.21	209.11
Nb	63.055	74.19	82.78	75.89	82.42	68.13	67.89	74.64	69.69
Cs	3.685	3.705	2.99	5.57	7.60	2.22	3.1	1.84	1.67
Ba	1837.14	2051.65	2180.65	1954.3	2911.72	1835.25	1694.44	1923.37	1946.91
La	82.58	87.87	97.9	84.56	135.52	93.80	77.06	95.89	80.525
Ce	141.91	156.00	179.51	161.07	222.48	157.00	146.38	167.58	144.39
Pr	14.22	14.97	17.42	15.04	22.66	16.13	14.51	18.84	12.86
Nd	49.00	47.20	56.26	52.29	97.13	56.61	51.08	63.45	50.01
Sm	7.82	12.41	12.02	8.59	29.16	6.47	7.39	8.42	8.41
Eu	2.09	3.05	2.77	2.80	3.08	1.13	1.73	3.02	2.19
Gd	5.26	2.54	7.01	2.89	-	6.36	9.5	6.29	7.02
Tb	0.75	0.77	0.77	1.12	1.92	1.06	0.92	1.42	0.58
Dy	5.605	3.39	5.42	3.74	10.94	6.16	1.31	5.99	3.1
Ho	0.66	0.77	1.20	0.79	4.44	1.90	0.55	1.36	0.42
Er	2.25	3.35	2.78	1.67	-	2.29	2.44	3.35	1.40
Tm	0.38	0.30	0.36	0.38	-	0.6	0.44	0.26	0.31
Yb	2.25	4.21	3.94	1.90	-	3.1	2.68	9.56	1.69
Lu	0.33	0.23	0.41	0.47	-		0.36	0.77	1.23
Hf	4.78	1.91	4.22	4.86	-	5.42	3.10	1.70	1.74
Ta	2.40	2.74	2.51	4.26	5.45	2.65	3.02	2.19	2.44
Pb	67.27	82.68	75.65	75.92	80.46	57.46	53.65	64.11	51.56
Th	28.94	40.97	43	36.15	68.42	40.68	33.46	38.43	35.45
U	12.36	12.99	16.55	16.46	28.09	17.15	12.80	14.93	14.54

Tab. 3.6A Average concentration of single glass shards

AS1a	*continue EP4*					
Fragments	11	28	19	16	20	29
Li	65.5	23.63	42.22	32.24	27.93	25.85
B	353.85	29.21	88.19	48.26	66.05	83.64
Na	47919.86	28103.26	69492.44	45734.62	46800.88	64149.21
Mg	11805.65	8965.775	12461.14	12851.5	11538.01	11729.91
Si	228780.9	182059.1	240021.9	192064.19	187521.4	204184.2
Ca43	55603.74	55603.74	68245.53	76253.15	55319.31	56685.48
Sc	37.11	3.68	3.71	4.43	4.12	3.01
Ti	5903.42	4089.63	5789.79	4626.18	4831.85	4733.09
V	212.815	159.025	220.49	196.25	186.56	173.53
Cr	-	100.7	<7.62	<1.72	<2.44	10.91
Co	33.67	15.73	28.43	15.61	17.1	17.12
Ni	-	7.03	2.45	4.91	2.14	19.02
Zn	149.18	53.185	169.32	107.5	102.03	76.86
Rb	151.665	76.48	177.62	68.29	144.04	190.15
Sr	1787.855	1923.125	1933.25	1827.56	1410.5	1669.09
Y	29.44	20.7	26.53	20.84	20.61	29.05
Zr	239.85	186.015	234.91	258.72	201.21	237.56
Nb	93.535	53.25	78.2	71.82	69.26	67.11
Cs	4.075	1.615	5.18	1.91	3.54	7.22
Ba	2777.985	1672.235	2533.25	2682.01	1676.7	2032.8
La	118.73	71.38	85.47	81.63	76.51	84.91
Ce	203.935	118.905	182.67	140.77	147.62	133.62
Pr	19.97	12.47	20.3	15.37	15.15	14.48
Nd	96.63	47.88	64.36	43.47	54.59	53.08
Sm	12.1	6.725	11.45	10.55	10.95	9.73
Eu	-	1.575	2.32	2.33	2.66	2.54
Gd	6.9	3.51	6.45	6.18	5.93	6.13
Tb	-	0.85	0.98	0.97	0.702	1
Dy	4.8	5.285	5.14	3.5	4.22	5.13
Ho	1.8	1.14	1.31	0.96	0.929	1.09
Er	10.29	2.225	2.65	3.01	2.39	2.31
Tm	1.32	0.555	0.4	0.412	0.316	0.398
Yb	-	1.31	3.66	2.95	1.85	2.22
Lu	3.85	0.44	0.332	0.267	0.3	0.362
Hf	-	3.455	4.52	2.92	3.65	4.63
Ta	1.91	0.725	3.49	3.27	2.64	3.17
Pb	89.42	45.645	118.54	48.07	78.9	64.93
Th	39.42	27.945	40.77	31.54	30.9	36.64
U	26.205	11.27	14.03	10.07	12.37	13.46

Tab. 3.7A Average concentration of single glass shards

AS1a	EP5		
Fragments	14	15	1
Li	35.28	42.19	34.94
B	40.43	65.67	44.48
Na	31054.69	30184.83	29853.83
Mg	11294.16	10011.32	14102.03
Si	180390.5	170538.4	199619.3
Ca43	56389.89	56389.89	56389.9
Sc	4.965	3.14	6.54
Ti	5099	5456.115	6042.417
V	207.70	199.60	231.05
Cr	-	52.21	31.69
Co	19.97	18.16	19.69
Ni	8.71	4.98	4.62
Zn	112.79	107.43	95.79
Rb	99.37	83.70	149.20
Sr	1741.56	1686.94	1529.89
Y	31.85	25.87	30.34
Zr	254.54	248.60	289.24
Nb	66.83	76.24	70.5
Cs	3.10	2.03	5.15
Ba	1854.53	1939.74	2016.22
La	85.86	83.80	86.83
Ce	149.35	148.905	151.37
Pr	14.77	16.30	15.94
Nd	53.88	41.55	57.72
Sm	7.47	12.05	8.5
Eu	3.083	1.47	2.2
Gd	4.54	6.375	6.52
Tb	0.96	0.87	0.85
Dy	5.77	5.89	6.4
Ho	1.00	0.93	1.08
Er	1.38	2.13	2.195
Tm	0.255	0.35	0.60
Yb	3.72	5.12	4.32
Lu	0.27	0.69	0.39
Hf	4.71	1.93	3.63
Ta	2.43	2.785	3.13
Pb	76.39	75.41	50.40
Th	34.53	45.36	36.5
U	12.07	14.01	13.62

Tab. 3.8A Average concentration of single glass shards

AS1a	EP6								
Fragments	22	2	10	11	12	28	29	16	14
Li	29.54	51.18	58.08	38.77	52.67	20.13	35.57	24.73	34.70
B	58.59	50.71	68.36	77.17	77.32	43.80	54.18	28.32	65.09
Na	30985.47	35643.55	41513.16	24948.75	42416.35	25141.13	35063.28	23355.10	36808.37
Mg	10907.01	8338.07	9013.49	12311.14	6216.42	8097.29	8130.17	10945.50	9466.47
Si	208815.34	218930.26	242853.66	163816.10	217306.47	149640.10	188196.71	148306.08	202572.32
Ca43	54889.02	54889.02	54889.02	54889.03	54889.03	54889.04	54889.03	54889.03	54889.03
Sc	4.46	4.78	-	5.85	-	-	4.67	4.47	3.85
Ti	4691.37	4649.22	5444.04	6322.66	4547.19	4557.85	4959.89	5244.19	7407.00
V	185.82	201.30	219.45	233.55	162.30	189.07	197.28	180.87	375.93
Cr	<63.53	61.15	62.26	-	-	-	-	-	-
Co	20.99	16.33	21.87	20.05	19.75	14.75	13.66	16.93	24.49
Ni	<6.19	-	-	-	-	-	5.77	4.75	-
Zn	102.01	83.89	144.39	92.40	145.79	97.23	143.86	77.75	133.93
Rb	219.05	147.29	180.64	72.33	94.57	58.39	124.28	87.34	85.12
Sr	1202.68	1965.13	1673.70	1246.32	2294.50	1484.66	1685.39	1236.13	1885.62
Y	33.23	27.24	27.83	30.83	29.98	28.33	27.98	26.91	33.87
Zr	293.05	233.47	234.30	273.93	251.35	210.64	245.00	247.37	270.20
Nb	68.33	74.01	86.56	65.61	95.74	53.39	73.89	51.02	91.71
Cs	10.55	5.32	6.33	1.78	4.70	2.34	3.48	2.73	2.87
Ba	1841.16	2092.90	2278.16	1532.47	2432.26	1394.25	1935.58	1282.70	2121.31
La	80.26	92.06	106.09	86.87	117.20	79.87	95.70	65.05	109.54
Ce	170.98	153.29	185.33	159.42	201.43	138.53	163.87	121.81	183.35
Pr	15.76	14.91	17.51	18.54	16.88	14.62	16.49	13.02	19.48
Nd	52.61	69.05	55.85	58.55	60.13	50.32	55.76	47.01	66.59
Sm	10.52	9.21	9.99	11.71	9.46	9.08	12.55	9.23	12.58
Eu	1.43	2.52	2.32	2.67	2.65	2.85	2.12	2.11	3.64
Gd	6.20	5.10	10.37	7.89	6.36	8.05	9.80	6.01	10.20
Tb	1.21	1.08	1.00	1.21	1.39	0.97	0.92	0.91	0.84
Dy	3.73	4.20	3.42	6.64	5.54	4.83	4.46	6.45	7.89
Ho	0.67	0.95	1.05	0.89	1.65	1.01	1.08	0.87	1.09
Er	1.89	1.59	2.48	2.33	2.38	2.11	3.39	2.14	2.84
Tm	0.41	0.37	0.60	0.44	0.44	0.17	0.41	0.46	0.51
Yb	3.98	2.60	2.33	2.20	3.92	2.39	1.88	2.02	2.14
Lu	0.35	0.20	0.55	0.45	0.28	0.55	0.42	0.37	0.48
Hf	6.91	3.87	4.24	3.94	2.95	3.35	4.28	3.46	2.38
Ta	3.06	3.15	4.01	3.51	3.26	2.47	3.02	2.12	4.15
Pb	67.31	73.74	78.73	56.26	93.54	41.02	52.57	35.87	68.47
Th	38.66	42.16	46.43	29.91	49.19	30.08	38.48	28.21	48.22
U	15.05	17.33	21.80	12.33	17.32	11.71	15.00	10.24	19.09

Tab. 3.8A Average concentration of single glass shards

AS1a	*continue EP6*								
Fragments	14	22	28	29	12	23	8	17	20
Li	24.65	23.4	30.59	28.84	19.69	30.58	48.21	28.32	28.73
B	74.98	50.51	90.18	72.02	105.11	58.34	284.92	87.15	81.86
Na	39704.71	42876.41	58368.23	68160.47	61300.27	67028.79	157001.4	64307.39	59671.68
Mg	6415.9	15005	10398.62	7985.1	5949.88	9235.63	13812.36	11282.9	10613.22
Si	191829.7	143188.5	190408.9	175500.8	241588.1	215649.2	859094.3	222668.1	306204.7
Ca43	50650.43	54762.89	55993.92	57383.9	58736.25	74125.77	94511.73	59516.02	54087.26
Sc	2.11	4.97	1.84	1.63	1.41	2.23	<2.50	4.14	3.09
Ti	4135.52	6183.85	5320.55	4332.67	3774.68	5790.33	9229.01	5369.07	5590.09
V	156.11	187.94	185.84	138.93	141.59	171.07	411.35	193.58	170.1
Cr	3.83	6.2	<2.53	4.98	9.36	6.62	<19.81	<4.14	<7.06
Co	12.04	18.58	18.7	13.55	13.01	16.41	19.94	19.39	19.87
Ni	2.89	4.33	2.21	2.51	1.5	2.19	<5.15	3.1	2.73
Zn	81.6	85.08	96.01	81.19	118.99	93.46	358.44	78.71	82.69
Rb	224.58	78.55	85.73	83.45	94.83	98.96	1121.73	140.23	590.25
Sr	1609.14	1245.41	1784.7	2216.36	2322.66	2880.41	3649.89	2088.53	1727.22
Y	21.13	27.87	26.84	25.8	22.04	25.32	38.54	28.96	29.8
Zr	197.19	255.12	239.15	194.39	199.12	220.15	732.46	261.14	220.73
Nb	61.78	53.29	83.96	70.88	83.63	89.77	140.94	82.05	76.44
Cs	9.4	3.05	3.03	2.76	3.81	2.62	47.26	4.94	29.68
Ba	2187.5	1380.51	2144.08	2013.87	2368.55	2482.58	6837.04	2187.63	2986.14
La	73.72	73.4	101.21	99.25	97	96.76	128.64	96.63	115.49
Ce	154.11	120.32	175.32	155.25	164.49	154.5	298.86	158.46	201.73
Pr	14.98	14.99	18.15	17.14	18.41	19.64	23.25	16.89	21.34
Nd	66.89	55.38	55.52	61.25	67.65	53.36	73.44	55.15	72.86
Sm	8.97	10.13	9.19	10.02	10.13	10.17	26.72	11.07	9.83
Eu	1.84	2.65	2.74	2.5	2.5	2.99	2.36	2.56	2.97
Gd	6.34	8.16	6.86	7.85	7.46	5.89	10.03	7.52	7.86
Tb	0.73	0.89	0.89	0.91	0.94	0.91	1.05	1.07	1.09
Dy	5.13	5.35	5.98	4.33	4.87	5.32	8.75	5.84	5.4
Ho	0.76	0.82	1.12	0.82	0.82	0.76	1.17	0.89	1.08
Er	2.7	2.53	3.34	2.66	1.93	2.9	4.22	2.21	2.74
Tm	0.21	0.46	0.35	0.28	0.18	0.33	0.65	0.24	0.41
Yb	2.44	2.96	2.86	2.8	1.67	2.77	3.4	2.65	2.29
Lu	0.19	0.40	0.32	0.30	0.15	0.25	1.22	0.23	0.47
Hf	3.37	5.42	3.71	2.41	3.37	3.69	10.68	4.54	4.54
Ta	2.71	2.72	3.62	2.73	3.84	3.54	9.91	3.56	3.32
Pb	49.01	42.54	69.98	51.78	70.19	49.24	191.42	68.91	54.54
Th	36.09	27.64	40.24	35.62	40.02	43.85	90.12	39.35	40.4
U	11.47	9.21	14.95	12.32	15.93	12.94	27.27	10.89	12.11

Tab. 3.9A Average concentration of single glass shards

AS1a	EP8								
Fragments	3	16	17	18	19	11	14	16	17
Li	34.27	34.85	31.503	48.5	<12.19	43.63	21.32	27.34	14.25
B	88.92	159.29	84.63	97.59	152.88	19.12	22.53	24.48	26.86
Na	27734.98	36772.33	31315.89	40878.32	26937.17	38291.12	27716.43	29649.86	28484.96
Mg	8340.26	6857.73	8286.55	9604.53	7323.34	9155.34	6778.81	7228.27	9910.85
Si	139833.1	175961.4	183857.1	219401.3	150291.8	174866.2	186471.6	168853.4	201548.4
Ca43	52601.99	52601.99	52601.99	52601.99	52601.98	52601.98	52601.98	52601.98	52601.98
Sc	-	20.81	-	-	<7.76	4.3	-	<2.52	4.5
Ti	4110.12	4029.75	4735.30	5092.71	4489.12	5213.50	4409.76	3985.77	5719.38
V	156.32	154.25	202.82	238.31	185.51	197.37	176.51	151.4	227.83
Cr	-	-	-	-	<87.44	82.01	-	<48.07	-
Co	16.97	16.48	16.49	24.18	17.43	16.27	17.42	16.67	19.39
Ni	-	20.89	21.55	-	<9.86	4.92	-	<5.30	-
Zn	79.86	80.87	99.40	85.17	89.68	115.67	110.34	67.93	109.81
Rb	55.95	73.28	65.92	195.46	49.14	199.25	93.08	67.29	145.83
Sr	1230.66	1609.80	1591.61	1573.74	1378.32	1481.57	1903.65	1970.68	1594.98
Y	25.195	26.01	25.58	21.51	20.46	26.61	24.32	22.50	31.32
Zr	224.95	188.40	204.21	228.66	167.92	221.15	213.34	200.76	253.02
Nb	60.72	72.39	78.91	88.37	59.06	79.50	66.72	64.86	76.65
Cs	1.96	2.61	1.42	6.51	2.85	7.20	1.73	1.98	3.32
Ba	1478.54	1978.01	1925.33	2177.82	1565.22	1988.80	1809.89	1655.02	2147.09
La	78.13	87.50	85.87	98.6	72.14	83.745	79.27	79.58	99.625
Ce	136.48	166.27	166.61	186.59	135.66	149.09	138.62	131.50	179.23
Pr	13.70	14.83	15.27	18.25	12.57	14.335	12.62	13.26	16.9
Nd	52.32	55.29	58.55	46.73	44.38	48.52	44.86	50.86	61.48
Sm	6.60	8.68	7.92	11.62	7.02	7.52	5.56	6.29	8.77
Eu	1.725	2.54	2.34	2.21	2.48	1.815	2.19	2.05	2.42
Gd	3.8	4.7	9.25	11.37	4.17	6.09	5.45	5.78	5.18
Tb	0.75	0.64	0.76	1.06	0.81	0.785	0.585	0.49	0.67
Dy	4.26	3.33	5.08	3.44	5.59	3.955	4.265	3.64	4.48
Ho	0.81	0.99	1.35	1.45	0.38	0.595	0.805	0.68	0.97
Er	-	2.89	1.89	2.84	<0.00	2.595	2.92	1.19	2.88
Tm	0.29	0.69	0.27	0.63	0.61	0.23	0.28	0.23	0.3
Yb	-	6.07	6.77	3.24	1.8	2.07	2.145	2.04	2.56
Lu	0.73	0.49	0.44	0.34	<0.16	0.115	0.375	0.152	0.435
Hf	4.72	4.11	4.90	3.17	2.47	3.65	4.93	2.68	3.825
Ta	1.76	3.35	3.45	4.15	1.86	2.785	2.49	2.85	2.59
Pb	46.89	62.23	65.74	90.41	46.31	48.43	54	57.05	70.03
Th	35.88	41.95	38.68	38.73	28.27	31.31	33.82	33.44	38.96
U	13.24	14.65	18.03	16.31	12.9	12.465	13.95	12.53	13.98

Acknowledgements

I would like to thank Prof. Raffaello Cioni for his precious advices and continuing support and helpful suggestions along the way, and especially for his critical reading of this thesis. I also want to thank Antonella Bertagnini for her valuable suggestions during the phases of acquisitions of images and microanalysis at SEM laboratory at the University of Pisa. All the stratigraphic information around the Vesuvius area were collected with the assistance of Raffaello Cioni, Antonella Bertagnini, Daniele Andronico and Paul Cole. I am also grateful to Massimo Tiepolo for introduce me at the LA-ICP-MS instrumentation, at laboratory of University of Pavia, and for his helping in the critical review of my data.

References

Andronico D., Calderoni G., Cioni R., Sbrana A., Sulpizio R., Santacroce R., (1995). Geological map of Somma-Vesuvius volcano. Periodico di Mineralogia, vol. 64 (1–2), pp. 77–78.

Andronico D., Cioni R., (2002). Contrasting styles of Mount Vesuvius activity in the period between the Avellino and Pompeii Plinian eruptions, and some implications for assessment of future hazards. Bulletin of Volcanology, vol. 64, pp. 372–391.

Arnò V., Principe C., Rosi M., Santacroce R., Sbrana A., Sheridan M.F., (1987). Eruptive history. In: Santacroce R (ed) Somma Vesuvius. CNR Quaderni Ricerca Sci, vol. 114, pp. 53–103.

Arrighi S., Principe C., Rosi M., (2001). Violent strombolian and subplinian eruptions at Vesuvius during post-1631 activity. Bulletin of Volcanology, vol. 63 (2-3), pp. 126-150.

Arrowsmith P., (1987). Laser ablation of solids for elemental analyses by inductively coupled plasma-mass spectrometry. Analytical Chemistry, vol. 59, pp. 1437-1444.

Auger E., Gasparini P., Virieux J., Zollo A., (2001). Seismic Evidence of an Extended Magmatic sill Under Mt. Vesuvius. Science, 9918.

Barberi F., Macedonio G., Pareschi M.T., Santacroce R., (1990). Mapping the tephra fallout risk: an example from Vesuvius, Italy. Nature, vol. 344, pp. 142–144.

Bertagnini A., Landi P., Rosi M., Vigliargio A., (1998). The Pomici di Base plinian eruption of Somma-Vesuvius. Journal of Volcanology Geothermal Research, vol. 83 (3-4), pp. 219-239.

Blatt H., Middleton G., Murray R., (1980). Origin of sedimentary rocks. Prentice-Hall, NJ. 782 p.

Blong R.J., (1984). Volcanic hazards. Academic Press, Australia, pp 1–424.

Bonadonna C., Ernst G.G.J., Sparks R.S.J., (1998). Thickness variations and volume estimates of tephra fall deposits: the importance of particle Reynolds number. Journal of Volcanology and Geothermal Research, vol. 81, pp. 173-187.

Bonadonna C., Macedonio G., Sparks R.S.J., (2002a). Numerical modelling of tephra fallout associated with dome collapses and Vulcanian explosion : application to hazard assesment on Montserrat. In : Druitt T.H., Kokelaar B.P. (eds) The eruption of Soufriere Hills Volcano, Montserrat, from 1995 to 1999. Memoir, Geological Society, London, pp 517-537.

Bonadonna C., Phillips J.C., Houghton B.F., (2005). Modeling tephra sedimentation from Ruapehu weak plume eruption. Journal of Geophisical Research, 110, B08209, doi :10.1029/2004JB003515.

Bursik M., (1993). Subplinian eruption mechanisms inferred from volatile and clast dispersal data. Journal of Volcanology and Geothermal Research, vol. 57, pp.57–60.

Büttner R., Dellino P., La Volpe L., Lorenz V., Zimanowski B., (2002). Thermohydraulic explosions in phreatomagmatic eruptions as evidenced by the comparison between pyroclasts and products from Molten Fuel Coolant Interaction experiments. Journal of Geophysical Research, vol. 107, NO. B11, 2277, doi:10.1029/2001JB000511.

Büttner R., Dellino P., Zimanowski B., (1999). Identifying modes of magma/water interaction from the surface features of ash particles. Nature, vol. 401, pp. 688-690.

Carey S., Sigurdsson H., (1987). Temporal variations in column height and magma discharge rate during the 79 A.D. eruption of Vesuvius. Geological Society of American Bulletin, vol. 99 (2), pp. 303–314.

Carey S., Sparks R.S.J., (1986). Quantitative models of the fallout and dispersal of tephra from volcanic eruption columns. Bulletin of Volcanology, vol. 48, pp. 109–125.

Cashman K.V., (1992). Groundmass crystallization of Mount St Helens dacite 1980-1986: a tool for interpreting shallow magmatic processes. Contributions to Mineralogy and Petrology, vol. 109, pp. 431-49.

Cashman K.V., (1993). Relationship between plagioclase crystallization and cooling rate in basaltic melts. Contributions to Mineralogy and Petrology, vol. 113, pp.126-42.

Cashman K.V., Blundy J., (2000). Degassing and crystallization of ascending andesite and dacite. Philosophical Transactions of the Royal Society of London, vol. 358, pp. 1487–1513.

Cashman K.V., Marsh B.D., (1988). Crystal size distribution (CSD) in rocks and the kinetics and dynamics of crystallization II. Makaopuhi lava lake. Contrib Mineral Petrol 99:292–305 sections: estimation of crystal habit and true size. American Mineralogist, vol. 79, pp. 113–119.

Cashman K.V., Sturtevant B., Papale P., Navon O., (2000). Magmatic fragmentation. In: Sigurdsson H (ed) Encyclopedia of volcanoes. Academic Press, New York, pp. 421–430.

Cioni R., Bertagnini A., Santacroce R., Andronico D., (2007). Esplosive activity and eruption scenarios at Somma-Vesuvius (Italy): a review. Journal and Volcanology and Geothermal Research, in press.

Cioni R., Civetta L., Marianelli P., Métrich N., Santacroce R., Sbrana A., (1995). Compositional layering and syneruptive mixing of a periodically refilled shallow magma

chamber: the AD 79 Plinian eruption of Vesuvius. Journal of Petrology, vol. 36 (3), pp. 739-776.

Cioni R., D'Oriano C., Bertagnini A., (2007). Fingerprinting ash deposits by their physical and textural features. Journal of Volcanology and Geophysical Research, on-line available only (http://www.earth-prints.org/handle/2122/2991).

Cioni R., Marianelli P., Santacroce R., (1998). Thermal and compositional evolution of the shallow magma chambers of Vesuvius: evidence from pyroxene phenocrysts and melt inclusions. Journal of Geophysical Research, vol. 103, pp. 18277–18294.

Cioni R., Santacroce R., Sbrana A., (1999b). Pyroclastic deposits as a guide for reconstructing the multi-stage evolution of the Somma-Vesuvius caldera. Bulletin of Volcanology, vol. 60, pp. 207-222.

Cioni R., Sbrana A., Vecci R., (1992) Morphologic features of juvenile pyroclasts from magmatic and phreatomagmatic deposits of Vesuvius. Journal of Volcanology and Geothermal Research, vol. 51, pp. 61–78.

Connor C.B., Hill B.E., Winfrey B., Franklin N.M., La Femina P.C., (2001). Estimation of volcanic hazard from tephra fallout. Natural Hazards Review, vol. 2, pp. 33-42.

D'Oriano C., Poggianti E., Bertagnini A., Cioni R., Landi P., Polacci M., Rosi M., (2005). Changes in eruptive style during the A.D. 1538 Monte Nuovo eruption (Phlegrean Fields, Italy): the role of syneruptive crystallization. Bulletin of Volcanology, vol. 67, pp. 601-621.

Davis J.C., (2003). Statistics and data analysis in geology, John Wiley and Sons, 638 p.

Dehoff R.T., (1991). A geometrically general theory of diffusion controlled coarsening. Acta Metallurgica et Materialia, vol. 39, pp. 2349-60.

Delibrias G., Di Paola G.M., Rosi M., Santacroce R., (1979). La storia eruttiva del complesso vulcanico Somma-Vesuvio ricostruita dalle successioni piroclastiche del Monte Somma. Rendiconti della Società Italiana di Mineralogia e Petrologia, vol. 35, pp. 411–438.

Dellino P., La Volpe L., (1995). Fragmentation versus transportation mechanisms in the pyroclastic sequence of Monte Pilato-Rocche Rosse (Lipari, Italy). Journal of Volcanology and Geothermal Research, vol. 64, pp. 211-232.

Dellino P., La Volpe L., (1996). Image processing analysis in reconstructing fragmentation and transportation mechanism of pyroclastic deposits. The case of Monte Pilato–Rocche Rosse eruptions, Lipari (Aeolian islands, Italy). Journal of Volcanology and Geothermal Research, vol. 71, pp. 13-29.

Eirìksson J., Sigurgeirsson M., Hoelstad T., (1994). Image analysis and morphometry of hydromagmatic and magmatic tephra grains, Reykjanes volcanic system, Iceland. Jokull, vol 44, pp. 41– 56.

Fenn P.M., (1977). The nucleation and growth of alkali feldspars from hydrous melts. Can Mineral, vol. 15, pp. 135–161.

Fierstein J., Hildreth W., (1992). The plinian eruption of 1912 at Novarupta, Katmai National Park, Alaska. Bulletin of Volcanology, vol. 54, pp. 646-684.

Fierstein J., Nathenson M., (1992). Another look at the calculation of fallout tephra volumes. Bulletin of Volcanology, vol. 54, pp. 156–167.

Fisher R.V., Schmincke H.U., (1984). Pyroclastic rocks. Springer, Berlin Heidelberg New York.

Foley S.F., Jenner G.A., (2004). Trace element partitioning in lamproitic magmas—the Gaussberg olivine leucitite. Lithos, vol. 75, pp. 19– 38.

Fulignati P., Marianelli P., Santacroce R., Sbrana A., (2000). The skarn shell of the 1944 Vesuvius magma chamber. Genesis and P-T-X conditions from melt and fluid inclusion data. European Journal of Mineralogy, vol. 12 (5), pp. 1025-1039.

Gao S., Liu X., Yuan H., Hattendorf B., Günther D., Chen L., Hu S., (2002). Determination of forty two major and trace elements in USGS and NIST SRM glasses by Laser Ablation-Inductively Coupled Plasma-Mass Spectrometry. Geostandards Newsletter, vol. 26, pp. 181-196.

Gardner C.A., Cashman K.V., Neal C.A., (1998). Tephra-fall deposits from the 1992 eruption of Crater Peak, Alaska: implications of clast textures for eruptive processes. Bulletin of Volcanology, vol. 59, pp. 537–555.

Gardner J.E., Burgisser A., Hort M., Rutherford M., (2006). Experimental and model constraints on degassing of magma during ascent and eruption. Geological Society of America, Special Paper 402, pp.99-113. DOI: 10.1130/2006.2402(04).

Gardner J.E., Thomas R.M.E., Jaupart C., Tait S., (1996). Fragmentation of magma during Plinian volcanic eruptions. Bulletin of Volcanology, vol. 58, pp. 144–162.

Geschwind C.H. and Rutherford M. J., (1995). Crystallization of microlites during magma ascent: the fluid mechanics of 1980–1986 eruptions at Mount St Helens. Bulletin of Volcanology, vol. 57 (5), pp. 356-370.

Günther D., Heinrich C.A, (1999). Comparison of ablation behaviour of 266 nm ND:YAG and 193 nm ArF excimer lasers for LA-ICP-MS analysis. Journal of Analitical Athomic Spectrometry, vol. 14, pp. 1396-1374.

Günther D., Jackson S.E., Longerich H., (1999). Laser ablation and arc/spark solid sample introduction into inductively coupled plasma-mass spectrometers. Spectrochimica Acta, vol. 54B, pp. 381-409.

Halter W.E., Pettke T., Heinrich C.A., Rothen-Rutishauser B., (2002). Major to trace element analysis of melt inclusions by laser-ablation ICP-MS: methods of quantification. Chemical Geology, vol. 183, pp. 63–86.

Hammer J.E., Cashman K.V., Hoblitt R.P., Newman S., (1999). Degassing and microlite crystallization during pre-climactic events of the 1991 eruption of Mt. Pinatubo, Philippines. Bulletin of Volcanology, vol. 60, pp. 355–380.

Hammer J.E., Rutherford M. J., (2002). An experimental study of the kinetics of decompression-induced crystallization in silicic melt. Journal of Geophysical Research, vol. 107, NO. B1, 2021, 10.1029/2001JB000281.

Hanson G.N, (1980). Rare Earth Elements in petrogenetic studies of igneous systems. Annual Review of Earth and Planetary Sciences, vol. 8, pp. 371-406.

Hedberg H.D., (1994). International stratigraphic guide, 2nd edn. The International Union of Geological Sciences and The Geological Society of America, Boulder.

Heiken G., (1972). Morphology and Petrography of Volcanic Ashes. Geology Society of America Bulletin, vol., 83, pp. 1961-1988.

Heiken G., (1974). An atlas of volcanic ash. Smithsonian Contributions of Earth Science, vol. 12, pp. 1-101.

Heiken G., Wohletz K.H., (1985). Volcanic Ash. University of California Press, Berkeley, California, 245p.

Heiken G., Wohletz, K., (1991). Fragmentation processes in explosive volcanic eruptions. In *Sedimentation in Volcanic Settings* (R. V. Fisher and G. Smith, eds.), Society of Economic Paleontologist and Mineralogist Spec. Pub., vol. 45, pp. 19-26.

Higgins M. D., (1994). Determination of crystal morphology and size from bulk measurements on thin sections: numerical modelling. American mineralogist, vol. 79, pp. 113-19.

Higgins M. D., (1996). Crystal size distributions and other quantitative textural measurements in lavas and tuff from Mt Taranaki (Egmond volcano), New Zealand. Bulletin of Volcanology, vol. 58, pp. 194-204.

Higgins M.D., (2000). Measurement of Crystal Size Distributions. American Mineralogist, vol. 85, pp. 1105-1116.

Higgins M.D., Roberge J., (2007). Three magmatic components in the 1973 eruption of Eldfell volcano, Iceland: Evidence from plagioclase crystal size distribution (CSD) and geochemistry. Journal of Volcanology and Geothermal Research, vol. 161,pp. 247–260.

Honnorez J., Kirst P., (1975). Submarine basaltic volcanism: Morphometric parameters for discriminating hyaloclastites from hyalotuffs, Bulletin of Volcanology, vol. 39, pp. 441–465.

Horn I. and Günther D., (2000). Strategies in U/Pb geochronology by LA-ICP-MS using 266 and 193 nm ablation system. Geoanalysis Abstract.

Horwell C. J., Sparks R.S.J., Brewer T.S., Llewellin E.W., Williamson B.J., (2003). Characterization of respirable volcanic ash from the Soufrière Hills volcano, Montserrat, with implications for human health hazards. Bulletin of Volcanology, vol. 65, pp. 346–362.

Houghton B.F., Smith R.T., (1993). Recycling of magmatic clasts during explosive eruptions: Estimating the true juvenile content of phreatomagmatic volcanic deposits, Bulletin of Volcanology, vol. 55, pp. 414– 420.

Houghton B.F., Wilson C.J.N., (1989). A vesicularity index for pyroclastic deposits. Bulletin of Volcanology, vol. 51, pp. 451–462.

Inmann D.L., (1952). Measures for describing the size distribution of sediments. Journal of Sedimentary Petrology, vol. 22, pp. 125–145.

Ippolito F., Ortolani F., Russo M., (1973). Struttura marginale tirrenica dell'Appennino campano: reinterpretazioni di dati di antiche ricerche di idrocarburi. Memorie della Società Geologica Italiana, vol. 12, pp. 227-250.

Jackson S.E., (2001). The application of Nd:YAG lasers in LA-ICP-MS. In: P.J. Sylvester, Editors, Laser Ablation-ICP-Mass Spectrometry in the Earth Sciences: Principles and Applications, Mineralog. Assoc. Canada (MAC) Short Course Series vol. 29**,** Mineralogical Association of Canada, pp. 29–45.

Jackson, J. E.,(1991). *A User's Guide to Principal Components,* John Wiley and Sons, Inc. pp. 1-25.

Johnston D.M., Houghton B.F., Neall V.E., Ronan K.R., Paton D., (2000). Impact of the 1945 and 1995–96 Ruapehu eruptions, New Zealand: an example of increasing societal vulnerability. Geological Society of American Bulletin, vol. 112, pp. 720–726.

Johnston-Lavis H.J., (1884). The Geology of Monte Somma and Vesuvius, being a Study in Vulcanology Quarterly Journal of the Geological Society*;* vol. 40 (1-4); pp. 35-119. doi: 10.1144/GSL.JGS.1884.40.01-04.05

Kaminsky E., Jaupart C., (1998). The size distribution of pyroclasts and the fragmentation sequence in explosive volcanic eruptions. Journal of Geophysical Research-Solid Earth, vol. 103(B12), pp. 29759-29779.

Klug C., Cashman K., (1994). Vesiculation of May 18, 1980 Mount St Helens magma. Geology, vol. 22, pp. 468-72.

Klug C., Cashman K.V., (1996). Permeability development in vesiculating magmas: implications for fragmentation. Bulletin of Volcanology, vol. 58, pp. 87-100.

Klug C., Cashman K.V., C.R. Bacon C.R., (2002). Structure and physical characteristics of pumice from the climactic eruption of Mt Mazama (Crater Lake), Oregon. Bulletin of Volcanology, vol. 64, pp. 486–501.

Lirer L., Munno R., Petrosino P., Vinci A., (1993). Tephrostratigraphy of the A.D. 79 pyroclastic deposits in the perivolcanic area of Vesuvius (Italy). Journal of Volcanology and Geothermal Research, vol. 58, pp. 133-149.

Lirer L., Pescatore T., Booth B., Walker G.P.L., (1973). Two Plinian pumice-fall deposits from Somma-Vesuvius, Italy. Geological Society of American Bulletin, vol. 84, pp. 759–772.

Lirer L., Vinci A., Alberico I., Gifuni T., Bellucci F., Petrosino P., Tinterri R., (2001). Occurrence of inter-eruption debris flow and hyperconcentrated flood-flow deposits on Vesuvio volcano, Italy. Sedimentary Geology**,** vol. 1, pp. 151-167.

Lofgren G., (1980). Experimental studies on the dymanic crystallization of silicate melts. In: Hargraves, R.B. (ed) Physics of Magmatic Processes. Princeton, N.J.: Princeton Univeristy Press, pp. 487-551.

Longerich H., W. Diegor, (2001). Introduction to mass spectrometry. In: P.J. Sylvester, Editors, Laser Ablation-ICP-Mass Spectrometry in the Earth Sciences: Principles and Applications, Mineralog. Assoc. Canada (MAC) Short Course Series vol. 29**,** Mineralogical Association of Canada, pp. 1–19.

Maria A., Carey S., (2002). Using fractal analysis to quantitatively characterize the shape of volcanic particles. Journal of Geophysical Research, vol. 107 (B11), 2283, doi:10.1029/2001JB000822.

Marianelli P., Métrich N., Sbrana A., (1999). Shallow and deep reservoir involved in magma supply of the 1944 eruption of Vesuvius. Bulletin of Volcanology, vol. 61 (1-2), pp. 48-63.

Marsh B. D., (1998). On the interpretation of crystal size distributions in magmatic systems. Journal of Petrology, vol. 39, pp. 553-600.

Marsh B.D., (1988). Crystal size distribution (CSD) in rocks and the kinetics and dynamics of crystallization I. Theory. Contributions to Mineralogy and Petrology, vol. 99, pp. 277-91.

Martin-Del Pozzo A.L., González-Morán T., Espinasa-Pereña R., Butron M.A. and Reyes M., (2007). Characterization of the Recent Ash Emission at Popocatepetl Volcano, Mexico, in press.

Moore K.R., Duffell H., Nichol A., Searl A., (2002). Monitoring of airborne particulate matter during the eruption of Soufrière Hills Volcano, Montserrat. In: Druitt T.H., Kokelaar B.P. (eds) The eruption of Soufrière Hills Volcano, Montserrat, from 1995 to 1999. Memoir, Geological Society, London, pp. 557-566.

Morra V., Lustrino M., Melluso L., Ricci G., Vannucci R., Zanetti A., d'Amelio A., (2003). Trace element partition coefficients between feldspar, clinopyroxene, biotite, ti-magnetite, apatite and felsic potassic glass from Campi Flegrei (S. Italy). Geophysical Research Abstracts, vol. 5, 05966.

Morrissey M., Zimanowski B., Wohletz K., Buettner R., (2000). Phreatomagmatic fragmentation. In: Sigurdsson H (ed) Encyclopedia of volcanoes. Academic, San Diego, pp. 431–445.

Norman M.D., Griffin W.L., Pearson N.J., Garcia M.O., O'Reilly S.Y., (1998). Quantitative analysis of trace element abundances in glasses and minerals: a comparison of laser ablation inductively coupled plasma mass spectrometry, solution inductively coupled plasma mass spectrometry, proton microprobe and electron microprobe. Journal of Analytical Atomic Spectrometry, vol. 13, pp. 477–482.

Ono K., Watanabe K., Hoshizumi H., Ikebe S., (1995). Ash eruption of the Nakadake crater, Aso Volcano, Southwestern Japan. Journal of Volcanology and Geothermal Research, vol. 66, pp. 137–148.

Ortolani F., Aprile F., (1978). Nuovi dati sulla struttura profonda della Piana Campana a sudest del fiume Volturno. Bollettino della Società Geologica Italiana, vol. 97, pp. 591-608.

Ortolani F., Pagliuca S., (1987). Relationships between volcanism and structures in Campania during the Quaternary. In: P. Di Girolamo (Ed.), The volcaniclastic rocks of Campania (Southern Italy). Rend. Acc. Sc. Fis. Mat. in Napoli. Sp. Is., pp. 215-231.

Patacca E., Sartori R., Scandone P., (1990). Thyrrhenian basin and Apenninic arcs: kinematics relations since late Tortonian Times. Memorie della Società Geologica Italiana, vol. 45, pp. 425-451.

Pearce N.J.G., Denton J.S., Perkins W.T., Westegate J.A., (2007). Correlation and characterisation of individual glass shards from tephra deposits using trace element laser

ablation ICP-MS analyses: current status and future potential. Journal of Quaternary Science (in press), DOI: 10.1002/jqs.1092.

Pearce N.J.G., Perkins W.T., Westgate J.A., Gorton M.P., Jackson S.E., Neal C.R., Chenery S.P., (1997). A compilation of new and published major and trace element data for NIST SRM 610 and NIST SRM 612 glass reference materials. Geostandards Newsletter, vol. 21, pp. 115-144.

Pearce N.J.G., Westgate J.A., Perkins W.T., Eastwood W.J., Shane P., (1999). The application of laser ablation ICP-MS to the analysis of volcanic glass shards from tephra deposits: bulk glass and single shard analysis. Global and Planetary Change, vol. 21, pp. 151–171.

Pearce N.J.G., Westgate J.A., Perkins W.T., Preece S.J., (2004a). The application of ICP-MS methods to tephrochronological problems. Applied Geochemistry, vol. 19, pp. 289–322.

Perkins W.T., Pearce N.J.G., (1995). Mineral microanalysis by laserprobe inductively coupled plasma mass spectrometry. In Microprobe Techniques in the Earth Sciences, Potts PJ, Bowles JFW, Reed SJB, Cave MR (eds). The Mineralogical Society: London.

Perkins W.T., Pearce N.J.G., Westgate J.A., (1997). The development of Laser Ablation ICP-MS and Calibration Strategies: Example from the Analysis of trace elements in volcanic glass shards and sulphide minerals. Geostandards Newsletter, vol. 21, pp. 175-190.

Polacci M., Papale P., Rosi M., (2001). Textural heterogeneities in pumice from the 1991 climactic Pinatubo eruption, and implications for the magma ascent dynamics. Bulletin of Volcanology, vol. 63, pp. 83-97.

Pyle D.M., (1989). The thickness, volume and grain-size of tephra fall deposits. Bulletin of Volcanology, vol. 51, pp. 1-15.

Pyle D.M., (1995). Assessment of the minimum volume of tephra fall deposits. Journal of Volcanology and Geothermal Research, vol. 69, pp. 379-382.

Randoph A.D., Larson M.A., (1971). Theory of Particulate Processes. New York: Academic Press.

Riley C.M., Rose W.I., Bluth G.J.S., (2003). Quantitative shape measurements of distal volcanic ash. Journal of Geophysical Research, vol. 108 (B10), 2504, doi:10.1029/2001JB000818.

Ripley B.D., (1981). Spatial statistics. Wiley, New York

Rojas-Ramos M., Catalan-Vazques M., Martin-Del Pozzo A.L., Garcia-Ojeda E., Villalba-Caloca J., Perez-Neria J., (2001). A seven months prospective study of the respiratory

effects of exposure to ash from Popocatepetl volcano, Mexico**.** Environmental Geochemistry and Health, vol. 23**,** pp. 383–396.

Rolandi G., Maraffi S., Petrosino P., Lirer L., (1993a). The Ottaviano eruption of Somma-Vesuvio (8000 y. B.P.): a magmatic alternating fall and flow-forming eruption. Journal of. Volcanology and Geothermal Research, vol. 58 (1-4), pp. 43-65.

Rolandi G., Mastrolorenzo G., Barrella A.M., Borrelli A., (1993b). The Avellino plinian eruption of Somma-Vesuvius (3760 y. B.P.): the progressive evolution from magmatic to hydromagmatic style. Journal of Volcanology and Geothermal Research, vol. 58, pp. 67-88.

Rolandi G., Petrosino P., McGeehin J.P., (1998). The interplinian activity at Somma Vesuvius in the last 3500 years. Journal of Volcanology and Geothermal Research, vol. 82 (1-4), pp. 19-52.

Rose W.I., (1993). Comment on another look at the calculation of fallout tephra volumes. Bulletin of Volcanolgy, vol. 55, pp. 372-374.

Rose W.I., Bonis S., Stoiber R.E., Keller M., Bickfrod T., (1973). Studies of volcanic ash from two recent Central American eruptions. Bulletin of Volcanology, vol. 37, pp. 338-364.

Rosi M., Principe C., Vecci R., (1993). The 1631 Vesuvius eruption. A reconstruction based on historical and stratigraphical data. Journal of Volcanology and Geothermal Research, vol. 58 (1-4), pp. 151-182.

Rosi M., Santacroce R., (1983). The A.D. 472 "Pollena" eruption: volcanological and petrological data for this poorly-known, Plinian-type event at Vesuvius. Journal of Volcanology and Geothermal Research, vol. 17, pp. 249-271.

Russ J.C. (1986). Practical Stereology. New York: Plenum Press.

Santacroce R., (1987). Somma Vesuvius. CNR Quaderni della Ricerca Scientifica, vol. 114, pp. 251.

Santacroce R., Bertagnini A., Civetta L., Landi P., Sbrana A., (1993). Eruptive dynamics and petrogenetic processes in a very shallow magma reservoir: the 1906 eruption of Vesuvius. Journal of Petrology, 34 (2), pp. 383-425.

Santacroce R., Cioni R., Sulpizio R., Zanchetta G., Donahue D.J., Joron J. L., Marianelli P., Sbrana A., (2007). Age and whole rock-glass compositions of proximal pyroclastics from the major explosive eruptions of Somma-Vesuvius: a review as a tool for distal tephrostratigraphy. Journal of Volcanology and Geothermal Research, in press.

Scandone P., (1979). Origin of the Tyrrenian Sea and the Calabrian Arc. Bollettino della Società Geologica Italiana, vol. 98, pp. 27–34.

Scasso R., Corbella H., Tiberi P., (1994). Sedimentological analysis of the tephra from 12-15 August 1991 eruption of Hudson Volcano. Bulletin of Volcanology, vol. 56, pp. 121-132.

Self S., Sparks R.S.J., (1978). Characteristics of widespread pyroclastic deposits formed by the interaction of silicic magma and water. Bulletin of Volcanology, vol. 41 (3), pp. 196-212.

Sheridan M.F., Marshall J.R., (1983). Interpretation of pyroclast surface features using SEM images. Journal of Volcanolology and Geothermal Research, vol. 16, pp. 153-159.

Sigurdsson H., Carey S., Cornell W., Pescatore T., (1985). The eruption of Vesuvius in A.D. 79. National. Geographic Research, vol. 1, pp. 332–387.

Sparks R.S.J., (1997). Causes and consequences of pressurization in lava dome eruptions. Earth and Planetary Science Letters, vol. 150, pp. 177–189.

Sparks R.S.J., Bursik M.I., Ablay G.J., Thomas R.M.E., Carey S :N., (1992). Sedimentation of tephra by volcanic plumes. 2. Controls on thickness and grain-size variations of tephra fall deposits. Bulletin of Volcanology, vol. 54, pp. 685-695.

Spieler, O., Alidibirov M., and Dingwell D.B., (2004a). Magma fragmentation speed: An experimental determination, Journal of Volcanology and Geothermal Research, vol. 129, pp. 109– 123.

Spieler, O., Kennedy B., Kueppers U., Dingwell D.B., Scheu B., and Taddeucci J., (2004b). The fragmentation threshold of pyroclastic rocks. Earth and Planetary Science Letters, vol. 226 (2004), pp. 139– 148.

Stothers R.B., Rampino M.R., (1983). Volcanic eruptions in the Mediterranean before A.D. 630 from written and archaeological sources. Journal of Geophysical Research, vol. 88, pp. 6357–6371.

Sulpizio R., Mele D., Dellino P., La Volpe L., (2005). A complex, Subpliniantype eruption from low-viscosity, phonolitic to tephri-phonolitic magma: the AD 472 (Pollena) eruption of Somma-Vesuvius, Italy. Bulletin of Volcanology, vol. 67, pp. 743- 767.

Taddeucci J., Pompilio M., Scarlato P., (2002). Monitoring the explosive activity of the July-August 2001 eruption of Mt. Etna (Italy) by ash characterization. Geophysical Research Letters, vol. 29, NO 8, 1230, doi: 10.1029/2001GL014372.

Taddeucci J., Pompilio M., Scarlato P.G., (2004). Conduit processes during the July–August 2001 explosive activity of Mt. Etna (Italy): inferences from glass chemistry and crystal size distribution of ash particles. Journal of Volcanology and Geothermal Research, vol. 137, pp. 33-54.

Taddeucci J., Spieler O., Kennedy B., Pompilio M., Dingwell D.B., Scarlato P., (2004). Experimental and analytical modeling of basaltic ash explosions at Mount Etna, Italy, 2001. Journal of Geophysical Research, vol. 109, B08203, doi:10.1029/2003JB002952.

Toulkeridis T., Buchwaldt R.**,** Addison A., (2007). When volcanoes threaten, scientists warn: The case of Tungurahua. Geotimes*,* vol. 52, pp. 36-39.

Underwood E.E., (1970). Quantitative Stereology. Reading, M.A. : Addison-Wesley van der Berg, E.H., Meesters, A.G.c.A., Kenter, J.A.M. & Sclager W. (2002). Automated separation of touching grains in digital images of thin sections*1. Computers & Geosciences, vol. 28, pp. 179-90.

Walker G.P.L., (1973). Explosive volcanic eruptions – a new classification scheme. Geologische Rundschau, vol. 62, pp. 431–446.

Walker G.P.L., (1981b). Plinian eruptions and their products. Bulletin of Volcanology, vol. 44, pp. 223–240.

Walker G.P.L., Croasdale R., (1971). Characteristics of some basaltic pyroclastics. Bulletin of Volcanology, vol. 35, pp.1-15

Waters C., Boudreau A.E., (1996). A reevaluation of crystal size distributions in chromite cumulates. American Mineralogist, vol. 81, pp.1452-1459.

White W. M, 2007. Geochemistry, an on-line Textbook, www.geo.cornell.edu/geology/classes/geo455/Chapters.HTML.

Wilhelm S., Woerner G., (1996). Crystal size distributions in Jurassic Ferrar flows and sills (Victoria Land, Antarctica): evidence for processes of cooling, nucleation, and crystallisation. Contribution to Mineralogy and Petrology, vol.125, pp. 1–15.

Wilson L., Walker G.P.L, (1987). Explosive volcanic-eruptions, 6, Ejecta dispersal in plinian eruptions- The control of eruption conditions and atmospheric properties. Geophysical Journal of the Royal Astronomical Society, vol. 89, pp. 657-679.

Wohletz K.H., (1983). Mechanisms of hydrovolcanic pyroclast formation: grain-size, scanning electron microscopy, and experimental studies. Journal of Volcanology and Geothermal Research, vol. 17, pp. 31–63.

Zimanowski B., Büttner R., Lorenz V., (1997). Premixing of magma and water in MFCI experiments. Bulletin of Volcanology, vol. 58, pp. 491-495.

Zimanowski B., Wohletz K.H., Dellino P., Büttner R., (2003). The volcanic ash problem. Journal of Volcanology and Geothermal Research, vol. 122, pp. 1-5.